Controlled release of therapeutics from orthopaedic implants

David James King

Submitted in fulfilment of the requirements for the
Degree of Doctor of Philosophy

School of Engineering
College of Science and Engineering
University of Glasgow

May 2020

Abstract

The scientific literature contains a variety of experimental studies centred on the theme of drug delivery from orthopaedic implants (OIs). These experiments cover a wide range of ideas, including the design of novel implant coatings to contain and control drug release; fabrication and testing of prototype drug-filled devices and; preliminary investigations into the effect of the drug when released into the biological environment. There are a multitude of issues that arise from the use of OIs and of these, the problem of orthopaedic associated infection receives particular attention. A key challenge is the prevention of bacterial infection in order to avoid the failure of the associated implant-a serious complication for patients and a significant burden on health care provider resources. A mathematical study is presented in this thesis which covers a wide variety of topics: ranging from a more fundamental investigation into the use of porosity to control the delivery of drug through to more practical modelling of two seemingly similar prototype orthopaedic fixation pins that have vastly different drug release properties. A common theme is the consideration of how experimental conditions shape the outcome of the experiment and indeed the mathematical model adopted. In order to be able to effectively control the release of drug from an orthopaedic implant, one has to have sufficient knowledge of the purpose of the drug: this determines the required dose and release rate. Thus, towards the end of the thesis, a gradual investigation of the growth of bacteria subject to antibiotic release from the aforementioned pins is carried out, to model the interplay between the two processes.

There are several conclusions that arise from the research contained within this thesis. These include: there exists little-to-no mathematical modelling in the field of drug release from OIs; porosity is likely a very fruitful approach to control the release of a drug from an OI; the conditions in which an experiment is carried out is crucial; the dissolving process of a drug is an important process and one that may be the governing means of limiting the rate of drug release; the use of 1D modelling is sometimes sufficient to answer key questions; there is a need for collaborative efforts between mathematicians and experimentalists for the goal of effective drug-releasing OIs to be realised and; the desired outcome, where infection is concerned, is highly dependent on the drug release profile and, critically, the implant surface concentration of, and potency of, the antibiotic delivered.

Contents

Acknowledgements

It has been a long process that led to the construction of this thesis. I have no doubt that it would not be in its current form without being under the supervision of Dr. Sean McGinty. Sean, you gave me the opportunity to work with you, and I thank you for it, I am ever grateful. You have been a great source of encouragement and knowledge to me and my only regret is that I do not share the same passion for football as you do. Regardless, I consider you a friend who has stuck by me when I felt lost and frustrated with my research. I would like to thank Dr. Giuseppe Pontrelli and Dr. Martin Meere, for offering advice and being a source of inspiration. Although not directly involved with my PhD, I wish to thank Professor Sean McKee for providing feedback and insight from the monthly group meetings, your enthusiasm is infectious. I also wish to thank Prof. Nigel Mottram and Dr. Wilson Lamb, who throughout my undergraduate years studying Mathematics, inspired me, and in part, made me who I am today.

Lastly, I want to thank my family for their continued support throughout my PhD. To my mother, Alyson King, thank you for being my friend and providing the emotional support I needed, I knew I could count on you. To my father, David Brown, although you are no longer with us, I know you were proud of me and I thank you for being there for me when I needed you. Finally, even though they will not understand, I thank my snakes Wee Man, Monty and Julius Squeezer, for being a great comfort for me throughout my PhD.

Declaration

With the exception of chapters 1 and 2, which contain necessary introductory material, all work in this thesis was carried out by the author unless otherwise explicitly stated.

Publications and conferences

- D. King and S. McGinty, "Assessing the potential of mathematical modelling in designing drug-releasing orthopaedic implants," Journal of Controlled Release, vol. 239, pp. 49–61, 2016
- S. McGinty, D. King, and G. Pontrelli, "Mathematical modelling of variable porosity coatings for controlled drug release," Medical Engineering and Physics, vol. 45, pp. 51–60, 2017
- Modelling & Experiments in Drug Delivery Systems (MEDDS), University of Coimbra, Portugal, 2016
- Centre for Mathematics Applied to the Life Sciences (CMALS) & SoftMech Modelling Week with Industry, University of Glasgow, Scotland, 2016
- United Kingdom & Ireland Controlled Release Society (UKICRS), University of Strathclyde, Scotland, 2017
- Centre for Mathematics Applied to the Life Sciences (CMALS) Poster presentation at BME away day, Mar Hall, Scotland, 2017
- Modelling & Experiments in Drug Delivery Systems (MEDDS), University of Glasgow, Scotland, 2018
- Centre for Mathematics Applied to the Life Sciences (CMALS) presentation, University of Glasgow, Scotland, 2019

Chapter 1

Introduction

For millions of people the world over, orthopaedic implants (OIs) have allowed for restored mobility, reduced pain and an overall improvement in quality of life [1]. Some examples of current OIs are plates, screws and intramedullary rods for fracture stabilisation and fixation and complete joint replacements such as intervertebral discs, prosthetic hips and knees. OIs that serve as fixation devices provide mechanical stabilisation that allows for load sharing and optimal bone positioning, thus permitting the healing process of bone to occur in more favourable conditions. In the event that a specific bone or joint has deteriorated beyond useful function, a prosthetic can be used as a substitute to restore lost function.

More contemporary OIs began as simple mechanical devices, however, complications arose from their use that could not be overlooked. The physical effect an OI has on bone and surrounding soft tissues; the potential of postsurgical infection; osseointegration (the fixation of the OI to existing bone, such that function and structural rigidity are achieved); the possible foreign body response and; the material used in OI construction are some factors that must be considered.

The endeavour to overcome these complications has resulted in many experimental approaches, investigating the various characteristics of OIs. Alongside the necessary mechanical properties required of any OI [2–4], the materials of their construction must be biocompatible [2,5] and so many studies have been conducted which examine the biocompatibility of novel OI materials [2, 3]. These pieces of research look into aspects such as corrosion resistance and possible cytotoxic effects [2–4].

Aside from any material constraints, one possible avenue of tackling the challenges that can arise from the interaction of an OI and the bioenvironment (e.g. osseointegration, infection, pain and inflammation) is through the local delivery of therapeutics. Postsurgical infection receives much of the focus when considering OI usage. This is not surprising when looking at the economic impact such as in 2005, in the USA, the cost of knee revision surgery alone due to infection was $1.27 billion [6]. In the UK, if infection rates of both primary hip and knee arthroplasties undertaken by the NHS were akin to infection rates within specialist hospitals (0.2%), the predicted savings are over £300 million [6]. However, despite the care taken to sterilise

surgical equipment and the implant to be fitted, infections do occur [5, 7–10].

Local delivery of drugs within an orthopaedic setting is not a new idea. Antibiotics have been locally delivered routinely in surgery, such as joint replacements, for a number of years. However, the method of delivery is for the drug to be mixed within the bone cement that is used for securing the implant in place [5, 9], rather than contained within, or attached to, the implant. This results in little to no control over the release and the antibiotic is usually delivered at concentrations much greater than the Minimum Inhibitory Concentration (MIC) of bacteria [11]. Moreover, the dependency on the porosity and surface area of the bone cement results in difficulty in the control and reproducibility of a desired release profile. Additionally, these problems are compounded by the unpredictable drying process of the bone cement, which results in the formation of cracks and other defects [11]. There has, therefore, been a move away from OIs which require the use of bone cement in recent times. One of the main reasons for this change has been the introduction of newer OI materials which possess a rough surface which can provide a "snug fit", meaning that bone cement is no longer required. From this, there is also the added benefit that there is no longer a wait time for the bone cement to dry. In principle, antibiotics could be coated onto the rough surface of these newer implants, however, no such approach is in regular clinical practice. The local delivery of antibiotics could be the way forward, yet when it comes to OI applications, research has been limited and is likely an area that would yield benefits from not only continued research, but also interdisciplinary approaches.

Experimental research investigating ways to locally deliver drugs from OIs have typically confined a drug within a hollow portion of the studied device [11–13]. There are also approaches looking into modifying the surface/structure of a device [14–16] and applying a coating on the surface of the device [1, 5] as ways to contain a drug. The drug may be an antibacterial/antimicrobial agent to fight off/prevent infection; growth factors to encourage bone healing; an anti-inflammatory to help with the foreign body response or; analgesics for pain relief. The experimental research undertaken thus far shows potential for the development of drug-eluting OIs. However, one significant issue concerning the design of drug releasing OIs is that whilst controlled release would be a great benefit, it is often not apparent what the required release profile is. Controlled release is of paramount importance since toxic effects may occur should the drug concentration be too high and conversely, if the drug concentration is too low, the therapeutic effect may be diminished. The challenge therefore is to be able to maintain a suitable drug concentration such that the therapeutic effect of a drug can be maintained, which in some cases may be for a prolonged period. Adding to this challenge, it should be noted that in the case of antibiotics, the delivery should not allow for the drug concentration to be maintained below the MIC of the infecting bacteria, as long-term exposure is linked with antibiotic resistance [2]. To harness control of the release of drug for a given OI, a sound understanding of drug release mechanisms is necessary.

Valuable insight has been obtained via the numerous experimental approaches in the field. However, when a number of conceivable mechanisms are involved, the relative importance of each is not necessarily clear, thus predicting the effects of changes in system parameters can be challenging. From an experiment it may be the case that diffusion appears to be the dominant release mechanism for a given drug. However, if the drug is replaced with another of a markedly lower solubility, then the release rate of the drug is more likely to be dominated by the rate of dissolution. The variation of other system parameters such as material porosity and thickness of a drug releasing coating; the material the coating is comprised of or; the physico-chemical properties of the drug, may result in the dominant release mechanism altering and could introduce further effects such as swelling, erosion, degradation and even interactions between the drug and the OI material.

There is a distinct lack of mathematical modelling of drug release from OIs in the literature. A few exceptions include simple empirical models, which cannot alone solve the controlled release issue. A mechanistic mathematical description can assist in determining the key drug release mechanisms and reveal the rate limiting processes. The estimation of the values of parameters controlling the system; the quantification of the effect of the interaction with the biological environment and; the assistance in the design of optimisation strategies for controlled drug release are other benefits of mathematical modelling. An important note is that OIs were never designed to carry and release drugs, so integrating drugs into OIs and controlling their release is an immense challenge [17].

Chapter 2

Mathematical modelling of drug releasing OIs: an underexplored research area

2.1 Experimental approaches to enhance current knowledge on drug release

The mechanical and biological processes of bone healing are what will determine the clinical outcome. Therefore, it is essential that OIs must integrate with bone successfully to allow the healing to continue unhindered and assist, if possible. There have been many research approaches investigating various avenues to ensure more reliable OIs. From the experimental literature, there are two prevalent ideas for achieving this, either improving current OIs or producing new device concepts with a view of combining drug release with such a device. Such experiments include prototype drug-filled OI designs [11–13]; the application of a drug releasing coating to the surface of an OI [1, 18]; modifying the surface and/or inner structure of an OI to act as a drug reservoir [16, 19] and; experimenting with new materials for OI construction which could hold drugs [2,20]. This chapter highlights some of the more motivating experimental investigations that cover a broad range of ideas. The questions that arise from such studies and what the potential next steps in the research could be are discussed alongside prospective mathematical modelling techniques.

2.1.1 Drug filled OI designs

With a view to preventing localised infection, Gimeno et al. [12] investigated the release characteristics of the two antibiotics, Linezolid and Cefazolin, from prototype fixation-like pins (Figure 2.1, Image 1). These pins featured a hollow portion in which an antibiotic can be placed in its dry powdered form. All pins were constructed of medical grade stainless-steel, were 25 mm long, with an outer diameter of 6 mm and a wall thickness of 1.6 mm. The key difference between the pins were the number of orifices that were machined into the wall of each which

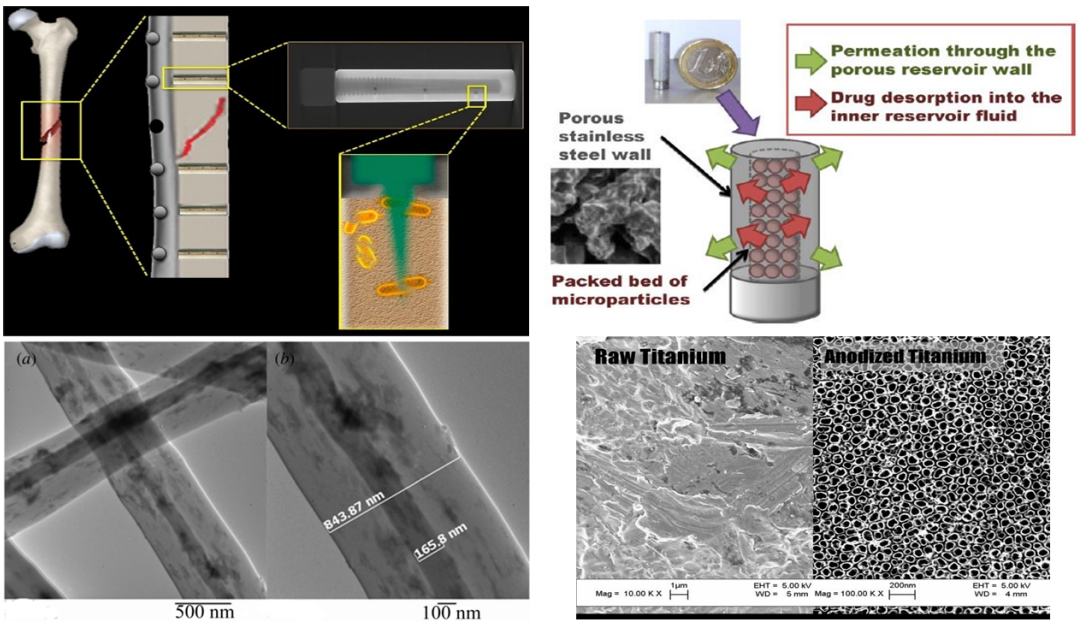

Figure 2.1: A selection of experimental approaches: Image 1 (top left): prototype drug releasing tube by Gimeno et al. [12]. Image 2 (top right): a similar prototype drug releasing tube with porous walls by Perez et al. [13]. Image 3 (bottom left): a view of the nanofibres experimented with by Song et al. [21]. Image 4 (bottom right): an example of a nanotubular surface in the experiments by Aninwene et al. [19].

resulted in pins having either 2, 4, 6 or 8 equidistant orifices, each with a diameter of 0.5 mm. In brief, the *in vitro* experiment was to submerge each of the pins in simulated body fluid (SBF) and measure the amount of antibiotic present in the fluid medium at various time points. The *in vitro* experiments were performed in triplicate, under stirred conditions and without renewal of the SBF. The results demonstrated that the release rate of the antibiotics could be altered by the variation of the number of orifices the pin had. This experiment was a proof-of-concept that drug-holding, hollow fixation pins could be a way of delivering drugs locally. In spite of a difference in solubility by an order of magnitude, the release profiles of the two drugs were similar in the 2-orifice pin case, whilst in the other cases, the difference in the release profiles was more appreciable (Figure 2.2). Also, in the case of the 6 and 8-orifice pins, the release profiles for Linezolid show a plateauing behaviour at early times which were not explained by the authors. Coinciding with the drug release experiment, the authors also demonstrated that the pins were able to release enough antibiotic to combat a bacterial population within the SBF. Each antibiotic was used in the 4 and 6 orifice pins, along with controls with no antibiotic. It was found that both drugs were able to dissolve and diffuse through the orifices into the surrounding medium and begin to eliminate the bacteria, which suggests that these hollow fixation pins could be a way to prevent OI associated infection. As expected, the bacterial population increased within the control setups.

Continuing the pursuit to prevent OI associated infection Perez et al. [13], studied the drug releasing traits of Linezolid from similar pins to that of Gimeno et al. [12]. However, instead

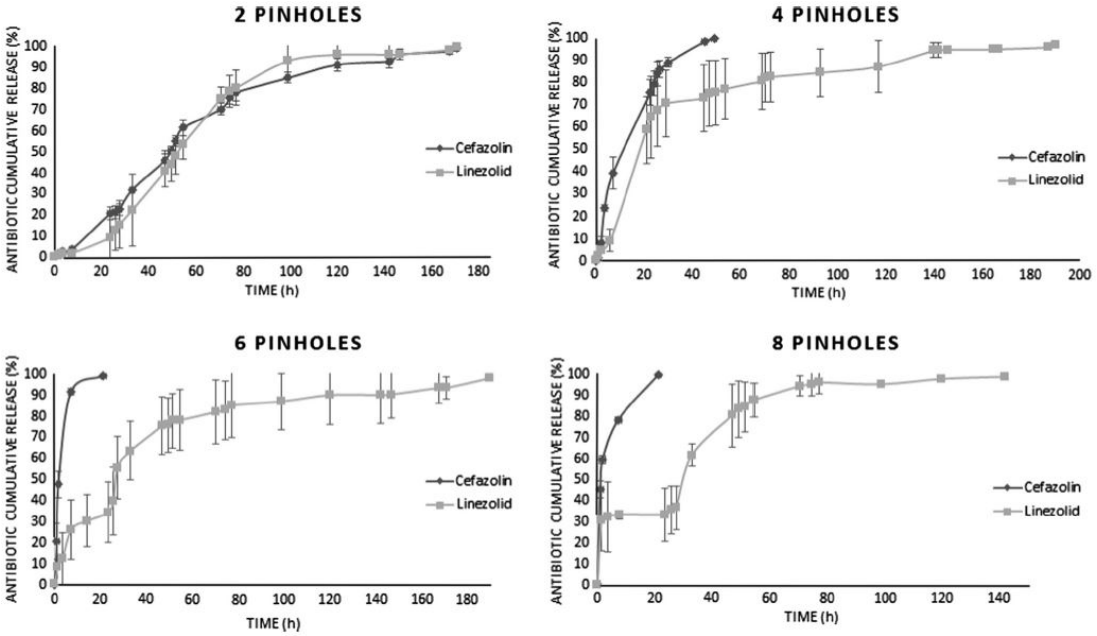

Figure 2.2: Release profiles for drug-filled tubes with varied numbers of orifices. Reproduced from [12].

of orifices to allow the antibiotic to be released, these pins featured a porous wall and rather than loading the antibiotic directly into the hollow portion of the pin, the drug was loaded into spherical mesoporous silica microparticles (Figure 2.1, Image 2) (Figure 2.3(a)). Under stirred conditions, three identical pins were submerged in SBF and the concentration of Linezolid released was measured at several time points. The authors noted that in the later stages of the experiment the final concentration was lower than expected. It was suggested that the SBF had become saturated and so was renewed to permit further release (Figure 2.3(b)). Perez et al. also conducted a bactericidal study and showed that the pin was able to release a sufficient amount of Linezolid to reduce bacterial numbers by three orders of magnitude. The potential flexibility of this device is noted since one could alter the characteristics of both the silica particles and the porous wall of the pin independently to achieve the desired release profile.

This porous pin design was further investigated by Gimeno et al. [11], however, the silica particles were omitted and the hollow section of the pin was loaded with Linezolid powder. This new investigation also featured an *in vivo* ovine study to determine if the porous pin could deliver antibiotic adequately to prevent an infection from taking hold. Biofilm forming bacteria were applied directly to the site of implant insertion and the results showed that after 7 and 9 days, there was no sign of infection, whereas in the control setup, an infection took hold. The authors also carried out a drug release study, by submerging the pin in SBF, their results showed that approximately 75% of the Linezolid was released after 4 days and the remaining drug continued being released over the subsequent 3 days. One particularly interesting outcome is the shape of the release profile, it is almost linear (Figure 2.4) until the later portions of the experiment. This is fairly similar to the release profile from the same porous pin with silica particles in the hollow

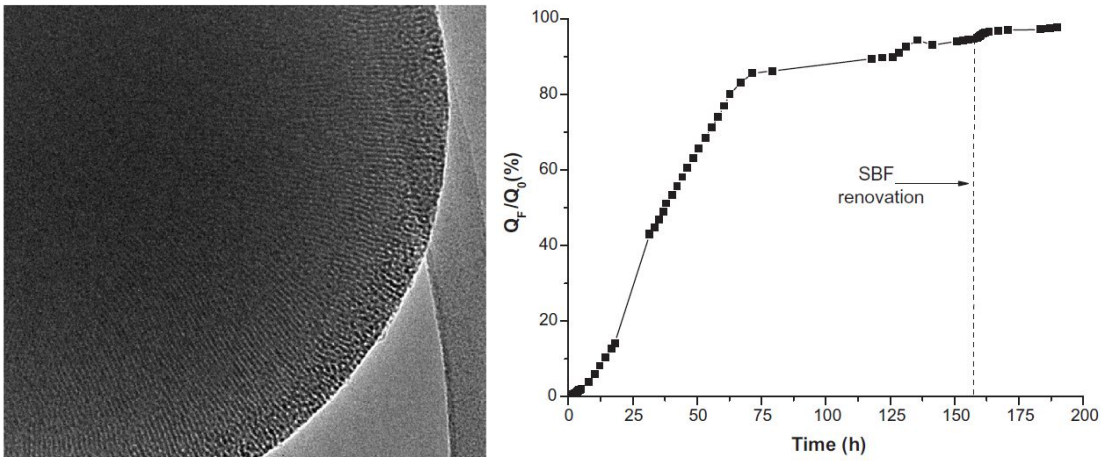

(a) (b)

Figure 2.3: (a) Transmission Electron Microscopy image of a mesoporous silica particle used in the experiment, with visible pores. For a sense of scale, the image is approximately 400 nm across. Adapted from [13]. (b) Release profile from two-stage antibiotic releasing implant, indicating that drug release continued after renewing release media. $Q_F/Q_0(\%)$ represents the cumulative % of drug released. Reproduced from [13].

centre, except for the slight initial delay (Figure 2.3(b)). Otherwise, the release in both plots are almost linear at early times and gently curve towards 100%, which is most likely due to the drugs in either experiment having fully dissolved.

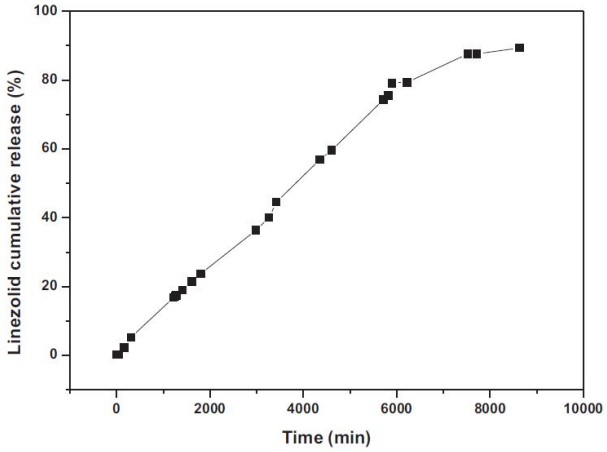

Figure 2.4: Cumulative drug release from a porous hollow implant, showing an almost linear profile. Reproduced from [11].

2.1.2 Drug releasing coatings for OIs

Coatings that release drugs for OIs have garnered much attention in the literature [1, 2, 7, 18, 22]. Such coatings are able to take numerous forms, such as Hydroxyapatite, which has good biocompatibility, but also has been demonstrated to be able to retain and release drugs [1, 2, 18].

However, concerns have been raised about the lack of controllability of the release [21]. Other candidate coatings include durable/biodegradable polymers [10, 23], gels [24] and nanofibers [21, 25].

Kaur et al. investigated the drug releasing potential of the biodegradable polymer poly-D,L-lactide (PDLLA) *in vitro* [23]. PDLLA is in current use as a coating for other medical devices because of its useful qualities: it is both biocompatible and mechanically stable [23]. There were two components to the investigation of particular interest: a bacterial adhesion test and a drug release experiment. For the bacterial adhesion study, the polymer was mixed with varying amounts of Linezolid to give mixtures that were 2.5%, 5% and 10% Linezolid. These mixtures were then used to coat Kirschner wires (K-wires). As controls two K-wires were used that were free of drug, with one having a polymer only coating and the other being a bare wire. These K-wires were then immersed in phosphate buffered saline (PBS) solution containing methicillin-resistant staphylococcus aureus (MRSA). Measurements of the biomass adhering to each wire was carried out using Colony Forming Unit (CFU) and ATP detection assays. The K-wires that were coated with the PDLLA/Linezolid mixtures performed admirably and as expected the drug-free wires seen bacterial growth for all times (Figure 2.5). The results show that the bacteria had difficulty multiplying on the surface of the PDLLA/Linezolid coated wires, a result which could go a long way in preventing infection. It is reported by the authors that the efficacy of devices like the K-wires is dependent on the release profile. It is imperative that the antibiotic concentration is above the MIC and so a high level of initial release followed by a sustained release is what is needed to achieve this. The authors also point out that despite the bacteria not being completely wiped out, the serious reduction in their numbers could allow the immune system to handle the remaining bacteria, thus reducing the likelihood of postsurgical infection.

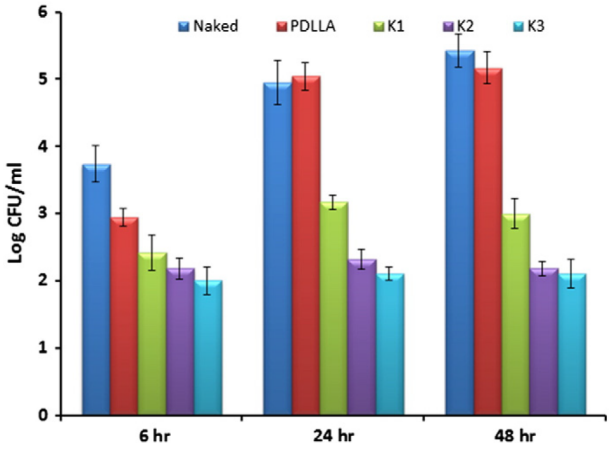

Figure 2.5: Total biomass of MRSA adhered to the various K-wires configurations. PDLLA/Linezolid mixtures used: 2.5%, 5% and 10% indicated by K1, K2 and K3 respectively. Reproduced from [23].

The other interesting part of the study was an investigation into the release of Linezolid from the PDLLA/Linezolid coated K-wires. Each wire was placed into separate tubes containing

PBS solution and at several time points, a sample was taken, and the concentration of Linezolid was determined by two method. One approach was to take the samples and expose them to methicillin-sensitive staphylococcus aureus (MSSA) bacteria and then measure the zone of inhibition to determine the concentration of Linezolid from a standard curve. The other method used was a colorimetric assay in which the samples were treated in accordance with a known method and the level of absorbance of 750nm light alongside a standard curve were used to determine the Linezolid concentration. The results show that a Linezolid concentration above the MIC of MSSA, was sustained for all wires (Figure 2.6). Wires K2 and K3 were reported to sustain Linezolid release and although the concentrations at the end of the experiment were minimal, they were still considerably higher than the MIC. Wire K1 as expected eluted the lowest amount of Linezolid, with a peak around 24 hours and subsequent decline for the remainder of the experiment duration.

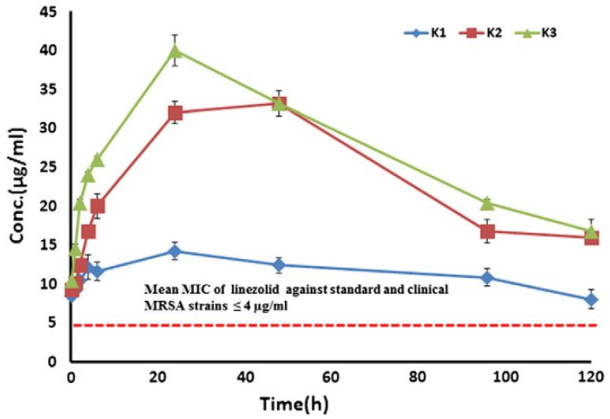

Figure 2.6: Concentration profiles of drug released from K-wires. Three PDLLA/Linezolid mixtures used: 2.5%, 5% and 10% indicated by K1, K2 and K3 respectively. Reproduced from [23].

Argarate et al. [10] investigated the drug-eluting qualities of the biodegradable polymer poly(L-lactic acid) (PLLA), coated onto poly(D,L-lactide-co-lactide) (PLDL) disks. Two drugs were used in the experiment: Dexamethasone (DM) and Eugenol (EG), which gave the coated PLDL disks antibacterial and anti-inflammatory abilities. The disks were coated via a dipping process into solutions of varying concentrations of PLLA. It was observed that the thickness of the coating could be altered through altering the concentration of PLLA in the dipping solution, with increasing concentration increasing the coating thickness. The *in vitro* drug release experiments featured three sets of coating configurations for the disks: a direct coating of EG; a coat of PLLA/EG and; a layer of PLLA/EG followed by a second coat of PLLA/DM. The coated disks were immersed in PBS solution and samples of the solution were taken and replace with fresh PBS at time intervals up to 8 weeks, to determine the amount of drug released.

The authors note of their results (Figure 2.7(a)) that the direct application of EG to the disk surfaces resulted in relatively rapid release compared to the single and two-layer coatings. This is an expected result since the drug is in direct contact with the PBS release medium. It was also

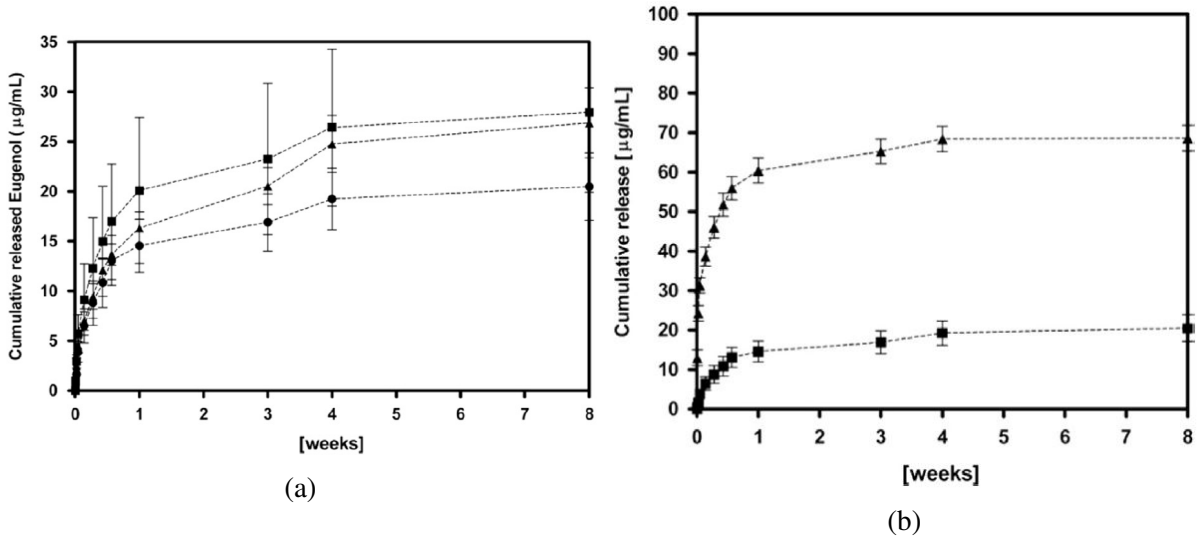

(a) (b)

Figure 2.7: (a) Cumulative release of the drugs from PLDL disks with various coating methods: a direct coating of EG to the disk surface (■), a single layer coating of PLLA/EG (▲) and a two layer coating with the inner layer containing EG and the outer layer containing DM (●). Reproduced from [10]. (b) Cumulative release of the drugs from PLDL disks with two coats of PLLA: The inner layer containing EG (■) and the outer layer containing DM (▲). Reproduced from [10].

shown that the two-layer coated disks released a lesser total amount of drug over the course of the experiment when compared to the disks with a single coating. The authors suggested that this could be due to the presence of the second coat and thus increase the diffusion distance for a drug particle to travel.

The results from the release study in the case of the two-layer coated disks (Figure 2.7(b)) show that DM was released much more quickly than EG, this is likely the consequence of DM being present in the outer layer. This resulted in quick release within the first week, continued sustained release up to 4 weeks and afterwards began to plateau up to 8 weeks. The inner layer managed to release most of the EG within the first 4 days of the experiment after which release plateaued up to 8 weeks. The authors went on to conclude that the controlled sequential release of two drugs from a two-layered coating of PLLA on implants is conceivable. It is also noteworthy that the authors obtained a uniformly distributed coating on the disks, which also featured a rough surface, which could assist in the adhesion of osteoblasts to the implant surface, thus helping to achieve osseointegration.

Radin et al. [24] investigated the release of Vancomycin from thin sol-gel films applied to titanium alloy plates, which is a material used in implant manufacture. The authors were inspired to conduct this research as sol-gel films are biocompatible and at room temperature, silica sol-gels are porous and nanostructured, features which are suited for controlled release of drugs. The research looked at two components of interest: the degradation of the sol-gel films and the release of Vancomycin into a PBS release media, which was renewed daily. The experimental setup involved the repeated dipping of titanium alloy strips into sol-gel solutions containing

differing Vancomycin concentrations, to build layers on the surface of the strips.

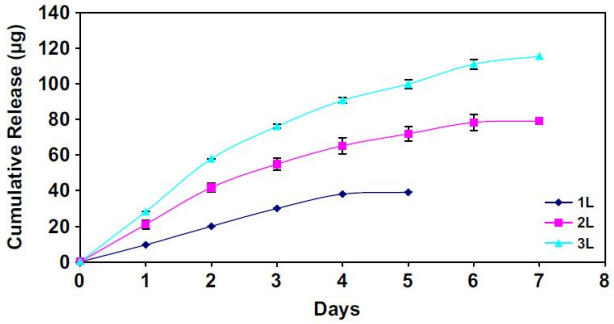

Figure 2.8: Cumulative release of vancomycin from sol-gel films with different layers (L). Reproduced from [24].

The results show that the release rate of Vancomycin from the coatings that consisted of two and three layers was considerably greater than that of a single layer of the sol-gel. Along with a quicker release rate, it was found that the duration of release and the total amount of Vancomycin release was also greater (Figure 2.8).

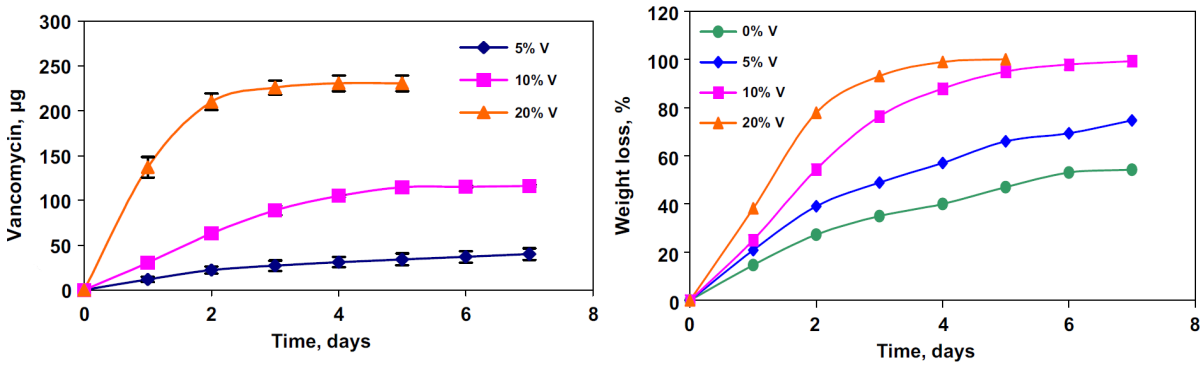

Figure 2.9: (a) Cumulative release of Vancomycin. Reproduced from [24]. (b)Weight loss of the films due to degradation. Reproduced from [24]. Each film was composed of three layers with varying percentage loadings of Vancomycin.

The authors inferred from the results that there is a connection between the degradation of the sol-gel coating and the release rates (Figure 2.9). The results suggest that the quicker the sol-gel degrades, the faster the Vancomycin is released. This suggests that a governing release mechanism in the release of Vancomycin from the sol-gel films is the degradation of the coatings. For long-term release, the authors determined that multi-layer coatings could be a reliable approach and the fine tuning of the release profile could be done by varying the parameters during the production of the sol-gel. The authors also note the possibility of combining layers with different drugs in each, such as antibiotics to fight infection and growth factors to aid in bone healing [24].

Song et al. [21] fabricated two-layer nanofibres (NFs) and investigated their osseointegration qualities and potential as a controlled drug release device. The NFs feature a distinctive core-sheath structure (Figure 2.1, Image 3), with the outer sheath formed from a mixture of polycaprolactone (PCL) and collagen (Col) and the inner core constructed from polyvinyl alcohol (PVA) and hydroxyapatite nanorods (HA). The PCL/Col sheath was noted as being suitable for its role as an outer barrier due to its slow degradation rate and thus ability to reduce the drug release rate. The inclusion of HA in the core of the NFs increased the mechanical strength of the NFs, but also provided a rough surface to mimic the surface of bone and it is within the core of the NFs that a drug can be held for delivery. The authors conducted drug release and bactericidal studies.

The drug release experiments conducted to assess the potential of the NFs as a drug-delivering coating involved the use of two drugs: the antibiotic Doxycycline (Doxy) and the anti-inflammatory Dexamethasone (Dex). NFs loaded with either Doxy or Dex were immersed in distilled water, which was neither stirred nor renewed, and concentrations of the drugs were determined with a spectrometer. The results showed that PVA fibres mixed with Doxy exhibited a burst release of the drug within the first 10 hours and full release within 48 hours. The addition of a PCL sheath however, extended the duration of Doxy release to over 700 hours and was believed to be the case due to the slow degradation of the PCL sheath. The release of Dex displayed similar behaviour to Doxy when mixed with PVA fibres, with a burst release in the initial 10 hours and complete elution within 48 hours. The addition of a PCL sheath extended the release duration to over to 150 hours, with yet another increase in duration when Dex was also included in the PCL sheath. In the bactericidal study involving MRSA, it was found that when Doxy was blended with both the sheath and the core of the NFs, release was sustained and continued for 152 hours, providing a long-lasting antibacterial effect. It was concluded by the authors that the results demonstrated that the NFs were capable of delivering Doxy in a controlled manner such that it effectively inhibited MRSA from colonisation and thus reduce the likelihood of infection *in vitro*. Through the measurement of the adhesion of cells to the NFs, the experimental results also showed that the NFs exhibited good biocompatibility and osteoconductivity.

2.1.3 Surface and structure alterations of OI materials for drug release

The materials that are used for OI construction have also been given considerable attention in the literature. There are many aspects to this research area as proposed materials must not have a deleterious effect on the body and must have the necessary physical properties before they can be used. Such properties may be mechanical in nature, such as material strength in the form of compression, tensile and fatigue. Other material characteristics may be consequential, such as a toxic influence on surrounding tissues. The innate properties are not the only consideration, for example, how and where the material will be used will also impact its suitability, for example, corrosion and attrition resistance may be required over others [2]. Focussing on the controlled

delivery of drug from OIs, one area that has produced many published works is the investigation of nanotubes. The alteration of a material surface such that it forms nanotubes presents several advantages, for example, they could act as reservoirs for a drug on the surface of an OI [2, 14, 16, 18] and some nanotubes are noted to have great mechanical strength, which could be used as a way to reinforce OIs [14, 18]. It has also been suggested that the nanotubes of some metal oxides could improve osseointegration [14, 16, 18] and cell viability [16, 18, 22] since the rough surface produced by nanotubes is more similar to bone than materials with a smooth surface [14, 16, 18, 19].

Aninwene et al. investigated the effect of a drug-coated anodised nanotubular surface (Figure 2.1, Image 4) on the adhesion of osteoblasts [19]. The surface roughness of titanium is increased through anodising, this means the surface is more akin to bone. The inspiration behind this research is because it is surfaces like bone that osteoblasts tend to attach to because of the chemistry involved and the surface roughness [19]. The authors remarked that these nanotubes could have the potential to act as reservoirs for anti-inflammatories, antibiotics and drugs which promote the growth of bone [19].

In the experiments, the authors prepared anodised and non-anodised titanium samples, which through physical adsorption or by soaking with SBF, were loaded with either a mixture of penicillin/streptomycin or dexamethasone. These drug-loaded samples then had osteoblasts seeded onto them, which were then cultured. The findings of the experiments showed that the osteoblasts adhered in far greater numbers to the anodised versus non-anodised titanium (Figure 2.10). Additionally, the titanium samples loaded with drugs by soaking with SBF, released more drug than the samples load by physical adsorption. These are encouraging results since the enhanced adhesion of osteoblasts to the nanotube surface of anodised titanium is a potential way to promote better osseointegration. The additional drug delivery prospects from the nanotubes would go a long way in addressing the other issues from the use of OIs, in particular, postsurgical infection.

Lyndon et al. reviewed numerous examples of metallic implant drug/device combinations and outlined some promising materials for use in orthopaedic applications [2]. One material in particular was a biodegradable porous magnesium foam investigated by Aghion et al. as way to carry and release drugs. The authors used a powdered form of a magnesium alloy to create the magnesium foam. The level of porosity of the resultant foam was determined by the quantity of spacer material (ammonium hydrogen carbonate with a diameter range of 50-200 μm) used in the mixture. The final stage in the preparation of the magnesium foam was to evaporate the spacer material using a high temperature. In the experiment, two mixtures were used which contained 10% and 25% spacer material, which gave the magnesium foams an average pore size of 40μm and 140μm respectively. The authors noted that the 25% spacer material mixture produced a foam which contained many more interconnected pores than the 10% mixture, whose interconnected pores were only close to the surface. This was recognised as a limiting factor in

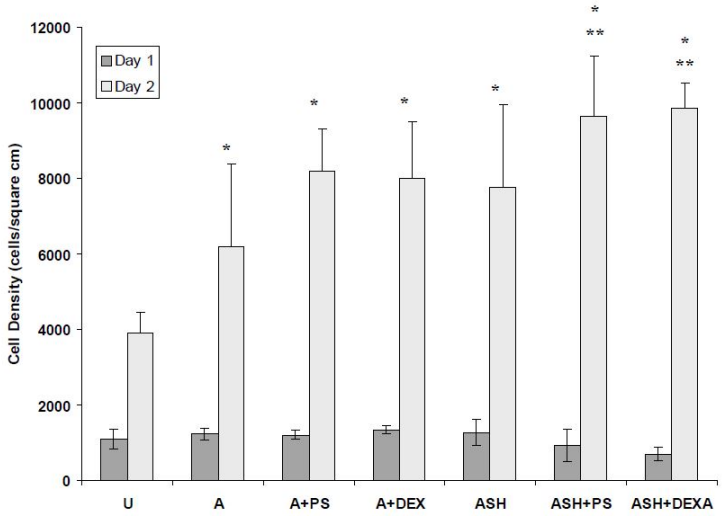

Figure 2.10: Osteoblast density after culturing for 1 and 2 days, following drug release from anodised nanotubes. **Abbreviations:** U, unanodised Ti; A, anodised Ti; A+PS, anodised+penicillin/streptomycin physical adsorption; A+DEX, anodised+dexamethasone physical adsorption; ASH, anodised, heat-treated and SBF-soaked Ti; ASH+PS, as previous but with penicillin/streptomycin; ASH+DEXA, as previous but with dexamethasone. Reproduced from [19].

how much drug could be retained and then released by the 10% spacer material foam. The antibiotic gentamicin was loaded into the magnesium foams by immersion in a concentrated gentamicin solution and then evaporating the water, leaving behind solid gentamicin within the foams.

The gentamicin-loaded foams were submerged in PBS solution and the concentration of gentamicin was measured at various time points. The results showed that the foam made from 10% spacer material released gentamicin relatively quickly. This result is most likely due to the lack of interconnected pores throughout this foam. In contrast, the 25% spacer foam, whose interconnected pores were much greater in number and hence increased porosity, was able to hold and release considerably more gentamicin (Figure 2.11(a)).

The result of the experiment demonstrated that the porosity of the magnesium foam can be changed by using varying amounts of spacer material. The consequence of this being with greater porosity comes a greater capacity for holding a drug. The authors noted that the degradation rate of the magnesium foam increased with increasing spacer material content (Figure 2.11(b)). This was expected since the greater the amount of spacer material used, increased the level of porosity and thus increased the surface area of the magnesium foam exposed to the PBS solution [20]. However, the authors note that the time taken for a high spacer material foam to degrade completely may limit the foam to applications where prolonged periods of time in the healing process are absent [20].

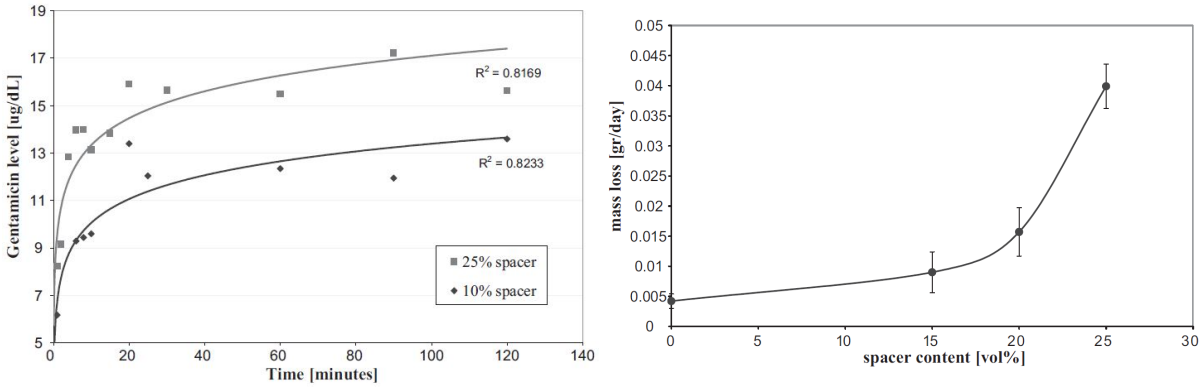

(a) (b)

Figure 2.11: (a) Concentration profiles of gentamicin release from magnesium foams with 10% and 25% spacer material. Reproduced from [20]. (b) Mass loss of magnesium foam in PBS solution against spacer content. Reproduced from [20].

2.2 Mathematical methods

As has been demonstrated in the preceding section, there is much in the way of experimental approaches that investigate the potential of drug release from OIs. However, it appears that mathematical modelling of drug release from OIs *specifically* is non-existent. This is rather odd considering the innumerable examples of mathematical modelling research which has been conducted in other drug release applications. Such applications include the modelling of drug release from particular implants, such as coronary stents, or from specific materials and structures, such as porous layers and nanotubes, some of which may be used in OI construction. It is therefore possible that there is published modelling research that through modification could find future use in the design of drug-releasing OIs. The literature suggests that the release of drugs from OIs is increasing in acceptance as the future of orthopaedic medicine. Therefore, it would be prudent to consider the research conducted on other types of implants. In the early development of coronary stents, for example, a purely empirical method was used to inform their design, specifically via a combination of *in vitro* tests and *ex vivo*/*in vivo* animal studies. However, it came to be understood that the use of computational and mathematical modelling could reduce the number of experiments needed and also potentially save on the cost and time requirements of further experimentation [26, 27]. Moreover, mathematical modelling can provide additional insights and understanding, which is not easily attainable from experiments alone.

It is wise to remember that a mathematical model and an experiment are approximation tools. A model of drug release from an implant may fit experimental data very well and thus could be considered sufficient. However, the release process may not be modelled fully, as it is usually the case that simplifications are required. A predictive mathematical model can be a useful tool for the enhancement of understanding of the whole release process. The confidence in such a model can be increased through the variation of experimental conditions and comparing

the data with the model prediction. With validation of the model, input parameters can be varied and the release profiles compared, this can be done without the need to repeat similar experiments [26, 28].

2.2.1 Drug release mechanisms

There is a necessary level of understanding of the mechanisms that can control drug release before one can examine a system mathematically. This can be challenging since these are often not known for a particular system *a priori*. However, through the comparison of experimental data and the results of an initial model, one can determine if further mechanisms are required or if current mechanisms are redundant. The release of drug from an implant can be the result of several mechanisms, for example, diffusion, dissolution, convection, erosion, swelling and degradation and others. However, it is recognised that the reason for a particular drug release scenario is frequently due to a combination of different mechanisms [26, 27, 29]. There is a level of ambiguity however, with the term "release mechanism" as noted by Fredenberg et al. [30]. Depending on the context it could indicate the manner in which drug particles are transported or alternatively, it could be a description of the processes that can affect the release rate. Fredenberg et al. note that the release mechanisms involved with poly(lactic-co-glycolic acid)-based (PLGA) implants are diffusion, erosion and osmotic pumping. The processes that govern the release rate are believed to be initially diffusion-controlled, with erosion/degradation in the subsequent stages [30]. The authors point out that additional knowledge is essential to form a clearer understanding of the whole system, which will arise from insight into the fundamental processes which drive release mechanisms, for example, erosion, hydrolysis and water absorption [30]. The authors continue by stating that in the case of PLGA-based implants, there are four ways for the release of drug to occur: the erosion of the polymer; drug transport through the polymer; drug transport through water within pores and; osmotic pumping [30]. It is from an understanding of the mechanisms of drug release and the processes that govern them, that a greater comprehension of drug delivery will arise, which in turn will inform the mathematical modelling.

2.2.2 Some existing mathematical models describing release mechanisms

There exists a myriad of mathematical models that attempt to describe drug release mechanisms in a wide array of applications. For example, McGinty and Pontrelli [31] created a general model which coupled drug release and tissue absorption, which may have applicability in the modelling of particular OIs.

The two regions in the idealised geometry of Figure 2.12 are denoted by a subscript 0 for the drug-loaded polymer layer of thickness l_0 and 1 for the tissue layer of thickness l_1. This notation is similarly applied to the variables and parameters used in the model. The two variables b and

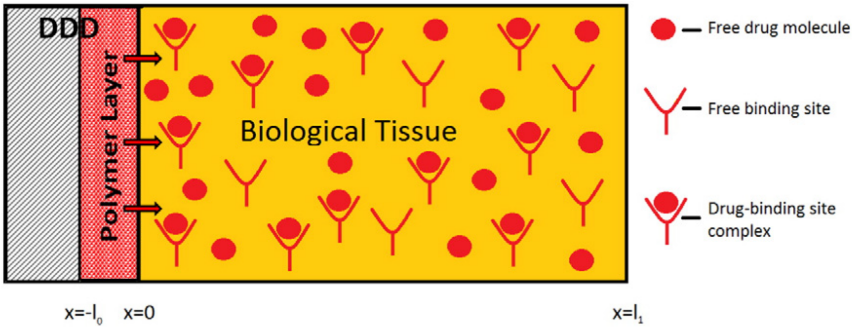

Figure 2.12: The geometry considered by McGinty and Pontrelli. Reproduced from [31].

c represent the bound and free drug respectively. The polymer layer parameters D_0, β_0 and S denote the drug diffusion coefficient in the polymer, drug solubility and the drug dissolution rate, respectively. The tissue layer parameters v_1 and D_1 signify the fluid velocity and diffusion coefficients within the tissue, respectively. Additionally, k_1^f, k_1^r and b_{max} are the drug binding and unbinding rates and the density of binding sites, respectively. The value of the parameter α is within the range $0 \leq \alpha \leq 1$ and is dependent on the dissolution model considered. The Noyes-Whitney approach to dissolution is the assumption that the dissolution rate is proportional to the difference in the drug solubility and the drug concentration [32], which would correspond to a linear dissolution equation with $\alpha = 0$. A nonlinear dissolution model was also considered in which $\alpha = 2/3$. This nonlinear model was provided by Hixson and Crowell [33], who considered how the changes to the surface of dissolving particles influenced the dissolution rate. Later work by Frenning [34] considered this nonlinear dissolution model within the context of drug delivery. McGinty and Pontrelli note that the value of α is likely subject to the chemical properties and structure of the dissolving drug. How the drug is contained within the device and the geometry of the device itself may also have a role in the influence of α. Therefore, there are other possible values that α could take that are very much applicable. It is in light of this that McGinty and Pontrelli additionally consider the case where $\alpha = 1$ which gives the simplest nonlinear coupling between the bound and free drug phases. The model is given by:

$$\frac{\partial b_0}{\partial t} = -\beta_0 b_0^\alpha \left(S - c_0\right), \quad -l_0 < x < 0, \quad t > 0, \tag{2.1}$$

$$\frac{\partial c_0}{\partial t} = D_0 \frac{\partial^2 c_0}{\partial x^2} + \beta_0 b_0^\alpha \left(S - c_0\right), \quad -l_1 < x < 0, \quad t > 0, \tag{2.2}$$

$$\frac{\partial b_1}{\partial t} = k_1^f c_1 \left(b_{max} - b_1\right) - k_1^r b_1, \quad 0 < x < l_1, \quad t > 0, \tag{2.3}$$

$$\frac{\partial c_1}{\partial t} = D_1 \frac{\partial^2 c_1}{\partial x^2} - v_1 \frac{\partial c_1}{\partial x} - k_1^f c_1 \left(b_{max} - b_1\right) + k_1^r b_1, \quad 0 < x < l_1, \quad t > 0, \tag{2.4}$$

$$-D_0 \frac{\partial c_0}{\partial x} = -D_1 \frac{\partial c_1}{\partial x} + v c_1, \quad -D_1 \frac{\partial c_1}{\partial x} = P\left(c_0 - c_1\right), \quad x = 0, \quad t > 0, \tag{2.5}$$

$$-D_0 \frac{\partial c_0}{\partial x} = \gamma_0 c_0, \quad x = -l_0, \quad t > 0, \tag{2.6}$$

$$-D_1\frac{\partial c_1}{\partial x} + v_1 c_1 = \gamma_1 c_1, \quad x = l_1, \quad t > 0, \tag{2.7}$$

$$c_0 = 0, \quad -l_1 \leq x \leq 0, \quad b_0 = 0, \quad 0 < x \leq l_1, \quad t = 0, \tag{2.8}$$

$$c_1 = 0, \quad -l_1 < x \leq 0, \quad b_1 = B, \quad 0 < x \leq l_1, \quad t = 0. \tag{2.9}$$

The model is adaptable in that it permits the coupling of the diffusion and dissolution processes in a polymer layer, with the latter depending on the solubility of the drug and the dissolution rate. There are some assumptions made in the generation of the model which include the instantaneous wetting of the polymer and the idealised one-dimensional (1D) geometry. The distinction of this model from others in the literature however, is the inclusion of drug transport in tissue after release. Models which account for the biological impact on the release and function of a drug are likely to be necessary when *in vivo* scenarios are to be modelled. Thus, the generality of this model is what opens it to see use in a variety of cases where a mix of diffusion, advection and drug binding are present. Arguably the main feature of the model is the ability to consider a variety of binding mechanisms which may be a combination of linear/nonlinear, reversible/irreversible and saturable/non-saturable processes [31]. Therefore, the binding processes of drugs released from OIs to tissue could be potentially studied with this model. McGinty and Pontrelli also note that special cases of the model which could arise under certain circumstances that allow one process to become more influential than any other. One example given is the scenario in which the drug has a very low initial concentration and/or a very high solubility. This would likely result in rapid drug dissolution, meaning that a model centred on diffusion may be sufficient [31]. The authors also include a case study in which the model is used to predict release of drug from a drug-eluting stent (DES). The predictions show reasonable agreement with experimental data in Figure 2.13 [31].

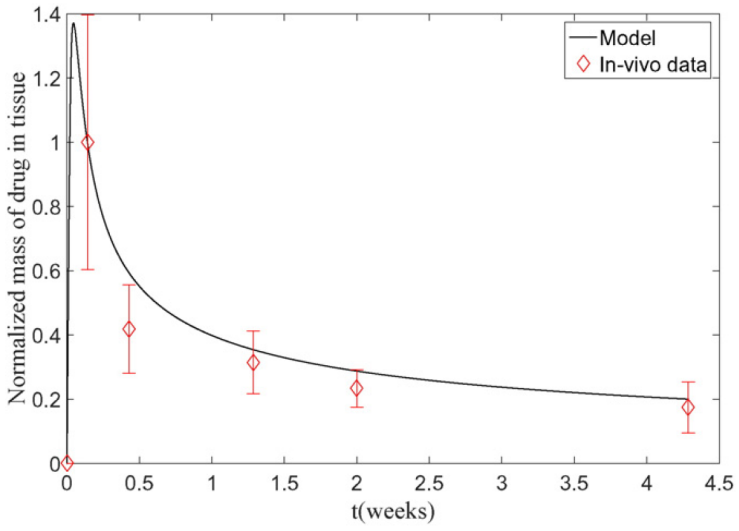

Figure 2.13: Model and *in vivo* experimental data comparison of total mass of drug in tissue. Plot points are normalised with respect to the mass of first experimental time point (day 1). Reproduced from [31].

An article by Lauzon et al. reviewed delivery systems of growth factors and presented several existing mathematical “models” that have the potential to model growth factor release. The models presented considered only the release of growth factors and not the transport and interaction with tissue. The transport mechanisms of the semi-empirical/empirical and mechanistic models shown are diffusion, erosion and swelling. The authors note another mechanism which involves the potential interaction between the delivery device and the drug, which are known as “Affinity-based models” [35]. The models considered do have limitations in that they largely centre on assumptions such as constant diffusivity and infinite sink boundary conditions. It is also noted that some models do not include the influence of other processes which could affect the release, such as consumption of the drug in the tissue. There is some caution to be taken though as the tabulated presentation of the “models” by Lauzon et al. may suggest that a “pick and mix" method to mathematical modelling is suitable and in such a case, one would select a model based on the system under examination. This however, is not always appropriate: simply picking from a list of models does not provide the necessary details of its applicability regarding modelling assumptions, which will inform how the underlying equations are derived. One major consequence is that all the models presented are in 1D, but one must understand if such a simplification is justified as there are devices which cannot be reduced to such a simple geometry. Another part of the modelling process to consider is how the experiments were carried out, for instance, was the release setup stirred? If not, then perhaps infinite sink conditions are not suitable.

The authors do acknowledge that the presented models may not be suitable for modelling the release of growth factors. One major consideration is that the size of a growth factor protein relative to a drug particle may be much greater [36], which suggests that the size of molecules may need to be accounted for in a model. Although flexible, mathematical modelling must be applied with some foresight and knowledge of the phenomena that govern release. Additionally, device geometry and experimental conditions must also be included in the modelling process. There are general models in the literature however, this generality may only be applicable within a set of precise circumstances. Suppose a model of a particular system has reliable predictive abilities, then what is known about the validity of this model if for example there is a change to device geometry of experimental procedure? One should certainly not assume that it is still valid, in fact one may need to go back to the drawing board. Although the modelling process can be meticulous at times, it does have its place in the understanding of drug delivery as a whole. The examination of the fundamental processes in a mathematical way may provide insight as to the processes that drive drug release. Some of these processes within a given system may be more influential than others and so their identification is paramount when in quest of controlled drug delivery from OIs. With background on the subject of release mechanisms, the following sections highlight some other mathematical modelling research and what may be learned from these works.

2.2.3 Mathematical modelling of drug release from some potential OI materials

Tzur-Balter et al. studied the release of the anti-cancer drug Mitoxantrone (MTX) from mesoporous silicon and mathematically modelled the release [37]. The experiment consisted of two samples of the mesoporous silicon, one in an unaltered form (PSi) and the other altered chemically with 1-dodecene (d-PSi). This chemical treatment is hydrosilylation, which generates hydrogen bonding on the surface of the silicon, which results in a more stable silicon sample [38]. The silicon samples were then loaded with MTX and immersed in PBS solution, with MTX release measured via media sampling and replacing the sample volume with fresh PBS solution.

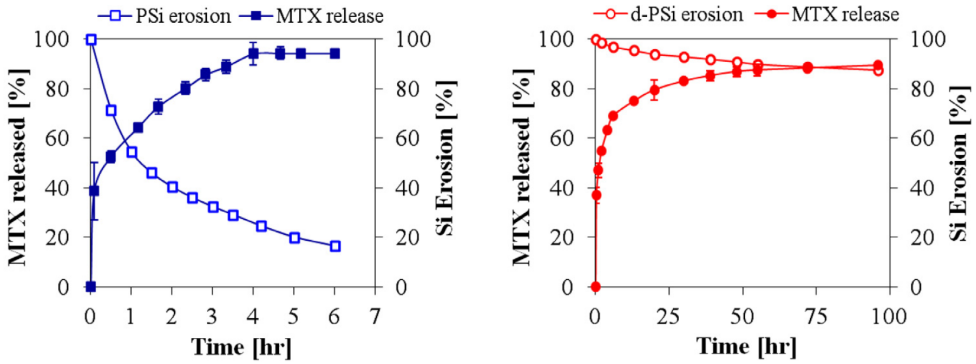

Figure 2.14: MTX release and silicon degradation plots. The left image is for the unaltered silicone sample (PSi) and the right image is for the chemically altered silicon sample (d-PSi). Reproduced from [37].

The experimental results (Figure 2.14) show that the d-Psi sample was able to extend the release of MTX over a considerably longer period of time and resist erosion to a greater degree when compared to the Psi sample. Based on these results, the authors hypothesised that the release of MTX from the Psi sample was due to two mechanisms: the erosion of the sample and diffusion of MTX [37]. Given that the d-Psi sample had not eroded nearly as much and that the release was considerably slower, the authors suggested that the release of MTX was governed mainly by diffusion [37].

The mathematical modelling portion of the work by Tzur-Balter et al. used a fairly simple model which combined the diffusion of MTX and the erosion of the silicon samples. The modelling consisted of a 1D domain of length L $(0 \leq z \leq L)$, a zero-flux condition at $z = 0$, an infinite sink condition at $z = L$ and initial concentration C_0 (Figure 2.15). Based on Fick's second law, the authors used Crank's known classical solution [39], which was altered to include the effects of the erosion of the silicon samples:

$$q(t) = 1 - \frac{m(t)}{m_0} = 1 - \frac{8}{\pi^2} \sum_{n=0}^{\infty} (2n+1)^{-2} \exp\left[\left(-\frac{2n+1}{2L} \right)^2 \int_0^t \sigma(t) dt \right], \tag{2.10}$$

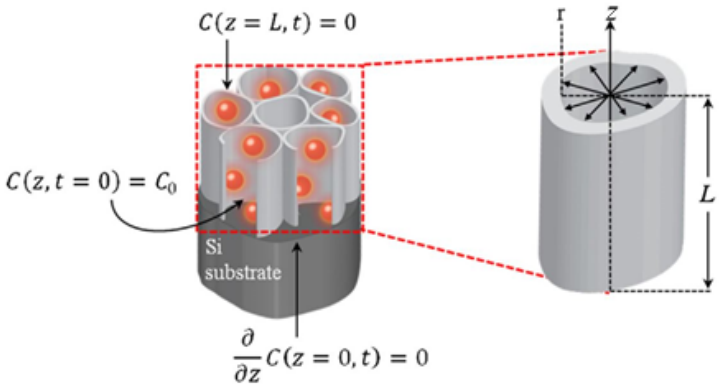

Figure 2.15: Image showing an idealised porous section of a silicon sample and where the boundary conditions are applied, along with the initial condition. Reproduced from [37].

where the cumulative fraction of drug released is given by q, $m(t)$ is the mass of MTX in the domain at time t and m_0 is the initial mass of MTX. The authors assumed that the influence of erosion of the silicon sample would only affect diffusivity, therefore the drug release equation was altered to reflect this. This time-dependent diffusivity of MTX, as a result of erosion, is represented by $\sigma(t)$, which includes one of two polynomial functions, $f_2(x)$ or $g_2(x)$, where $x = D_s/D_p$, which is the ratio of the hydrodynamic diameter of the solute and the average pore diameter [37]. Therefore, x is a measure of the level of accessibility of the pores to the solute. Function $f_2(x)$ accounts for the hampered Brownian motion of the solute inside the pores, however, the authors note this function does not account for pore wall-solvent-solute interactions, solute polydispersity or pore shape. Additionally, $f_2(x)$ does not account for the increase in Silicon concentration due to the degradation of the pores and its potential interaction with the solute and solvent. To address this, the authors adopted another function $g_2(x)$, which accounted for all of these processes [37].

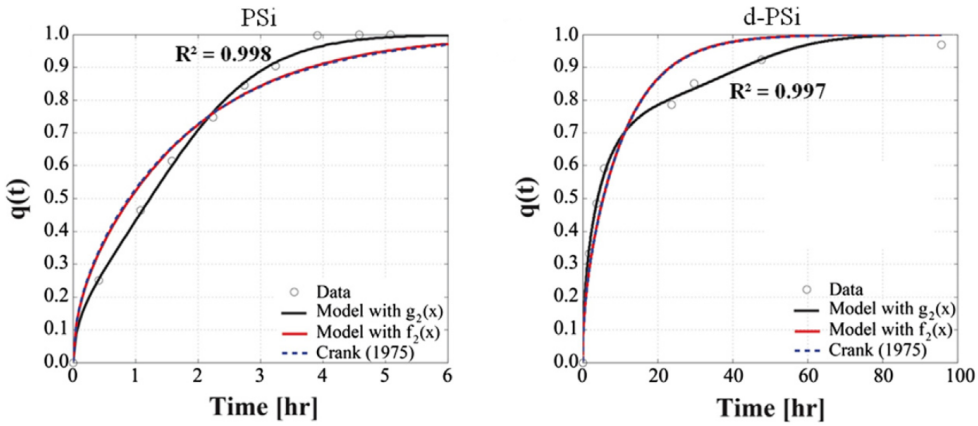

Figure 2.16: Image showing the comparison of predicted MTX release from the model of Tzur-Balter et al. $(g_2(x))$, a model which does not consider the influence of erosion $(f_2(x))$ and the unaltered Crank solution. Plotted alongside the model predictions is the experimental data from both mesoporous silicon samples. Reproduced from [37].

The model using $g_2(x)$ was able to fit the experimental results well and to further its validity, release profiles from the unaltered Crank solution and a similar model which utilised $f_2(x)$ were compared (Figure 2.16). The two models for comparison did not fit the data well, with both overestimating the release in the early stages and underestimating in the later stages. To showcase the adaptability of the model, the authors fit the model to experimental data from the work of Anglin et al. [40], which focussed on the release of dexamethasone from dodecyl modified porous silicon. The model involving $g_2(x)$ is a relatively good fit to the data when compared to the original Crank solution and the model with function $f_2(x)$ (Figure 2.17). Tzur-Balter et al. do note that if there had also been data on the mass change of the silicon during degradation, then their model would be a considerably better fit [37].

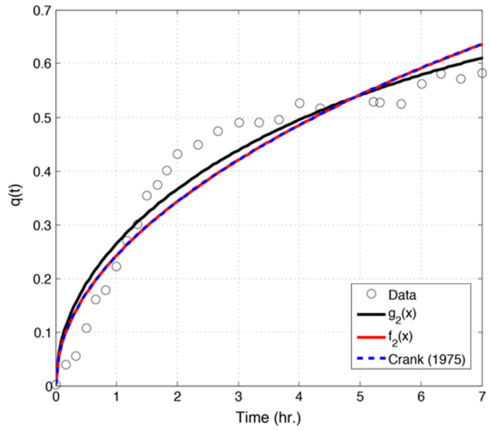

Figure 2.17: Plot showing the predicted release of Dexamethasone by the model of Tzur-Balter et al. $(g_2(x))$, the model which ignores the influence of erosion $(f_2(x))$ and the unaltered Crank solution. The experimental data obtained by Anglin et al. [40] is plotted alongside the predictions. Reproduced from [37].

Kumeria et al. investigated Indomethacin release from nanoporous anodic alumina (NAA) (Figure 2.18(a)) whilst under dynamic flow conditions (Figure 2.18(b)) [15]. Aluminium foils were prepared such that a self-ordered, nanoporous structure was produced on their surface, with a pore diameter and depth of 30-35nm and 4.5-5μm respectively [15].The authors loaded the NAA samples with Indomethacin in three ways: firstly, the drug was loaded into the pores and adhered to the surface, secondly, the drug was loaded only into the pores and lastly, the drug was adhered the surface only [15]. The prepared samples were then immersed in PBS solution and subjected to a variety of flow speeds, which were 0, 10, 30 and 50 μL/min. The authors used reflectometric interference spectroscopy to measure the *in-situ* release of Indomethacin from the NAA samples via a change in effective optical thickness [15]. The authors note that the conventional approach to evaluating drug release, being batch observation under static conditions, does not include the dynamic *in vivo* effects on the release [15]. The inspiration to include flow conditions arises from the fact that whilst under static conditions, the release media is constantly receiving drug. This could eventually lead to the saturation of the release medium and from that

a reduction in the concentration gradient, which will have an impact on the release rate. This effect could potentially give rise to inaccurate results, therefore, it was seen as a more accurate approach and more akin to the *in vivo* scenario, to examine drug release *in-situ*, under flow conditions.

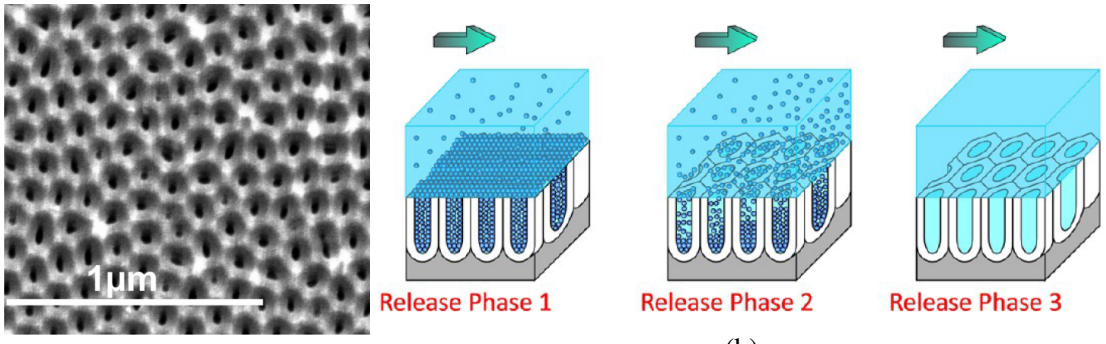

(a) (b)

Figure 2.18: (a) Scanning electron microscope image of the top of a of prepared NAA sample showing the top of the nanoporous surface. Adapted from [15]. (b) Illustration of drug release phases from nanoporous alumina under dynamic flow. Reproduced from [15].

The results were compared to drug release data under static conditions and theoretical data via a modified Higuchi equation to ascertain the foremost mechanism of release [15]. The release results from the static conditions show a burst release from the NAA samples, with approximately 75% of the Indomethacin being released in the first 100 minutes (Figure 2.21(a)). During the subsequent 4 days the release is then steady until complete (Figure 2.21(b)). The Higuchi equation is based on Fick's second law and is used to model drug release from insoluble matrices [15]. It includes the assumptions of infinite sink conditions and an initial drug concentration which is much greater than the solubility of the drug. This equation is able to describe the diffusion governed release of water-soluble and poorly water-soluble drugs from non-degradable porous devices [15]. The modified Higuchi equation used by Kumeria et al. was:

$$\frac{m(t)}{M} = at^{1/2} + b \Rightarrow \frac{dm(t)}{dt} = kt^{-1/2}, \tag{2.11}$$

where a and b are fitting parameters, M is the initial mass of drug and k is $Ma/2$. Fitting parameter b was an addition to the standard Higuchi equation to capture the effects of fluid flow on the release of Indomethacin. However, this only has the effect of shifting the curve up and down the y-axis in a plot. Therefore, the addition of parameter b is not likely to adequately capture the influence the flow has on the release.

Flow Rate (μL/min)	k (μg/min$^{1/2}$)	Coefficient of Determination (R^2)
0	3.02 ± 0.02	0.95
10	2.23 ± 0.02	0.95
30	2.80 ± 0.06	0.99
50	12.47 ± 0.04	0.96

Table 2.1: Table showing the rate constants k obtained via the fitting of the modified Higuchi equation [15]

The authors confirmed that the release of Indomethacin was inversely proportional to the square root of time, this fact is obtained from the Higuchi equation directly. Through the fitting of the model to the release results, the authors were able to determine the release rates of Indomethacin from the NAA samples. Kumeria et al. noted that the flow rates 10 and 30 μL/min gave rise to release rates that were comparable to the release rate obtained from static conditions. In contrast to the lower flow rates, the flow rate of 50 μL/min, the release rate was approximately 4 times the release rate under static conditions. The results established that the release rate of Indomethacin was increased when faster fluid flow was introduced. Through a combination of the experimental results and the simple mathematical model, the authors concluded that fluid flow can have a significant influence on the release rate of a drug [15]. The model fitting produced high coefficients of determination, which validated that the release was dependent on the square root of time, an important attribute of diffusion [15].

2.2.4 Mathematical modelling of drug release from porous structures

McGinty et al. produced a mathematical model to predict drug release from nanoporous materials, with special cases of drug release from smooth surface and nanotubular systems [41]. Although the focus of their work was on polymer-free DES, the authors note that the model could in principle be applied to general drug-releasing implants with a nanoporous structure. The model assumes that the drug must dissolve on a moving boundary before diffusive transport through the water-filled pores and the release medium can occur (Figure 2.19). Also considered is the possibility that drug particles may adhere to the walls of the pores, to account for this a linear reversible reaction component is used in the model. A variety of scenarios are considered and the model is derived based on the assumption that the release medium is unstirred.

The concentrations of the drug in water, within the pores and adhered to the pore walls are denoted by c_w, c_p and c_b respectively. D_w, D_a and D_e are the free, apparent and effective diffusion coefficients respectively, c_s is the drug solubility, K is the dissociation constant. Parameters ϕ and ϕ_b represent the overall porosity and the volume fraction of the pores in which drug particles could adhere to the pore walls, L_d is the initial thickness of the layer of drug within the porous

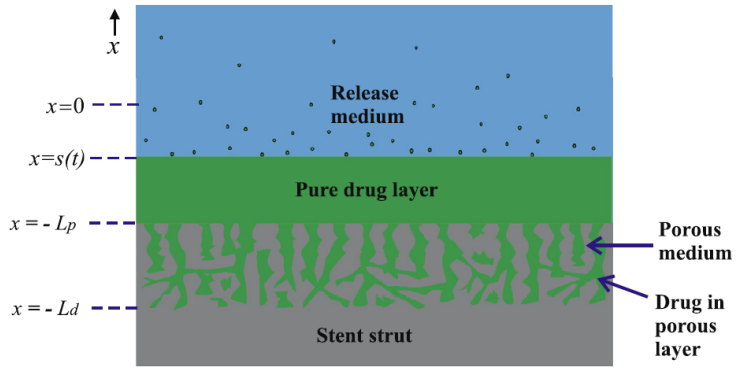

Figure 2.19: Figure showing an example geometry considered by the authors with a bulk nanoporous layer and coated with a pure drug layer. The release medium is assumed to be semi-infinite. Reproduced from [41].

region and c_0 denotes the initial drug concentration. The location of the moving boundary $s(t)$ is governed by an appropriate Stefan condition. With the equilibrium assumption (adsorption and desorption rates are much quicker than the diffusivity), the model is:

$$\frac{\partial c_w}{\partial t} = D_w \frac{\partial^2 c_w}{\partial x^2}, \quad 0 < x < \infty, \quad t > 0, \tag{2.12}$$

$$\frac{\partial c_p}{\partial t} = D_a \frac{\partial^2 c_p}{\partial x^2}, \quad c_b = \frac{\phi c_p}{\phi_b K}, \quad s(t) < x < 0, \quad t > 0, \tag{2.13}$$

$$c_p = c_w, \quad -D_e \frac{\partial c_p}{\partial x} = -D_w \frac{\partial c_w}{\partial x} \quad \text{on} \quad x = 0, \quad t > 0, \tag{2.14}$$

$$c_p = c_s, \quad -D_a \frac{\partial c_p}{\partial x} = \frac{ds}{dt} \quad \text{on} \quad x = s(t), \quad t > 0, \tag{2.15}$$

$$c_w \to 0 \quad \text{as} \quad x \to \infty, \quad t > 0, \quad c_w = 0 \quad \text{at} \quad t = 0, \quad x > 0, \tag{2.16}$$

$$c_p = c_0 \quad \text{at} \quad t = 0, \quad -L_d < x < 0, \quad s(t = 0) = 0. \tag{2.17}$$

The diffusion coefficient associated with this equation was known as the apparent diffusion coefficient due to the many effects the parameter accounted for. These effects included adsorption, desorption, porosity, tortuosity and constrictivity [41]. The well-posed moving boundary problem was solved analytically using the self-similarity method by way of the Boltzmann variable $x/\sqrt{t}$. The ability to obtain an analytical solution provides the advantage of being able to compute the release profile directly. The solutions to the model (2.12-2.17) are:

$$c_w(x,t) = \frac{c_s \operatorname{erfc}\left(\dfrac{x}{2\sqrt{D_w t}}\right)}{1 - \dfrac{\sqrt{D_a D_w}}{D_e} \operatorname{erf}\left(-\dfrac{\theta}{2\sqrt{D_a}}\right)}, \quad 0 < x < \infty, \quad t > 0, \tag{2.18}$$

$$c_p(x,t) = \frac{c_s\left(1 - \frac{\sqrt{D_a D_w}}{D_e}\operatorname{erf}\left(\frac{x}{2\sqrt{D_a t}}\right)\right)}{1 - \frac{\sqrt{D_a D_w}}{D_e}\operatorname{erf}\left(-\frac{\theta}{2\sqrt{D_a}}\right)}, \quad 0 < x < \infty, \quad t > 0, \tag{2.19}$$

where θ is determined by solving:

$$\frac{\theta}{2\sqrt{D_a}}\exp\left(\frac{\theta^2}{4D_a}\right)\left(1 - \frac{\sqrt{D_a D_w}}{D_e}\operatorname{erf}\left(-\frac{\theta}{2\sqrt{D_a}}\right)\right) = \frac{1}{\sqrt{\pi}}\frac{\sqrt{D_a D_w}}{D_e}\frac{c_s}{c_0 - c_s}. \tag{2.20}$$

The other cases considered are accounted for by altering the model slightly, such as choosing particular values for some parameters. These cases include modelling release from a nanotubular system, release from a smooth surface system in which pure drug is directly coated to a DES and the case where the drug solubility is very low relative to the initial concentration ($c_s \ll c_0$). Lastly, as part of the unstirred set of cases, a two-stage release is considered, in which drug a pure drug layer is released from the DES surface and then further release of drug stored in the nanoporous structure. The authors also consider cases in which the release medium is stirred including release from a nanoporous DES and release from a pure drug layer like in the unstirred case [41]. Key system parameters which have a governing influence on the release are identified through a sensitivity analysis. Device design suggestions are provided by the authors such that a required release profile may be generated that is appropriate for a specific application. Through mathematical analysis of the underlying equations, the authors demonstrated that the rate of drug dissolution in the stirred case was an order of magnitude quicker than in the unstirred case.

2.2.5 Mathematical modelling of drug release from stents and lessons to be learned

One area which has received much mathematical modelling attention is in the understanding of drug release from coronary stents and the mechanisms that drive it. Through a multidisciplinary approach, the modelling of stents has been used in conjunction with experimentation to model drug release from a variety of stents and help determine the governing release mechanisms [28]. A review article by McGinty [28] categorised modelling research into three groups, those of: drug release from durable and biodegradable polymer coatings; uptake of drug into arterial tissues through the use of diffusion-convection-reaction equations and; the coupling of the release of drug and tissue absorption. The models range from simple 1D single layer convection-diffusion systems to multi-layered 3D systems which include the effects of nonlinear saturable binding, anisotropy and coupling with blood flow. The model outputs include analytical and numerical solutions. The review by McGinty emphasises that for mathematical modelling to give the greatest benefit, the model must reflect the experimental conditions which produced the raw data. The author also notes the importance for mathematical modelling to run simultane-

ously with experimentation and the accuracy of which are only as good as the accuracy of the experimental inputs. This is especially the case when the model output is particularly sensitive to variation one or more parameters.

For instance, Sirianni et al. modelled the release of drug from a commercially available stent and noted that models based on diffusion, dissolution and osmotic gradients were able to achieve a good fit with their experimental data [42]. The agreeable fit to the experimental data was possible through the variation of the model parameters, although some parameter values were unrealistic [42]. This example serves to underline the necessary care required when deriving a mathematical model for a given system and its output interpretation, this is particularly the case if many system parameters have been inversely estimated. Although a model may fit experimental data well with a particular set of parameters, the addition of other parameters to account for other processes will reduce the confidence in the model [42]. One alternative is through the use of a simpler semi-empirical model such as the Peppas equation [43], which utilises a small number of nonphysical parameters. However, a mechanistic model has the advantage over semi-empirical models in that its parameters are physically relevant and may, in principle, be experimentally determined. With accurate parameters and experimental validation, the confidence increase in the predictive capabilities of a mechanistic model outweigh the benefits of other modelling approaches. When considering drug release mechanisms and likely coatings, stents are similar to OIs, however, the environments where they are used are very different. For instance, coronary stents will experience pulsatile blood flow which is a stark contrast to what an OI must undergo, such as greater mechanical loading. However, the differences in the biological setting between these devices does not impede the use of mathematical modelling. On the contrary, mathematical modelling has been employed in various applications, each presenting different biological environment challenges. For example, ocular drug delivery [44], such as therapeutic eye drops, results in the drug experiencing fluid flow in the form of the lacrimal fluid of the eye; tablets may be used to deliver a drug [45] and so the drug is immersed in gastric fluid and surrounded by the gastro-intestinal tract and; in transdermal drug delivery, such as patches, the drug must pass through a relatively tough barrier, the stratum corneum, before it is able to reach the capillary beds.

Despite the bioenvironmental challenges, mathematical modelling has been a useful tool in the prediction of drug release and in the optimising of device design. However, it is often the case that due to the time and cost constraints associated with *in vivo* experimentation, experimentalists and device manufacturers regularly examine drug release in an *in vitro* environment. Irrespective of the bioenvironment destined for the device, such *in vitro* experiments are usually conducted under static or agitated release mediums. Although such conditions are not necessarily able to imitate the *in vivo* case accurately, they are able to produce a useful release profile, which may be compared with the results of other device designs. Additionally, the *in vitro* case allows one to test the repeatability of the release profile relatively easily compared to the *in vivo*

case. Also, when *in vitro* experimentation is compared with a suitable mathematical model, insight may be obtained as to what the mechanisms of release are and the relative importance of each. Therefore, the lack of *in vivo* experimentation need not hamper the research effort. The mathematical approaches which can simulate drug release under static or agitated conditions can form an additional layer of assistance when attempting to characterise drug release and the mechanisms involved. It must be stressed however, that the potential influence of the bioenvironment on the release can be important, more so if the intention is the comparison with *in vivo* data. Bozsak et al., for instance, coupled blood flow and the binding of drug in tissue to their model of drug release from stents [46]. From their work, the authors acknowledge that to be able to fully optimise stent design, then such a comprehensive model is necessary. As it stands, the literature highlights the benefits and challenges of OIs, however, they are far from insurmountable. The release of drug from coronary stents was studied thoroughly through a combination of experimentation and mathematical modelling which yielded positive results. It is for these reasons that orthopaedic devices should receive the mathematical modelling treatment to aid in the prediction of drug release and assist in implant design.

2.3 Summary and thesis outline

This chapter clearly highlights the significant level of activity within the experimental research community to investigate ways of incorporating drugs within OIs. It further highlights the lack of mathematical modelling of drug release from OIs whilst showcasing several existing mathematical models from other applications that may prove a useful starting point for modelling in this new area. Whilst the experimental approaches do vary considerably, a number of common themes emerge:

1. The use of porosity to control drug release [11, 13, 19, 20];
2. The influence of the particular experimental conditions on drug release [10, 12, 19–21, 23, 24];
3. Using antibiotic release as a means of combating infection [10–13, 19–21, 23, 24].

The remainder of this thesis is dedicated to exploring these issues through mathematical modelling. In chapter 3, the extent to which drug release can be controlled by varying the porosity of a material is explored through a relatively simple two-layer diffusion model. Chapter 4 considers the porous pin by Gimeno et al. [11] and provides a model to describe dissolution and subsequent drug release under a variety of experimental conditions, making use of analytical and numerical solutions and spanning 1D-3D models. In chapter 5, drug release from the pin featuring different numbers of orifices by Gimeno et al. [12] is modelled. Particular attention

is paid to demonstrating that a 3D model is required and on the influence of the stirring experimental conditions on drug release from the pin. In chapter 6, a simple model of bacterial colonisation is presented, including an exploration of how drug release from the afore-modelled OIs (chapters 4-5) influence infection dynamics. Finally, in chapter 7, the results of the research are summarised, along with some suggestions for future work.

Chapter 3

Modelling of drug release from variable porosity systems

In chapter 2, many examples of experimental approaches to containing and controlling release of drugs from OIs were highlighted. A common theme was the use of porosity to control the release of a drug and much of the experimental research was focussed on the containment, transport through and release of drug from a single porous coating (layer). In this chapter, through the development of a relatively simple mathematical model, the extent to which porosity, and specifically variable porosity, can assist in the control of the release of drug from an OI is investigated.

There are two important components to a porous medium that can influence how a drug particle moves through it: the level of porosity and the tortuosity. The porosity of a porous medium is the ratio of the volume of void spaces within the medium to the total volume of the medium [47]. The tortuosity of a porous medium is a measure of how circuitous the pores of the medium are, which may result in longer diffusion distances for a drug particle [48]. It is evident that the movement of drug particles in a porous medium will be influenced by the relative thickness of each layer, the initial drug distribution throughout the layers and the relative levels of porosity. By generating release profiles based on a mathematical model, one can assess the impact of varying design parameters such as coating porosity; how the drug is loaded and its distribution; the physicochemical properties of the drug and; the type of release medium. Here, a two-layered structure is considered over a single layer and the basic question of what effect the contrast in microstructural properties (porosity, tortuosity) across the layers has on the drug release process is examined. The key difference between the layers is their respective effective diffusivities, although in principle, their thickness and initial drug loading could also be different. Through analysis of an appropriate mathematical model of the drug release process, it may be possible to determine the benefits of substituting single-layer porous coatings with two-layer or multi-layer coatings and, perhaps most usefully, determine the microstructural properties of corresponding layers so that a pre-defined drug release profile is obtained. Multi-layer systems are also worth

investigating since in principle, the porosity can be spatially varying and the simplest way to account for this is to add layers.

It is important to examine how porosity and tortuosity are accounted for when investigating mass transport through a porous medium. Consider a representative elementary volume of a porous medium, with porosity, ϕ, and tortuosity, τ. Within the medium there is a smaller, effective diffusion coefficient, D^e, due to a smaller cross-sectional area for diffusion, relative to a free-fluid phase. Suppose there are two pores, A and B, which span the medium (Figure 3.1). Particles that move along pore A must travel a longer diffusive distance than particles travelling through pore B.

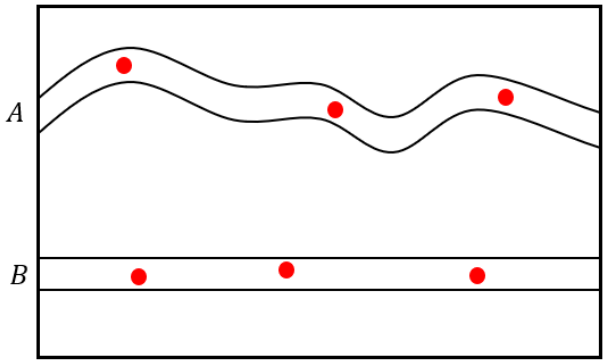

Figure 3.1: Illustration showing a tortuous pore (A) and a linear pore (B) in a porous medium in which drug particles (red dots) must travel.

This results in the apparent concentration gradient being less than the free concentration gradient. This effect can be accounted for most simply through an adjustment to Fick's first law [48, p. 191] [49, 50]:

$$\boldsymbol{J} = -D^e \nabla c_V = -\frac{\phi}{\tau} D \nabla c_V, \tag{3.1}$$

where D is the free-diffusion coefficient and c_V is the volume-averaged concentration. This measure of the flux and concentration gradient are with respect to the overall physical dimensions of the porous media, not just the void spaces where diffusion may occur. Therefore, rather than a volume-averaged concentration over the entire porous media, an intrinsic concentration, c, is used, which accounts for the concentration of drug solely within the voids of the porous medium. This intrinsic concentration is defined to be the ratio of the mass of drug within the voids and the volume of the voids accessible to the drug particles. This alternative definition of concentration may be achieved through the multiplication of the time derivative of concentration with ϕ in the diffusion equation:

$$\phi \frac{\partial c}{\partial t} = D^e \nabla^2 c. \tag{3.2}$$

It should be noted that equations (3.1-3.2) are a simplification that assumes the porous media is homogeneous and the impact of the media's porosity and tortuosity on drug transport through the media is a change to the drug's free-diffusion coefficient. Although equation (3.2) is a

simplified model of drug transport through porous media, it has formed the basis of scientific research in a number of applications, including catalytic reactors and porous electrode theory [51] [52, p. 104]. It is likely that the level of porosity and the tortuosity are linked in some way and this may be accounted for through the use of the Millington and Quirk or Bruggeman relations, for example, which are defined as $\tau = \phi^{-1/3}$ and $\tau = \phi^{-1/2}$, respectively [53, 54]. There also exists stochastic approaches to modelling diffusion through porous media, such as random walk models [50]. However, research into diffusive transport through porous media is a large field of interest in its own right, with many of the modelling approaches depending on the scale of the pores. If, for example, the pores of a porous media are on the nanoscale, then it is likely that a transport model would involve Knudsen diffusion. For the work in this thesis, it is assumed that the overall effect of porosity on drug transport may be accounted for through equation (3.2).

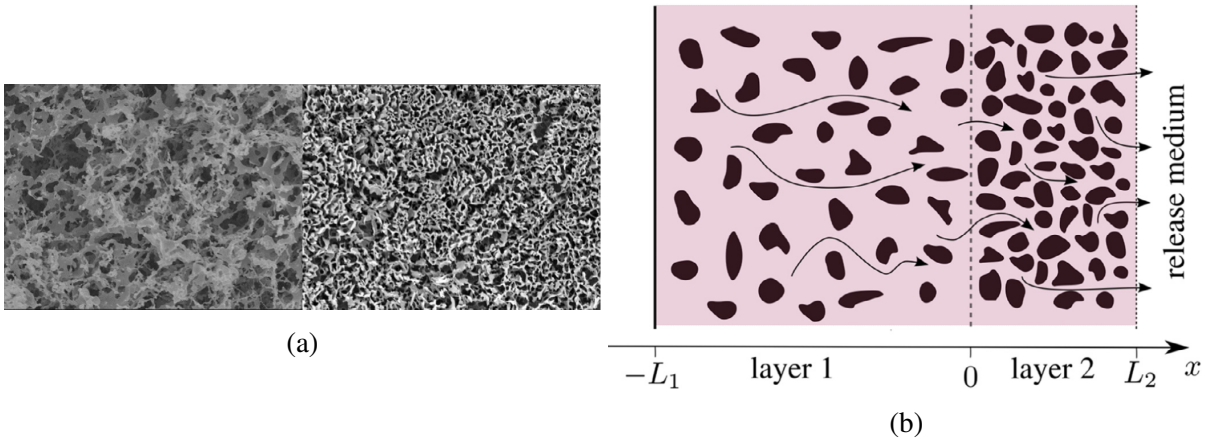

(a) (b)

Figure 3.2: (a) Example of two adjacent polymer coatings with different microstructural properties that could be used as a method of controlling release of drug through layering of the polymers. Adapted from [55]. (b) Idealised 1D geometry comprised of two porous layers, of differing thickness, for drug release into a release medium. Positions $x = -L_1$ and $x = -L_2$ denote the leftmost and rightmost boundaries of the layers and $x = 0$ marks the position of the interface between the layers. Figure not to scale. Adapted from [56]

3.1 Mathematical formulation

A 1D model is developed to answer the basic question: to what extent can variable porosity control the release of a drug? Among the many benefits of a 1D model is the possibility of obtaining an analytical solution. Based upon realistic porous structures (Figure 3.2(a)), a simplified two-layer counterpart can be created (Figure 3.2(b)). The two layers have thicknesses L_1 and L_2, with porosities ϕ_1 and ϕ_2, respectively, and for later convenience, define $L = L_1 + L_2$. Let the intrinsic drug concentrations in layers 1 and 2 be denoted by $c_1(x, t)$ and $c_2(x, t)$, respectively. Variables x and t denote space and time, respectively. Since it is assumed that diffusion is the

governing transport mechanism, the effective diffusion coefficients associated with concentrations c_1 and c_2 are D_1^e and D_2^e, respectively. These effective diffusion coefficients are defined as $D_1^e = \phi_1^e D^w/\tau_1$ and $D_2^e = \phi_2^e D^w/\tau_2$, where D^w is the free diffusion coefficient of the drug in water and τ_1 and τ_2 are the tortuosities of each layer, which are a measure of the meandering structure of the pores [48]. Parameters ϕ_1^e and ϕ_2^e are the effective porosities of each layer through which drug transport may occur. These parameters may in fact be less than the overall porosities ϕ_1 and ϕ_2, which are the ratios of void volume to the physical volume [48], due to the presence of inaccessible voids within the porous structure of the two layers. With the assumptions that the polymer coating is quickly wetted and the drugs are readily soluble, the model for diffusion in a two-layer porous (composite) media is:

$$\phi_1 \frac{\partial c_1}{\partial t} = D_1^e \frac{\partial^2 c_1}{\partial x^2}, \quad -L_1 < x < 0, \quad t > 0, \tag{3.3}$$

$$\phi_2 \frac{\partial c_2}{\partial t} = D_2^e \frac{\partial^2 c_2}{\partial x^2}, \quad 0 < x < L_2, \quad t > 0, \tag{3.4}$$

$$-D_1^e \frac{\partial c_1}{\partial x} = K_1 c_1, \quad x = -L_1, \quad t > 0, \tag{3.5}$$

$$-D_1^e \frac{\partial c_1}{\partial x} = P(c_1 - c_2), \quad -D_1^e \frac{\partial c_1}{\partial x} = -D_2^e \frac{\partial c_2}{\partial x}, \quad x = 0, \quad t > 0, \tag{3.6}$$

$$-D_2^e \frac{\partial c_2}{\partial x} = K_2 c_2, \quad x = L_2, \quad t > 0, \tag{3.7}$$

$$c_1 = c_1^0, \quad -L_1 \leq x \leq 0, \quad c_2 = c_2^0, \quad 0 < x \leq L_2, \quad t = 0. \tag{3.8}$$

For generality, the boundary conditions employed at either end of the domain are presented as a mixed-type (3.5 and 3.7), in which inputs K_1 and K_2 may be derived from experimentally measured flux. The generalisation of these conditions permits the use of extreme boundary conditions, specifically zero-flux and infinite sink conditions, which can be achieved through specific choices for the values of K_1 and K_2. The zero-flux boundary condition in the context of an experiment means that a particle cannot pass through a solid structure, such as a stainless-steel outer wall of an implant. With reference to experimental conditions, the infinite sink condition is placed at the boundary where a drug particle is released into the surrounding medium where it is assumed that the drug concentration cannot build up and reduce the concentration gradient. In practice this is achieved either through the use of a large volume of release medium, with or without stirring, or by replenishing the media at regular intervals. Continuity of flux (3.6) is applied to the interface between the two layers. The remaining boundary condition required to close the system is expressed in terms of flux and is able to account for imperfect contact between the two porous layers or partitioning of the drug via a mass transfer coefficient P. Initial drug concentrations in the two layers are defined to be the constants c_1^0 and c_2^0.

A specific case is considered in which some of these boundary conditions are less general but nonetheless applicable, these are zero-flux, infinite sink and continuity of concentration boundary conditions. The full solution to the general model is presented in Section 3.2.5. Equation

(3.5) permits the possibility that drug may enter the domain at $x = -L_1$, for a zero-flux condition, simply let $K_1 = 0$, giving:

$$-D_1^e \frac{\partial c_1}{\partial x} = 0, \quad x = -L_1, \quad t > 0. \tag{3.9}$$

Equation (3.7) describes the flux of drug leaving the porous medium, to obtain the infinite sink condition, take the limit as $K_2 \to \infty$:

$$c_2 = 0, \quad x = L_2, \quad t > 0. \tag{3.10}$$

In the specific case, at the interface it is assumed that the porous layers are in perfect contact and the drug does not partition, to account for this, continuity of concentration at the interface is applied. Taking the limit as $P \to \infty$, the simplified interface conditions are:

$$c_1 = c_2, \quad -D_1^e \frac{\partial c_1}{\partial x} = -D_2^e \frac{\partial c_2}{\partial x}, \quad x = 0, \quad t > 0. \tag{3.11}$$

With the simplified boundary conditions obtained (3.9-3.11), the new model is:

$$\phi_1 \frac{\partial c_1}{\partial t} = D_1^e \frac{\partial^2 c_1}{\partial x^2}, \quad -L_1 < x < 0, \quad t > 0, \tag{3.12}$$

$$\phi_2 \frac{\partial c_2}{\partial t} = D_2^e \frac{\partial^2 c_2}{\partial x^2}, \quad 0 < x < L_2, \quad t > 0, \tag{3.13}$$

$$- D_1^e \frac{\partial c_1}{\partial x} = 0, \quad x = -L_1, \quad t > 0, \tag{3.14}$$

$$c_1 = c_2, \quad -D_1^e \frac{\partial c_1}{\partial x} = -D_2^e \frac{\partial c_2}{\partial x}, \quad x = 0, \quad t > 0, \tag{3.15}$$

$$c_2 = 0, \quad x = L_2, \quad t > 0, \tag{3.16}$$

$$c_1 = c_1^0, \quad -L_1 \leq x \leq 0, \quad c_2 = c_2^0, \quad 0 < x \leq L_2, \quad t = 0. \tag{3.17}$$

The simplified model given by (3.12)-(3.17) may be nondimensionalised using the following relations:

$$c_1' = \frac{c_1}{c_1^0}, \quad c_2' = \frac{c_2}{c_1^0}, \quad x' = \frac{x}{L}, \quad t' = \frac{D_1^e t}{\phi_1 L^2}.$$

Dropping the primes for clarity and defining $\delta = L_1/L$, $\chi = D_2^e/D_1^e$, $\phi = \phi_2/\phi_1$, $C^0 = c_2^0/c_1^0$ and simplifying with $\bar{\chi} = \chi/\phi$ and $\bar{\delta} = 1 - \delta$ gives the nondimensional model of diffusive transport through composite porous media:

$$\frac{\partial c_1}{\partial t} = \frac{\partial^2 c_1}{\partial x^2}, \quad -\delta < x < 0, \quad t > 0, \tag{3.18}$$

$$\frac{\partial c_2}{\partial t} = \bar{\chi} \frac{\partial^2 c_2}{\partial x^2}, \quad 0 < x < \bar{\delta}, \quad t > 0, \tag{3.19}$$

$$\frac{\partial c_1}{\partial x} = 0, \quad x = -\delta, \quad t > 0, \tag{3.20}$$

$$c_1 = c_2, \quad \frac{\partial c_1}{\partial x} = \chi \frac{\partial c_2}{\partial x}, \quad x = 0, \quad t > 0, \tag{3.21}$$

$$c_2 = 0, \quad x = \bar{\delta}, \quad t > 0, \tag{3.22}$$

$$c_1 = 1, \quad -\delta \leq x \leq 0, \quad c_2 = C^0, \quad 0 < x \leq \bar{\delta}, \quad t = 0. \tag{3.23}$$

3.2 Solution procedure

The model (3.18-3.23) is solved via the Laplace Transform (LT) which has the following definition [57]:

Definition 1 *Let $f(t)$ be a function of t specified for $t > 0$. Then the Laplace transform of $f(t)$, denoted by $\mathcal{L}[f(t)]$, is defined by:*

$$\mathcal{L}[f(t)] = f(s) = \int_0^\infty e^{-st} f(t) dt.$$

It is assumed that $f(t)$ is defined for all $t \in (0, \infty)$, s is real and that the integral is convergent. A necessary condition for convergence [58] is when $s > \alpha$, where α is a constant and $f(t)$ satisfies:

$$|f(t)| = O\left(e^{\alpha t}\right) \quad \text{as} \quad t \to \infty.$$

The LT of numerous functions and derivatives are standard results and are available in many books, such as [57, 59]. The transformed solutions will be denoted by an overbar (e.g. $\bar{c}(x, s)$). Taking the LT of (3.18) and solving the resulting ordinary differential equation (ODE), subject to (3.20), gives:

$$\bar{c_1}(x, s) = B(s) \left[\frac{\cosh(\sqrt{s}(x + \delta))}{\sinh(\sqrt{s}\delta)} \right] + \frac{1}{s}.$$

Similarly, the LT of (3.19) and solving the resulting ODE, subject to (3.22), gives:

$$\bar{c_2}(x, s) = D(s) \left[\frac{\sinh\left(\sqrt{\frac{s}{\bar{\chi}}}(x - \bar{\delta})\right)}{\cosh\left(\sqrt{\frac{s}{\bar{\chi}}}\bar{\delta}\right)} \right] + \frac{C^0}{s} \left[\frac{\cosh\left(\sqrt{\frac{s}{\bar{\chi}}}\bar{\delta}\right) - \cosh\left(\sqrt{\frac{s}{\bar{\chi}}}x\right)}{\cosh\left(\sqrt{\frac{s}{\bar{\chi}}}\bar{\delta}\right)} \right].$$

The interface conditions (3.21) can now be applied to obtain the relationship between $B(s)$ and $D(s)$. Starting with continuity of concentration:

$$B(s) = \left(D(s) \left[\frac{-\sinh\left(\sqrt{\frac{s}{\bar{\chi}}}\bar{\delta}\right)}{\cosh\left(\sqrt{\frac{s}{\bar{\chi}}}\bar{\delta}\right)} \right] + \frac{C^0}{s} \left[\frac{\cosh\left(\sqrt{\frac{s}{\bar{\chi}}}\bar{\delta}\right) - 1}{\cosh\left(\sqrt{\frac{s}{\bar{\chi}}}\bar{\delta}\right)} \right] - \frac{1}{s} \right) \frac{\sinh(\sqrt{s}\delta)}{\cosh(\sqrt{s}\delta)}. \tag{3.24}$$

Taking the LT of the equation for continuity of flux results in the simple relation:

$$B(s) = \sqrt{\chi\phi}D(s). \tag{3.25}$$

With the relationship between $B(s)$ and $D(s)$ found, equations (3.24) and (3.25) can be combined to obtain explicit expressions for $B(s)$ and $D(s)$:

$$B(s) = \frac{\sqrt{\chi\phi}\sinh(\sqrt{s}\delta)\left(\cosh\left(\sqrt{\frac{s}{\bar{\chi}}}\bar{\delta}\right)(C^0-1)-C^0\right)}{s\left(\sqrt{\chi\phi}\cosh\left(\sqrt{\frac{s}{\bar{\chi}}}\bar{\delta}\right)\cosh(\sqrt{s}\delta)+\sinh\left(\sqrt{\frac{s}{\bar{\chi}}}\bar{\delta}\right)\sinh(\sqrt{s}\delta)\right)}, \tag{3.26}$$

$$D(s) = \frac{\sinh(\sqrt{s}\delta)\left(\cosh\left(\sqrt{\frac{s}{\bar{\chi}}}\bar{\delta}\right)(C^0-1)-C^0\right)}{s\left(\sqrt{\chi\phi}\cosh\left(\sqrt{\frac{s}{\bar{\chi}}}\bar{\delta}\right)\cosh(\sqrt{s}\delta)+\sinh\left(\sqrt{\frac{s}{\bar{\chi}}}\bar{\delta}\right)\sinh(\sqrt{s}\delta)\right)}. \tag{3.27}$$

With expressions (3.26) and (3.27), explicit forms of the transformed equations $\bar{c_1}(x,s)$ and $\bar{c_2}(x,s)$ can be obtained:

$$\bar{c_1}(x,s) = \frac{\sqrt{\chi\phi}\cosh\left(\sqrt{s}(x+\delta)\right)\left(\cosh\left(\sqrt{\frac{s}{\bar{\chi}}}\bar{\delta}\right)(C^0-1)-C^0\right)}{s\left(\sqrt{\chi\phi}\cosh\left(\sqrt{\frac{s}{\bar{\chi}}}\bar{\delta}\right)\cosh(\sqrt{s}\delta)+\sinh\left(\sqrt{\frac{s}{\bar{\chi}}}\bar{\delta}\right)\sinh(\sqrt{s}\delta)\right)}+\frac{1}{s}, \tag{3.28}$$

$$\begin{aligned}\bar{c_2}(x,s) = {} & \frac{\sinh\left(\sqrt{\frac{s}{\bar{\chi}}}(x-\bar{\delta})\right)\sinh(\sqrt{s}\delta)\left(\cosh\left(\sqrt{\frac{s}{\bar{\chi}}}\bar{\delta}\right)(C^0-1)-C^0\right)}{s\cosh\left(\sqrt{\frac{s}{\bar{\chi}}}\bar{\delta}\right)\left(\sqrt{\chi\phi}\cosh\left(\sqrt{\frac{s}{\bar{\chi}}}\bar{\delta}\right)\cosh(\sqrt{s}\delta)+\sinh\left(\sqrt{\frac{s}{\bar{\chi}}}\bar{\delta}\right)\sinh(\sqrt{s}\delta)\right)} \\ & -\frac{C^0\cosh\left(\sqrt{\frac{s}{\bar{\chi}}}x\right)}{s\cosh\left(\sqrt{\frac{s}{\bar{\chi}}}\bar{\delta}\right)}+\frac{C^0}{s}.\end{aligned} \tag{3.29}$$

It is a fairly trivial task to apply LTs to a mathematical model to obtain the transformed solution. However, inversion of the transformed solutions $\bar{c_1}(x,s)$ and $\bar{c_2}(x,s)$ back to functions of the original variables requires considerably more effort. The inversion process may be carried out through the use of the following two theorems [57, 58]:

Theorem 1 (The Complex Inversion Formula) *If $f(s) = \mathcal{L}[f(t)]$, then $\mathcal{L}^{-1}[f(s)]$ is given by:*

$$\mathcal{L}^{-1}[f(s)] = f(t) = \frac{1}{2\pi i}\int_{\gamma-i\infty}^{\gamma+i\infty} e^{st}f(s)ds, \quad t>0, \tag{3.30}$$

and $f(t) = 0$ for $t < 0$.

Theorem 2 (Uniqueness theorem) *If*

$$f(s) = \int_0^\infty e^{-st} f(t)dt, \quad s > \alpha, \tag{3.31}$$

is satisfied by a continuous function $f(t)$, there is no other continuous function which satisfies equation (3.31).

Theorems 1 and 2 provide a direct approach to obtain the unique inverse LT for a given function $f(s)$. The integral in (3.30) is performed along the line $s = \gamma$ in the complex plane, where $s = x + iy$ (Figure 3.3). The real number γ is chosen such that $s = \gamma$ lies to the right of all singularities of $f(s)$, be they poles, branch points or essential singularities. In practice, the integral in (3.30) is evaluated using the contour integral:

$$\frac{1}{2\pi i} \oint_C e^{st} f(s)dt,$$

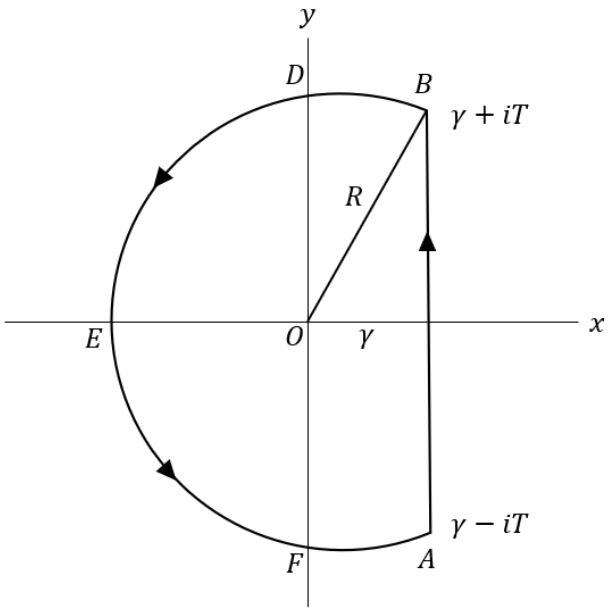

Figure 3.3: A Bromwich contour, C.

where C is the contour shown in Figure 3.3, which is composed of the arc $BDEFA$ (Γ) of a circle of radius R, centred at O and the line segment AB. By subtracting the integral along the circle arc Γ from the closed contour integral along C, then (3.30) may be evaluated:

$$f(t) = \lim_{R\to\infty} \frac{1}{2\pi i} \int_{\gamma-i\infty}^{\gamma+i\infty} e^{st} f(s)ds = \lim_{R\to\infty} \frac{1}{2\pi i} \left[\oint_C e^{st} f(s)ds - \int_\Gamma e^{st} f(s)ds \right], \tag{3.32}$$

since $T = \sqrt{R^2 - \gamma^2}$, as $R \to \infty$ then $T \to \infty$. For (3.32) to be valid, then the integral along Γ must approach zero as $R \to \infty$. A sufficient condition for this to be true is the following theorem [57]:

Theorem 3 *If constants $M > 0$ and $k > 0$ can be found such that on Γ,*

$$|f(s)| < \frac{M}{R^k}, \quad \textit{then} \quad \lim_{R\to\infty} \int_\Gamma e^{st} f(s) ds = 0.$$

The remaining contour integral may then be evaluated using the following theorem [58]:

Theorem 4 (The Residue Theorem) *Let C be a positively orientated simple closed contour in the complex plane and let f be a function defined on C, except for some points $a_1, a_2 ... a_k$ inside C, then:*

$$\oint_C e^{st} f(s) ds = 2\pi i \sum_{k=1}^{k} \textit{Res}(e^{st} f(s), a_k).$$

For a pole a_k of order n, then [60]:

$$\textit{Res}(e^{st} f(s), a_k) = \frac{1}{(n-1)!} \lim_{s\to a_k} \left[\frac{d^{n-1}}{ds^{n-1}} ((s-a_k)^n e^{st} f(s)) \right]. \tag{3.33}$$

Theorem 4 and (3.33) may now be used on the transformed solutions (3.28) and (3.29). Starting with (3.28), $s = 0$ is a simple pole of order one and has a residue of -1. The inverse LT of $1/s$ has the standard result of 1 and this will cancel with the residue of $s = 0$, leaving only the case where an infinite number of simple poles exists at $s = s_n$, which are the roots of the transcendental equation:

$$\left(\sqrt{\chi\phi} \cosh\left(\sqrt{\frac{s}{\bar{\chi}}} \bar{\delta} \right) \cosh\left(\sqrt{s}\delta\right) + \sinh\left(\sqrt{\frac{s}{\bar{\chi}}} \bar{\delta} \right) \sinh\left(\sqrt{s}\delta\right) \right) = 0. \tag{3.34}$$

The residue at $s = s_n$ is given by:

$$\begin{aligned} &\lim_{s\to s_n} \left[\bar{c_1}(x,s)(s-s_n) e^{st} \right] \\ &= \lim_{s\to s_n} \left[\frac{\sqrt{\chi\phi} \cosh\left(\sqrt{s}(x+\delta)\right) \left(\cosh\left(\sqrt{\frac{s}{\bar{\chi}}} \bar{\delta} \right) (C^0 - 1) - C^0 \right) e^{st}}{s} \right] \\ &\times \lim_{s\to s_n} \left[\frac{s - s_n}{\sqrt{\chi\phi} \cosh\left(\sqrt{\frac{s}{\bar{\chi}}} \bar{\delta} \right) \cosh(\sqrt{s}\delta) + \sinh\left(\sqrt{\frac{s}{\bar{\chi}}} \bar{\delta} \right) \sinh(\sqrt{s}\delta)} \right]. \end{aligned}$$

The second limit of the above expression has an indeterminant form. However, using L'Hôpital's

rule, the limit can be obtained:

$$\lim_{s\to s_n}\left[\frac{s-s_n}{\sqrt{\chi\phi}\cosh\left(\sqrt{\frac{s}{\bar{\chi}}}\bar{\delta}\right)\cosh(\sqrt{s}\delta)+\sinh\left(\sqrt{\frac{s}{\bar{\chi}}}\bar{\delta}\right)\sinh(\sqrt{s}\delta)}\right],$$

$$=\lim_{s\to s_n}\left[\begin{array}{r}\frac{\delta}{2\sqrt{s}}\left[\sqrt{\chi\phi}\sinh\left(\sqrt{s}\delta\right)\cosh\left(\sqrt{\frac{s}{\bar{\chi}}}\bar{\delta}\right)+\cosh\left(\sqrt{s}\delta\right)\sinh\left(\sqrt{\frac{s}{\bar{\chi}}}\bar{\delta}\right)\right]\\ +\frac{\bar{\delta}}{2\sqrt{s\bar{\chi}}}\left[\sqrt{\chi\phi}\cosh\left(\sqrt{s}\delta\right)\sinh\left(\sqrt{\frac{s}{\bar{\chi}}}\bar{\delta}\right)+\sinh\left(\sqrt{s}\delta\right)\cosh\left(\sqrt{\frac{s}{\bar{\chi}}}\bar{\delta}\right)\right]\end{array}\right]^{-1}.$$

Evaluating the limits, gives the residue of the infinite number of simple poles:

$$\frac{2\sqrt{\chi\phi}\cosh\left(\sqrt{s_n}(x+\delta)\right)\left(\cosh\left(\sqrt{\frac{s_n}{\bar{\chi}}}\bar{\delta}\right)(C^0-1)-C^0\right)e^{s_nt}}{\sqrt{s_n}\left[\begin{array}{r}\delta\left[\sqrt{\chi\phi}\sinh\left(\sqrt{s}\delta\right)\cosh\left(\sqrt{\frac{s}{\bar{\chi}}}\bar{\delta}\right)+\cosh\left(\sqrt{s}\delta\right)\sinh\left(\sqrt{\frac{s}{\bar{\chi}}}\bar{\delta}\right)\right]\\ +\frac{\bar{\delta}}{\sqrt{\bar{\chi}}}\left[\sqrt{\chi\phi}\cosh\left(\sqrt{s}\delta\right)\sinh\left(\sqrt{\frac{s}{\bar{\chi}}}\bar{\delta}\right)+\sinh\left(\sqrt{s}\delta\right)\cosh\left(\sqrt{\frac{s}{\bar{\chi}}}\bar{\delta}\right)\right]\end{array}\right]}.$$

With the residue found, the semi-analytical solution for $c_1(x,t)$ can be determined as an infinite sum over the solutions of (3.34):

$$c_1(x,t)=\sum_{n=1}^{\infty}\frac{2\sqrt{\chi\phi}\cosh\left(\sqrt{s_n}(x+\delta)\right)\left(\cosh\left(\sqrt{\frac{s_n}{\bar{\chi}}}\bar{\delta}\right)(C^0-1)-C^0\right)e^{s_nt}}{\sqrt{s_n}\left[\begin{array}{r}\delta\left[\sqrt{\chi\phi}\sinh\left(\sqrt{s}\delta\right)\cosh\left(\sqrt{\frac{s}{\bar{\chi}}}\bar{\delta}\right)+\cosh\left(\sqrt{s}\delta\right)\sinh\left(\sqrt{\frac{s}{\bar{\chi}}}\bar{\delta}\right)\right]\\ +\frac{\bar{\delta}}{\sqrt{\bar{\chi}}}\left[\sqrt{\chi\phi}\cosh\left(\sqrt{s}\delta\right)\sinh\left(\sqrt{\frac{s}{\bar{\chi}}}\bar{\delta}\right)+\sinh\left(\sqrt{s}\delta\right)\cosh\left(\sqrt{\frac{s}{\bar{\chi}}}\bar{\delta}\right)\right]\end{array}\right]},\tag{3.35}$$

and the application of (3.20) shows that the boundary condition is satisfied.

Equation (3.29) has simple poles at $s=0$ in all of the fractions, which have the following residues respectively: 0, $-C^0$ and C^0, which of course sum to 0. The first fraction in (3.29) has infinitely many simple poles at:

$$\cosh\left(\sqrt{\frac{s}{\bar{\chi}}}\bar{\delta}\right)=0,\tag{3.36}$$

letting s_l denote this sequence of infinite poles, then:

$$s_l=\frac{-\bar{\chi}\pi^2\left(2m-1\right)^2}{4\bar{\delta}^2}\Rightarrow\sqrt{\frac{s_l}{\bar{\chi}}}=\frac{i\pi\left(2m-1\right)}{2\bar{\delta}}\quad l=1,2,3,...$$

and the residue, through the use of L'Hôpital's rule, is:

$$\begin{aligned}
&\lim_{s\to s_l}\left[\bar{c_2}(x,s)(s-s_l)e^{st}\right]\\
&=\lim_{s\to s_l}\left[\frac{\sinh\left(\sqrt{\frac{s}{\bar{\chi}}}(x-\bar{\delta})\right)\sinh(\sqrt{s}\delta)\left(\cosh\left(\sqrt{\frac{s}{\bar{\chi}}}\bar{\delta}\right)(C^0-1)-C^0\right)e^{st}}{s\left(\sqrt{\chi\phi}\cosh\left(\sqrt{\frac{s}{\bar{\chi}}}\bar{\delta}\right)\cosh(\sqrt{s}\delta)+\sinh\left(\sqrt{\frac{s}{\bar{\chi}}}\bar{\delta}\right)\sinh(\sqrt{s}\delta)\right)}\right]\\
&\times\lim_{s\to s_l}\left[\frac{(s-s_l)}{\cosh\left(\sqrt{\frac{s}{\bar{\chi}}}\bar{\delta}\right)}\right]\\
&=-\frac{4(-1)^{l+1}C^0\cos\left(\frac{\pi(2l-1)}{2\bar{\delta}}x\right)\exp\left(-\frac{\bar{\chi}\pi^2(2l-1)^2}{4\bar{\delta}^2}t\right)}{\pi(2l-1)}\qquad l=1,2,3,....
\end{aligned}\tag{3.37}$$

Another source of infinitely many simple poles exists in the first fraction of (3.29) at $s=s_m$, are found by solving:

$$\left(\sqrt{\chi\phi}\cosh\left(\sqrt{\frac{s}{\bar{\chi}}}\bar{\delta}\right)\cosh\left(\sqrt{s}\delta\right)+\sinh\left(\sqrt{\frac{s}{\bar{\chi}}}\bar{\delta}\right)\sinh\left(\sqrt{s}\delta\right)\right)=0.\tag{3.38}$$

Since equation (3.38) is identical to equation (3.34), the poles are the same, thus following the same procedure, the residue is:

$$\frac{2\sinh\left(\sqrt{\frac{s_m}{\bar{\chi}}}(x-\bar{\delta})\right)\sinh\left(\sqrt{s_m}\delta\right)\left(\cosh\left(\sqrt{\frac{s_m}{\bar{\chi}}}\bar{\delta}\right)(C^0-1)-C^0\right)e^{s_mt}}{\left[\begin{array}{l}\sqrt{s_m}\cosh\left(\sqrt{\frac{s_m}{\bar{\chi}}}\bar{\delta}\right)\\ \times\left[\begin{array}{r}\delta\left[\sqrt{\chi\phi}\sinh\left(\sqrt{s_m}\delta\right)\cosh\left(\sqrt{\frac{s_m}{\bar{\chi}}}\bar{\delta}\right)+\cosh\left(\sqrt{s_m}\delta\right)\sinh\left(\sqrt{\frac{s_m}{\bar{\chi}}}\bar{\delta}\right)\right]\\ +\frac{\bar{\delta}}{\sqrt{\bar{\chi}}}\left[\sqrt{\chi\phi}\cosh\left(\sqrt{s_m}\delta\right)\sinh\left(\sqrt{\frac{s_m}{\bar{\chi}}}\bar{\delta}\right)+\sinh\left(\sqrt{s_m}\delta\right)\cosh\left(\sqrt{\frac{s_m}{\bar{\chi}}}\bar{\delta}\right)\right]\end{array}\right]\end{array}\right]}.\tag{3.39}$$

Finally, there are the infinite number of simple poles in the second fraction of (3.29), in which the poles are the solutions of:

$$\cosh\left(\sqrt{\frac{s}{\bar{\chi}}}\bar{\delta}\right)=0.\tag{3.40}$$

Since (3.40) is identical to (3.36) found in the first fraction of (3.29), the poles are also identical,

therefore the residue is:

$$\lim_{s\to s_p}\left[-\frac{(s-s_p)C^0\cosh\left(\sqrt{\frac{s}{\bar{\chi}}}x\right)e^{st}}{s\cosh\left(\sqrt{\frac{s}{\bar{\chi}}}\bar{\delta}\right)}\right]$$
$$=\frac{4(-1)^{p+1}C^0\cos\left(\frac{\pi(2p-1)}{2\bar{\delta}}x\right)\exp\left(-\frac{\bar{\chi}\pi^2(2p-1)^2}{4\bar{\delta}^2}t\right)}{\pi(2p-1)},\quad p=1,2,3,... \tag{3.41}$$

With the residues in the case of (3.29) found, the solution for $c_2(x,t)$ can be determined. Since residues (3.37) and (3.41) sum to 0 and (3.38) is identical to (3.34), the solution $c_2(x,t)$ can also be summed over n as with $c_1(x,t)$:

$$c_2(x,t)=$$
$$\sum_{n=1}^{\infty}\frac{2\sinh\left(\sqrt{s_n}\delta\right)\sinh\left(\sqrt{\frac{s_n}{\bar{\chi}}}(x-\bar{\delta})\right)\left(\cosh\left(\sqrt{\frac{s_n}{\bar{\chi}}}\bar{\delta}\right)(C^0-1)-C^0\right)e^{s_nt}}{\left[\begin{array}{l}\sqrt{s_n}\cosh\left(\sqrt{\frac{s_n}{\bar{\chi}}}\bar{\delta}\right)\\ \times\left[\begin{array}{r}\delta\left[\sqrt{\chi\phi}\sinh\left(\sqrt{s_n}\delta\right)\cosh\left(\sqrt{\frac{s_n}{\bar{\chi}}}\bar{\delta}\right)+\cosh\left(\sqrt{s_n}\delta\right)\sinh\left(\sqrt{\frac{s_n}{\bar{\chi}}}\bar{\delta}\right)\right]\\ +\frac{\bar{\delta}}{\sqrt{\bar{\chi}}}\left[\sqrt{\chi\phi}\cosh\left(\sqrt{s_n}\delta\right)\sinh\left(\sqrt{\frac{s_n}{\bar{\chi}}}\bar{\delta}\right)+\sinh\left(\sqrt{s_n}\delta\right)\cosh\left(\sqrt{\frac{s_n}{\bar{\chi}}}\bar{\delta}\right)\right]\end{array}\right]\end{array}\right]}, \tag{3.42}$$

and with the application of (3.22), the boundary condition is satisfied.
Solution equations (3.34), (3.35) and (3.42) can be rewritten via:

$$s_n=-\alpha_n^2\Rightarrow\sqrt{s_n}=i\alpha_n,$$

to give:

$$\sqrt{\chi\phi}\cos\left(\alpha_n\delta\right)\cos\left(\frac{\alpha_n\bar{\delta}}{\sqrt{\bar{\chi}}}\right)-\sin\left(\alpha_n\delta\right)\sin\left(\frac{\alpha_n\bar{\delta}}{\sqrt{\bar{\chi}}}\right)=0, \tag{3.43}$$

$$c_1(x,t)=\sum_{n=1}^{\infty}\frac{2\sqrt{\chi\phi}\cos\left(\alpha_n\left(x+\delta\right)\right)\left(\cos\left(\frac{\alpha_n\bar{\delta}}{\sqrt{\bar{\chi}}}\right)(1-C^0)+C^0\right)e^{-\alpha_n^2t}}{\alpha_n\left[\begin{array}{r}\delta\left[\sqrt{\chi\phi}\sin\left(\alpha_n\delta\right)\cos\left(\frac{\alpha_n\bar{\delta}}{\sqrt{\bar{\chi}}}\right)+\cos\left(\alpha_n\delta\right)\sin\left(\frac{\alpha_n\bar{\delta}}{\sqrt{\bar{\chi}}}\right)\right]\\ +\frac{\bar{\delta}}{\sqrt{\bar{\chi}}}\left[\sqrt{\chi\phi}\cos\left(\alpha_n\delta\right)\sin\left(\frac{\alpha_n\bar{\delta}}{\sqrt{\bar{\chi}}}\right)+\sin\left(\alpha_n\delta\right)\cos\left(\frac{\alpha_n\bar{\delta}}{\sqrt{\bar{\chi}}}\right)\right]\end{array}\right]}, \tag{3.44}$$

$$c_2(x,t) = \sum_{n=1}^{\infty} \frac{2\sin(\alpha_n\delta)\sin\left(\frac{\alpha_n}{\sqrt{\bar{\chi}}}\left(x-\bar{\delta}\right)\right)\left(\cos\left(\frac{\alpha_n\bar{\delta}}{\sqrt{\bar{\chi}}}\right)(C^0-1)-C^0\right)e^{-\alpha_n^2 t}}{\left[\begin{array}{l}\alpha_n\cos\left(\frac{\alpha_n\bar{\delta}}{\sqrt{\bar{\chi}}}\right) \\ \times\left[\begin{array}{r}\delta\left[\sqrt{\chi\phi}\sin(\alpha_n\delta)\cos\left(\frac{\alpha_n\bar{\delta}}{\sqrt{\bar{\chi}}}\right)+\cos(\alpha_n\delta)\sin\left(\frac{\alpha_n\bar{\delta}}{\sqrt{\bar{\chi}}}\right)\right] \\ +\frac{\bar{\delta}}{\sqrt{\bar{\chi}}}\left[\sqrt{\chi\phi}\cos(\alpha_n\delta)\sin\left(\frac{\alpha_n\bar{\delta}}{\sqrt{\bar{\chi}}}\right)+\sin(\alpha_n\delta)\cos\left(\frac{\alpha_n\bar{\delta}}{\sqrt{\bar{\chi}}}\right)\right]\end{array}\right]\end{array}\right]}. \quad (3.45)$$

Model solution equations (3.43-3.45) may be simplified to:

$$\left(\sqrt{\chi\phi}+1\right)\cos\left(\alpha_n\left(\delta+\frac{\bar{\delta}}{\sqrt{\bar{\chi}}}\right)\right)+\left(\sqrt{\chi\phi}-1\right)\cos\left(\alpha_n\left(\delta-\frac{\bar{\delta}}{\sqrt{\bar{\chi}}}\right)\right)=0, \quad (3.46)$$

$$c_1(x,t) = \sum_{n=1}^{\infty} \frac{4\sqrt{\chi\phi}\cos(\alpha_n(x+\delta))\left(\cos\left(\frac{\alpha_n\bar{\delta}}{\sqrt{\bar{\chi}}}\right)(1-C^0)+C^0\right)e^{-\alpha_n^2 t}}{\alpha_n\left[\begin{array}{l}\left(\sqrt{\chi\phi}+1\right)\left(\delta+\frac{\bar{\delta}}{\sqrt{\bar{\chi}}}\right)\sin\left(\alpha_n\left(\delta+\frac{\bar{\delta}}{\sqrt{\bar{\chi}}}\right)\right) \\ +\left(\sqrt{\chi\phi}-1\right)\left(\delta-\frac{\bar{\delta}}{\sqrt{\bar{\chi}}}\right)\sin\left(\alpha_n\left(\delta-\frac{\bar{\delta}}{\sqrt{\bar{\chi}}}\right)\right)\end{array}\right]}, \quad (3.47)$$

$$c_2(x,t) = \sum_{n=1}^{\infty} \frac{4\sin(\alpha_n\delta)\sin\left(\frac{\alpha_n}{\sqrt{\bar{\chi}}}\left(x-\bar{\delta}\right)\right)\left(\cos\left(\frac{\alpha_n\bar{\delta}}{\sqrt{\bar{\chi}}}\right)(C^0-1)-C^0\right)e^{-\alpha_n^2 t}}{\left[\begin{array}{l}\alpha_n\cos\left(\frac{\alpha_n\bar{\delta}}{\sqrt{\bar{\chi}}}\right) \\ \times\left[\begin{array}{l}\left(\sqrt{\chi\phi}+1\right)\left(\delta+\frac{\bar{\delta}}{\sqrt{\bar{\chi}}}\right)\sin\left(\alpha_n\left(\delta+\frac{\bar{\delta}}{\sqrt{\bar{\chi}}}\right)\right) \\ +\left(\sqrt{\chi\phi}-1\right)\left(\delta-\frac{\bar{\delta}}{\sqrt{\bar{\chi}}}\right)\sin\left(\alpha_n\left(\delta-\frac{\bar{\delta}}{\sqrt{\bar{\chi}}}\right)\right)\end{array}\right]\end{array}\right]}, \quad (3.48)$$

3.2.1 Special cases

There exists two analytical solutions from special cases that arise from when the microstructural properties in both layers are identical ($\chi = \phi = 1$):

$$c(x,t) = \frac{4}{\pi}\sum_{n=1}^{\infty}\frac{(-1)^n}{2n-1}\left[\begin{array}{l}\cos\left(\frac{(2n-1)\pi}{2}(x+\delta)\right)\exp\left(-\frac{(2n-1)^2\pi^2 t}{4}\right) \\ \times\left[(-1)^{n+1}\sin\left(\frac{(2n-1)\pi\delta}{2}\right)\left(C^0-1\right)-C^0\right]\end{array}\right], \quad -\delta < x < \bar{\delta},$$

and additionally when the drug loading is uniform ($\chi = \phi = C^0 = 1$), a solution similar to Crank's classical solution [39] is obtained:

$$c(x,t) = \frac{4}{\pi}\sum_{n=1}^{\infty}\frac{(-1)^{n+1}}{2n-1}\left[\cos\left(\frac{(2n-1)\pi}{2}(x+\delta)\right)\exp\left(-\frac{(2n-1)^2\pi^2 t}{4}\right)\right], \quad -\delta < x < \bar{\delta}.$$

3.2.2 Equations for mass

Dimensionally, the mass of drug at some time t is:

$$M(t) = M_1(t) + M_2(t) = A\left[\int_{-L_1}^{0}\phi_1 c_1(x,t)dx + \int_{0}^{L-L_1}\phi_2 c_2(x,t)dx\right],$$

where $M_1(t)$ and $M_2(t)$ are the masses of drug in layer 1 and layer 2 respectively, A is the total cross-sectional area of the planar surface of the porous structure. Mass can be normalised via M^0, the total initial mass of drug in the pores:

$$M^0 = M_1^0 + M_2^0 + = A\phi_1 c_1^0 L_1 + A\phi_2 c_2^0 (L - L_1).$$

Using the nondimensional relations, the initial mass of drug, M^0, may be expressed as:

$$M^0 = AL\phi_1 c_1^0\left(\delta + (1-\delta)\phi C^0\right).$$

Therefore, the normalised mass is:

$$\frac{M(t)}{M^0} = M'(t') = \frac{AL\phi_1 c_1^0}{AL\phi_1 c_1^0\left(\delta + (1-\delta)\phi C^0\right)}\left[\int_{-\delta}^{0} c_1'(x',t')dx' + \phi\int_{0}^{1-\delta} c_2'(x',t')dx'\right],$$

then simplifying and dropping the primes for clarity:

$$M(t) = \frac{1}{(\delta + (1-\delta)\phi C^0)}\left[\int_{-\delta}^{0} c_1(x,t)dx + \phi\int_{0}^{1-\delta} c_2(x,t)dx\right].$$

Where the integrals are equal to:

$$\int_{-\delta}^{0} c_1(x,t)dx = \sum_{n=1}^{\infty}\frac{4\sqrt{\chi\phi}\sin(\alpha_n\delta)\left(\cos\left(\frac{\alpha_n\bar{\delta}}{\sqrt{\bar{\chi}}}\right)(1-C^0)+C^0\right)e^{-\alpha_n^2 t}}{\alpha_n^2\left[\begin{array}{l}\left(\sqrt{\chi\phi}+1\right)\left(\delta+\frac{\bar{\delta}}{\sqrt{\bar{\chi}}}\right)\sin\left(\alpha_n\left(\delta+\frac{\bar{\delta}}{\sqrt{\bar{\chi}}}\right)\right)\\ +\left(\sqrt{\chi\phi}-1\right)\left(\delta-\frac{\bar{\delta}}{\sqrt{\bar{\chi}}}\right)\sin\left(\alpha_n\left(\delta-\frac{\bar{\delta}}{\sqrt{\bar{\chi}}}\right)\right)\end{array}\right]},$$

$$\int_0^{1-\delta} c_2(x,t)dx = \sum_{n=1}^{\infty} \frac{4\sqrt{\bar{\chi}}\sin\left(\alpha_n\delta\right)\left(\cos\left(\frac{\alpha_n\bar{\delta}}{\sqrt{\bar{\chi}}}\right)-1\right)\left(\cos\left(\frac{\alpha_n\bar{\delta}}{\sqrt{\bar{\chi}}}\right)\left(C^0-1\right)-C^0\right)e^{-\alpha_n^2 t}}{\left[\begin{array}{l}\alpha_n^2\cos\left(\frac{\alpha_n\bar{\delta}}{\sqrt{\bar{\chi}}}\right) \\ \times\left[\begin{array}{l}\left(\sqrt{\chi\phi}+1\right)\left(\delta+\frac{\bar{\delta}}{\sqrt{\bar{\chi}}}\right)\sin\left(\alpha_n\left(\delta+\frac{\bar{\delta}}{\sqrt{\bar{\chi}}}\right)\right) \\ +\left(\sqrt{\chi\phi}-1\right)\left(\delta-\frac{\bar{\delta}}{\sqrt{\bar{\chi}}}\right)\sin\left(\alpha_n\left(\delta-\frac{\bar{\delta}}{\sqrt{\bar{\chi}}}\right)\right)\end{array}\right]\end{array}\right]}.$$

3.2.3 Release profile

The fraction of drug released at some time t can be found via:

$$M_{frac}(t) = \frac{M^0 - M(t)}{M^0} = 1 - \frac{M(t)}{M^0}.$$

Therefore, the fraction of drug released is:

$$M_{frac}(t) = 1 - M(t) = 1 - \frac{1}{\left(\delta + \bar{\delta}\phi C^0\right)}\left[\int_{-\delta}^{0} c_1(x,t)dx + \phi\int_0^{1-\delta} c_2(x,t)dx\right], \qquad (3.49)$$

which is a function that can be used to generate a plot of cumulative release of a drug as a percentage vs time, known as a release profile.

3.2.4 Release profile special cases

For the special case in which $\chi = \phi = 1$, the fraction of drug released is:

$$M_{frac}(t)$$
$$= 1 + \frac{8}{\pi^2\left(\delta+\bar{\delta}C^0\right)}\sum_{n=1}^{\infty}\frac{1}{(2n-1)^2}\left[\begin{array}{l}\left[(-1)^{n+1}\sin\left(\frac{(2n-1)\pi\delta}{2}\right)\left(C^0-1\right)-C^0\right] \\ \times\exp\left(-\frac{(2n-1)^2\pi^2 t}{4}\right)\end{array}\right],$$

and for the second special case where $\chi = \phi = C^0 = 1$, the fraction of drug released is:

$$M_{frac}(t) = 1 - \frac{8}{\pi^2}\sum_{n=1}^{\infty}\frac{1}{(2n-1)^2}\exp\left(-\frac{(2n-1)^2\pi^2 t}{4}\right).$$

3.2.5 Full model solution

Although the simplified model (3.18-3.23) is the focus of this chapter, the full model, with more general boundary conditions, may be more realistic in other scenarios. For example, the simplified model assumes that there is perfect contact between the porous layers and the overall structures coincide, despite a potential difference in their respective porosities. However, this may not always be applicable and to account for this, the full model (3.3-3.8) utilises a mass transfer coefficient to allow for misaligned pores. Additionally, the full model also features general flux conditions. The nondimensional full model is the combination of transport equations (3.18-3.19), initial conditions (3.23) and the following nondimensional general boundary (3.50, 3.52) and interface conditions (3.51), derived using the same scalings as in the case of the simplified model:

$$-\frac{\partial c_1}{\partial x} = \Gamma_1 c_1, \quad x = -\delta, \quad t > 0, \tag{3.50}$$

$$\frac{\partial c_1}{\partial x} = \Pi(c_1 - c_2), \quad \frac{\partial c_1}{\partial x} = \chi \frac{\partial c_2}{\partial x}, \quad x = 0, \quad t > 0, \tag{3.51}$$

$$-\chi \frac{\partial c_2}{\partial x} = \Gamma_2 c_2, \quad x = \bar{\delta}, \quad t > 0, \tag{3.52}$$

where $\Pi = PL/D_1^e$, $\Gamma_1 = K_1 L/D_1^e$ and $\Gamma_2 = K_2 L/D_1^e$. The solution to this full model is solved and reported in [56]. The semi-analytical solution to the nondimensional full model is:

$$c_1(x,t) = \sum_{m=1}^{\infty} A_m \tilde{X}_{1,m} \exp\left(-\lambda_{1,m}^2 t\right),$$

$$c_2(x,t) = \sum_{m=1}^{\infty} A_m \tilde{X}_{2,m} \exp\left(-\bar{\chi}\lambda_{2,m}^2 t\right),$$

where:

$$A_m = \frac{\displaystyle\int_{-\delta}^{0} \tilde{X}_{1,m} dx + \phi C^0 \int_{0}^{\bar{\delta}} \tilde{X}_{2,m} dx}{\displaystyle\int_{-\delta}^{0} \tilde{X}_{1,m}^2 dx + \phi \int_{0}^{\bar{\delta}} \tilde{X}_{2,m}^2 dx},$$

$$\tilde{X}_{1,m} = \tilde{a}_{1,m} \cos\left(\lambda_{1,m} x\right) + \tilde{b}_{1,m} \sin\left(\lambda_{1,m} x\right),$$

$$\tilde{X}_{2,m} = \tilde{a}_{2,m} \cos\left(\lambda_{2,m} x\right) + \sin\left(\lambda_{2,m} x\right),$$

$$\tilde{a}_{2,m} = \frac{\chi\lambda_{2,m} + \Gamma_2 \tan\left(\lambda_{2,m}\bar{\delta}\right)}{\chi\lambda_{2,m} \tan\left(\lambda_{2,m}\bar{\delta}\right) - \Gamma_2},$$

$$\tilde{a}_{1,m} = \tilde{a}_{2,m} - \frac{\chi}{\Pi}\lambda_{2,m},$$

$$\tilde{b}_{1,m} = \sqrt{\chi\phi}.$$

The required eigenvalue pairs $(\lambda_{1,m}, \lambda_{2,m})$ are found by solving:

$$\begin{aligned}
&(\lambda_1 \sin(\lambda_1\delta) + \Gamma_1 \cos(\lambda_1\delta)) \\
&\times \left[\Pi\left(\chi\lambda_2 \cos\left(\lambda_2\bar{\delta}\right) + \Gamma_2 \sin\left(\lambda_2\bar{\delta}\right)\right) + \chi\lambda_2\left(\Gamma_2 \cos\left(\lambda_2\bar{\delta}\right) - \chi\lambda_2 \sin\left(\lambda_2\bar{\delta}\right)\right)\right] \\
&-\Pi\sqrt{\chi\phi}\,(\lambda_1 \cos(\lambda_1\delta) - \Gamma_1 \sin(\lambda_1\delta)) \\
&\times \left(\Gamma_2 \cos\left(\lambda_2\bar{\delta}\right) - \chi\lambda_2 \sin\left(\lambda_2\bar{\delta}\right)\right) = 0.
\end{aligned}$$

The nondimensional mass of drug in each layer is:

$$M_1(t) = \frac{1}{\delta + \bar{\delta}\phi C^0} \sum_{m=1}^{\infty} A_m \left(\frac{\tilde{a}_{1,m} \sin(\lambda_{1,m}\delta) + \tilde{b}_{1,m}\left(\cos(\lambda_{1,m}\delta) - 1\right)}{\lambda_{1,m}}\right) \exp\left(-\lambda_{1,m}^2 t\right),$$

$$M_2(t) = \frac{\phi}{\delta + \bar{\delta}\phi C^0} \sum_{m=1}^{\infty} A_m \left(\frac{\tilde{a}_{2,m} \sin\left(\lambda_{2,m}\bar{\delta}\right) - \cos\left(\lambda_{2,m}\bar{\delta}\right) + 1}{\lambda_{2,m}}\right) \exp\left(-\bar{\chi}\lambda_{2,m}^2 t\right),$$

and from these nondimensional mass equations, the drug release profile may be calculated and is defined $M_{frac} = 1 - (M_1(t) + M_2(t))$.

3.3 Results and discussion

A sensitivity analysis is conducted to provide insight into what system parameters are the most influential on the shape of the release profile and to what extent. Therefore, some initial parameter values are required to generate suitable ranges for the model parameters. Particles which are freely diffusing in liquids have diffusion coefficients which are typically of the order $10^{-10} - 10^{-9}\mathrm{m}^2\mathrm{s}^{-1}$ [61]. Effective porosities will assume values within the range $0 < \phi_i^e < 1$ $(i = 1, 2)$ although, in reality, values will likely be restricted to $0.1 - 0.9$ due to mechanical and drug-loading constraints. Values for tortuosity are typically found in the range $1 < \tau_i < 6$, however, values as high as 10 have been reported [48]. Considering this range of values, it is reasonable to assume that effective diffusion coefficients, D_i^e, will fall within the range $10^{-11} - 10^{-9}\mathrm{m}^2\mathrm{s}^{-1}$. Since the purpose of the model is to determine the potential benefits of replacing a drug-releasing single porous layer, with a composite porous layer of identical thickness and initial mass of drug, the range of values for χ should encompass the extreme values of the typical ranges for D_i^e and ϕ_i^e. Therefore, the values considered for ratio of the effective diffusion coefficients, χ, are $1/10$, 1 and 10. The parameter δ will influence the relative thicknesses of the two layers and the values chosen are 0.25, 0.5 or 0.75. Since the model is nondimensional, no specific values for initial drug loading in each layer are chosen, so values simulated for C^0 are 0 (no drug in layer 2), 1 (same initial concentration in each layer) and 10 (an order of magnitude

greater initial drug concentration in layer 2 than in layer 1). It may be shown that:

$$C^0 = \frac{\left(\frac{M^0}{M_1^0} - 1\right)\delta}{\phi\,(1-\delta)}. \tag{3.53}$$

Since M^0 is fixed, then if ϕ remains constant, any change to C^0 must be accommodated through a redistribution of the initial mass between the two layers, as seen in equation (3.53).

The effect of varying the ratio of the porosity of the two layers, ϕ, is a little more complicated to probe. Any changes to ϕ will cause changes in χ, so much so that the parameter cannot be tested in isolation. This dependency may be shown by considering the definition of χ:

$$\chi = \frac{D_2^e}{D_1^e} = \frac{\frac{\phi_2^e D^w}{\tau_2}}{\frac{\phi_1^e D^w}{\tau_1}} = \frac{\phi_2^e \tau_1}{\phi_1^e \tau_2}. \tag{3.54}$$

It is observed that since ϕ_2^e and ϕ_1^e are constrained by ϕ_1 and ϕ_2, respectively ($\phi_2^e \leq \phi_2$ and $\phi_1^e \leq \phi_1$), then any change to ϕ will induce a change in the effective diffusivity in each layer, as shown in equation (3.54). Although χ may, in principle, be maintained at 1 if τ_1/τ_2 varies to compensate the change in ϕ_2^e/ϕ_1^e.

Equations (3.47), (3.48) and (3.49) are used for the sensitivity analysis, however, these equations feature infinite series whose infinite summation is unknown. The sum will have to be truncated to approximate the infinite sum. The truncation value chosen is N, the number of roots in a given interval of (3.46). The value of N will affect the accuracy of the results and should too few roots be used or missed entirely, the solution will not converge. The values of the system parameters will change (3.46) and hence the location of the roots. For a certain parameter set, more/less roots may be required for an accurate solution. To accomplish this, the initial root searching interval used in the simulations, is $[0, 100]$. To determine whether or not N is a sufficient number of roots to produce an accurate solution, the theoretical masses $M_{S_{N+1}}$ and M_{S_N} for the sequences of roots S_{N+1} and S_N, are considered and if:

$$100 \times \frac{\int_0^t M_{S_{N+1}}(t)dt - \int_0^t M_{S_N}(t)dt}{\int_0^t M_{S_N}(t)dt} < 1\%,$$

for some time t, then N is deemed sufficiently accurate. To ensure smooth plots for concentration profiles and release profiles, the intervals considered for the nondimensional variables x and t, are divided into 100 equally spaced increments.

3.3.1 Baseline study

To be able to assess the effect that altering the parameters will have on the concentration profiles, generated by (3.47) and (3.48), and the release profiles, generated by (3.49), a baseline study is considered. This study assumes that the layers of the porous media have the same structural properties and initial drug concentration ($\chi = \phi = C^0 = 1$). The net result is a reduction of the model to essentially a single-layer system. All simulated parameter values are presented in Table 3.1.

Study	χ	C^0	ϕ	δ
Baseline	1	1	1	0.5
1	0.1 10	1	1	0.25 0.5 0.75
2	1	0 10	1	0.25 0.5 0.75

Table 3.1: Table of parameter values used in the simulations.

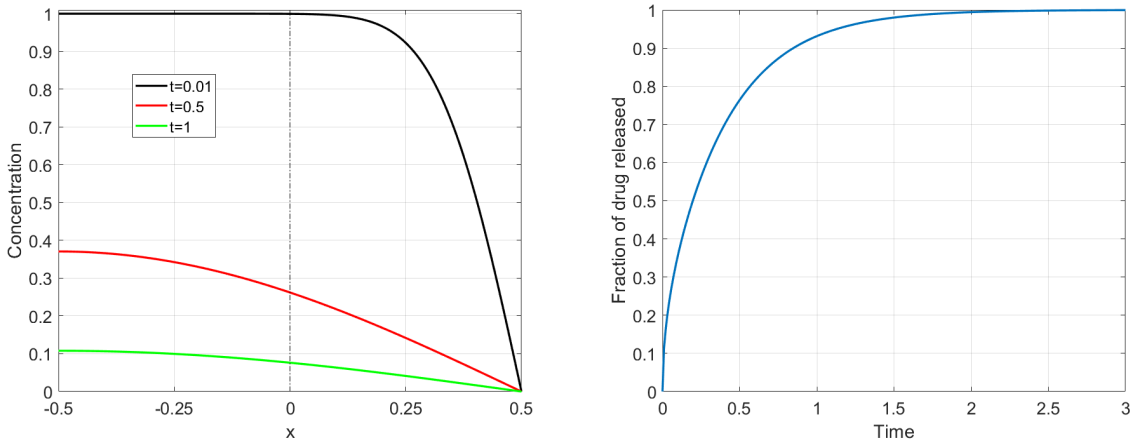

(a) (b)

Figure 3.4: Baseline case: (a) Nondimensional concentration profiles versus nondimensional space at three nondimensional times. The vertical dashed line in (a) is to mark where the interface between the layers lies. (b) Fraction of drug released versus nondimensional time. For all cases $N = 32$.

Figure 3.4 shows the results of the baseline study. Due to the parameter values ($\chi = \phi = C^0 = 1$) and the perfect contact at the interface between the layers, the problem is essentially one-layer. Therefore, the shape of the concentration profiles and the release profile, are not

influenced by the location of the interface. There is a delay in the release of drug from layer 1, whilst the drug in layer 2 is released relatively quickly. From the release profile, complete release is achieved at approximately a nondimensional time of $t = 3$.

3.3.2 Sensitivity analysis

To assess the influence varying system parameters has on the shape of the release profile, each parameter is considered separately, varied around the baseline values and the resultant release and concentration profiles compared. Two studies are considered: Study 1 and Study 2, in which the effect of varying χ and C^0, respectively, are investigated. In each case, the value of δ is varied between the three values in Table 3.1. It is assumed that the overall thickness of the layers, L, and the initial mass, M^0, are constant.

3.3.3 Study 1: effect of varying effective diffusivity ratio χ

The influence of varying the relative structural parameters between the layers is assessed. In column (a) of Figure 3.5, χ is chosen such that the effective diffusivity within layer 2 is a tenth that of layer 1, while in column (b) the effective diffusivity is ten times greater. Figure 3.5 features three plots in each column, one for each value of δ considered. When $\chi = 1/10$, drug transport from layer 1 is hindered by the much lower effective diffusivity in layer 2, this results in a delay in the release of drug from layer 1 and so the concentration remains relatively high (Figure 3.5 (a)). When $\chi = 10$ the transport of drug within layer 2 is boosted considerably, and this results in a quicker release of drug from layer 1. This results in a rapidly depleting concentration in both layers (Figure 3.5 (b)).

A noteworthy feature of the concentration plots (Figure 3.5 (a)), is the linearity of the profile when $\delta = 0.25$, $\delta = 0.75$, in layers 1 and 2, respectively, for certain times. This phenomena can be explained by the order of magnitude difference in the values of effective diffusivities between the layers. This results in a near-negligible derivative of concentration with respect to time, therefore the solution is approximately linear. This can be seen when considering equation (3.12) and using the same scaling for concentration and a slight alteration to the scaling for time:

$$t' = \frac{D_2^e t}{\phi_1 L^2} \Rightarrow \chi \frac{\partial c_1}{\partial t} = \frac{\partial^2 c_1}{\partial x^2}.$$

When $\chi = 1/10$, this equation is approximated by the much simpler second-order ODE:

$$\frac{d^2 c_1}{dx^2} = 0 \Rightarrow c_1 = A(t)x + B(t),$$

where $A(t)$ and $B(t)$ are time-dependent scalars, whose values will depend on the boundary conditions. The similar behaviour in layer 2, when $\delta = 0.75$, can also be explained via a similar

approach with equation (3.13). In Figure 3.5 (b), the concentration profiles at early times in layer 1 produce a "bump" close to the interface with layer 2. This is likely due to the order of magnitude greater effective diffusivity in layer 2 and so, as particles reach the interface, they will experience a sudden increase in transport rate.

The release profiles for these two cases are shown alongside the baseline release profile for comparison in Figure 3.6. The variation of δ highlights a relationship between χ and δ. In the case where $\chi = 1/10$ and as δ is increased (layer 2 becomes narrower), the release of drug is quicker. This is expected behaviour since drug particles will have to traverse a shorter distance with a smaller effective diffusivity as δ increases. Conversely, when $\chi = 10$ and as δ is increased, the release begins to slow down considerably. This can be explained by drug particles having to travel through a progressively thicker layer 1 with an effective diffusivity which is an order of magnitude lower than that in layer 2.

The plots generated in this study demonstrate that structural parameter χ has the potential to be strongly influential in altering the release rate (shape of the release profile) and therefore, the duration of release. This result is expected though as χ consists of not only the effective levels of porosity of each layer, but also the level of tortuosity. These are arguably the main structural design parameters of the layers. Not only does χ feature heavily in the solutions (3.47) and (3.48), but also in equation (3.46), which is crucial in obtaining the results. The results also suggest that it is the combination of parameters ϕ and τ that will define the release profile since a value of $\chi = 10$ may be achieved through increasing the effective porosity of layer 2 relative to layer 1 or via increasing the tortuosity of layer 1 relative to layer 2.

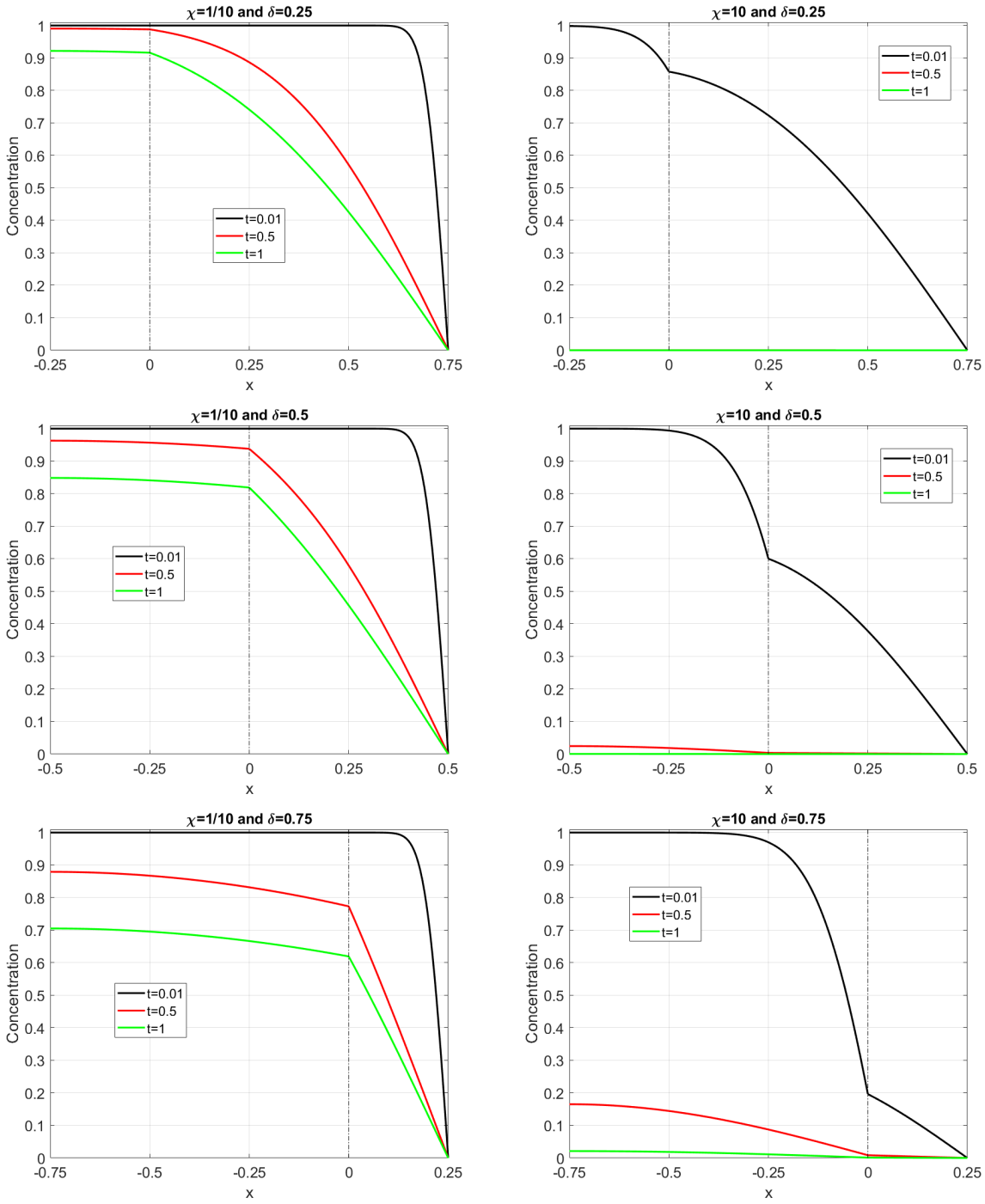

(a) (b)

Figure 3.5: Nondimensional concentration profiles versus nondimensional space at three nondimensional times for $\delta = 0.25$, $\delta = 0.5$ and $\delta = 0.75$ for two values of χ, with (a) $\chi = 1/10$ (as δ increases $N = 83, 66, 49$) and (b) $\chi = 10$ (as δ increases $N = 16, 21, 26$).

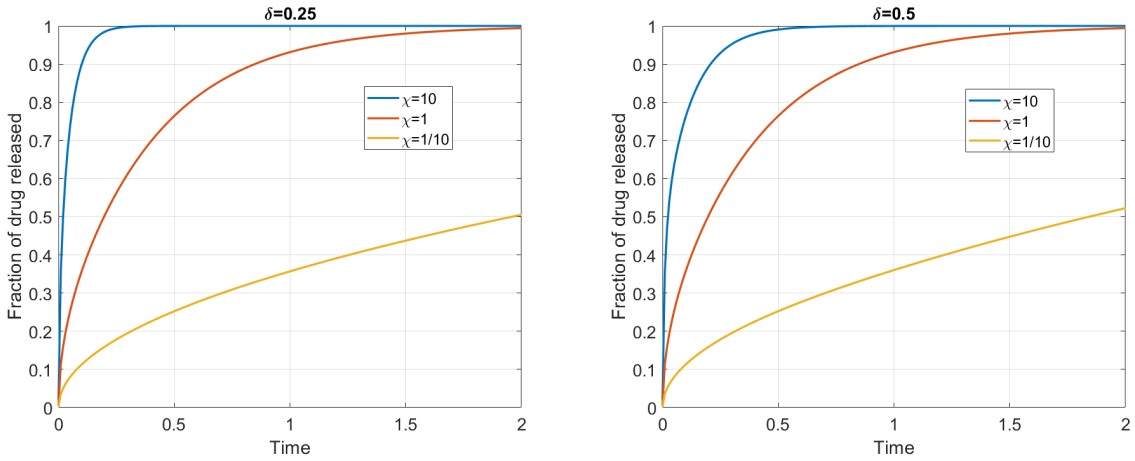

(a)

(b)

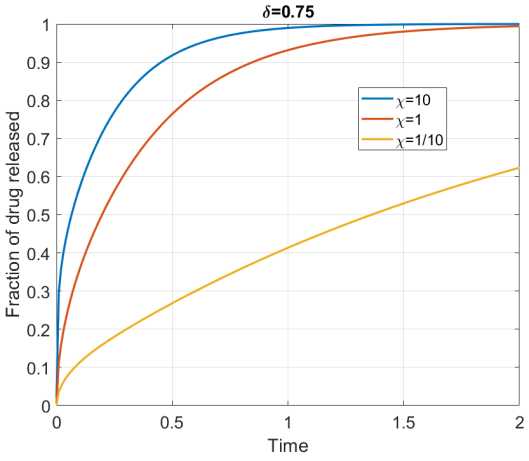

(c)

Figure 3.6: Fraction of drug released versus nondimensional time for different values of χ with (a) $\delta = 0.25$ $(N = 83, 32, 16)$ (b) $\delta = 0.5$ $(N = 66, 32, 21)$ and (c) $\delta = 0.75$ $(N = 49, 32, 26)$, with increasing χ. Approximate time for complete release with $\chi = 1/10$: (a) $t = 20$, (b) $t = 18$ and (c) $t = 12$

3.3.4 Study 2: effect of varying initial concentration ratio C^0

The effect of varying the ratio of initial concentrations of the two layers is investigated. In Figure 3.7 (a), C^0 is set to zero, this means that there is no initial drug concentration in layer 2. In Figure 3.7 (b), C^0 is set such that the initial concentration in layer 2 is ten times greater than the initial concentration in layer 1. With $C^0 = 0$, drug is observed entering layer 2 rapidly and the drug concentration dropping quickly over time. With increasing δ, it appears as though the concentrations are greater at the same time points in Figure 3.7 (a). By fixing the values of ϕ, δ and M^0, any variation in C^0 must induce a change in M_1^0 and by extension, M_2^0. Therefore, to keep the total mass of drug constant, the distribution of this total drug mass will be distributed differently when C^0 is altered. Thus, the concentrations shown in Figure 3.7 (a), although the nondimensional scale is the same, the curves will be scaled with a different value of c_1^0, as δ is

increased, which can be seen in equation (3.53). This is also true of the concentration plots in Figure 3.7 (b), as c_2^0 is dependent on the value of c_1^0 through the definition of C^0. With $C^0 = 10$ it is observed that drug from layer 2 diffuses into layer 1 due to the large concentration gradient between the layers. As drug diffuses into layer 1 and is released from layer 2, the concentration gradient will change direction. Therefore, drug will then diffuse from layer 1 to layer 2 until complete release is achieved. This scenario is unlikely to be desirable as it may influence the drug release profile unnecessarily. The value of δ appears to have a considerable effect on the release process. In Figure 3.7 (a), where $C^0 = 0$, when $\delta = 0.75$, there is a relatively short diffusion distance in layer 2 compared to when $\delta = 0.25$. This results in a shorter delay for release of drug to occur since drug particles will have to travel a shorter distance. Also, in Figure 3.7 (b), where $C^0 = 10$, when $\delta = 0.75$, the large concentration gradient which exists between the two layers is diminished more quickly and complete release is attained rapidly when compared to the concentration plots for $\delta = 0.25$. When comparing the release profiles of Figure 3.8 to those of Figure 3.6, the influence that the variation of C^0 has on the release profile is considerably smaller than the influence of χ. Interestingly, despite some variation in the early stages of release, the time until complete release is approximately identical for all plots in Figure 3.8.

The variation of C^0 may have suitable applications in certain scenarios, for example, it may be advantageous for there to be a delay before drug release occurs, therefore, $C^0 = 0$ may be a feasible parameter value and could take the form of a drug-free top-coat. It may also be useful for a large burst release to occur initially in certain circumstances, such as antibiotic delivery, therefore, $C^0 = 10$ may be a useful parameter value to achieve this. However, from Figure 3.8, the time for complete release is approximately identical, so rather than a parameter to alter the shape of the release profile, C^0 could be used as a means of controlling the total amount of drug delivered, which will depend on the application. One noteworthy observation is the small point of inflection at the start of the release profile for $C^0 = 0$, which is likely due to drug from layer 1 having to diffuse into, the initially empty, layer 2. This may also be a desirable scenario in some applications, however, it is possible that drug could enter layer 2 during the manufacturing process.

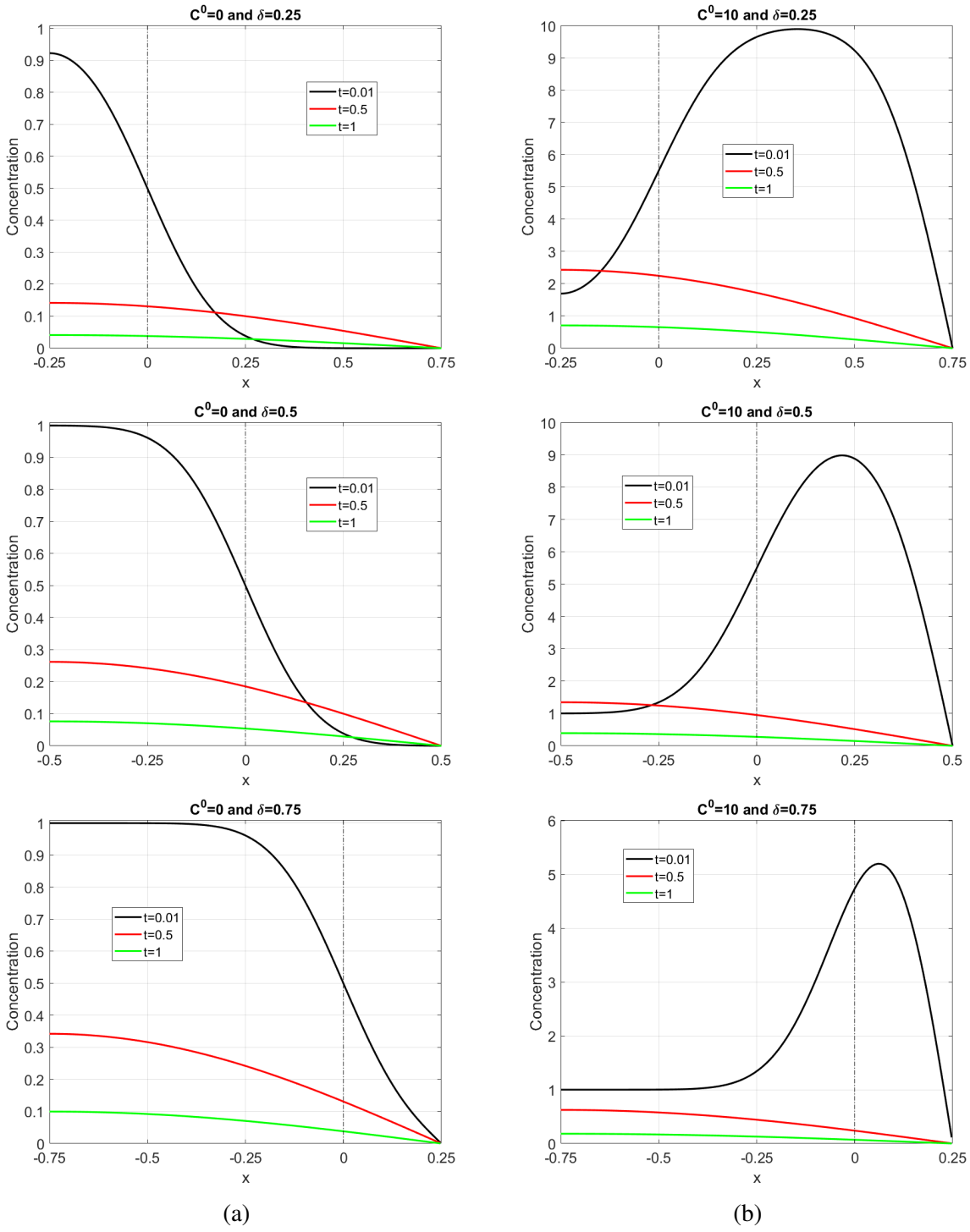

Figure 3.7: Nondimensional concentration profiles versus nondimensional space for $\delta = 0.25$, $\delta = 0.5$ and $\delta = 0.75$ for two values of C^0, with (a) $C^0 = 0$ and (b) $C^0 = 10$ at three nondimensional times. For all cases $N = 32$. Since M^0 is kept constant, varying C^0 results in a different value of normalising concentration, c_1^0, between the left and right plot columns, i.e. even though the vertical axis has the same scale between the left and right plot columns, the corresponding dimensional values of concentration will differ.

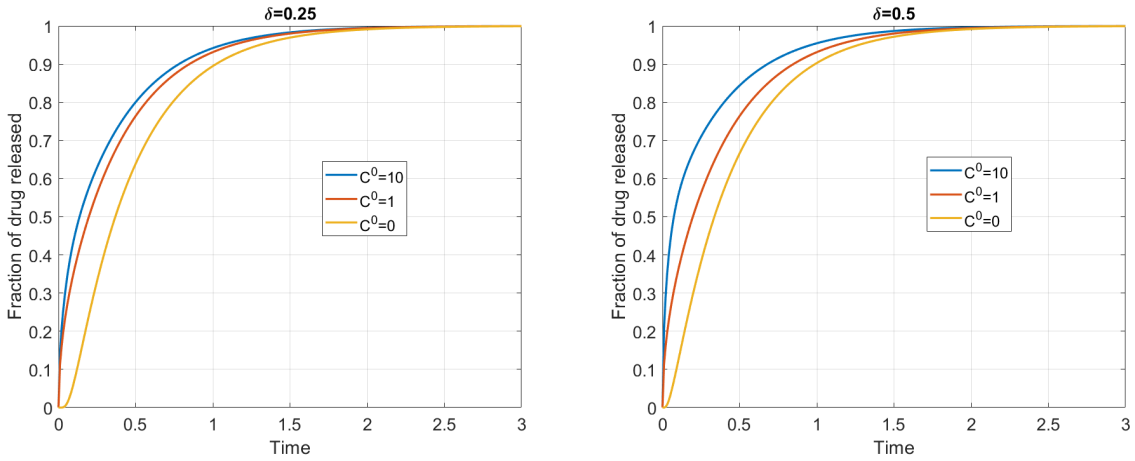

(a)

(b)

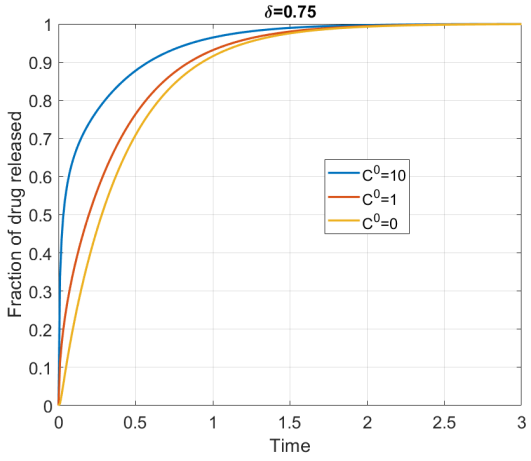

(c)

Figure 3.8: Fraction of drug released versus nondimensional time for different values of C^0 with (a) $\delta = 0.25$, (b) $\delta = 0.5$ and (c) $\delta = 0.75$. For all cases $N = 32$.

3.3.5 Practical examples of model use

There are certain scenarios that could be realised through the use of the model in this chapter via certain combinations of parameter values. One possibility is delaying the release of drug and an example of suitable parameter values that can achieve this are $\chi = 0.1$, $\phi = 9$, $C^0 = 0$ and $\delta = 0.25$. From Figure 3.9, it is observed that drug release is delayed until an approximate nondimensional time of $t = 3$.

Another possible scenario is where drug is released quickly, such as the need to infuse the surface of an OI and the surrounding tissues with an antibiotic to kill any potential bacteria, thus preventing OI associated infection. An example parameter combination that can give rise to this scenario is $\chi = 10$, $\phi = 1/9$, $C^0 = 10$ and $\delta = 0.25$. From Figure 3.10, there is a very rapid release initially and a sustained release until approximately $t = 0.2$ nondimensional time.

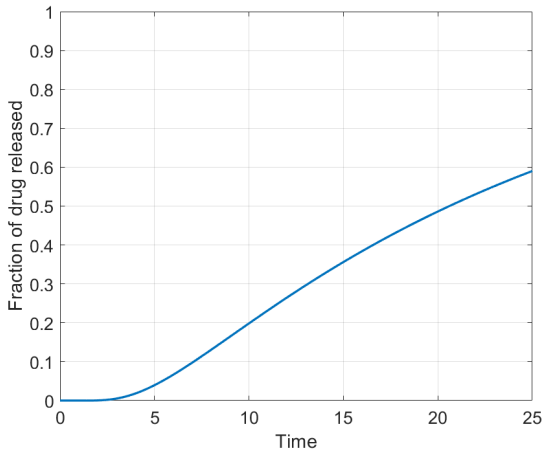

Figure 3.9: Fraction of drug released versus nondimensional time showing a delay in the release of drug. Where $\chi = 0.1$, $\phi = 9$, $C^0 = 0$, $\delta = 0.25$ and $N = 234$.

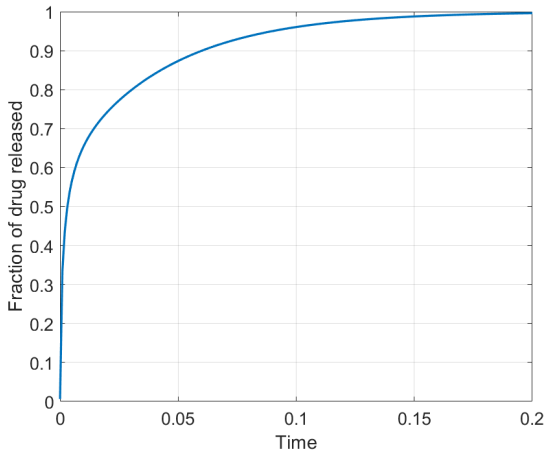

Figure 3.10: Fraction of drug released versus nondimensional time showing rapid release of drug. Where $\chi = 10$, $\phi = 1/9$, $C^0 = 10$, $\delta = 0.25$ and $N = 74$.

3.3.6 Conclusions

In this chapter, a mathematical model of the diffusion of drug through two porous layers was presented and the influence of the model parameters on the concentration and release profiles was investigated. The results of the sensitivity analysis demonstrated that through the use of variable porosity coatings, a greater degree of controlled drug release may be achieved, be it in the form of release duration or in the quantity of drug delivered within a required time. The variation of δ and C^0 had some influence on the concentration and release profiles, however, it would appear from this study that the most influential parameter was χ. This is somewhat expected since χ is comprised of both the porosity and the tortuosity of each layer. These parameters govern the microstructural properties of each layer and hence the effective diffusive transport through the layers. Therefore, it is reasonable to conclude that χ may be the dominant parameter in the model and so provides considerable flexibility and tuneability from a design/manufacturing

point of view.

This model is an example of how simple the process of generating release profiles is, and in some cases, where a semi-analytical or fully-analytical solution is available, a mere few seconds is required. In theory, the transport and release of a variety of drugs and porosity levels, potentially providing wildly different parameter values, may be modelled relatively quickly when compared to the time scales required for drug-release experiments. Such experiments also require monetary costs to be met, however, with a validated mathematical model, theoretical simulation after initial experimentation removes the need for further experimental investigation. There are limitations with this model, chief among which is the assumption that the drug is initially in a solute phase, which could limit the practical use in cases where the drug is poorly soluble. Therefore, one possible enhancement to this model would be the inclusion of the drug dissolution process. It should be noted that this work is quite general and not focussed on a particular implant/device. In the next chapter, however, a specific device is investigated (a porous prototype fixation pin) and this model is adapted accordingly.

Chapter 4

Modelling drug release from porous-walled orthopaedic pins

In chapter 2, it was found that many drug-release studies that focus on the potential for drug-releasing OIs featured porosity as a key means of controlling the release. In chapter 3, a mathematical model was devised and studied to assess the extent to which variable porosity systems can provide a flexible method of control in the context of drug delivery. In this chapter, the aim is to devise a mathematical model of drug release from a particular prototype device, specifically the porous pin by Gimeno et al. (Figure 4.1 (a)) [11], and conduct a sensitivity analysis on the various system parameters and how they influence the release profile.

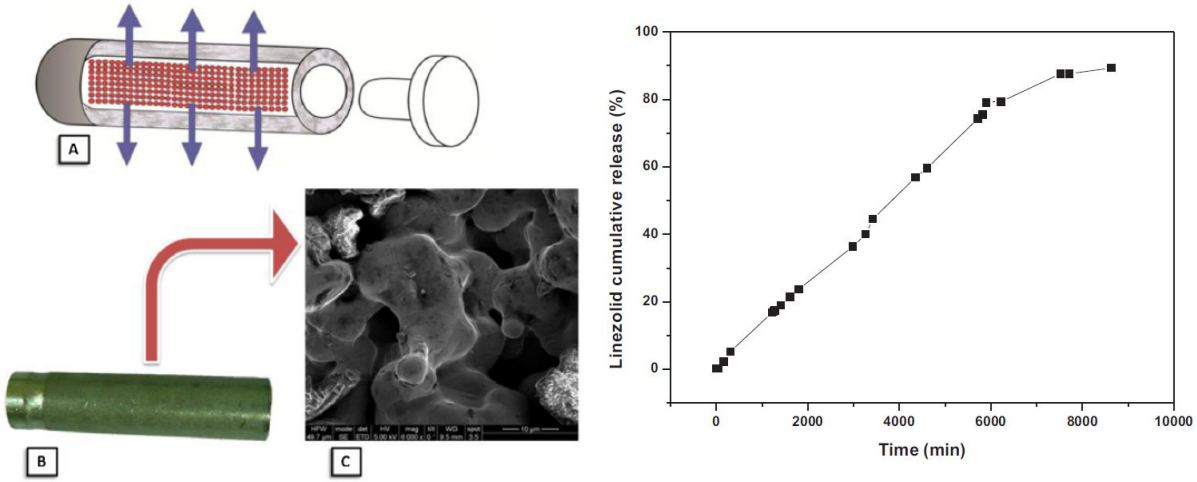

(a) (b)

Figure 4.1: (a) A: Illustration of the porous pin with blue arrows showing drug transport through the porous wall of the pin. B: The real macroporous stainless steel pin. C: Scanning electron microscopy view of the porous wall of the pin, with a volumetric porosity of $17\,\%$. (b) Release profile of Linezolid expressed as a percentage of the Linezolid initially loaded in the porous pin.

The primary reason for modelling this particular device is due to the availability of some information on the experimental setup, such as the volume of the release medium and the physical

dimensions of the pin, which is crucial in setting up a mathematical model. There is also some limited drug release data (Figure 4.1 (b)), which may be used to attempt to validate the model. It is stated that the implants have a porous length of $25.4\,\mathrm{mm}$, an outside diameter of $6.35\,\mathrm{mm}$ and a wall thickness of $1.6\,\mathrm{mm}$ [11]. The release media volume was $100\,\mathrm{mL}$ of SBF and the release data was obtained without renewal of the release media [11].

4.1 Preliminary model

For an initial model, it is assumed that diffusion is the sole component driving drug transport and that the porous pin is comprised of two distinct regions, the inner drug core, with radius L_d and the porous wall of the pin, with thickness L_p, with the subscript d and p denoting the inner drug core and the porous wall, respectively. The inner drug core has length H, effectively the height of the pin. In these regions, the respective drug concentrations are defined $c_d(r,\theta,z,t)$ and $c_p(r,\theta,z,t)$, the intrinsic drug concentration within the porous wall. Along with the concentration definitions are the constant initial concentrations $c_d = c_d^0$ and $c_p = 0$. The position of the interface between the drug and porous layers and the position of the outer edge of the porous region are defined as $L_1 = L_d$ and $L_2 = L_d + L_p$, respectively (Figure 4.2 (b)). Additionally, the level of porosity and tortuosity of the porous wall are defined as ϕ and τ, respectively. The value of τ used throughout the chapter is 3, which is considered an average value of the typical range of tortuosities. The rationalisation for this average value is that solutes diffuse in 3D and thus have three directions of travel and so will travel around three times the distance compared to just one direction [48]. The diffusivity of drug within the inner drug layer is assumed to be the free-diffusion coefficient, D_f, which for this chapter is assumed to be both constant and isotropic, and takes the greatest value in the typical range of diffusion coefficients in liquids, which is $1 \times 10^{-9}\,\mathrm{m}^2/\mathrm{s}$. From the free-diffusion coefficient, the effective diffusion coefficient within the porous wall, D_p, can be calculated via $D_p = \phi_e D_f/\tau$, following chapter 3 [48], where ϕ_e is the effective porosity of the porous wall and is assumed to be $90\,\%$ of the overall porosity, ϕ, for this chapter. Additionally, the angular and vertical position variables are defined as θ, $0 < \theta \leq 2\pi$, and z, $0 \leq z \leq H$, respectively. Assuming that the drug is in the solute phase, the 3D diffusion model is:

$$\frac{\partial c_d}{\partial t} = D_f \nabla^2 c_d, \quad 0 < r < L_1, \quad 0 < \theta \leq 2\pi, \quad 0 < z < H, \quad t > 0, \tag{4.1}$$

$$\phi \frac{\partial c_p}{\partial t} = D_p \nabla^2 c_p, \quad L_1 < r < L_2, \quad 0 < \theta \leq 2\pi, \quad 0 < z < H, \quad t > 0, \tag{4.2}$$

$$-\hat{\boldsymbol{n}} \cdot D_f \nabla c_d = 0, \quad r = 0, \quad 0 < \theta \leq 2\pi, \quad 0 < z < H, \quad t > 0, \tag{4.3}$$

$$-\hat{\boldsymbol{n}} \cdot D_f \nabla c_d = 0, \quad 0 < r < L_1, \quad -\hat{\boldsymbol{n}} \cdot D_p \nabla c_p = 0, \quad L_1 < r < L_2,$$
$$0 < \theta \leq 2\pi, \quad z = 0,\, H, \quad t > 0, \tag{4.4}$$
$$c_d = c_p, \quad -\hat{\boldsymbol{n}} \cdot D_f \nabla c_d = -\hat{\boldsymbol{n}} \cdot D_p \nabla c_p,$$

$$r = L_1, \quad 0 < \theta \leq 2\pi, \quad 0 < z < H, \quad t > 0, \tag{4.5}$$

$$c_p = 0, \quad r = L_2, \quad 0 < \theta \leq 2\pi, \quad 0 < z < H, \quad t > 0, \tag{4.6}$$

$$c_d = c_d^0, \quad 0 \leq r \leq L_1, \quad 0 < \theta \leq 2\pi, \quad 0 \leq z \leq H, \quad t = 0, \tag{4.7}$$

$$c_p = 0, \quad L_1 < r \leq L_2, \quad 0 < \theta \leq 2\pi, \quad 0 \leq z \leq H, \quad t = 0, \tag{4.8}$$

where $\hat{\boldsymbol{n}}$ is the outward facing unit normal to applicable boundary surfaces.

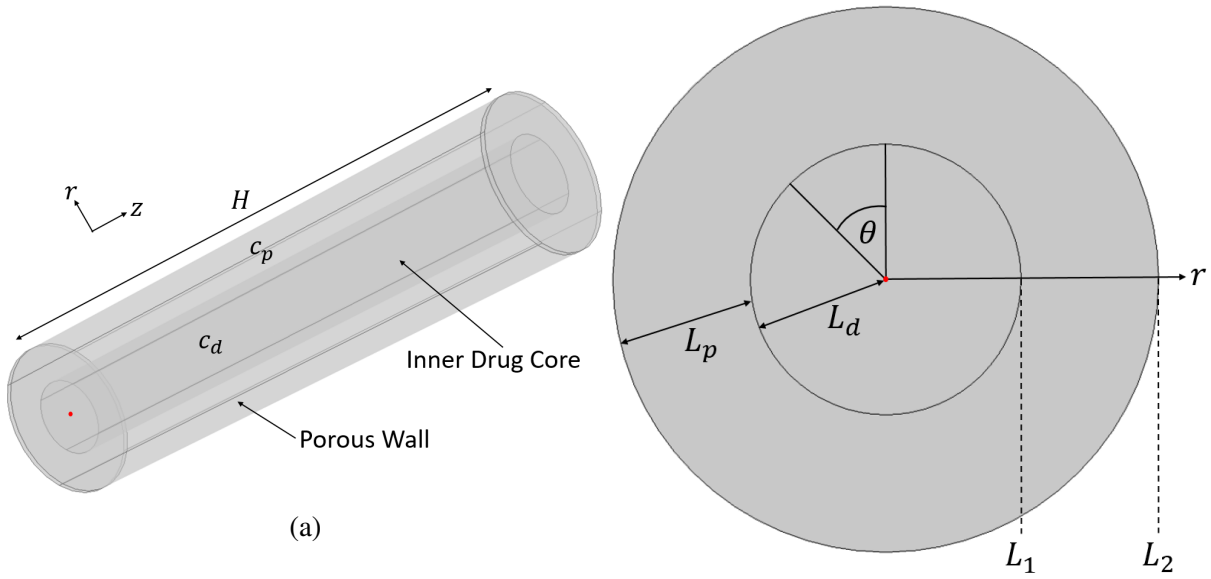

Figure 4.2: (a) 3D porous pin geometry with the ends of the geometry capped to prevent drug transport through either end of the pin. Variables c_d and c_p highlight the regions where the concentrations are defined. The red dot marks the position of the origin. (b) A 2D cross-sectional slice at the bottom of the 3D geometry, to clearly show the inner drug core radius, L_d, and the porous wall thickness, L_p. The image also shows how θ is defined, the angle of rotation around the central axis. The red dot marks the position of the origin.

Figure 4.2 shows the 3D geometry considered and a cross-sectional slice of the geometry, indicating the locations of c_d and c_p and how geometric parameters are defined. Model equations (4.1-4.8) consists of a pair of coupled diffusion equations (4.1-4.2) which model diffusive drug transport through the inner drug core and the porous wall, respectively. Equation (4.3) is a compatibility condition, which ensures that the solution is finite when $r = 0$. Equations (4.4) are zero-flux boundary conditions, which are applied to the top and bottom of the pin geometry, such that drug cannot cross the solid boundary. Equations (4.5) are continuity of concentration and flux conditions which are applied at the interface between the drug region and the porous wall at $r = L_1$. Equation (4.6) is an infinite sink condition, which is used in lieu of a release medium for model simplification. This is likely suitable since the release medium in the experimental setup is stirred and is comprised of $100\,\mathrm{mL}$ of SBF, which is much greater than the volume of the pin, which is approximately $0.8\,\mathrm{mL}$. The applicability of the infinite sink condition will be

explored later in the chapter. Equations (4.7-4.8) are the initial conditions applied to each region of the pin. The model is normalised via the following scalings:

$$c_d' = \frac{c_d}{c_d^0}, \quad c_p' = \frac{c_p}{c_d^0}, \quad z' = \frac{z}{L_d}, \quad r' = \frac{r}{L_d}, \quad t' = \frac{D_f}{L_d^2}t,$$

additionally, for simplification, $D = D_p/D_f$. Dropping the primes for clarity, the nondimensional model is:

$$\frac{\partial c_d}{\partial t} = \nabla^2 c_d, \quad 0 < r < 1, \quad 0 < \theta \leq 2\pi, \quad 0 < z < H/L_d, \quad t > 0, \tag{4.9}$$

$$\phi\frac{\partial c_p}{\partial t} = D\nabla^2 c_p, \quad 1 < r < L_2/L_d, \quad 0 < \theta \leq 2\pi, \quad 0 < z < H/L_d, \quad t > 0, \tag{4.10}$$

$$\hat{\boldsymbol{n}} \cdot \nabla c_d = 0, \quad r = 0, \quad 0 < \theta \leq 2\pi, \quad 0 < z < H/L_d, \quad t > 0, \tag{4.11}$$

$$\hat{\boldsymbol{n}} \cdot \nabla c_d = 0, \quad 0 < r < 1, \quad \hat{\boldsymbol{n}} \cdot \nabla c_p = 0, \quad 1 < r < L_2/L_d,$$
$$0 < \theta \leq 2\pi, \quad z = 0, H/L_d, \quad t > 0, \tag{4.12}$$

$$c_d = c_p, \quad \hat{\boldsymbol{n}} \cdot \nabla c_d = \hat{\boldsymbol{n}} \cdot D\nabla c_p, \tag{4.13}$$
$$r = 1, \quad 0 < \theta \leq 2\pi, \quad 0 < z < H/L_d, \quad t > 0,$$

$$c_p = 0, \quad r = L_2/L_d, \quad 0 < \theta \leq 2\pi, \quad 0 < z < H/L_d, \quad t > 0, \tag{4.14}$$

$$c_d = 1, \quad 0 \leq r \leq 1, \quad 0 < \theta \leq 2\pi, \quad 0 \leq z \leq H/L_d, \quad t = 0, \tag{4.15}$$

$$c_p = 0, \quad 1 < r \leq L_2/L_d, \quad 0 < \theta \leq 2\pi, \quad 0 \leq z \leq H/L_d, \quad t = 0, \tag{4.16}$$

4.1.1 Model reduction

From Figure 4.1 (a), the porous pin is approximately cylindrical in shape, therefore, it may be possible to reduce the geometry through the use of symmetry. If this were to be achievable, then a 3D model may not be required if a 1D model can produce the same results. The main benefits to this are a reduction in computation costs and the possibility that analytical, or even semi-analytical, solutions may be obtainable. To explore if symmetry can be exploited, equations (4.9-4.16) of the 3D diffusion model were transformed into the required 1D and 2D equivalent models by neglecting the θ and z components of the model equations.

The 3D, 2D and 1D models were solved numerically by means of the finite element method (FEM), using the commercial software package COMSOL Multiphysics®, version 5.3a. It should be noted that although the 1D model is solved numerically using a cylindrical coordinate system (the radial coordinate only), the 2D and 3D models were numerically solved in the software using the Cartesian coordinate system. This is the default coordinate system and does not affect the results for the 2D and 3D models. The basic operation in the software involves designing a model geometry, which is discretised with a finite number of elements to form an approximation of the original geometry. Points where mesh elements meet are known as nodes. The meshing may be performed manually, or it may be done with built-in meshing tools with a

variety of mesh density settings. For the model (4.9-4.16) the "Extremely Fine" mesh settings were used to generate a mesh based on tetrahedral elements for the 3D model and triangular elements for the 2D model, these meshes are shown in Figure 4.3. The "Extremely Fine" mesh settings were also used to discretise the interval geometry of the 1D model, consisting of 101 equally spaced points. To determine if the chosen mesh was suitable, a much finer custom mesh was constructed and the results were compared. There was no appreciable difference in the release profiles generated for the 3D, 2D or 1D models, therefore, the "Extremely Fine" mesh settings were deemed suitable. Since the studies are time-dependent, the original equations are approximated locally by ODEs at each node of the mesh, then a system of simultaneous ODEs are compiled and can be solved by various methods. Depending on the chosen physics, a suitable default solver is selected from the several built-in methods, which may also be changed within the solver settings. In the case of the diffusive transport models, the generalized minimal residual method (GMRES), an iterative method for solving nonsymmetric systems of linear equations, was used. The implicit Backward Differentiation Formula (BDF) of orders one and two, was used as the time-advancing solver. Free time-stepping was used for efficiency, the time-step taken at a particular point may be smaller or greater than the previous time-step. This is done within the software by checking if the solution varies considerably at the current time, subject to the specified tolerance levels, and if the solution does vary too much, then the software reduces the size of the time-step.

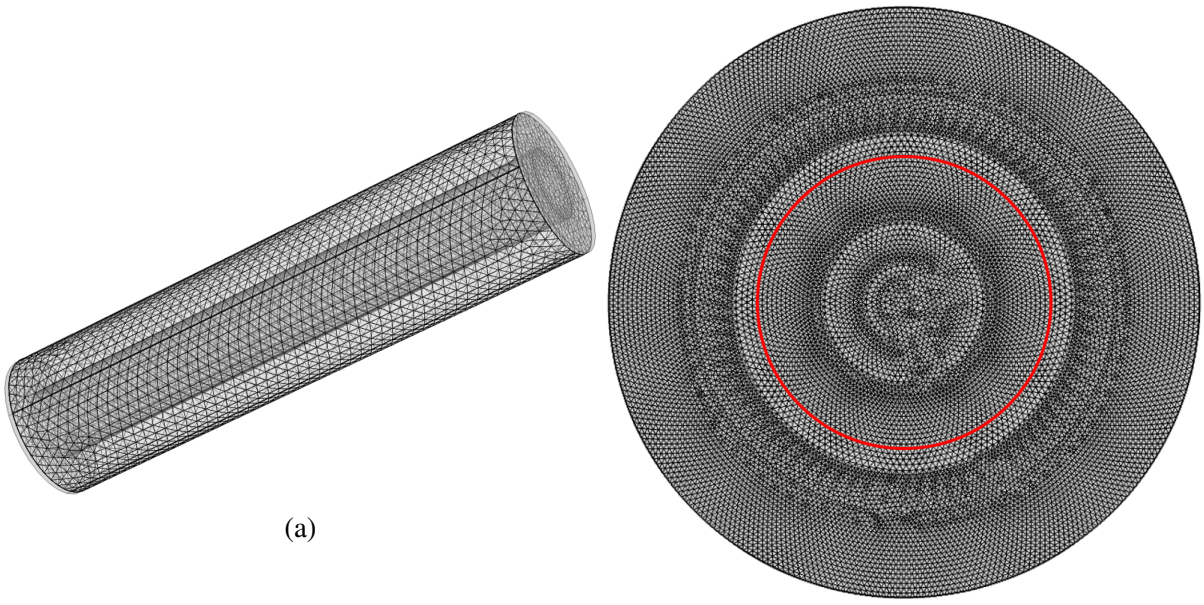

(a) (b)

Figure 4.3: (a) FEM mesh generated for the 3D porous pin geometry. Mesh consists of $136,059$ domain elements, $11,316$ boundary elements, and 664 edge elements. (b) FEM mesh generated for the 2D porous pin geometry. Mesh consists of $24,930$ domain elements and 472 boundary elements. The red circle indicates the interface between the two regions of the geometry.

Figure 4.2 shows the 3D and 2D geometries and the 1D geometry is the interval $[0, L_1] \cup$

$[L_1, L_2]$, or nondimensionally, $[0, 1] \cup [1, L_2/L_d]$. Figure 4.3 shows the 3D and 2D meshes used for the study. To determine if the porous pin is a suitable candidate for 1D mathematical modelling, the release profiles of all models are compared. This requires one to know the mass of drug in each region for each model at any given time, which are defined $M_d(t)$ and $M_p(t)$, the masses of drug within the inner drug region and the porous wall, respectively. From this, the total mass, $M(t) = M_d(t) + M_p(t)$, can be determined. Dimensionally, the mass of drug at some time t for the models is:

$$M(t) = M_d(t) + M_p(t) = \int_0^H \int_0^{2\pi} \int_0^{L_1} c_d \, r \, dr \, d\theta \, dz + \phi \int_0^H \int_0^{2\pi} \int_{L_1}^{L_2} c_p \, r \, dr \, d\theta \, dz.$$

Mass can be normalised via M_d^0, the total initial mass of drug in the core of the pin:

$$M_d^0 = \pi L_d^2 H c_d^0,$$

hence, normalised mass is:

$$\frac{M(t)}{M_d^0} = \frac{c_d^0 L_d^3}{\pi L_d^2 H c_d^0} \left[\int_0^{H/L_d} \int_0^{2\pi} \int_0^1 c_d' \, r' \, dr' \, d\theta' \, dz' + \phi \int_0^{H/L_d} \int_0^{2\pi} \int_1^{L_2/L_d} c_p' \, r' \, dr' \, d\theta' \, dz' \right].$$

Simplifying and dropping the primes for clarity:

$$\frac{M(t)}{M_d^0} = \frac{L_d}{\pi H} \left[\int_0^{H/L_d} \int_0^{2\pi} \int_0^1 c_d \, r dr \, d\theta \, dz + \phi \int_0^{H/L_d} \int_0^{2\pi} \int_1^{L_2/L_d} c_p \, r \, dr \, d\theta \, dz \right].$$

The release profile is:

$$\begin{aligned} M_{frac}(t) &= \frac{M_d^0 - M(t)}{M_d^0} = 1 - \frac{M(t)}{M_d^0} \\ &= 1 - \frac{L_d}{\pi H} \left[\int_0^{H/L_d} \int_0^{2\pi} \int_0^1 c_d \, r dr \, d\theta \, dz + \phi \int_0^{H/L_d} \int_0^{2\pi} \int_1^{L_2/L_d} c_p \, r \, dr \, d\theta \, dz \right]. \end{aligned} \tag{4.17}$$

For the 1D model, equation (4.17) will simplify to the summation of the integrals along the radial line. The required mass equations for the 2D and 3D models are similar to equation (4.17), however, the integrals are solved in the Cartesian coordinate system in the software. The required integrals are performed within the software using Gaussian quadrature.

4.1.2 Model results and discussion

The diffusion models are solved computationally and the release data from all three models are plotted to generate release profiles and the plots are compared. Parameter values may be inferred

from [11]. The parameter values used in the model reduction study are shown in Table 4.1.

Parameter	Value
L_d	$1.575\,\text{mm}$ [11]
L_p	$1.6\,\text{mm}$ [11]
H	$25.4\,\text{mm}$ [11]
ϕ	0.17 [11]
ϕ_e	$0.9 \times \phi$
τ	3
D_f	$1 \times 10^{-9}\,\text{m}^2/\text{s}$
$D_p = \phi_e D_f/\tau$	$5.1 \times 10^{-11}\,\text{m}^2/\text{s}$

Table 4.1: Table of parameter values used in the model reduction study.

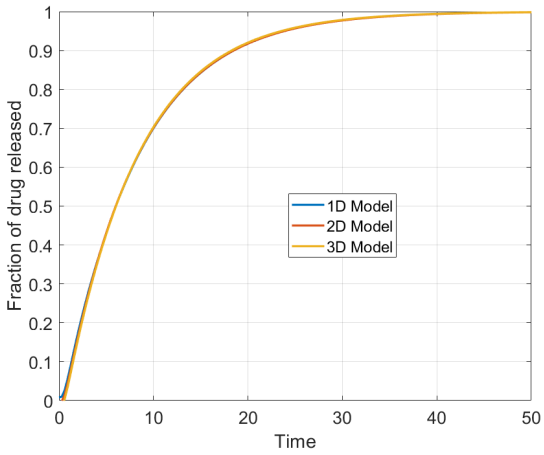

Figure 4.4: Plot showing fraction of drug released, versus nondimensional time, for the porous pin for the 1D, 2D and 3D models.

The results plotted in Figure 4.4 show that the use of a 1D model is sufficient in the modelling of drug release from the porous pin. This is expected when considering the lines of symmetry of a cylinder. This 1D diffusion model will be solved semi-analytically in Section 4.2. There is one other aspect to the experimental setup that must be considered: the release medium is stirred. This agitation of the release medium may have an impact on the release process by potentially providing a considerable advective component to the transport of the drug and hence, influencing the release of the drug. To investigate this, in Section 4.1.3 a system of fluid dynamic equations are coupled with advection-diffusion equations and the release results compared to a purely diffusive case. In all cases, the drug is assumed to be in the solute phase.

4.1.3 Influence of fluid flow on release of drug from the porous pin

In the experiments by Gimeno et al., the porous pins were submerged in $100\,\mathrm{mL}$ of SBF within an unknown container. It is also noted that the experimental set-up included stirring, the method of which is not reported. Assuming that the porous pin is submerged in the release media within a beaker and that the stirring is supplied by the beaker rotating at a set number of revolutions per minute (RPM), specifically, $30\,\mathrm{RPM}$ ($\pi\,\mathrm{rad/s}$), the theoretical influence the rotating fluid would have on the release of the drug may be determined. This value of rotational speed was chosen as the authors reported this speed in other published work [12]. Although a 1D approximation is suitable for the purely diffusive case, it is not suitable to gauge the importance a stirred release medium has on the release of a drug. Therefore, a full 3D model is used to investigate this.

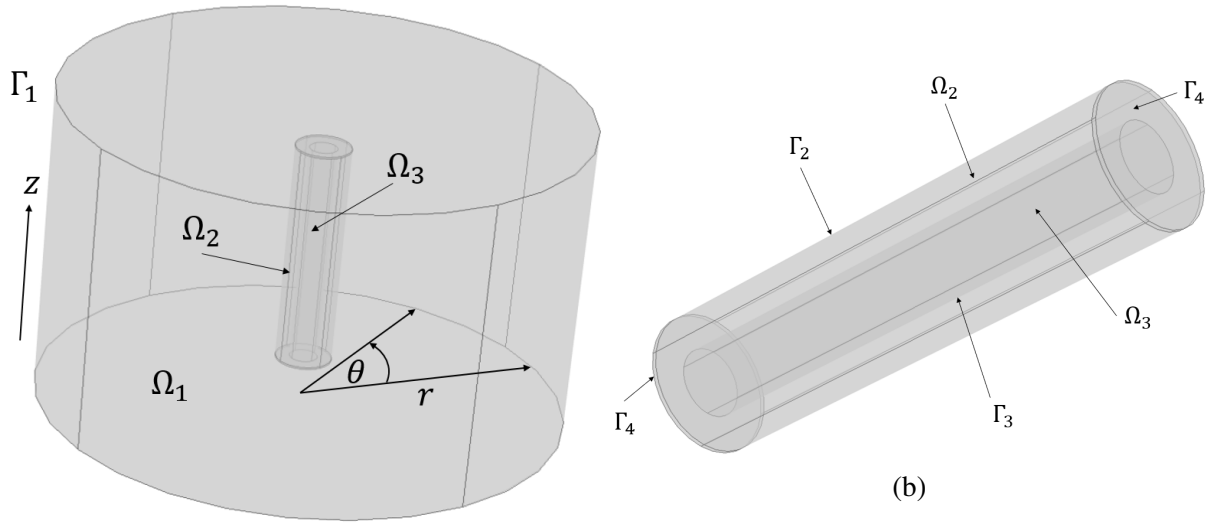

Figure 4.5: (a) 3D geometry of the porous pin experimental set-up, where the domains Ω_1, Ω_2 and Ω_3 represent the release medium, the porous wall of the pin and the inner drug core of the pin, respectively. Γ_1 is the outer boundary of the release medium, θ is the angle that Ω_1 makes with respect to its original position as it rotates and r is the radius from the central z-axis to the outer wall. (b) Close-up of the 3D porous pin that highlights Ω_2 and Ω_3. The outer boundary of the porous wall of the pin in contact with the release medium is denoted Γ_2 and the interface between the inner drug core and the porous wall is represented by Γ_3. The collection of boundaries that form the top and bottom caps of the pin are designated Γ_4

It should be noted that the following 3D model is solved in COMSOL Multiphysics®, version 5.3a, using the software's default Cartesian coordinate system. As the model is 3D choosing a cylindrical coordinate system will only give the same results. Additionally, the θ and r shown in in Figure 4.5 (a) are not model variables, they are separately defined within the software to be able to define a moving wall boundary condition, described shortly. To model the potential influence that fluid flow has on the release drug from the porous pin, some assumptions are made. It is assumed that the container for the release medium is a beaker of radius $30\,\mathrm{mm}$ [62] and since the volume of release medium is known, the height of the release medium, H_m, may

be easily calculated to provide an as accurate a representation as possible for the model. The porous pin geometry (Figure 4.5 (b)) is then suspended in the centre of the beaker geometry as seen in Figure 4.5 (a). Correspondence with the authors provided some experimental details of other work, which involved similar devices being suspended in the centre of a release medium. Therefore, it is assumed that in the case of the porous pin, a similar setup was used. Another unknown from the experiment is how the stirring of the release medium is performed. Without this knowledge, for the sake of simplicity, it is assumed that the beaker containing the release medium is rotated about its central axis. In this scenario, the walls of the beaker will provide the driving-force for the release medium to flow via a no-slip/no-penetration condition. Additionally, the release medium is assumed to be water as the fluid properties of SBF, such as density and kinematic viscosity, are unknown.

While the fluid is in motion, the resultant velocity field is denoted $\boldsymbol{u}$, which has velocity components (u_x, u_y, u_z). As the outer boundary of the release medium is rotated, the thin film of fluid close to the boundary assumes the velocity of this moving boundary. This results in an angular motion of the fluid, decreasing in magnitude as the radial distance from the outer boundary approaches the centre. However, the porous wall of the pin presents a wholly different environment for the fluid to navigate. The equations proposed to model fluid behaviour in the system are as follows:

$$\frac{\partial \boldsymbol{u}}{\partial t} = \nu \nabla^2 \boldsymbol{u} - (\boldsymbol{u} \cdot \nabla)\, \boldsymbol{u} - \frac{1}{\rho} \nabla p, \quad \text{in } \Omega_1 \text{ and } \Omega_3, \quad t > 0, \tag{4.18}$$

$$\frac{1}{\phi} \frac{\partial \boldsymbol{u}}{\partial t} = \frac{\nu}{\phi} \nabla^2 \boldsymbol{u} - \frac{1}{\phi^2} (\boldsymbol{u} \cdot \nabla)\, \boldsymbol{u} - \frac{1}{\rho} \nabla p - \frac{\nu}{\kappa} \boldsymbol{u}, \quad \text{in } \Omega_2, \quad t > 0, \tag{4.19}$$

$$\nabla \cdot \boldsymbol{u} = 0, \quad \text{in } \Omega_1,\ \Omega_2 \text{ and } \Omega_3, \quad t > 0, \tag{4.20}$$

with the following boundary conditions:

$$\boldsymbol{u} = (-r \sin(\theta), r \cos(\theta), 0)\, u, \quad \text{on } \Gamma_1, \quad t > 0, \tag{4.21}$$

$$\boldsymbol{u}_{ns} = \boldsymbol{u}_{br}, \quad p_{ns} = p_{br}, \quad \text{on } \Gamma_2 \text{ and } \Gamma_3, \quad t > 0, \tag{4.22}$$

$$\boldsymbol{u} = \boldsymbol{0}, \quad \text{on } \Gamma_4, \quad t > 0, \tag{4.23}$$

$$p = 0, \quad \text{at an arbitrary point} \quad t \geq 0 \tag{4.24}$$

$$\boldsymbol{u} = \boldsymbol{0}, \quad \text{in } \Omega_1,\ \Omega_2 \text{ and } \Omega_3, \quad t = 0. \tag{4.25}$$

Model equations (4.18-4.25) consist of the time-dependent, incompressible Navier-Stokes (4.18), Brinkman (4.19) and continuity equations (4.20). The Brinkman equation is used over Darcy's Law for modelling fluid flow through the porous wall of the pin because it is a more appropriate way to account for fluid-porous transitions [47, p. 16]. Parameters ρ and ν are the density and kinematic viscosity of the fluid (the ratio of the fluid properties of dynamic viscosity and density), respectively, and κ and ϕ are the permeability and the porosity of the porous wall of the

pin (Ω_2), respectively. A moving wall boundary condition (4.21), with angular velocity magnitude u, is applied to Γ_1. Boundary conditions (4.22) ensure continuity of the velocity field and pressure across the boundaries Γ_2 and Γ_3. The subscript ns and br are to indicate the velocity field and pressure associated with one of the governing flow equations, either Navier-Stokes (ns) or Brinkman (br). A no-slip/no-penetration boundary condition (4.23) is applied to Γ_4. The pressure, p, is set to be zero at an arbitrary point in the form of a pressure point constraint (4.24). This is necessary as it is not possible to specify the pressure level using a boundary condition, thus by constraining the pressure at a single point, the numerical solution can output the appropriate pressure gradient. Lastly, the fluid is at rest initially, as indicated by initial condition (4.25).

To model the potential influence of fluid flow on drug-release from the porous pin, the fluid dynamic equations (4.18-4.25) are coupled with a set of advection-diffusion equations. Since the release medium is now accounted for, $c_m(x, y, z, t)$ is defined as the concentration of drug within the release medium. Additionally, the drug concentration in the inner drug core and in the porous wall of the pin are defined $c_d(x, y, z, t)$ and $c_p(x, y, z, t)$, respectively. The proposed model is:

$$\frac{\partial c_m}{\partial t} = D_f \nabla^2 c_m - \boldsymbol{u} \cdot \nabla c_m, \quad \text{in } \Omega_1, \quad t > 0, \tag{4.26}$$

$$\phi \frac{\partial c_p}{\partial t} = D_p \nabla^2 c_p - \boldsymbol{u} \cdot \nabla c_p, \quad \text{in } \Omega_2, \quad t > 0, \tag{4.27}$$

$$\frac{\partial c_d}{\partial t} = D_f \nabla^2 c_d - \boldsymbol{u} \cdot \nabla c_d, \quad \text{in } \Omega_3, \quad t > 0, \tag{4.28}$$

$$\frac{\partial \boldsymbol{u}}{\partial t} = \nu \nabla^2 \boldsymbol{u} - (\boldsymbol{u} \cdot \nabla)\, \boldsymbol{u} - \frac{1}{\rho} \nabla p, \quad \text{in } \Omega_1 \text{ and } \Omega_3, \quad t > 0, \tag{4.29}$$

$$\frac{1}{\phi} \frac{\partial \boldsymbol{u}}{\partial t} = \frac{\nu}{\phi} \nabla^2 \boldsymbol{u} - \frac{1}{\phi^2} (\boldsymbol{u} \cdot \nabla)\, \boldsymbol{u} - \frac{1}{\rho} \nabla p - \frac{\nu}{\kappa} \boldsymbol{u}, \quad \text{in } \Omega_2, \quad t > 0, \tag{4.30}$$

$$\nabla \cdot \boldsymbol{u} = 0, \quad \text{in } \Omega_1, \Omega_2 \text{ and } \Omega_3, \quad t > 0, \tag{4.31}$$

Equations (4.26-4.31) consist of coupled advection-diffusion equations (4.26-4.28) and the incompressible form of the Navier-Stokes (4.29), Brinkman (4.30) and continuity equations (4.31). These governing equations are paired with the boundary and initial conditions:

$$c_d = c_p, \quad \hat{\boldsymbol{n}} \cdot (-D_f \nabla c_d + c_d \boldsymbol{u}) = \hat{\boldsymbol{n}} \cdot (-D_p \nabla c_p + c_p \boldsymbol{u}), \quad \text{on } \Gamma_3, \quad t > 0, \tag{4.32}$$

$$c_p = c_m, \quad \hat{\boldsymbol{n}} \cdot (-D_p \nabla c_p + c_p \boldsymbol{u}) = \hat{\boldsymbol{n}} \cdot (D_f \nabla c_m + c_m \boldsymbol{u}), \quad \text{on } \Gamma_2, \quad t > 0, \tag{4.33}$$

$$\hat{\boldsymbol{n}} \cdot (-D_f \nabla c_m + c_m \boldsymbol{u}) = 0, \quad \boldsymbol{u} = (-r \sin(\theta), r \cos(\theta), 0)\, u, \quad \text{on } \Gamma_1, \quad t > 0, \tag{4.34}$$

$$\boldsymbol{u} = \boldsymbol{0}, \quad -\hat{\boldsymbol{n}} \cdot D_f \nabla c_d = -\hat{\boldsymbol{n}} \cdot D_p \nabla c_p = -\hat{\boldsymbol{n}} \cdot D_f \nabla c_m = 0, \quad \text{on } \Gamma_4, \quad t > 0, \tag{4.35}$$

$$\boldsymbol{u}_{ns} = \boldsymbol{u}_{br}, \quad p_{ns} = p_{br}, \quad \text{on } \Gamma_2 \text{ and } \Gamma_3, \quad t > 0, \tag{4.36}$$

$$p = 0, \quad \text{at an arbitrary point}, \quad t \geq 0, \tag{4.37}$$

$$c_d = c_d^0, \quad \text{in } \Omega_3, \quad c_p^0 = 0, \quad \text{in } \Omega_2, \quad c_m^0 = 0, \quad \text{in } \Omega_1, \quad t = 0, \tag{4.38}$$

$$\boldsymbol{u} = \mathbf{0}, \quad \text{in } \Omega_1,\ \Omega_2 \text{ and } \Omega_3, \quad t = 0. \tag{4.39}$$

Continuity of concentration and flux conditions (4.32-4.33) are applied to boundaries Γ_2 and Γ_3. On Γ_1, a zero-flux boundary condition is applied to prevent drug from leaving the system, alongside the moving wall condition, which provides the force to cause the fluid to move (4.34). On Γ_4, a no-slip/no-penetration condition is applied along with a zero-flux condition, which prevents drug moving through the top and bottom caps of the porous pin geometry (4.35). Initially, there is a non-uniform initial drug concentration (4.38) and the fluid is assumed to initially be at rest throughout the entire geometry (4.39). The model equations (4.26-4.39) are nondimensionalised with the following scalings:

$$c_i' = \frac{c_i}{c_d^0}, \quad x' = \frac{x}{L_d}, \quad y' = \frac{y}{L_d}, \quad z' = \frac{z}{L_d}, \quad t' = \frac{D_f}{L_d^2}t, \quad p' = \frac{L_d^2}{\rho D_f^2}p, \quad \boldsymbol{u'} = \frac{L_d}{D_f}\boldsymbol{u},$$

where $i = d, p, m$. Dropping the primes for clarity, these scalings result in the nondimensional model:

$$\frac{\partial c_m}{\partial t} = \nabla^2 c_m - \boldsymbol{u} \cdot \nabla c_m, \quad \text{in } \Omega_1, \quad t > 0, \tag{4.40}$$

$$\phi\frac{\partial c_p}{\partial t} = D\nabla^2 c_p - \boldsymbol{u} \cdot \nabla c_p, \quad \text{in } \Omega_2, \quad t > 0, \tag{4.41}$$

$$\frac{\partial c_d}{\partial t} = \nabla^2 c_d - \boldsymbol{u} \cdot \nabla c_d, \quad \text{in } \Omega_3, \quad t > 0, \tag{4.42}$$

$$\frac{\partial \boldsymbol{u}}{\partial t} = Sc\nabla^2 \boldsymbol{u} - (\boldsymbol{u} \cdot \nabla)\,\boldsymbol{u} - \nabla p, \quad \text{in } \Omega_1 \text{ and } \Omega_3, \quad t > 0, \tag{4.43}$$

$$\frac{1}{\phi}\frac{\partial \boldsymbol{u}}{\partial t} = \frac{Sc}{\phi}\nabla^2 \boldsymbol{u} - \frac{1}{\phi^2}(\boldsymbol{u} \cdot \nabla)\,\boldsymbol{u} - \nabla p - \frac{L_d^2 Sc}{\kappa}\boldsymbol{u}, \quad \text{in } \Omega_2, \quad t > 0, \tag{4.44}$$

$$\nabla \cdot \boldsymbol{u} = 0, \quad \text{in } \Omega_1, \Omega_2 \text{ and } \Omega_3, \quad t > 0, \tag{4.45}$$

with the nondimensional boundary and initial conditions:

$$c_d = c_p, \quad \hat{\boldsymbol{n}} \cdot (-\nabla c_d + c_d\boldsymbol{u}) = \hat{\boldsymbol{n}} \cdot (-D\nabla c_p + c_p\boldsymbol{u}), \quad \text{on } \Gamma_3, \quad t > 0, \tag{4.46}$$

$$c_p = c_m, \quad \hat{\boldsymbol{n}} \cdot (-D\nabla c_p + c_p\boldsymbol{u}) = \hat{\boldsymbol{n}} \cdot (\nabla c_m + c_m\boldsymbol{u}), \quad \text{on } \Gamma_2, \quad t > 0, \tag{4.47}$$

$$\hat{\boldsymbol{n}} \cdot (-\nabla c_m + c_m\boldsymbol{u}) = 0, \quad \boldsymbol{u} = \frac{L_d^2}{D_f}(-r\sin(\theta), r\cos(\theta), 0)\,u, \quad \text{on } \Gamma_1, \quad t > 0, \tag{4.48}$$

$$\boldsymbol{u} = \mathbf{0}, \quad \hat{\boldsymbol{n}} \cdot \nabla c_d = \hat{\boldsymbol{n}} \cdot \nabla c_p = \hat{\boldsymbol{n}} \cdot \nabla c_m = 0, \quad \text{on } \Gamma_4, \quad t > 0, \tag{4.49}$$

$$\boldsymbol{u}_{ns} = \boldsymbol{u}_{br}, \quad p_{ns} = p_{br}, \quad \text{on } \Gamma_2 \text{ and } \Gamma_3, \quad t > 0, \tag{4.50}$$

$$p = 0, \quad \text{at an arbitrary point}, \quad t \geq 0, \tag{4.51}$$

$$c_d = 1, \quad \text{in } \Omega_3, \quad c_p^0 = 0, \quad \text{in } \Omega_2, \quad c_m^0 = 0, \quad \text{in } \Omega_1, \quad t = 0, \tag{4.52}$$

$$\boldsymbol{u} = \mathbf{0}, \quad \text{in } \Omega_1,\ \Omega_2 \text{ and } \Omega_3, \quad t = 0, \tag{4.53}$$

where $D = D_p/D_f$ and Sc is the Schmidt number which is defined as the ratio of kinematic viscosity to the free-diffusion coefficient (ν/D_f).

A required parameter that is not known is the level of permeability of the pin's porous wall, κ. Therefore, an estimation of the permeability is sought. Yang et al. derived an analytical expression for permeability, assuming isotropic porosity, as a function of two parameters: porosity and pore size [63]. Based upon the notion of a representative elementary volume, referred to by the authors as a "unit cell", and research conducted by other groups, Yang et al. provide the following expression:

$$\kappa = \frac{\phi\left(1-(1-\phi)^{1/3}\right)}{108\left((1-\phi)^{1/3}-(1-\phi)\right)}P^2, \tag{4.54}$$

where P is the cross-sectional pore size. Equation (4.54) was used by the authors to unify experimental data for a range of porosities and pore sizes, with good estimation results. However, it must be noted that the range of values that the experimental data covered were porosities and pore sizes in the ranges of $0.55-0.98$ and $0.254-5.08\,\mathrm{mm}$, respectively. Assuming that equation (4.54) is valid, to estimate the permeability of the porous wall, an idea of the pore size is required. Figure 4.1 (a) shows a scanning electron microscopy view of the pin's porous wall with a scale of $10\,\mu\mathrm{m}$, assuming that this is a representative value of the pore sizes and using the level of porosity of the porous pin, an estimation of the permeability can be made. Another parameter required is the kinematic viscosity, ν, of the assumed release medium fluid, water. It is stated by Gimeno et al. that the experimental setup was at $37\,^{\circ}C$. Therefore, the following empirical expressions for the density and dynamic viscosity of water [64, p. 1862], which are functions of temperature, T, in $^{\circ}C$, were used:

$$\begin{aligned}
\rho &= \frac{\begin{pmatrix} 999.83952 + 16.945176\times T - 7.9870401\times 10^{-3}T^2 \\ -46.170461\times 10^{-6}T^3 + 105.56302\times 10^{-9}T^4 - 280.54253\times 10^{-12}T^5 \end{pmatrix}}{1+16.879850\times 10^{-3}T}, \\
\mu &= 1.002\times 10^{-3}10^{B}, \\
B &= \frac{1.3272(20-T)-0.001053(T-20)^2}{T+105}.
\end{aligned}$$

4.1.4 Equations for mass

The dimensional equations for the mass of drug in each region are:

$$M_{\Omega_1}(t) = \int_{\Omega_1} c_m\, d\Omega_1, \quad M_{\Omega_2}(t) = \phi\int_{\Omega_2} c_p\, d\Omega_2, \quad M_{\Omega_3}(t) = \int_{\Omega_3} c_d\, d\Omega_3,$$

where $d\Omega_j = dxdydz$, with $j = 1,2,3$. The equations for mass can be normalised with M_d^0, the initial drug mass. As this is a purely numerical investigation, not only are the drug masses in each region approximated, but so too is the initial drug mass, which can be calculated via the

integral:

$$M_d^0 = c_d^0 \int_{\Omega_3} d\Omega_3.$$

Using the nondimensional scalings, the normalised equations for mass are:

$$\frac{M_{\Omega_1}(t)}{M_d^0} = \frac{c_d^0 L_d^3 \int_{\Omega_1'} c_m' \, d\Omega_1'}{c_d^0 L_d^3 \int_{\Omega_3'} d\Omega_3'}, \quad \frac{M_{\Omega_2}(t)}{M_d^0} = \frac{c_d^0 L_d^3 \phi \int_{\Omega_2'} c_p' \, d\Omega_2'}{c_d^0 L_d^3 \int_{\Omega_3'} d\Omega_3'}, \quad \frac{M_{\Omega_3}(t)}{M_d^0} = \frac{c_d^0 L_d^3 \int_{\Omega_3'} c_d' \, d\Omega_3'}{c_d^0 L_d^3 \int_{\Omega_3'} d\Omega_3'}.$$

Simplifying and dropping the primes for clarity:

$$\frac{M_{\Omega_1}(t)}{M_d^0} = \frac{\int_{\Omega_1} c_m \, d\Omega_1}{\int_{\Omega_3} d\Omega_3}, \quad \frac{M_{\Omega_2}(t)}{M_d^0} = \frac{\phi \int_{\Omega_2} c_p \, d\Omega_2}{\int_{\Omega_3} d\Omega_3}, \quad \frac{M_{\Omega_3}(t)}{M_d^0} = \frac{\int_{\Omega_3} c_d \, d\Omega_3}{\int_{\Omega_3} d\Omega_3}.$$

4.1.5 Release profile

The release profile may be calculated through the mass of drug lost from the porous pin:

$$\begin{aligned} M_{frac}(t) &= \frac{M_d^0 - (M_{\Omega_2}(t) + M_{\Omega_3}(t))}{M_d^0} = 1 - \frac{M_{\Omega_2}(t) + M_{\Omega_3}(t)}{M_d^0} \\ &= 1 - \frac{\phi \int_{\Omega_2} c_p \, d\Omega_2 + \int_{\Omega_3} c_d \, d\Omega_3}{\int_{\Omega_3} d\Omega_3}. \end{aligned}$$

The simpler method to calculate the release profile is to determine the mass which accumulates in the release medium:

$$M_{frac}(t) = \frac{M_{\Omega_1}(t)}{M_d^0} = \frac{\int_{\Omega_1} c_m \, d\Omega_1}{\int_{\Omega_3} d\Omega_3}. \tag{4.55}$$

4.1.6 Model results and discussion

Model equations (4.40-4.53) were solved numerically and the drug release data was obtained using COMSOL Multiphysics®, version 5.3a. Special attention was made to the construction of a suitable mesh, in that additional boundary layers were applied to Γ_1 and the mesh was considerably denser within the domains Ω_2 and Ω_3 to assist in improving conservation of mass. Additionally, the advection-diffusion equations of the model were solved whilst in conservative form: this typically leads to a more accurate approximation of the numerical solution and therefore improves mass conservation of drug. To give a measure of accuracy, each mesh considered

was used in the time-dependent study and the theoretical mass within the whole system was calculated. If mass conservation is achieved, then this value should be constant:

$$\int_{\Omega_1} c_m \, d\Omega_1 + \phi \int_{\Omega_2} c_p \, d\Omega_2 + \int_{\Omega_3} c_d \, d\Omega_3 = \text{ a constant.}$$

In particular, this constant is equal to the initial drug mass. Since the model is solved numerically, this constant will be approximated and so the difference between the largest and smallest mass values were taken. If the percentage difference between these values was less than $1\,\%$, mass was assumed to be sufficiently conserved. The final mesh used was custom made, was constructed from tetrahedral elements, and consisted of $243,870$ domain elements, 8652 boundary elements, and 652 edge elements. Mesh elements had a maximum and minimum nondimensional size of 1.97 and 0.587, respectively, and a maximum growth rate of 1.15. The mesh was made using the "Normal" mesh setting calibrated for "Fluid Dynamics", for all regions, however, 3 additional boundary layers were added to each surface to aid computational accuracy in fluid/boundary interactions. This mesh (Figure 4.6) gave an error in mass conservation of much less than $1\,\%$ and was used in all studies.

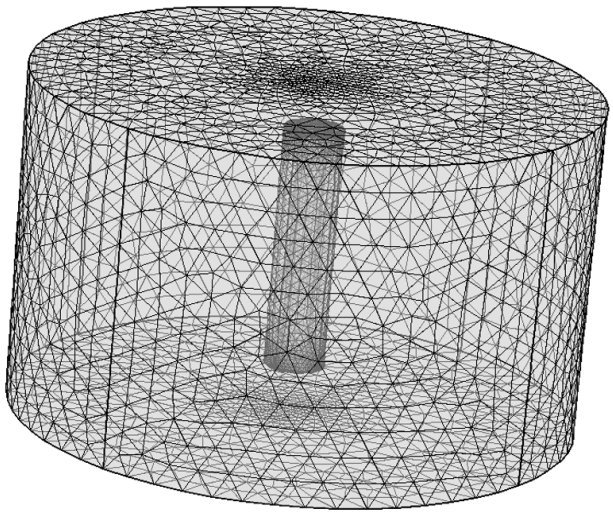

Figure 4.6: FEM mesh generated for the 3D porous pin geometry for the influence of flow study. Mesh consists of $243,870$ domain elements, 8652 boundary elements, and 652 edge elements.

In addition to the time-dependent model, a similar steady state model was also derived in which the stationary velocity field was calculated and this acted as input for the advection-diffusion equations. A model based purely on diffusion was also derived for comparison purposes. The additional models can be formulated by neglecting relevant parts of the model equations (4.40-4.53) to give steady-state and the diffusion-only equivalent models. All models were solved using the GMRES iterative method, alongside the BDF to handle time advancement, where applicable. The integrals in release profile equation (4.55) were calculated in the software using Gaussian quadrature. To assess whether or not the inclusion of fluid flow is necessary, the

release profiles of the three models were compared: the time-dependent model (4.40-4.53), its steady-state and diffusion-only equivalents. Parameter values used in the simulations are those in Table 4.1, together with the new parameters for the flow inclusion study in Table 4.2.

Parameter	Value
L_m	$30\,\mathrm{mm}$ [62]
H_m	$35.65\,\mathrm{mm}$
u	$\pi\,\mathrm{rad/s}$ [11]
κ	$8.63 \times 10^{-14}\,\mathrm{m}^2$ [63]
ν	$6.96 \times 10^{-7}\,\mathrm{m}^2/\mathrm{s}$ [64]

Table 4.2: Table of parameter values used in the influence of flow studies.

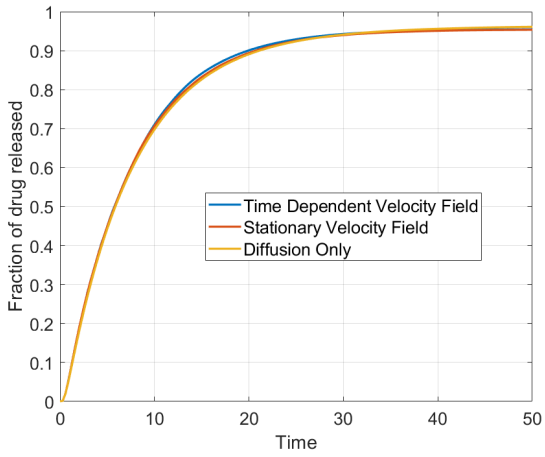

Figure 4.7: Plot showing fraction of drug released, versus nondimensional time, for the porous pin for the three models considered.

Figure 4.7 shows that when compared to a diffusion-only problem, the inclusion of fluid flow has a negligible impact on the release of drug from the porous pin. Since there is no appreciable influence by fluid flow, the 1D approximation is viable. This result is somewhat expected considering the reasonably low level of porosity and the calculated permeability of the porous wall of the pin: 0.17 and $8.63 \times 10^{-14}\,\mathrm{m}^2$, respectively. Given the values of these parameters, it is not surprising that fluid flow is hindered to insignificant levels within the porous pin. A suitable measure of the influence fluid flow has on the release of drug from the porous pin is to compare it to the diffusive transport rate in the pin's inner drug region (Ω_3) and porous wall (Ω_2). This can be achieved via an average Péclet number (Pe), which is the ratio of advective to diffusive transport rates and may be calculated from:

$$Pe_{\Omega_2} = \frac{u_{\Omega_2} L_p}{D_p}, \quad Pe_{\Omega_3} = \frac{u_{\Omega_3} L_d}{D_f},$$

where u_{Ω_2} and u_{Ω_3} are the average fluid velocity magnitudes within the pin's porous wall and inner drug core, respectively. The calculated Péclet numbers of the pin's porous wall and inner drug core are approximately 0.022 and 0.0012, respectively. These numbers suggest that the transport due to advection is much slower than what diffusion can achieve. This evidence further suggests that modelling fluid flow within the pin is not important when considering drug-release from this porous pin.

4.2 1D radial diffusion model

The previous section demonstrated that drug release from the porous pin is a 1D problem. This is not unexpected since the geometry is symmetric both angularly and along the z-axis, and although the wall of the pin is porous, the low level of its porosity and permeability restrict the flow of fluid within the pin. This permits the reduction of the geometry to a radial line from the centre of the inner drug core, through the porous and the bulk release medium layers (Figure 4.8).

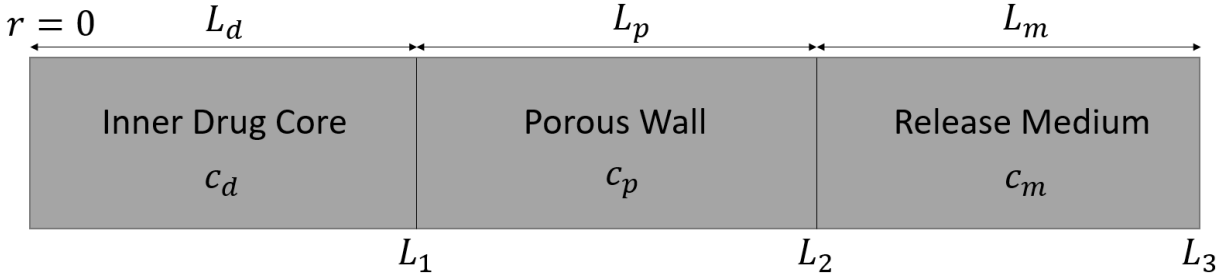

Figure 4.8: 1D geometry showing the drug, porous and release medium regions, with their respective concentrations $c_d(r,t)$, $c_p(r,t)$ and $c_m(r,t)$ and thicknesses L_d, L_p and L_m. The position of boundaries and interfaces are marked with $r = 0$, L_1, L_2 and L_3.

Model parameters, inner drug core radius, porous layer thickness, interface and boundary locations are as they were defined earlier in the chapter. However, as the model is based on a 1D cylindrical coordinate system, the drug concentrations in the inner drug core, the porous wall and the release medium are now defined: $c_d(r,t)$, $c_p(r,t)$ and $c_m(r,t)$. As before, the position of the boundaries and the interfaces are a combination of the thicknesses of each layer. An additional boundary location is the endpoint of the release medium and is defined $L_3 = L_d + L_p + L_m$. Assuming that the drug is fully wetted and is readily soluble the proposed model is:

$$\frac{\partial c_d}{\partial t} = D_f \left(\frac{1}{r}\frac{\partial c_d}{\partial r} + \frac{\partial^2 c_d}{\partial r^2} \right), \quad 0 < r < L_1, \quad t > 0, \tag{4.56}$$

$$\phi\frac{\partial c_p}{\partial t} = D_p \left(\frac{1}{r}\frac{\partial c_p}{\partial r} + \frac{\partial^2 c_p}{\partial r^2} \right), \quad L_1 < r < L_2, \quad t > 0, \tag{4.57}$$

$$\frac{\partial c_m}{\partial t} = D_f \left(\frac{1}{r}\frac{\partial c_m}{\partial r} + \frac{\partial^2 c_m}{\partial r^2} \right), \quad L_2 < r < L_3, \quad t > 0, \tag{4.58}$$

$$-D_f \frac{\partial c_d}{\partial r} = 0, \quad r = 0, \quad t > 0, \tag{4.59}$$

$$c_d = c_p, \quad -D_f \frac{\partial c_d}{\partial r} = -D_p \frac{\partial c_p}{\partial r}, \quad r = L_1, \quad t > 0, \tag{4.60}$$

$$c_p = c_m, \quad -D_p \frac{\partial c_p}{\partial r} = -D_f \frac{\partial c_m}{\partial r}, \quad r = L_2, \quad t > 0, \tag{4.61}$$

$$-D_f \frac{\partial c_m}{\partial r} = 0, \quad r = L_3, \quad t > 0, \tag{4.62}$$

$$c_d = c_d^0, \quad 0 \leq r \leq L_1, \quad c_p = 0, \quad L_1 < r \leq L_2, \quad c_m = 0, \quad L_2 < r \leq L_3, \quad t = 0. \tag{4.63}$$

The model (4.56-4.63) consists of coupled diffusion equations (4.56-4.58) to describe diffusive mass transport in each layer. The endpoints of the geometry, where $r = 0$ and $r = L_3$, have zero-flux conditions applied (4.59, 4.62). At the interfaces, where $r = L_1$ and $r = L_2$, both continuity concentration and flux conditions are applied (4.60-4.61). It is assumed that initially, the drug is only present in the first layer, as shown by initial conditions (4.63). The model equations (4.56-4.63) are nondimensionalised with the following scalings:

$$c_i' = \frac{c_i}{c_d^0}, \quad r' = \frac{r}{L_d}, \quad t' = \frac{D_f}{L_d^2} t,$$

where $i = d, p, m$. For the sake of simplicity, let $D = D_p/D_f$, $r_2 = L_2/L_d$ and $r_3 = L_3/L_d$ and by definition $r_1 = 1$. Dropping the primes for clarity, the scalings give the following nondimensional model:

$$\frac{\partial c_d}{\partial t} = \left(\frac{1}{r} \frac{\partial c_d}{\partial r} + \frac{\partial^2 c_d}{\partial r^2} \right), \quad 0 < r < 1, \quad t > 0, \tag{4.64}$$

$$\phi \frac{\partial c_p}{\partial t} = D \left(\frac{1}{r} \frac{\partial c_p}{\partial r} + \frac{\partial^2 c_p}{\partial r^2} \right), \quad 1 < r < r_2, \quad t > 0, \tag{4.65}$$

$$\frac{\partial c_m}{\partial t} = \left(\frac{1}{r} \frac{\partial c_m}{\partial r} + \frac{\partial^2 c_m}{\partial r^2} \right), \quad r_2 < r < r_3, \quad t > 0, \tag{4.66}$$

$$\frac{\partial c_d}{\partial r} = 0, \quad r = 0, \quad t > 0, \tag{4.67}$$

$$c_d = c_p, \quad \frac{\partial c_d}{\partial r} = D \frac{\partial c_p}{\partial r}, \quad r = 1, \quad t > 0, \tag{4.68}$$

$$c_p = c_m, \quad D \frac{\partial c_p}{\partial r} = \frac{\partial c_m}{\partial r}, \quad r = r_2, \quad t > 0, \tag{4.69}$$

$$\frac{\partial c_m}{\partial r} = 0, \quad r = r_3, \quad t > 0, \tag{4.70}$$

$$c_d = 1, \quad 0 \leq r \leq 1, \quad c_p = 0, \quad 1 < r \leq r_2, \quad c_m = 0, \quad r_2 < r \leq r_3, \quad t = 0. \tag{4.71}$$

4.2.1 Solution procedure

Model equations (4.64-4.71) are solved via the Separation of Variables method. It is assumed that the solution in each layer has the following form:

$$c_i(r,t) = R_i(r)T_i(t), \quad i = d, p, m. \tag{4.72}$$

Substituting solution form (4.72) into equations (4.64-4.66) gives rise to the following ODEs in time, t:

$$\dot{T}_d(t) + \lambda_d^2 T_d(t) = 0, \quad \dot{T}_p(t) + \frac{D\lambda_p^2}{\phi} T_p(t) = 0, \quad \dot{T}_m(t) + \lambda_m^2 T_m(t) = 0,$$

where the single dot notation indicates the first derivative with respect to time. The ODEs have the solutions:

$$T_d(t) = \exp\left(-\lambda_d^2 t\right), \quad T_p(t) = \exp\left(-\frac{D\lambda_p^2}{\phi} t\right), \quad T_m(t) = \exp\left(-\lambda_m^2 t\right). \tag{4.73}$$

From the solutions in time (4.73), a relationship between the eigenvalues is obtained by setting $T_d(t) = T_p(t) = T_m(t)$:

$$\lambda_d^2 = \frac{D\lambda_p^2}{\phi} = \lambda_m^2, \tag{4.74}$$

Additionally, from the substitution of (4.72) into (4.64-4.66), a Sturm–Liouville eigenvalue problem is obtained. Where single and double superscript primes indicate the first and second spatial derivatives, respectively, the ODEs in space can be expressed in the following general form:

$$R_i''(r) + \frac{1}{r} R_i'(r) + \lambda_i^2 R_i(r) = 0, \tag{4.75}$$

with boundary conditions:

$$R_d'(r) = 0, \quad r = 0, \quad t > 0, \tag{4.76}$$

$$R_d(r) = R_p(r), \quad R_d'(r) = DR_p'(r), \quad r = 1, \quad t > 0, \tag{4.77}$$

$$R_p(r) = R_m(r), \quad DR_p'(r) = R_m'(r), \quad r = r_2, \quad t > 0, \tag{4.78}$$

$$R_m'(r) = 0, \quad r = r_3, \quad t > 0. \tag{4.79}$$

Equation (4.75) can be rearranged into the following form:

$$r^2 R_i''(r) + r R_i'(r) + \lambda_i^2 r^2 R_i(r) = 0. \tag{4.80}$$

This is in the form of Bessel's differential equation. Due to the Neumann (zero-flux) boundary conditions, $\lambda_i^2 \geq 0$. For $\lambda_i^2 = 0$, it is found that $R_d = R_p = R_m =$ a constant. Therefore,

$\dot{T}_i = 0 \Rightarrow T_i = \gamma$, a constant. For $\lambda_i^2 > 0$, (4.80) has the general solution [65–67]:

$$R_i(r) = \alpha_i J_0(\lambda_i r) + \beta_i Y_0(\lambda_i r), \tag{4.81}$$

where α_i and β_i are constants and $J_0(\lambda_i r)$ and $Y_0(\lambda_i r)$ are the zero-order Bessel functions of the first and second kind, respectively. More generally, Bessel functions of the first and second kind, of integer order ν, are defined as [65, 66]:

$$J_\nu(\lambda_i r) = \sum_{n=0}^{\infty} \frac{(-1)^n}{n!\Gamma(n+\nu+1)} \left(\frac{\lambda_i r}{2}\right)^{2n+\nu},$$

$$\begin{aligned} Y_\nu(\lambda_i r) =& \frac{2}{\pi} J_\nu(\lambda_i r) \ln\left(\frac{\lambda_i r}{2}\right) - \frac{1}{\pi} \sum_{n=0}^{\nu-1} \frac{(\nu-n-1)!}{n!} \left(\frac{\lambda_i r}{2}\right)^{2n-\nu} \\ & - \frac{1}{\pi} \sum_{n=0}^{\infty} \frac{(-1)^n}{n!\Gamma(n+\nu+1)} \left(\frac{\lambda_i r}{2}\right)^{2n+\nu} (\psi(n+\nu+1) + \psi(n+1)), \end{aligned}$$

where Γ and ψ are the gamma and digamma functions, respectively. With the general solutions obtained (4.81), the boundary conditions can be applied and starting with (4.76,4.79), it is found that $\beta_d = 0$, so that the solution remains finite, and that α_m can be expressed in terms of β_m, thus the solutions have the form:

$$R_d = \alpha_d J_0(\lambda_d r), \tag{4.82}$$

$$R_p = \alpha_p J_0(\lambda_p r) + \beta_p Y_0(\lambda_p r), \tag{4.83}$$

$$R_m = \beta_m \left(\frac{J_1(\lambda_m r_3) Y_0(\lambda_m r) - Y_1(\lambda_m r_3) J_0(\lambda_m r)}{J_1(\lambda_m r_3)} \right). \tag{4.84}$$

The continuity of concentration conditions in (4.77-4.78) allow α_d and β_m to be rewritten, giving:

$$\alpha_d = \frac{\alpha_p J_0(\lambda_p) + \beta_p Y_0(\lambda_p)}{J_0(\lambda_d)}, \tag{4.85}$$

$$\beta_m = \frac{J_1(\lambda_m r_3) [\alpha_p J_0(\lambda_p r_2) + \beta_p Y_0(\lambda_p r_2)]}{Y_0(\lambda_m r_2) J_1(\lambda_m r_3) - J_0(\lambda_m r_2) Y_1(\lambda_m r_3)}. \tag{4.86}$$

Through a combination of (4.85-4.86) and the continuity of flux conditions in (4.77-4.78), the following relations are obtained:

$$\lambda_d J_1(\lambda_d) [\alpha_p J_0(\lambda_p) + \beta_p Y_0(\lambda_p)] = D\lambda_p J_0(\lambda_d) [\alpha_p J_1(\lambda_p) + \beta_p Y_1(\lambda_p)], \tag{4.87}$$

$$\begin{aligned} & D\lambda_p [\alpha_p J_1(\lambda_p r_2) + \beta_p Y_1(\lambda_p r_2)] [Y_0(\lambda_m r_2) J_1(\lambda_m r_3) - J_0(\lambda_m r_2) Y_1(\lambda_m r_3)] \\ =& \lambda_m [\alpha_p J_0(\lambda_p r_2) + \beta_p Y_0(\lambda_p r_2)] [Y_1(\lambda_m r_2) J_1(\lambda_m r_3) - J_1(\lambda_m r_2) Y_1(\lambda_m r_3)]. \end{aligned} \tag{4.88}$$

Equations (4.87-4.88) can be rewritten with α_p and β_p as common factors:

$$\begin{aligned}&\alpha_p \left[\lambda_d J_1\left(\lambda_d\right) J_0\left(\lambda_p\right) - D\lambda_p J_0\left(\lambda_d\right) J_1\left(\lambda_p\right)\right] \\ =&\beta_p \left[D\lambda_p J_0\left(\lambda_d\right) Y_1\left(\lambda_p\right) - \lambda_d J_1\left(\lambda_d\right) Y_0\left(\lambda_p\right)\right],\end{aligned} \tag{4.89}$$

$$\begin{aligned}&\alpha_p \begin{bmatrix} D\lambda_p J_1\left(\lambda_p r_2\right)\left[Y_0\left(\lambda_m r_2\right) J_1\left(\lambda_m r_3\right) - J_0\left(\lambda_m r_2\right) Y_1\left(\lambda_m r_3\right)\right] \\ -\lambda_m J_0\left(\lambda_p r_2\right)\left[Y_1\left(\lambda_m r_2\right) J_1\left(\lambda_m r_3\right) - J_1\left(\lambda_m r_2\right) Y_1\left(\lambda_m r_3\right)\right] \end{bmatrix} \\ =&\beta_p \begin{bmatrix} \lambda_m Y_0\left(\lambda_p r_2\right)\left[Y_1\left(\lambda_m r_2\right) J_1\left(\lambda_m r_3\right) - J_1\left(\lambda_m r_2\right) Y_1\left(\lambda_m r_3\right)\right] \\ -D\lambda_p Y_1\left(\lambda_p r_2\right)\left[Y_0\left(\lambda_m r_2\right) J_1\left(\lambda_m r_3\right) - J_0\left(\lambda_m r_2\right) Y_1\left(\lambda_m r_3\right)\right] \end{bmatrix}.\end{aligned} \tag{4.90}$$

Equations (4.89-4.90) form a system of two homogeneous linear equations in the two unknowns α_p and β_p. One could make a simple substitution with these equations, however, this will give rise to the trivial solution of $\alpha_p = \beta_p = 0$. To avoid this, the determinant of the matrix of coefficients must be equal to zero, that is:

$$\begin{aligned}&\left(\begin{array}{l} \left[\lambda_d J_1\left(\lambda_d\right) J_0\left(\lambda_p\right) - D\lambda_p J_0\left(\lambda_d\right) J_1\left(\lambda_p\right)\right] \\ \times \begin{bmatrix} \lambda_m Y_0\left(\lambda_p r_2\right)\left[Y_1\left(\lambda_m r_2\right) J_1\left(\lambda_m r_3\right) - J_1\left(\lambda_m r_2\right) Y_1\left(\lambda_m r_3\right)\right] \\ -D\lambda_p Y_1\left(\lambda_p r_2\right)\left[Y_0\left(\lambda_m r_2\right) J_1\left(\lambda_m r_3\right) - J_0\left(\lambda_m r_2\right) Y_1\left(\lambda_m r_3\right)\right] \end{bmatrix} \end{array} \right) \\ -&\left(\begin{array}{l} \left[D\lambda_p J_0\left(\lambda_d\right) Y_1\left(\lambda_p\right) - \lambda_d J_1\left(\lambda_d\right) Y_0\left(\lambda_p\right)\right] \\ \times \begin{bmatrix} D\lambda_p J_1\left(\lambda_p r_2\right)\left[Y_0\left(\lambda_m r_2\right) J_1\left(\lambda_m r_3\right) - J_0\left(\lambda_m r_2\right) Y_1\left(\lambda_m r_3\right)\right] \\ -\lambda_m J_0\left(\lambda_p r_2\right)\left[Y_1\left(\lambda_m r_2\right) J_1\left(\lambda_m r_3\right) - J_1\left(\lambda_m r_2\right) Y_1\left(\lambda_m r_3\right)\right] \end{bmatrix} \end{array} \right) = 0.\end{aligned} \tag{4.91}$$

Transcendental equation (4.91) has infintely many roots which take the form of eigenvalue triplets $(\lambda_d, \lambda_p, \lambda_m)$. However, equation (4.91) may be expressed solely in terms of λ_d using (4.74), such that an eigen-condition is obtained. If satisfied, this condition gives α_p in terms of β_p and provides expressions for α_d and β_m, both in terms of β_p. For simplicity, the following function is defined:

$$\Lambda(\lambda_d, \lambda_p) = \frac{D\lambda_p J_0\left(\lambda_d\right) Y_1\left(\lambda_p\right) - \lambda_d J_1\left(\lambda_d\right) Y_0\left(\lambda_p\right)}{\lambda_d J_1\left(\lambda_d\right) J_0\left(\lambda_p\right) - D\lambda_p J_0\left(\lambda_d\right) J_1\left(\lambda_p\right)},$$

Therefore constants α_p, α_d and β_m of equations (4.82-4.84) are:

$$\alpha_p = \beta_p \Lambda(\lambda_d, \lambda_p), \tag{4.92}$$

$$\alpha_d = \beta_p \left(\frac{\Lambda(\lambda_d, \lambda_p) J_0\left(\lambda_p\right) + Y_0\left(\lambda_p\right)}{J_0\left(\lambda_d\right)} \right), \tag{4.93}$$

$$\beta_m = \beta_p \left(\frac{J_1\left(\lambda_m r_3\right)\left[\Lambda(\lambda_d, \lambda_p) J_0\left(\lambda_p r_2\right) + Y_0\left(\lambda_p r_2\right)\right]}{Y_0\left(\lambda_m r_2\right) J_1\left(\lambda_m r_3\right) - J_0\left(\lambda_m r_2\right) Y_1\left(\lambda_m r_3\right)} \right). \tag{4.94}$$

For every eigenvalue triplet $(\lambda_{d,g}, \lambda_{p,g}, \lambda_{m,g})$, $g = 1, 2, 3...$, the values of $\alpha_{p,g}$, $\alpha_{d,g}$ and $\beta_{m,g}$ are obtained from (4.92-4.94). The constants $\beta_{p,g}$ associated with each eigenvalue triplet may be calculated via the initial condition. Therefore, the corresponding eigenfunctions are:

$$\begin{aligned} R_{d,g} &= \beta_{p,g}\tilde{R}_{d,g}, \\ R_{p,g} &= \beta_{p,g}\tilde{R}_{p,g}, \\ R_{m,g} &= \beta_{p,g}\tilde{R}_{m,g}, \end{aligned}$$

where $\tilde{R}_{i,g}$ are:

$$\tilde{R}_{d,g} = \left(\frac{\Lambda(\lambda_{d,g}, \lambda_{p,g}) J_0(\lambda_{p,g}) + Y_0(\lambda_{p,g})}{J_0(\lambda_{d,g})} \right) J_0(\lambda_{d,g} r),$$

$$\tilde{R}_{p,g} = \Lambda(\lambda_{d,g}, \lambda_{p,g}) J_0(\lambda_{p,g} r) + Y_0(\lambda_{p,g} r),$$

$$\begin{aligned} \tilde{R}_{m,g} = &\left(\frac{\Lambda(\lambda_{d,g}, \lambda_{p,g}) J_0(\lambda_{p,g} r_2) + Y_0(\lambda_{p,g} r_2)}{Y_0(\lambda_{m,g} r_2) J_1(\lambda_{m,g} r_3) - J_0(\lambda_{m,g} r_2) Y_1(\lambda_{m,g} r_3)} \right) \\ &\times \left(J_1(\lambda_{m,g} r_3) Y_0(\lambda_{m,g} r) - Y_1(\lambda_{m,g} r_3) J_0(\lambda_{m,g} r) \right). \end{aligned}$$

The final solutions are then a linear superposition of the fundamental solutions R_i and T_i and have the form:

$$c_d(r,t) = \gamma + \sum_{g=1}^{\infty} \beta_{p,g} \tilde{R}_{d,g} \exp\left(-\lambda_{d,g}^2 t\right), \tag{4.95}$$

$$c_p(r,t) = \gamma + \sum_{g=1}^{\infty} \beta_{p,g} \tilde{R}_{p,g} \exp\left(-\frac{D\lambda_{p,g}^2}{\phi} t\right), \tag{4.96}$$

$$c_m(r,t) = \gamma + \sum_{g=1}^{\infty} \beta_{p,g} \tilde{R}_{m,g} \exp\left(-\lambda_{m,g}^2 t\right). \tag{4.97}$$

4.2.2 Application of the initial condition

Evaluating the solutions (4.95-4.97) at $t = 0$, the values of γ and $\beta_{p,g}$ can be determined. Starting with γ, the constant eigenfunction associated with the eigenvalue $\lambda_i = 0$, multiplying throughout by r, integrating over the domains and summing gives:

$$\gamma \int_0^1 r dr + \gamma\phi \int_1^{r_2} r dr + \gamma \int_{r_2}^{r_3} r dr = \int_0^1 r dr,$$

evaluating the integrals and solving for γ:

$$\gamma = \frac{1}{1 - \phi + r_2^2(\phi - 1) + r_3^2}. \tag{4.98}$$

For $\lambda_i > 0$, $\beta_{p,g}$ may be determined by evaluating the solutions at $t = 0$ and by multiplying (4.95) by $r\tilde{R}_{d,h}$, (4.96) by $r\tilde{R}_{p,h}$ and (4.97) by $r\tilde{R}_{m,h}$, $h = 1, 2, 3...$, integrating over the domains and summing:

$$\begin{aligned}
&\int_0^1 \sum_{g=1}^{\infty} \beta_{p,g} r\tilde{R}_{d,g}\tilde{R}_{d,h}dr \\
&+ \phi \int_1^{r_2} \sum_{g=1}^{\infty} \beta_{p,g} r\tilde{R}_{p,g}\tilde{R}_{p,h}dr \\
&+ \int_{r_2}^{r_3} \sum_{g=1}^{\infty} \beta_{p,g} r\tilde{R}_{m,g}\tilde{R}_{m,h}dr = \int_0^1 r\tilde{R}_{d,h}dr. \qquad (4.99)
\end{aligned}$$

In order to determine the value of $\beta_{p,g}$ within (4.99), the orthogonality condition of the eigenfunction system $(\tilde{R}_{d,g}, \tilde{R}_{p,g}, \tilde{R}_{m,g})$ must be established, that is:

$$\int_0^1 r\tilde{R}_{d,g}\tilde{R}_{d,h}dr + \phi \int_1^{r_2} r\tilde{R}_{p,g}\tilde{R}_{p,h}dr + \int_{r_2}^{r_3} r\tilde{R}_{m,g}\tilde{R}_{m,h}dr = 0, \quad g \neq h. \qquad (4.100)$$

Consider two different eigenvalues $\lambda_{d,g}$ and $\lambda_{d,h}$ and the corresponding eigenfunctions $\tilde{R}_{d,g}$ and $\tilde{R}_{d,h}$. Equation (4.75) can be rewritten as:

$$\frac{d}{dr}\left(r\tilde{R}'_{d,g}\right) + \lambda^2_{d,g} r\tilde{R}_{d,g} = 0, \qquad (4.101)$$

and similarly for $\tilde{R}_{d,h}$:

$$\frac{d}{dr}\left(r\tilde{R}'_{d,h}\right) + \lambda^2_{d,h} r\tilde{R}_{d,h} = 0. \qquad (4.102)$$

By multiplying (4.101) by $\tilde{R}_{d,h}$ and (4.102) by $\tilde{R}_{d,g}$, then subtracting the two:

$$\tilde{R}_{d,g}\frac{d}{dr}\left(r\tilde{R}'_{d,h}\right) - \tilde{R}_{d,h}\frac{d}{dr}\left(r\tilde{R}'_{d,g}\right) + \left(\lambda^2_{d,h} - \lambda^2_{d,g}\right) r\tilde{R}_{d,g}\tilde{R}_{d,h} = 0, \qquad (4.103)$$

integrating (4.103) and simplifying:

$$\begin{aligned}
\left(\lambda^2_{d,h} - \lambda^2_{d,g}\right)\int_0^1 r\tilde{R}_{d,h}\tilde{R}_{d,g}dr &= \left[r\tilde{R}_{d,h}\tilde{R}'_{d,g}\right]_0^1 - \left[r\tilde{R}_{d,g}\tilde{R}'_{d,h}\right]_0^1, \\
&= \tilde{R}_{d,h}(1)\tilde{R}'_{d,g}(1) - \tilde{R}_{d,g}(1)\tilde{R}'_{d,h}(1). \qquad (4.104)
\end{aligned}$$

Similarly for the eigenvalue pair $\lambda_{p,g}$ and $\lambda_{p,h}$ and the corresponding eigenfunctions $\tilde{R}_{p,g}$ and $\tilde{R}_{p,h}$, with the result multiplied by D:

$$D\left(\lambda^2_{p,h} - \lambda^2_{p,g}\right)\int_1^{r_2} r\tilde{R}_{p,h}\tilde{R}_{p,g}dr = D\left[r\tilde{R}_{p,h}\tilde{R}'_{p,g}\right]_1^{r_2} - D\left[r\tilde{R}_{p,g}\tilde{R}'_{p,h}\right]_1^{r_2},$$

$$= \left[r_2 \tilde{R}_{p,h}(r_2) D \tilde{R}'_{p,g}(r_2) - \tilde{R}_{p,h}(1) D \tilde{R}'_{p,g}(1) \right] - \left[r_2 \tilde{R}_{p,g}(r_2) D \tilde{R}'_{p,h}(r_2) - \tilde{R}_{p,g}(1) D \tilde{R}'_{p,h}(1) \right], \tag{4.105}$$

and again for the eigenvalue pair $\lambda_{m,g}$ and $\lambda_{m,h}$ and the associated eigenfunctions $\tilde{R}_{m,g}$ and $\tilde{R}_{m,h}$:

$$\left(\lambda_{m,h}^2 - \lambda_{m,g}^2\right) \int_{r_2}^{r_3} r \tilde{R}_{m,h} \tilde{R}_{m,g} dr = \left[r \tilde{R}_{m,h} \tilde{R}'_{m,g} \right]_{r_2}^{r_3} - \left[r \tilde{R}_{m,g} \tilde{R}'_{m,h} \right]_{r_2}^{r_3},$$
$$= \left[r_3 \tilde{R}_{m,h}(r_3) \tilde{R}'_{m,g}(r_3) - r_2 \tilde{R}_{m,h}(r_2) \tilde{R}'_{m,g}(r_2) \right] - \left[r_3 \tilde{R}_{m,g}(r_3) \tilde{R}'_{m,h}(r_3) - r_2 \tilde{R}_{m,g}(r_2) \tilde{R}'_{m,h}(r_2) \right]. \tag{4.106}$$

Combining equations (4.104-4.106) and using boundary conditions (4.76-4.79), the right-hand side of the resultant equation reduces to zero:

$$\begin{aligned} &\left(\lambda_{d,h}^2 - \lambda_{d,g}^2\right) \int_0^1 r \tilde{R}_{d,h} \tilde{R}_{d,g} dr \\ &+ D \left(\lambda_{p,h}^2 - \lambda_{p,g}^2\right) \int_1^{r_2} r \tilde{R}_{p,h} \tilde{R}_{p,g} dr \\ &+ \left(\lambda_{m,h}^2 - \lambda_{m,g}^2\right) \int_{r_2}^{r_3} r \tilde{R}_{m,h} \tilde{R}_{m,g} dr = 0, \end{aligned} \tag{4.107}$$

using the relationship between the eigenvalues (4.74), equation (4.107) reduces to:

$$\left(\lambda_{d,h}^2 - \lambda_{d,g}^2\right) \left(\int_0^1 r \tilde{R}_{d,h} \tilde{R}_{d,g} dr + \phi \int_1^{r_2} r \tilde{R}_{p,h} \tilde{R}_{p,g} dr + \int_{r_2}^{r_3} r \tilde{R}_{m,h} \tilde{R}_{m,g} dr \right) = 0, \tag{4.108}$$

thus demonstrating (4.100). Rewriting equation (4.99) and using orthogonality condition (4.100), the value of $\beta_{p,g}$ can be determined:

$$\beta_{p,g} = \frac{\int_0^1 r \tilde{R}_{d,g} dr}{\int_0^1 r \tilde{R}_{d,g}^2 dr + \phi \int_1^{r_2} r \tilde{R}_{p,g}^2 dr + \int_{r_2}^{r_3} r \tilde{R}_{m,g}^2 dr}. \tag{4.109}$$

The integrals within (4.109) can be calculated analytically by considering Bessel's differential equation of an arbitrary function $R(r)$:

$$\frac{d}{dr}\left(rR'\right) + \lambda^2 rR = 0, \tag{4.110}$$

and integrating over an arbitrary interval $[a, b]$:

$$\int_a^b rR dr = -\frac{1}{\lambda^2} \left[rR' \right]_a^b. \tag{4.111}$$

Considering (4.110) again, multiplying throughout by $2rR'$ and simplifying gives:

$$\frac{d}{dr}\left(rR'\right)^2 + \lambda^2 r^2 \frac{d}{dr}\left(R^2\right) = 0.$$

Integrating over an arbitrary interval $[a, b]$ gives rise to:

$$\int_a^b rR^2 dr = \frac{1}{2\lambda^2}\left[\left(rR'\right)^2 + \lambda^2 r^2 R^2\right]_a^b. \tag{4.112}$$

Using relations (4.111) and (4.112), an analytical expression for $\beta_{p,g}$ can be derived, the integrals within equation (4.109) are found to be:

$$\int_0^1 r\tilde{R}_{d,g} dr = \left(\frac{\Lambda(\lambda_{d,g}, \lambda_{p,g}) J_0\left(\lambda_{p,g}\right) + Y_0\left(\lambda_{p,g}\right)}{J_0\left(\lambda_{d,g}\right)}\right) \frac{J_1\left(\lambda_{d,g}\right)}{\lambda_{d,g}},$$

$$\int_0^1 r\tilde{R}_{d,g}^2 dr = \frac{1}{2}\left(\frac{\Lambda(\lambda_{d,g}\lambda_{p,g}) J_0\left(\lambda_{p,g}\right) + Y_0\left(\lambda_{p,g}\right)}{J_0\left(\lambda_{d,g}\right)}\right)^2 \left(J_1\left(\lambda_{d,g}\right)^2 + J_0\left(\lambda_{d,g}\right)^2\right),$$

$$\phi \int_1^{r_2} r\tilde{R}_{p,g}^2 dr =$$

$$\frac{\phi r_2^2}{2}\begin{pmatrix}\left(\Lambda(\lambda_{d,g}\lambda_{p,g}) J_1\left(\lambda_{p,g} r_2\right) + Y_1\left(\lambda_{p,g} r_2\right)\right)^2 \\ + \left(\Lambda(\lambda_{d,g}\lambda_{p,g}) J_0\left(\lambda_{p,g} r_2\right) + Y_0\left(\lambda_{p,g} r_2\right)\right)^2\end{pmatrix} - \frac{\phi}{2}\begin{pmatrix}\left(\Lambda(\lambda_{d,g}\lambda_{p,g}) J_1\left(\lambda_{p,g}\right) + Y_1\left(\lambda_{p,g}\right)\right)^2 \\ + \left(\Lambda(\lambda_{d,g}\lambda_{p,g}) J_0\left(\lambda_{p,g}\right) + Y_0\left(\lambda_{p,g}\right)\right)^2\end{pmatrix},$$

$$\int_{r_2}^{r_3} r\tilde{R}_{m,g}^2 dr = \left(\frac{\Lambda(\lambda_{d,g}\lambda_{p,g}) J_0\left(\lambda_{p,g} r_2\right) + Y_0\left(\lambda_{p,g} r_2\right)}{Y_0\left(\lambda_{m,g} r_2\right) J_1\left(\lambda_{m,g} r_3\right) - J_0\left(\lambda_{m,g} r_2\right) Y_1\left(\lambda_{m,g} r_3\right)}\right)^2$$
$$\times \begin{pmatrix}\frac{r_3^2}{2}\left(J_1\left(\lambda_{m,g} r_3\right) Y_0\left(\lambda_{m,g} r_3\right) - Y_1\left(\lambda_{m,g} r_3\right) J_0\left(\lambda_{m,g} r_3\right)\right)^2 \\ -\frac{r_2^2}{2}\begin{pmatrix}\left(J_1\left(\lambda_{m,g} r_3\right) Y_1\left(\lambda_{m,g} r_2\right) - Y_1\left(\lambda_{m,g} r_3\right) J_1\left(\lambda_{m,g} r_2\right)\right)^2 \\ + \left(J_1\left(\lambda_{m,g} r_3\right) Y_0\left(\lambda_{m,g} r_2\right) - Y_1\left(\lambda_{m,g} r_3\right) J_0\left(\lambda_{m,g} r_2\right)\right)^2\end{pmatrix}\end{pmatrix}.$$

In summary, the complete set of solutions are:

$$c_d(r,t) = \gamma + \sum_{g=1}^{\infty} \beta_{p,g} \tilde{R}_{d,g} \exp\left(-\lambda_{d,g}^2 t\right), \tag{4.113}$$

$$c_p(r,t) = \gamma + \sum_{g=1}^{\infty} \beta_{p,g} \tilde{R}_{p,g} \exp\left(-\frac{D\lambda_{p,g}^2}{\phi} t\right), \tag{4.114}$$

$$c_m(r,t) = \gamma + \sum_{g=1}^{\infty} \beta_{p,g} \tilde{R}_{m,g} \exp\left(-\lambda_{m,g}^2 t\right). \tag{4.115}$$

where:

$$\gamma = \frac{1}{1-\phi+r_2^2\left(\phi-1\right)+r_3^2},$$

$$\beta_{p,g} = \frac{\displaystyle\int_0^1 r\tilde{R}_{d,g}dr}{\displaystyle\int_0^1 r\tilde{R}_{d,g}^2dr+\phi\int_1^{r_2} r\tilde{R}_{p,g}^2dr+\int_{r_2}^{r_3} r\tilde{R}_{m,g}^2dr},$$

$$\tilde{R}_{d,g} = \left(\frac{\Lambda(\lambda_{d,g},\lambda_{p,g})J_0\left(\lambda_{p,g}\right)+Y_0\left(\lambda_{p,g}\right)}{J_0\left(\lambda_{d,g}\right)}\right)J_0\left(\lambda_{d,g}r\right),$$

$$\tilde{R}_{p,g} = \Lambda(\lambda_{d,g},\lambda_{p,g})J_0\left(\lambda_{p,g}r\right)+Y_0\left(\lambda_{p,g}r\right),$$

$$\tilde{R}_{m,g} = \left(\frac{\Lambda(\lambda_{d,g},\lambda_{p,g})J_0\left(\lambda_{p,g}r_2\right)+Y_0\left(\lambda_{p,g}r_2\right)}{Y_0\left(\lambda_{m,g}r_2\right)J_1\left(\lambda_{m,g}r_3\right)-J_0\left(\lambda_{m,g}r_2\right)Y_1\left(\lambda_{m,g}r_3\right)}\right)$$
$$\times\left(J_1\left(\lambda_{m,g}r_3\right)Y_0\left(\lambda_{m,g}r\right)-Y_1\left(\lambda_{m,g}r_3\right)J_0\left(\lambda_{m,g}r\right)\right).$$

The eigenvalues are obtained via solving the transcendental equation:

$$\left(\begin{array}{l}\left[\lambda_{d,g}J_1\left(\lambda_{d,g}\right)J_0\left(\lambda_{p,g}\right)-D\lambda_{p,g}J_0\left(\lambda_{d,g}\right)J_1\left(\lambda_{p,g}\right)\right]\\ \times\left[\begin{array}{l}\lambda_{m,g}Y_0\left(\lambda_{p,g}r_2\right)\left[Y_1\left(\lambda_{m,g}r_2\right)J_1\left(\lambda_{m,g}r_3\right)-J_1\left(\lambda_{m,g}r_2\right)Y_1\left(\lambda_{m,g}r_3\right)\right]\\ -D\lambda_{p,g}Y_1\left(\lambda_{p,g}r_2\right)\left[Y_0\left(\lambda_{m,g}r_2\right)J_1\left(\lambda_{m,g}r_3\right)-J_0\left(\lambda_{m,g}r_2\right)Y_1\left(\lambda_{m,g}r_3\right)\right]\end{array}\right]\end{array}\right)$$
$$-\left(\begin{array}{l}\left[D\lambda_{p,g}J_0\left(\lambda_{d,g}\right)Y_1\left(\lambda_{p,g}\right)-\lambda_{d,g}J_1\left(\lambda_{d,g}\right)Y_0\left(\lambda_{p,g}\right)\right]\\ \times\left[\begin{array}{l}D\lambda_{p,g}J_1\left(\lambda_{p,g}r_2\right)\left[Y_0\left(\lambda_{m,g}r_2\right)J_1\left(\lambda_{m,g}r_3\right)-J_0\left(\lambda_{m,g}r_2\right)Y_1\left(\lambda_{m,g}r_3\right)\right]\\ -\lambda_{m,g}J_0\left(\lambda_{p,g}r_2\right)\left[Y_1\left(\lambda_{m,g}r_2\right)J_1\left(\lambda_{m,g}r_3\right)-J_1\left(\lambda_{m,g}r_2\right)Y_1\left(\lambda_{m,g}r_3\right)\right]\end{array}\right]\end{array}\right)=0.$$

4.2.3 Equations for mass of drug

Dimensionally, the mass of drug at some time t in each region is:

$$M_d(t) = \int_0^z\int_0^{2\pi}\int_0^{L_1} c_d\, r\, dr\, d\theta\, dz,$$
$$M_p(t) = \phi\int_0^z\int_0^{2\pi}\int_{L_1}^{L_2} c_p\, r\, dr\, d\theta\, dz,$$
$$M_m(t) = \int_0^z\int_0^{2\pi}\int_{L_2}^{L_3} c_m\, r\, dr\, d\theta\, dz.$$

Mass can be normalised with M_d^0, the total initial mass of drug in region d. Since the inner drug core is cylindrical, M_d^0 is therefore:

$$M_d^0 = c_d^0\pi L_d^2 z.$$

Therefore, the normalised mass in each region is:

$$\begin{aligned}
\frac{M_d(t)}{M_d^0} &= \frac{1}{c_d^0 \pi L_d^2 z} 2\pi z c_d^0 L_d^2 \int_0^1 c_d' \, r' \, dr', \\
\frac{M_p(t)}{M_d^0} &= \frac{1}{c_d^0 \pi L_d^2 z} 2\pi z c_d^0 L_d^2 \phi \int_1^{r_2} c_p' \, r' \, dr', \\
\frac{M_m(t)}{M_d^0} &= \frac{1}{c_d^0 \pi L_d^2 z} 2\pi z c_d^0 L_d^2 \int_{r_2}^{r_3} c_m' \, r' \, dr'.
\end{aligned}$$

Simplifying and dropping the primes for clarity:

$$\frac{M_d(t)}{M_d^0} = 2 \int_0^1 c_d \, r \, dr, \quad \frac{M_p(t)}{M_d^0} = 2\phi \int_1^{r_2} c_p \, r \, dr, \quad \frac{M_m(t)}{M_d^0} = 2 \int_{r_2}^{r_3} c_m \, r \, dr.$$

The time dependent equations for nondimensional mass in each region can be computed from solutions (4.113-4.115) via integration:

$$\begin{aligned}
\frac{M_d(t)}{M_d^0} &= 2 \int_0^1 \left(\gamma + \sum_{g=1}^{\infty} \beta_{p,g} \tilde{R}_{d,g} \exp\left(-\lambda_{d,g}^2 t\right) \right) r \, dr, \\
&= 2 \left(\gamma_d + \sum_{g=1}^{\infty} \beta_{p,g} R_{d,g}^* \exp\left(-\lambda_{d,g}^2 t\right) \right),
\end{aligned}$$

where:

$$\begin{aligned}
\gamma_d &= \frac{1}{2\left(1 - \phi + r_2^2 \left(\phi - 1\right) + r_3^2\right)}, \\
R_{d,g}^* &= \left(\frac{\Lambda(\lambda_{d,g}, \lambda_{p,g}) J_0\left(\lambda_{p,g}\right) + Y_0\left(\lambda_{p,g}\right)}{J_0\left(\lambda_{d,g}\right)} \right) \frac{J_1\left(\lambda_{d,g}\right)}{\lambda_{d,g}}.
\end{aligned}$$

$$\begin{aligned}
\frac{M_p(t)}{M_d^0} &= 2\phi \int_1^{r_2} \left(\gamma + \sum_{g=1}^{\infty} \beta_{p,g} \tilde{R}_{p,g} \exp\left(-\frac{D\lambda_{p,g}^2}{\phi} t\right) \right) r \, dr, \\
&= 2\phi \left(\gamma_p + \sum_{g=1}^{\infty} \beta_{p,g} R_{p,g}^* \exp\left(-\frac{D\lambda_{p,g}^2}{\phi} t\right) \right),
\end{aligned}$$

where:

$$\begin{aligned}
\gamma_p &= \frac{\phi\left(r_2^2 - 1\right)}{2\left(1 - \phi + r_2^2\left(\phi - 1\right) + r_3^2\right)}, \\
R_{p,g}^* &= \Lambda(\lambda_{d,g}, \lambda_{p,g}) \frac{\left(r_2 J_1\left(\lambda_{p,g} r_2\right) - J_1\left(\lambda_{p,g}\right)\right)}{\lambda_{p,g}} + \frac{r_2 Y_1\left(\lambda_{p,g} r_2\right) - Y_1\left(\lambda_{p,g}\right)}{\lambda_{p,g}}.
\end{aligned}$$

$$\frac{M_m(t)}{M_d^0} = 2 \int_{r_2}^{r_3} \left(\gamma + \sum_{g=1}^{\infty} \beta_{p,g} \tilde{R}_{m,g} \exp\left(-\lambda_{m,g}^2 t\right) \right) r \, dr,$$

$$= 2\left(\gamma_m + \sum_{g=1}^{\infty} \beta_{p,g} R^*_{m,g} \exp\left(-\lambda^2_{m,g} t\right)\right),$$

where:

$$\gamma_m = \frac{(r_3^2 - r_2^2)}{2\left(1 - \phi + r_2^2\left(\phi - 1\right) + r_3^2\right)},$$

$$R^*_{m,g} = \left(\frac{\Lambda(\lambda_{d,g}, \lambda_{p,g}) J_0\left(\lambda_{p,g} r_2\right) + Y_0\left(\lambda_{p,g} r_2\right)}{Y_0\left(\lambda_{m,g} r_2\right) J_1\left(\lambda_{m,g} r_3\right) - J_0\left(\lambda_{m,g} r_2\right) Y_1\left(\lambda_{m,g} r_3\right)}\right) \times \frac{r_2}{\lambda_{m,g}} \left(Y_1\left(\lambda_{m,g} r_3\right) J_1\left(\lambda_{m,g} r_2\right) - J_1\left(\lambda_{m,g} r_3\right) Y_1\left(\lambda_{m,g} r_2\right)\right).$$

4.2.4 Release profile

The released profile can be found either by the loss of mass from the first two regions, d and p, or by the accumulation of mass in the release medium, which is then normalised with the initial mass in the system, M_d^0. Then the cumulative fraction released, M_{frac}, is:

$$\begin{aligned} M_{frac}(t) &= \frac{M_d^0 - (M_d(t) + M_p(t))}{M_d^0} = 1 - \left(\frac{M_d(t)}{M_d^0} + \frac{M_p(t)}{M_d^0}\right), \\ &= 1 - 2\left[\gamma_d + \sum_{g=1}^{\infty} \beta_{p,g} R^*_{d,g} \exp\left(-\lambda^2_{d,g} t\right) + \phi\left(\gamma_p + \sum_{g=1}^{\infty} \beta_{p,g} R^*_{p,g} \exp\left(-\frac{D\lambda^2_{p,g}}{\phi} t\right)\right)\right], \\ &= 1 - 2\left[\sum_{g=1}^{\infty} \beta_{p,g}\left(R^*_{d,g} \exp\left(-\lambda^2_{d,g} t\right) + \phi R^*_{p,g} \exp\left(-\frac{D\lambda^2_{p,g}}{\phi} t\right)\right)\right] \\ &- \frac{\phi\left(r_2^2 - 1\right) + 1}{1 - \phi + r_2^2\left(\phi - 1\right) + r_3^2}, \end{aligned}$$

the simpler approach to generating the release profile is to plot the growing mass in the release medium, this leads to a simpler expression for the release profile:

$$\begin{aligned} M_{frac}(t) = \frac{M_m(t)}{M_d^0} &= 2\left[\gamma_m + \sum_{g=1}^{\infty} \beta_{p,g} R^*_{m,g} \exp\left(-\lambda^2_{m,g} t\right)\right], \\ &= 2\sum_{g=1}^{\infty} \beta_{p,g} R^*_{m,g} \exp\left(-\lambda^2_{m,g} t\right) + \frac{(r_3^2 - r_2^2)}{1 - \phi + r_2^2\left(\phi - 1\right) + r_3^2}. \end{aligned} \tag{4.116}$$

4.2.5 Model results and discussion

Equations (4.113-4.115) are used to calculate the concentration solutions and equation (4.116) is used to calculate the release profile, however, these equations feature infinite series whose infinite summations are unknown. The sums will have to be truncated to approximate these infinite sums. The truncation value chosen is N, the number of roots of (4.91) in a given interval.

The value of N will affect the accuracy of the results and if too few roots are used or missed entirely, the solution will not converge. The values of the system parameters will change (4.91) and hence the location of the roots. For a certain parameter set, more/less roots may be required for an accurate solution. To accomplish this, the initial root searching interval used in the simulations is $[0, 100]$. To determine whether or not N is a sufficient number of roots to produce an accurate solution, the theoretical masses $M_{S_{N+1}}$ and M_{S_N} for the sequences of roots S_{N+1} and S_N, are considered and if:

$$100 \times \frac{\int_0^t M_{S_{N+1}}(t)dt - \int_0^t M_{S_N}(t)dt}{\int_0^t M_{S_N}(t)dt} < 1\%,$$

for some time t, then N is deemed sufficiently accurate. To ensure smooth plots for concentration profiles and release profiles, the intervals considered for the nondimensional variables r and t, are divided into 100 equally spaced increments. The solution of the 1D radial diffusion model can be evaluated using MATLAB®R2019a via a series of for-loops to calculate concentration and drug release data. Rather than solving the transcendental equation (4.91) in its current form, using relation (4.74), the equation may be transformed into an expression of one eigenvalue, which is simpler to solve. Additionally, solution equations (4.113-4.115) can also be rewritten using relation (4.74) for simplicity in their evaluation. The parameter values used in the evaluation are shown in Table 4.3.

Parameter	Value
L_d	1.575 mm [11]
L_p	1.6 mm [11]
L_m	30 mm
ϕ	0.17 [11]
ϕ_e	$0.9 \times \phi$
τ	3
D_f	1×10^{-9} m^2/s
$D_p = \phi_e D_f/\tau$	5.1×10^{-11} m^2/s

Table 4.3: Table of parameter values used in the evaluation of the 1D radial diffusion model.

Figure 4.9 (a) Shows an example concentration plot at three times, which demonstrates the zero-flux boundary conditions, in that drug cannot leave the system. The release medium accumulates drug until the steady-state, γ, is reached. Physically, γ is the steady-state concentration in which the initial drug concentration, c_d^0, is spread throughout all regions. Figure 4.9 (b) shows the release profile generated by the 1D radial diffusion model. Since the shape of the release

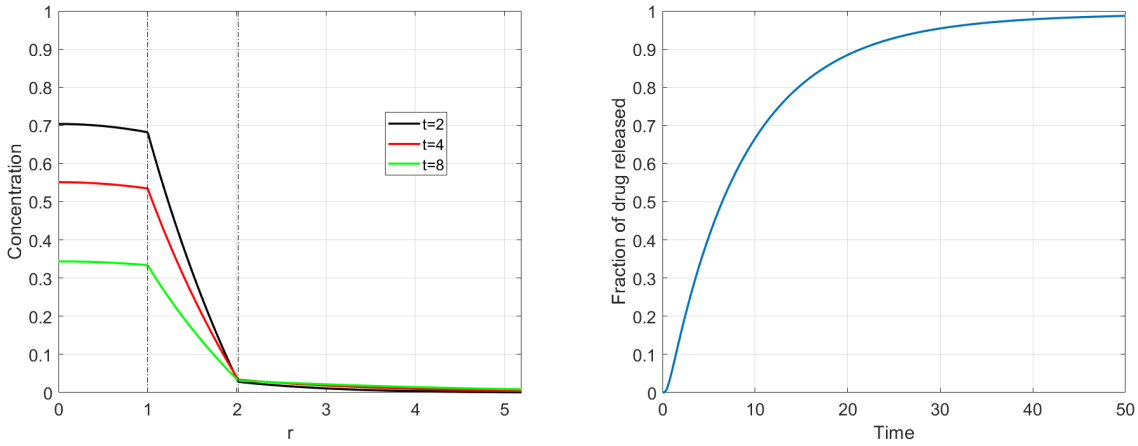

(a) (b)

Figure 4.9: (a) Magnified plot showing nondimensional concentration verses nondimensional space at three nondimensional times. (b) Plot showing fraction of drug release verses nondimensional time.

profile is a gentle curve, which is characteristic of pure-diffusion models, the 1D radial model is not sufficient to be able to replicate the near-linear release data in Figure 4.1 (b). Since the cylindrical geometry of the porous pin may be reduced to a 1D problem, this suggests that the coordinate system is not at fault. Further reading of the experimental details shows that the drug (Linezolid), is loaded into the porous pin in a dry, solid form. This means that the drug must transition into the solute phase (dissolve), before diffusion of drug particles out of the pin may occur. Since one of the assumptions in the 1D radial diffusion model was that the drug was already in the solute phase, it would appear that the next step in modelling drug-release from the porous pin must include the dissolution process.

4.3 1D radial diffusion-dissolution model

In previous sections, it was found that a mathematical model of drug release from the porous pin could be reduced to a 1D model, through a combination of symmetry and the insignificant influence the stirring of the release medium has on the transport of the drug. However, a purely diffusive process is not suitable to model the release of drug from the porous pin and a new process is included: drug dissolution. The dissolution model of choice is based on the Noyes-Whitney model of dissolution, which assumes that the rate of dissolution is proportional to the difference in the drug solubility and the concentration of dissolved drug [32]. Using the same geometry from Section 4.2 (Figure 4.8) and assuming that the drug is initially fully wetted, the proposed diffusion-dissolution model is:

$$\frac{\partial b}{\partial t} = -\beta b^{\alpha} \left(S - c_d\right), \quad 0 < r < L_1, \quad t > 0, \tag{4.117}$$

$$\frac{\partial c_d}{\partial t} = D_f \left(\frac{1}{r} \frac{\partial c_d}{\partial r} + \frac{\partial^2 c_d}{\partial r^2} \right) + \beta b^\alpha \left(S - c_d \right), \quad 0 < r < L_1, \quad t > 0, \tag{4.118}$$

$$\phi \frac{\partial c_p}{\partial t} = D_p \left(\frac{1}{r} \frac{\partial c_p}{\partial r} + \frac{\partial^2 c_p}{\partial r^2} \right), \quad L_1 < r < L_2, \quad t > 0, \tag{4.119}$$

$$\frac{\partial c_m}{\partial t} = D_f \left(\frac{1}{r} \frac{\partial c_m}{\partial r} + \frac{\partial^2 c_m}{\partial r^2} \right), \quad L_2 < r < L_3, \quad t > 0, \tag{4.120}$$

$$- D_f \frac{\partial c_d}{\partial r} = 0, \quad r = 0, \quad t > 0, \tag{4.121}$$

$$c_d = c_p, \quad -D_f \frac{\partial c_d}{\partial r} = -D_p \frac{\partial c_p}{\partial r}, \quad r = L_1, \quad t > 0, \tag{4.122}$$

$$c_p = c_m, \quad -D_p \frac{\partial c_p}{\partial r} = -D_f \frac{\partial c_m}{\partial r}, \quad r = L_2, \quad t > 0, \tag{4.123}$$

$$- D_f \frac{\partial c_m}{\partial r} = 0, \quad r = L_3, \quad t > 0, \tag{4.124}$$

$$b = b_0, \quad 0 \leq r \leq L_1, \quad c_d = 0, \quad 0 \leq r \leq L_1, \quad t = 0, \tag{4.125}$$

$$c_p = 0, \quad L_1 < r \leq L_2, \quad c_m = 0, \quad L_2 < r \leq L_3, \quad t = 0, \tag{4.126}$$

Model equations (4.117-4.126) are identical to the 1D diffusion model (4.56-4.63) considered in the previous section. However, there is an additional equation of variable, $b(r,t)$, the concentration of undissolved drug (4.117), which describes the dissolution process. The equation for drug transport in the inner drug region (4.118) has an added component, a reaction term which supplies drug in the solute phase to the inner drug region as b is depleted. There are also new parameters, which include, S, the solubility of the drug, β, the dissolution rate and b_0, the initial undissolved drug concentration. Also added to the model is α, which is a constant, the value of which is likely influenced by the geometrical configuration/device design and chemical properties of the drug. The work by Hixson and Crowell [33] modified the Noyes-Whitney dissolution model [32], in which a nonlinear version of dissolution model was derived, with $\alpha = 2/3$, to account for potential influences to the dissolution rate as the surface of dissolving drugs changed. Later work by Frenning [34] concluded that $\alpha = 2/3$ is likely the most suitable choice for drug delivery, provided that the solid drug particles are initially, approximately uniform in size and retain their shape during the dissolution process. Model equations (4.117-4.126) are nondimensionalised with the following scalings:

$$c_i' = \frac{c}{S}, \quad b' = \frac{b}{b_0}, \quad r' = \frac{r}{L_d}, \quad t' = \frac{D_f}{L_d^2} t,$$

where $i = d, p, m$. Dropping the primes for clarity, these scalings give the following nondimensional model:

$$\frac{\partial b}{\partial t} = -Da_{II} S^* b^\alpha \left(1 - c_d \right), \quad 0 < r < 1, \quad t > 0, \tag{4.127}$$

$$\frac{\partial c_d}{\partial t} = \left(\frac{1}{r} \frac{\partial c_d}{\partial r} + \frac{\partial^2 c_d}{\partial r^2} \right) + Da_{II} b^\alpha \left(1 - c_d \right), \quad 0 < r < 1, \quad t > 0, \tag{4.128}$$

$$\phi\frac{\partial c_p}{\partial t} = D\left(\frac{1}{r}\frac{\partial c_p}{\partial r} + \frac{\partial^2 c_p}{\partial r^2}\right), \quad 1 < r < r_2, \quad t > 0, \tag{4.129}$$

$$\frac{\partial c_m}{\partial t} = \left(\frac{1}{r}\frac{\partial c_m}{\partial r} + \frac{\partial^2 c_m}{\partial r^2}\right), \quad r_2 < r < r_3, \quad t > 0, \tag{4.130}$$

$$\frac{\partial c_d}{\partial r} = 0, \quad r = 0, \quad t > 0, \tag{4.131}$$

$$c_d = c_p, \quad \frac{\partial c_d}{\partial r} = D\frac{\partial c_p}{\partial r}, \quad r = 1, \quad t > 0, \tag{4.132}$$

$$c_p = c_m, \quad D\frac{\partial c_p}{\partial r} = \frac{\partial c_m}{\partial r}, \quad r = r_2, \quad t > 0, \tag{4.133}$$

$$\frac{\partial c_m}{\partial r} = 0, \quad r = r_3, \quad t > 0, \tag{4.134}$$

$$b = 1, \quad 0 \leq r \leq 1, \quad c_d = 0, \quad 0 \leq r \leq 1, \quad t = 0, \tag{4.135}$$

$$c_p = 0, \quad 1 < r \leq r_2, \quad c_m = 0, \quad r_2 < r \leq r_3, \quad t = 0, \tag{4.136}$$

where Da_{II} is the second Damköhler number and is equal to $L_d^2\beta b_0^\alpha/D_f$ and S^* is defined as S/b_0.

4.3.1 Equations for mass of drug

The dimensional mass in each region of the geometry may be found via:

$$M_d(t) = \int_0^z \int_0^{2\pi} \int_0^{L_1} b\, r\, dr\, d\theta\, dz + \int_0^z \int_0^{2\pi} \int_0^{L_1} c_d\, r\, dr\, d\theta\, dz,$$
$$M_p(t) = \phi \int_0^z \int_0^{2\pi} \int_{L_1}^{L_2} c_p\, r\, dr\, d\theta\, dz,$$
$$M_m(t) = \int_0^z \int_0^{2\pi} \int_{L_2}^{L_3} c_m\, r\, dr\, d\theta\, dz.$$

The mass in each region can be normalised via M_d^0, the total initial mass of undissolved drug in the core of the pin:

$$M_d^0 = \pi L_d^2 z b_0,$$

hence, the normalised mass in each region is:

$$\frac{M_d(t)}{M_d^0} = \frac{1}{\pi L_d^2 z b_0}\left[2\pi z b_0 L_d^2 \int_0^1 b\, r'\, dr' + 2\pi z S L_d^2 \int_0^1 c_d\, r'\, dr'\right],$$
$$\frac{M_p(t)}{M_d^0} = \frac{1}{\pi L_d^2 z b_0} 2\pi z \phi S L_d^2 \int_1^{r_2} c_p\, r'\, dr',$$
$$\frac{M_m(t)}{M_d^0} = \frac{1}{\pi L_d^2 z b_0} 2\pi z S L_d^2 \int_{r_2}^{r_3} c_m\, r'\, dr'.$$

Simplifying and dropping the primes for clarity:

$$\begin{aligned}
\frac{M_d(t)}{M_d^0} &= 2\left[\int_0^1 b\,r\,dr + S^*\int_0^1 c_d\,r\,dr\right],\\
\frac{M_p(t)}{M_d^0} &= 2\phi S^*\int_1^{r_2} c_p\,r\,dr,\\
\frac{M_m(t)}{M_d^0} &= 2S^*\int_{r_2}^{r_3} c_m\,r\,dr.
\end{aligned}$$

4.3.2 Release profile

The release profile may be obtained through the mass of drug released from the porous pin:

$$\begin{aligned}
M_{frac}(t) &= \frac{M_d^0 - (M_d(t) + M_p(t))}{M_d^0} = 1 - \left(\frac{M_d(t)}{M_d^0} + \frac{M_p(t)}{M_d^0}\right),\\
&= 1 - 2\left[\int_0^1 b\,r\,dr + S^*\left(\int_0^1 c_d\,r\,dr + \phi\int_1^{r_2} c_p\,r\,dr\right)\right],
\end{aligned}$$

or by the accumulation of mass in the release medium:

$$M_{frac}(t) = \frac{M_m(t)}{M_d^0} = 2S^*\int_{r_2}^{r_3} c_m\,r\,dr. \tag{4.137}$$

4.3.3 Sensitivity analysis

Model equations (4.127-4.136) were solved numerically using COMSOL®, version 5.3a, specifically using the direct PARDISO method, with the BDF to handle time advancement. The 1D geometry was discretised into 2500 spatial points, which was found to produce negligible error due to mass loss. The integral in the equation used to calculate the release profile (4.137) was performed within the software using Gaussian quadrature. A sensitivity analysis is a useful approach to obtain a thorough understanding of model performance. Therefore, key model parameters are fixed at baseline values (Table 4.4) and varied sequentially to determine their influence on the release profile and thus gauge their relative importance. The authors state that the porous pins used in their experiments were loaded with $95 - 120\,\mathrm{mg}$ of the drug for the release experiments. This imprecise drug loading introduces unnecessary uncertainty to the model output. However, for the sake of simplicity, it is assumed that the drug loading is $100\,\mathrm{mg}$ for the model sensitivity analysis and validation.

To adequately test the sensitivity of the release profile to changes in model parameters, a suitable range of parameter values is required. It is assumed that the baseline value for reaction exponent is $\alpha = 2/3$, due to the work of Frenning [34], therefore the range chosen for the sensitivity study was decided to be $1/3$ greater than, and less than, the baseline value. Additionally, $\alpha = 0$ is also included within the range of test parameter values to cover the simplest linear reaction, and so $0 \leq \alpha \leq 1$. The dissolution rate, β, is unknown and so the baseline

value of $\beta = 10^{-5}$ was chosen such that the associated second Damköhler number would be of order 1. Therefore, to cover a suitable range of possible values of β, it was decided that values which cover two orders of magnitude above and below the baseline value would be sufficient i.e. $10^{-7} \leq \beta \leq 10^{-3}$. The baseline value for the free-diffusion coefficient was chosen to be the upper limit of the accepted range of values for diffusivities in liquids. The lower limit within this range is 10^{-11} and so the values considered for the sensitivity analysis would cover the intermediate values within this range such that $10^{-11} \leq D_f \leq 10^{-9}$. The length scale of the release medium, L_m, is unknown and so a baseline value was chosen based upon known suitable sizes of beakers. Therefore, for the sensitivity study, it was decided that two values of L_m greater, and smaller, than the baseline would suffice to give an idea of what influence the variation of L_m would have on the release profile. The level of porosity of the pin is known, $\phi = 0.17$, therefore, since the value is on the lower end of possible porosity values, most values considered for the sensitivity analysis cover values higher in the porosity scale, with an additional value lower than the known value to cover extremely low porosities. Preliminary modelling suggested that the solubility of the drug would be very influential on the release profile and since the reported value of the drug used, $3\,\mathrm{kg/m^3}$, is relatively low, the values considered for the sensitivity study are all greater than this stated value.

Parameter	Value
L_d	$1.575 \times 10^{-3}\,\mathrm{m}$ [11]
L_p	$1.6 \times 10^{-3}\,\mathrm{m}$ [11]
L_m	$3 \times 10^{-2}\,\mathrm{m}$ [62]
τ	3 [48]
ϕ	0.17 [11]
ϕ_e	$0.9 \times \phi$
α	$2/3$ [34]
D_f	$1 \times 10^{-9}\,\mathrm{m^2/s}$
$D_p = \phi_e D_f/\tau$	$5.1 \times 10^{-11}\,\mathrm{m^2/s}$
β	$10^{-5}\,\mathrm{s^{-1}(m^{-3}kg)^{2/3}}$
b_0	$505.19\,\mathrm{kg/m^3}$ [11]
S	$3\,\mathrm{kg/m^3}$ [12]

Table 4.4: Baseline parameter values. These values are taken from the literature or inferred from [11]. The length scale of the release medium, L_m, is the same as was assumed in the influence of flow study. The initial mass concentration, b_0, is calculated from the assumed drug mass loading and dividing by the interior volume of the porous pin.

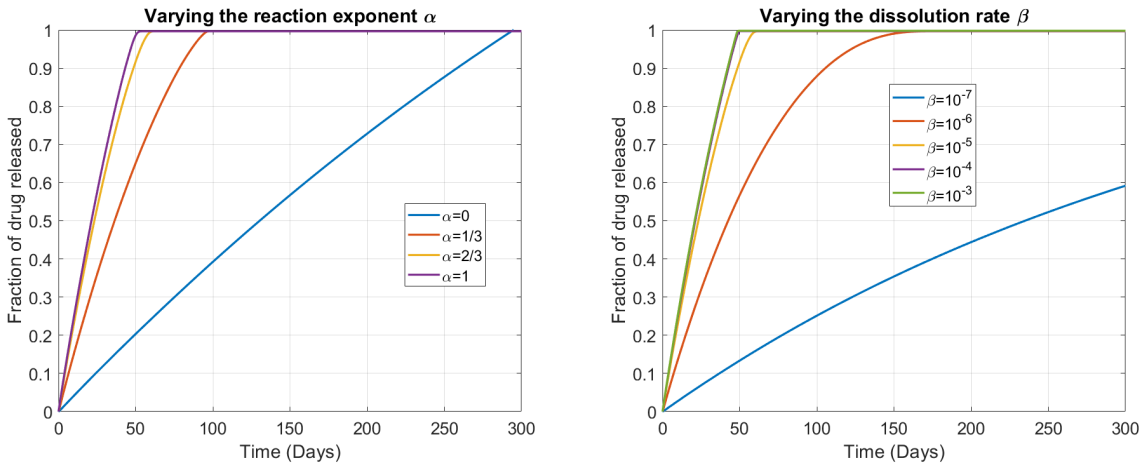

(a) (b)

Figure 4.10: Plots showing the release profiles obtained through varying the system parameters:(a) reaction exponent (α) (b) dissolution rate (β).

In Figure 4.10, plot (a) shows the effect of changing the value of the reaction exponent, α. Given the significant differences between most of the release profiles, this suggests that α is fairly influential which is also evidenced by the range of release times shown in Table 4.5. Although, this level of influence is reduced as α is increased. The spread of the plots generated is to be expected as this parameter can account for both linear and nonlinear dissolution processes.

In Figure 4.10, plot (b) shows the effect of varying the dissolution rate β. The plot displays the general behaviour one would expect, that is the higher the dissolution rate, the quicker the release. However, when increasing β from 10^{-4} to 10^{-3}, the difference in the release profiles is almost nonexistent. This outcome is also shown by the near-identical values for both $50\,\%$ and $95\,\%$ release times in Table 4.5. Given that there is no significant decrease in the release time, should one increase β further, it is reasonable to conclude that it will become even less apparent. Despite not being immediately clear why this is the case, looking at the change to the second Damköhler number (Da_{II}), it can be see why this is the case. The first three values of β, 10^{-7}, 10^{-6} and 10^{-5} (the baseline value of β) are associated with the second Damköhler numbers 0.016, 0.16 and 1.6, respectively. These values show the ratio of the dissolution reaction rate to the diffusive transport rate (or, equivalently, the ratio of the diffusion timescale to the dissolution reaction timescale). Initially, the dissolution timescale is larger than that of the diffusive timescale. As β is increased through two orders of magnitude, the associated Damköhler number increases and the dissolution timescale is reduced, so the release becomes quicker, as one would expect. This trend is also shown in Table 4.5, in that a sizable reduction in release times is gained by increasing β from 10^{-7} to 10^{-6}. However, the decrease in release times becomes limited with further increases to β since $Da_{II} \gg 1$, meaning the dissolution timescale is already much smaller than the diffusive timescale and so further increases to β will have a minimal effect, meaning the rate-limiting process in this scenario is diffusion. Physically, the

scenario would be that the reaction must wait for dissolved drug molecules to diffuse, so that further dissolution may occur.

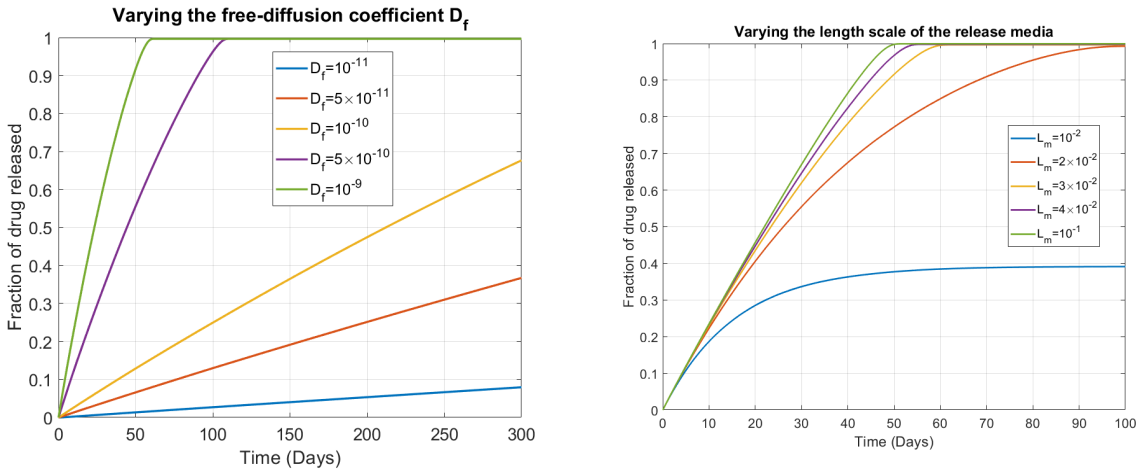

(a) (b)

Figure 4.11: Plots showing the release profiles obtained through varying the system parameters:(a) free-diffusion coefficient (D_f) (b) release medium length scale (L_m).

In Figure 4.11, plot (a) shows the effect of altering the free-diffusion coefficient, D_f, and displays the trend that one would expect, that is, the greater the free-diffusion coefficient, the quicker the release. This trend is also displayed in Table 4.5, which shows that for a one order of magnitude increase in D_f from 10^{-11} to 10^{-10}, an order of magnitude reduction in both the $50\,\%$ and $95\,\%$ release times is observed. Similarly, there is a further order of magnitude reduction in the $50\,\%$ and $95\,\%$ release times, by increasing D_f from 10^{-10} to 10^{-9}. The plot also shows a relatively large jump between the release profiles generated by D_f values of 10^{-10} and 5×10^{-10}. This can be explained by examining the Damköhler numbers associated with these free-diffusion coefficients, which are 16 and 3.1, respectively. These Damköhler numbers show that when increasing D_f from 10^{-10} to 5×10^{-10}, the reaction rate is no longer an order of magnitude greater than the diffusive rate. Therefore, both of these processes have fairly similar timescales, meaning that one process is not necessarily hampered by the other.

In Figure 4.11, plot (b) shows the effect of altering the length scale of the release medium, L_m. This shows a trend one would expect when considering the concentration gradient. With a larger release medium, the concentration gradient can be maintained relatively higher for longer since the diffusing drug particles take longer to reach the boundary. Therefore, one would expect a more significant difference in the later stages of release, but fairly similar release profiles during earlier times. This is the trend shown in Table 4.5: the $50\,\%$ release times show a difference of between one and three days with respect to the baseline case. In contrast, the $95\,\%$ release times display a more appreciable difference from the baseline case, which may be due to the effect of a larger release medium length scale allowing for a relatively higher concentration gradient to maintained for considerably longer. However, the effect of increasing L_m becomes

limited as there will be a point where the release medium is orders of magnitude greater in size, compared to the length scales of the drug and porous layers. So, when increasing L_m further, the release time reductions will be small. There is also a limit associated with L_m such that below this value, for a given solubility, complete release is impossible. This is evidenced by the release profile for when $L_m = 10^{-2}$, meaning that the minimum length scale for the release medium for complete release is dependent on the drug solubility.

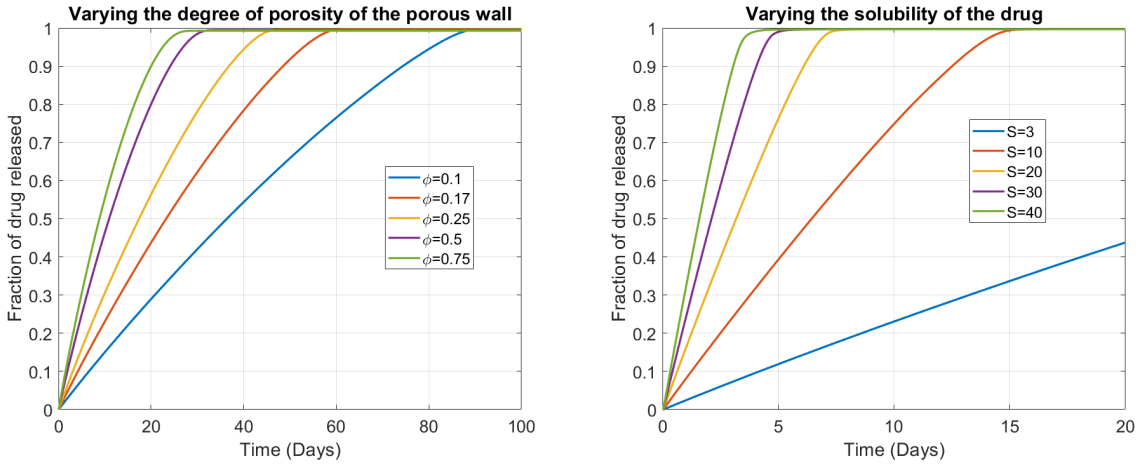

(a) (b)

Figure 4.12: Plots showing the release profiles obtained through varying the system parameters:(a) porosity (ϕ) (b) solubility (S).

In Figure 4.12, plot (a) shows the effect that altering the porosity, ϕ, of the porous wall has on the release profile. The trend shown is expected, that is the higher the degree of porosity, the faster the release of drug. This change is attributed to the change in the effective diffusion coefficient through the porous layer, which ranges from 3×10^{-11} to 2.25×10^{-10}. The effect porosity has on the release profile is less prominent than other parameters, however, this may be due to length scale of the pin's porous wall, which is $1.6\,\mathrm{mm}$. This is a relatively small distance for diffusion to occur and the associated diffusive timescale in the porous layer (L_p^2/D_p) ranges from approximately $3 - 24$ hours. When compared to the overall release times, the timescale for diffusion in the porous wall is relatively small. This suggests that the influence that porosity has on the release has much less variability when compared to the other parameters. This is evidenced by the times in Table 4.5, which show that increasing the level of porosity, the release times for $50\,\%$ and $95\,\%$ release, are reduced, albeit to a lower degree. However, these results do not necessarily mean that the porosity parameter is not a useful design parameter, as this is the type of parameter that could be used to fine-tune the release profile.

In Figure 4.12, plot (b) shows the effect that varying the drug solubility, S, has on the release profile. One can see that this parameter is particularly significant, perhaps even the dominant parameter, due to the drastic reduction in release times shown in Table 4.5 when compared to the baseline case. The other parameter ranges required considerably longer timescales for their

influence to be appreciable in the plots, i.e. in the region of $100 - 300$ days. This contrasts with the range of solubility values considered, in that marked differences in the release profiles are seen in a timescale of just 20 days. Also noteworthy is that the influence of solubility on the release profile is noticeable with less than an order of magnitude increase in the parameter. This suggests that the release profile is especially sensitive to changes in this parameter, which may also alter the influence that the other parameters have. Solubility having such an influential role in the release compared to the other parameters can be explained when considering the nondimensional solubility. With $S^* < 1$ in all cases considered, i.e. the solubility is less than the initial drug concentration, the free-drug phase is saturated immediately, specifically $c_d = S^*$. Therefore, excess drug must wait for drug in the solute phase to diffuse out of the system before any more drug may dissolve. By increasing S^*, more of the drug is able to dissolve and thus begin diffusing out of the drug layer, through the porous wall and out into the release medium, which will take less time to occur.

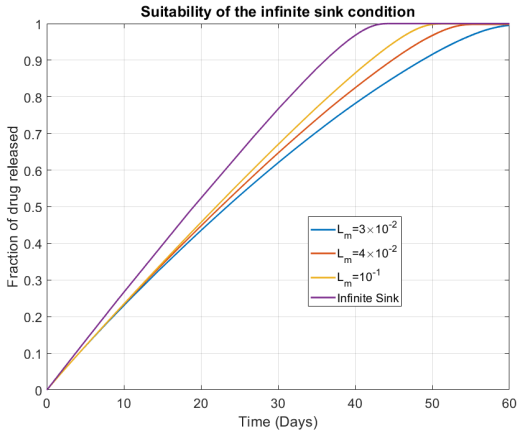

Figure 4.13: Plot showing the effect of replacing the release medium with an infinite sink condition.

Figure 4.13 shows the effect on the release profile when replacing the release medium with an infinite sink condition. As expected, the sink condition generates the fastest possible release profile when altering the length scale, L_m, of the release medium. This is because with the sink condition in place, the concentration gradient within the drug and porous layers is at its theoretical maximum value. This is akin to having a release medium of infinite size and so the sink condition is the theoretical upper limit on the release time.

	Second Damköhler number Da_{II}	**Normalised solubility S^***	**Time for 50 % release (Days)**	**Time for 95 % release (Days)**
Baseline	**1.6**	**0.0059**	**23**	**53**
Parameter	Second Damköhler number Da_{II}	Normalised solubility S^*	Time for 50 % release (Days)	Time for 95 % release (Days)
$\alpha = 0$	0.025	0.0059	130	276
$\alpha = 1/3$	0.2	0.0059	36	86
$\alpha = 1$	12.5	0.0059	21	47
$\beta = 10^{-7}$	0.016	0.0059	235	822
$\beta = 10^{-6}$	0.16	0.0059	43	122
$\beta = 10^{-4}$	16	0.0059	21	46
$\beta = 10^{-3}$	157	0.0059	21	45
$D_f = 10^{-11}$	157	0.0059	2088	4532
$D_f = 5 \times 10^{-11}$	31	0.0059	421	911
$D_f = 10^{-10}$	16	0.0059	212	460
$D_f = 5 \times 10^{-10}$	3.1	0.0059	44	98
$L_m = 10^{-2}$	1.6	0.0059	N/A	N/A
$L_m = 2 \times 10^{-2}$	1.6	0.0059	26	79
$L_m = 4 \times 10^{-2}$	1.6	0.0059	23	48
$L_m = 10^{-1}$	1.6	0.0059	22	45
$\phi = 0.1$	1.6	0.0059	36	81
$\phi = 0.25$	1.6	0.0059	17	41
$\phi = 0.5$	1.6	0.0059	11	27
$\phi = 0.75$	1.6	0.0059	9	23
$S = 10$	1.6	0.019	6	14
$S = 20$	1.6	0.039	3	7
$S = 30$	1.6	0.059	2	4
$S = 40$	1.6	0.079	2	3

Table 4.5: Release times for $50\,\%$ and $95\,\%$ across a variety of parameter ranges. All values are approximate and rounded.

4.3.4 Model calibration and validation

In the quest to produce a useful mathematical model, it must be validated against experimental data. In an ideal situation, all of the model parameters would be known, and then validation would be performed by solving the model with these parameters as inputs and then comparing with the experimental data. However, not all of the parameters are known *a priori* and of those whose values that are known, these are associated with some uncertainty. Therefore, in this section an attempt is made to calibrate the model using the release profile from [11]. Even if it is found that the model is capable of capturing the data, further experiments would be required to fully validate the model.

Since the raw experimental drug release data was not available directly from the authors, the data had to be extracted via other means. This was done by approximating the data point coordinates in Figure 4.1 (b) using an online tool [68]. The basic procedure is to upload an image of plotted data and specify the origin and the maximum and minimum values of the x and y axes. In the case of the porous pin drug release data, the x-axis was set from $0 - 10,000$ minutes and the y-axis was set to $0 - 100\,\%$, as shown in Figure 4.1 (b). This then allows the user to approximate the position coordinates of all data points by aiming a cursor at the centre of each data point in the image, which is recorded and may be exported as a table. Figure 4.14 shows the approximated data points of the original release data in Figure 4.1 (b). The approximated data used is divided by 100 to give release values in the range $[0, 1]$, the same range as generated by release profile equation (4.137), so that the data can be compared with the model output.

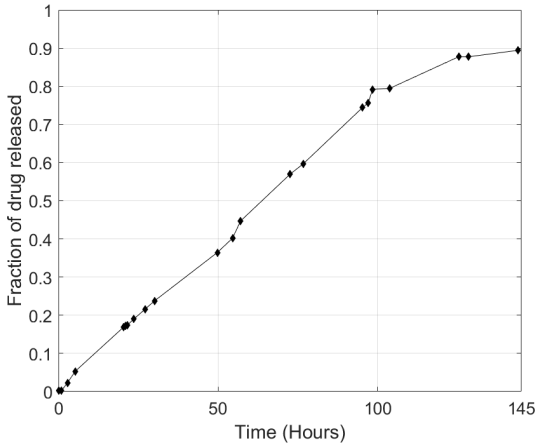

Figure 4.14: Plot showing the approximated drug release data.

Since all relevant model information is not available, it is useful to determine if the current model can replicate the experimental data through the determination of best-fitting parameters. A least squares approach is practical in this instance and the process involves solving the model numerically at the N number of time points (t_j) of the drug release data in Figure 4.14 and calculating the fraction of drug released $(M_{frac}(t_j))$. The experimental data $(E(t_j))$ can then be subtracted from the theoretical data of the same time point, then the squared difference between

the data points can be summed to give a measure of the error, the least squared error (LSE), for a given parameter value:

$$LSE = \sum_{j=1}^{N} \left(M_{frac}(t_j) - E(t_j) \right)^2 , \tag{4.138}$$

with a smaller summation meaning there is a closer agreement between the model and the experimental data. Equation (4.138) is the objective function and the desire is to minimise this function. In principle, several parameters can be fitted simultaneously. However, given the lack of data (one release profile with no error bars) and the linearity of the release profile, it was decided to focus instead on only two parameters, following from the results of the sensitivity analysis. This particular objective function is quadratic and there exists a value of the parameter of interest such that equation (4.138) is minimised. The "Parameter Sweep" functionality within COMSOL®, version 5.3a, was used to calculate $M_{frac}(t_j)$ over the range $0.04 \leq S^* \leq 0.05$, divided into 101 equally spaced points. Then equation (4.138) was used to calculate the LSE. From the results of the sensitivity analysis, drug solubility has a more significant influence on the release profile when compared to the other parameters and since parameters are grouped together in the nondimensional model, S^* was the first parameter to undergo the least squares fitting process, with the other parameters fixed at the baseline values. The results of the fitting process are shown in Figure 4.15.

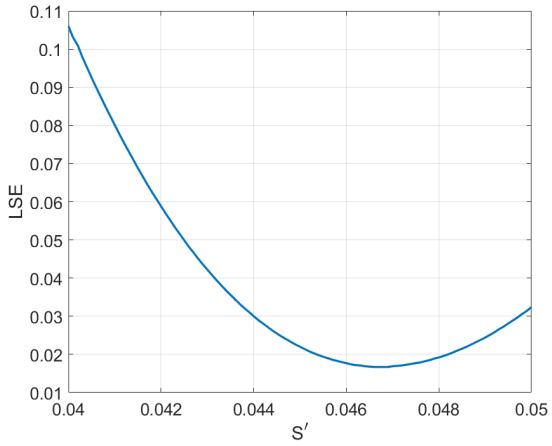

Figure 4.15: Example plot showing the output of the objective function (4.138) when determining the best fit value for S^*. The minimum shown in the plot indicates which value of S^*, in the range of values considered, provides the best fit to the experimental data.

The value of S^*, to three significant digits, which minimises the objective function (4.138), and hence, provides the best fit to the experimental data, was found to be 0.0468. Using this value of S^*, the procedure was repeated to find the best fitting second Damköhler number, Da_{II}, which was found to be 1.48. Using these parameter values, a release profile was generated and the results plotted alongside the experimental data (Figure 4.16).

The results suggest that the model is broadly capable of replicating drug release profile of

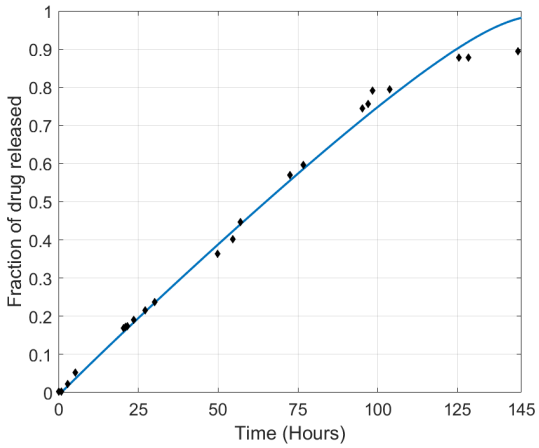

Figure 4.16: Plot showing the best fitting release profile compared to the experimental data.

the porous pin for most of the release duration, with only the end of the release process not being captured fully. A multi-objective optimisation, where fitting is performed for several parameters simultaneously (such as D_f, b_0, ϕ_e) may provide a closer fit to the data. However, this was deemed unnecessary for the following reasons: A mathematical model can only ever be as accurate as its inputs. There are many questions left unanswered from the work of Gimeno et al. [11] and not all information related to the experimental protocol is given in the publication, some of which is crucial to any mathematical modelling attempt. Arguably the most crucial issues are the uncertain masses of drug used in the release experiments and the lack of details of the vessel in which the release medium is contained. Without full knowledge of the mass of drug used and of the geometry of the release medium, the accuracy of any model relative to the experimental setup suffers. The experimental results suggest that full release was not achieved for the porous pin. This could be due to a variety of reasons, but more likely through a combination of drug solubility and an insufficient volume of release media. Therefore, the mass of drug used and the geometric details of the release medium container are necessary. The necessity of accurate geometric information is evidenced by Figure 4.11 (b), which shows that the drug release profile may be influenced by the length scale of the release medium.

4.3.5 Discussion

The commercial Linezolid used in the experiments (Zyvox®) is composed of many other components, not just the active ingredient, and these other components may have wildly different diffusivities and solubilities, for example. This is highlighted by the fact that each mL of prepared pharmacological solution contains just $2\,\mathrm{mg}$ of Linezolid, but it also contains $45.7\,\mathrm{mg}$ of glucose and $0.38\,\mathrm{mg}$ of sodium hydroxide [11]. In other words, most of the product is in fact glucose. This mix of different compounds makes the modelling process very challenging and assumptions have had to be made, specifically, the drug is only composed of the active ingredi-

ent and so the solubility refers to the Linezolid, not the Zyvox®. Another problem is the lack of information on drug solubilities in SBF. The solubility of the commercial drug used is reported as $3\,\mathrm{mg/mL}$, however, this is the solubility of the drug in water [11]. The SBF used as the release medium in the experiments contains a variety of ions, which of course have an electrical charge, which may influence the solubility of a drug. Additionally, the diffusivity of the drug in SBF is also unknown.

These issues cast unnecessary uncertainty with model parameters and so more assumptions must be made, reducing the usefulness of the model. Thus, as much knowledge of the experimental setup as possible is necessary when constructing a mathematical model and this example serves to highlight that the research area of drug delivery should be a multidisciplinary endeavour. Experimentalists must be able to discuss with theorists, and vice versa, to ensure that any mathematical model of drug release from a particular device has as few assumptions as possible and to keep uncertainty in parameter values and model results, to a minimum.

4.3.6 Conclusions

This chapter describes the mathematical modelling procedure undertaken to model drug release from a prototype drug-releasing porous fixation pin developed by Gimeno et al. [11]. The modelling process began with an initial 3D diffusion model and through numerical testing, it was concluded that a 1D mathematical modelling approach was sufficient. This is due to the symmetrical geometry of the porous pin and also due to the insignificant influence fluid flow has on the release of drug from the pin. Due to the cylindrical shape of the porous pin, the next step in the modelling methodology was to derive a 1D diffusion model based on the radial coordinate and obtain a semi-analytical solution. With the solution found, it was realised that this model would not be sufficient and that another key process in the release of drug from the porous pin was absent. It was believed that the missing model component was the dissolution process, this is evidenced by the fact that the drug used in the release experiments was loaded into the porous pins as a dry powder. The constructed model was used to carry out a sensitivity analysis to determine the influence the system parameters have on the release profile. Subsequently, the model was subjected to a least squares process to determine the values of two key nondimensional parameters that would allow the model to best replicate the experimental data. Lastly, the model performance was discussed with reference to the details of the experiment provided by Gimeno et al. [11].

Chapter 5

Modelling drug release from hollow orthopaedic pins with orifices

The previous chapter studied the theoretical release of drug from a porous pin. The device was chosen as porosity is a popular method of controlling drug release in experiments. Since it was concluded that fluid flow will produce an insignificant advective component to the transport within and out of the pin, coupled with symmetry, drug release was described with a 1D dissolution-diffusion model. In this chapter, a different prototype pin studied by Gimeno et al. [12] is examined and the methodology required to model release of drug from this device is explored.

The pin in question is a stainless steel medical grade tube of length $25\,\mathrm{mm}$, an outer diameter of $6\,\mathrm{mm}$ and a wall thickness of $1.6\,\mathrm{mm}$, with a hollow interior to enable a reservoir of drug for delivery. Four versions of this pin were used in the experiments, each with a differing number (2, 4, 6 or 8) of equidistant orifices of diameter $0.5\,\mathrm{mm}$ (Figure 5.1). The orifices are made by drilling the body of the pin, through to the opposite side, doubling the number of orifices. The drug-release experiments were conducted in triplicate and the pins were loaded with commercial linezolid (Zyvox®) or cefazolin sodium (Cefazolina Normon®) and submerged in $200\,\mathrm{mL}$ of SBF, stirred at $30\,\mathrm{RPM}$ ($\pi\,\mathrm{rad/s}$). The aim of this chapter is to devise a mathematical model of drug release from the orifice pin by Gimeno et al. (Figure 5.1 [12]), conduct a sensitivity analysis on the various system parameters and how they influence the release profile.

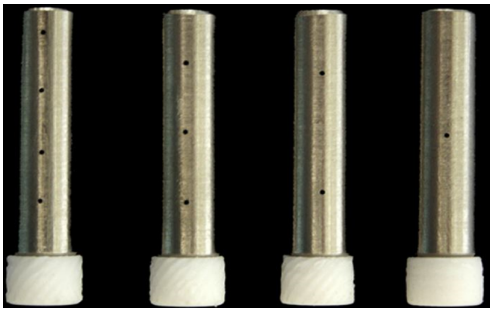

Figure 5.1: The pins used by Gimeno et al. [12] in the drug release and bactericidal experiments.

In chapter 4, it was initially not clear if fluid flow would have a notable impact on the release of drug from the porous pin, due to the small pore sizes of the pin's porous wall. However, a thorough mathematical investigation demonstrated that fluid flow had a negligible influence on the release of drug from the porous pin. Although in this chapter, the orifice pins have a mostly solid wall, impervious to fluid ingress, the orifices themselves are much larger ($0.5\,\mathrm{mm}$) than any pore in the wall of the porous pin (on the order of $10\,\mu\mathrm{m}$). Therefore, it is reasonable to suspect that fluid flow may have an appreciable influence on the release of drug from the orifice pins.

5.1 Influence of fluid flow on drug release from hollow orthopaedic pins with orifices

To be able to model the behaviour of the release medium fluid, important information is required, such as the properties of the fluid and accurate geometric details. The release medium used in the experiments is SBF, however, there is no source for parameter values of the physical properties of SBF, such as density and kinematic viscosity. Therefore, for all simulations, the release medium is assumed to be water. The dimensions of the orifice pins are provided within the publication of Gimeno et al. [12]. However, the type of release medium vessel is not. Following correspondence with the authors, it was revealed that the release medium and the drug-loaded orifice pins were contained within $250\,\mathrm{mL}$ conical flasks, whose dimensions are available from the manufacturer [69]. The experimental setups are atop rotating plates, which agitates the release media. It would be useful to gain an understanding of how the fluid is likely to behave in the orifice pins and to determine if fluid is able to flow in and out of the pins via the orifices or produce a velocity field like the cavity flow problem, for example [70]. To approximate the flow conditions, it is assumed that the outer boundary, Γ_1, shown in Figure 5.2 (a), is rotating, which will provide the driving force to the release medium such that it flows and will have velocity field $\boldsymbol{u} = (u_x, u_y, u_z)$. It should be noted that the θ and r shown in in Figure 5.2 (a), are not model variables, they are separately defined within COMSOL Multiphysics®, version 5.3a, to setup a moving wall boundary condition.

The following model is used to describe the motion of the release medium and is applied to the geometries for the two cases considered i.e. the 2 and 8-orifice pins. Only these two orifice configurations were investigated as they are the extreme cases and it can be reasoned that any results from a study of the 4 and 6-orifice pins would lie somewhere between the 2 and 8-orifice pins. Although the release medium vessel is a conical flask, only the volume occupied by the release medium is required and so the neck of the conical flask is not present. Figure 5.2 (a) shows the geometry used for all simulations in this chapter, albeit for a change in the number of orifices to represent the pin configuration i.e. 2 orifices instead of 8.

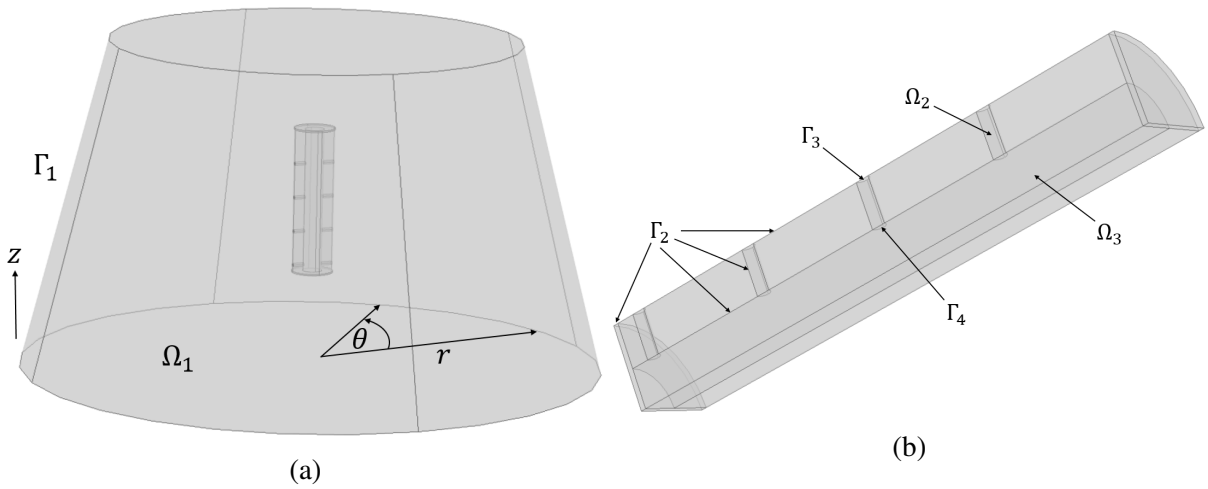

(a) (b)

Figure 5.2: (a) Geometry of the 8-orifice pin. The release medium fluid is represented by Ω_1, the set of orifices of the pin are denoted by Ω_2 and the inner drug core of the pin is designated Ω_3. The set of boundaries of the release medium are collectively represented by Γ_1. Spatial variables x and y extend outward from the central z-axis to the outer wall of the geometry. Spatial variable z is the height from the centre of the bottom boundary to the centre of the top boundary of Γ_1, with the positive direction shown alongside. Although not variables, it is useful to define two additional components: r is the radius from the central z-axis to the outer wall and θ is the angle which Ω_1 makes with respect to its original position as it rotates. (b) A close-up of a segment of the 8-orifice pin to more clearly show the drug core and the orifices, which go through the casing of the pin. Γ_2 represents the entire surface area of the pin, including the cylindrical walls of the orifices in each pin configuration. Additionally, Γ_3 and Γ_4 are the collection of the circular boundaries at the endpoints of the orifices, that connect the domains Ω_1 to Ω_2 and Ω_2 to Ω_3, respectively.

The model for describing fluid flow in the release medium is:

$$\nu\nabla^2\boldsymbol{u} - (\boldsymbol{u}\cdot\nabla)\,\boldsymbol{u} - \frac{1}{\rho}\nabla p = 0, \quad \nabla\cdot\boldsymbol{u} = 0, \quad \text{in } \Omega_1, \Omega_2 \text{ and } \Omega_3, \tag{5.1}$$

$$\boldsymbol{u} = (-r\sin(\theta), r\cos(\theta), 0)\,u, \quad \text{on } \Gamma_1, \tag{5.2}$$

$$\boldsymbol{u} = \boldsymbol{0}, \quad \text{on } \Gamma_2, \tag{5.3}$$

$$p = 0, \quad \text{at an arbitrary point.} \tag{5.4}$$

The model consists of the stationary form of the incompressible Navier-Stokes and the continuity equations (5.1), where ρ is the fluid density, p is the pressure and ν is the kinematic viscosity of the fluid. On the boundary Γ_1, a moving wall boundary condition (5.2) is applied, in which u is the magnitude of the angular velocity of the rotating wall in $\mathrm{rad/s}$, the angular velocity used in the simulations is $\pi\,\mathrm{rad/s}$. This condition ensures that the fluid at this boundary, takes the wall's angular velocity, this is the driving force behind the fluid flow. A no-slip/no-penetration boundary condition (5.3) is applied to the collection of boundaries that comprise the body of the pin, denoted by Γ_2. Since pressure is not specified explicitly on a boundary, a

pressure point constraint (5.4) is required and is applied to an arbitrary point to allow the numerical scheme to find a solution. The model was solved using COMSOL Multiphysics®, version 5.3a, specifically, the GMRES method was used to obtain the stationary solution. The built-in software meshing tools were used to create a tetrahedral element-based mesh using the "Normal" element size, calibrated for "Fluid Dynamics" physics (Figure 5.3). To determine if this mesh was suitable, a finer mesh setting was also used, however, no appreciable difference in the velocity field was found using this denser mesh.

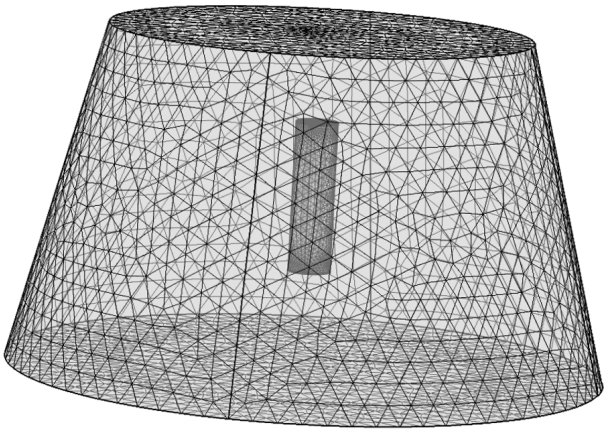

Figure 5.3: FEM mesh generated for the 3D 8-orifice pin geometry for the influence of flow study. Mesh consists of $217,071$ domain elements, $10,434$ boundary elements, and 928 edge elements. A similar mesh for the 2-orifice pin was also created which consisted of $178,296$ domain elements, 9050 boundary elements, and 728 edge elements.

The results shown in Figure 5.4, suggest that fluid flow into the orifice pins can occur and does not produce the velocity field pattern associated with the cavity flow problem [70]. Indeed, flow out of the pin was also shown to be possible. Although the velocity of the fluid in the orifices and the inner bulk domain of the pins is slow, in the order of $10^{-5}\,\mathrm{m/s}$, it is present and it may have a significant effect on the release of a drug from these pins. Interestingly, there is a region of recirculation in Figure 5.4 (b), which in principle, could trap drug particles within its cycle. Although in theory the release medium is able to flow in and out of the orifice pins, another important question is whether the flow is able to provide a significant advective component to the transport of a drug. To determine the influence of the flowing release medium, Péclet numbers are calculated based upon average fluid velocity magnitudes in each region:

$$Pe_{\Omega_1} = \frac{u_{\Omega_1} L_r}{D_f}, \quad Pe_{\Omega_2} = \frac{u_{\Omega_2} L_o}{D_f}, \quad Pe_{\Omega_3} = \frac{u_{\Omega_3} L_d}{D_f},$$

where u_{Ω_1}, u_{Ω_2} and u_{Ω_3} are the average velocity magnitudes in each domain and D_f is the free-diffusion coefficient. The length scales required to compute the Péclet numbers are L_r, L_o and L_d, which are the average radius of the release medium, the length of the orifices and the radius of the inner drug core, respectively. Although no drug transport is present in this simulation, it is assumed that $D_f = 10^{-9}\,\mathrm{m}^2/\mathrm{s}$, which is regarded as an upper limit in the range of diffusion

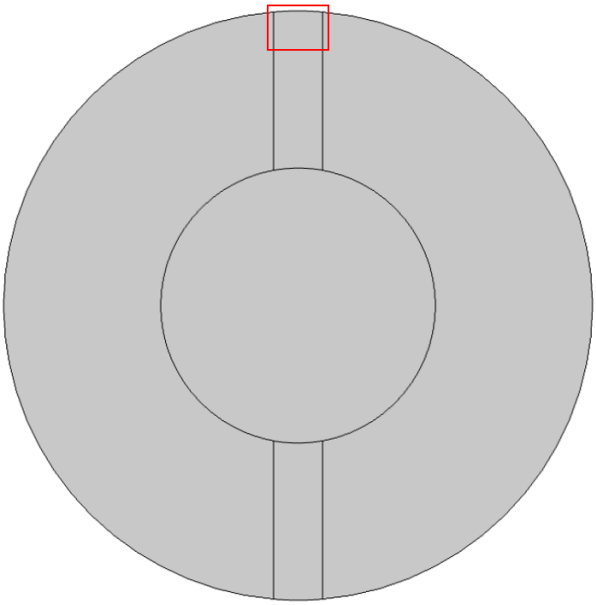

(a)

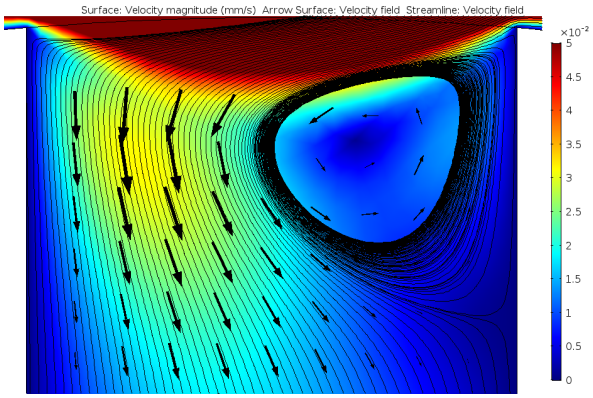

(b)

Figure 5.4: (a) A horizontal cross-sectional slice through the centre of the top pair of orifices of the 8-orifice pin. (b) Image of the velocity field within the red box region of the cross-sectional slice.

coefficient of solutes [61]. Therefore, if the advective component of drug transport is significant when compared to the upper limit of diffusivity of a solute, then it is likely important for all solute diffusion coefficients.

Domain	2-Orifice Pin	8-Orifice Pin
Ω_1	2.81×10^6	2.81×10^6
Ω_2	13.75	26.37
Ω_3	2.26×10^{-4}	0.834

Table 5.1: Average Péclet numbers within each domain for the 2 and 8-orifice pins.

Table 5.1 shows the average Péclet numbers for the different domains: the bulk release medium (Ω_1), the orifices (Ω_2) and the drug core of the pin (Ω_3). These Péclet numbers suggest that with an increasing number of orifices, there is a stronger velocity field throughout the pin. This is what one may expect to be the case since, with more open channels (orifices), the release medium will be more freely able to penetrate the pin and thus generate a more significant velocity field. The most noticeable difference lies in the Péclet numbers for the drug cores, with the 8-orifice pin showing a three orders of magnitude increase in the Péclet number when compared to the 2-orifice pin. Again, one can attribute this increase of Péclet number to the greater ease of access the fluid has with the 8-orifice pin.

Since the model demonstrates that fluid flow is likely a key component to the release of drug

from the orifice pins, due its appreciable influence compared to diffusion, it is wise to provide evidence that this is in fact the case. The concentration of drug in the solute phase, in each domain, is defined as $c_i(x, y, z, t)$, where $i = \Omega_1, \Omega_2, \Omega_3$. To model the potential influence of fluid flow on the release of drug, the following model was devised:

$$\frac{\partial c_{\Omega_1}}{\partial t} = D_f \nabla^2 c_{\Omega_1} - \boldsymbol{u} \cdot \nabla c_{\Omega_1}, \quad \text{in } \Omega_1, \quad t > 0, \tag{5.5}$$

$$\frac{\partial c_{\Omega_2}}{\partial t} = D_f \nabla^2 c_{\Omega_2} - \boldsymbol{u} \cdot \nabla c_{\Omega_2}, \quad \text{in } \Omega_2, \quad t > 0, \tag{5.6}$$

$$\frac{\partial c_{\Omega_3}}{\partial t} = D_f \nabla^2 c_{\Omega_3} - \boldsymbol{u} \cdot \nabla c_{\Omega_3}, \quad \text{in } \Omega_3, \quad t > 0, \tag{5.7}$$

$$\frac{\partial \boldsymbol{u}}{\partial t} = \nu \nabla^2 \boldsymbol{u} - (\boldsymbol{u} \cdot \nabla)\, \boldsymbol{u} - \frac{1}{\rho} \nabla p, \quad \nabla \cdot \boldsymbol{u} = 0, \quad \text{in } \Omega_1, \Omega_2 \text{ and } \Omega_3, \quad t > 0, \tag{5.8}$$

where the free-diffusion coefficient, D_f, is assumed to be constant and isotropic. These equations are coupled with the following boundary and initial conditions:

$$\hat{\boldsymbol{n}} \cdot (-D_f \nabla c_{\Omega_3} + c_{\Omega_3} \boldsymbol{u}) = 0, \quad \boldsymbol{u} = (-r \sin(\theta), r \cos(\theta), 0)\, u, \quad \text{on } \Gamma_1, \quad t > 0, \tag{5.9}$$

$$-\hat{\boldsymbol{n}} \cdot D_f \nabla c_{\Omega_1} = 0, \quad -\hat{\boldsymbol{n}} \cdot D_f \nabla c_{\Omega_2} = 0,$$

$$-\hat{\boldsymbol{n}} \cdot D_f \nabla c_{\Omega_3} = 0, \quad \boldsymbol{u} = \boldsymbol{0}, \quad \text{on } \Gamma_2, \quad t > 0, \tag{5.10}$$

$$c_{\Omega_1} = c_{\Omega_2}, \quad \hat{\boldsymbol{n}} \cdot (-D_f \nabla c_{\Omega_1} + c_{\Omega_1} \boldsymbol{u}) = \hat{\boldsymbol{n}} \cdot (-D_f \nabla c_{\Omega_2} + c_{\Omega_2} \boldsymbol{u}), \quad \text{on } \Gamma_3, \quad t > 0, \tag{5.11}$$

$$c_{\Omega_2} = c_{\Omega_3}, \quad \hat{\boldsymbol{n}} \cdot (-D_f \nabla c_{\Omega_2} + c_{\Omega_2} \boldsymbol{u}) = \hat{\boldsymbol{n}} \cdot (-D_f \nabla c_{\Omega_3} + c_{\Omega_3} \boldsymbol{u}), \quad \text{on } \Gamma_4, \quad t > 0, \tag{5.12}$$

$$p = 0, \quad \text{at an arbitrary point}, \quad t \geq 0, \tag{5.13}$$

$$c_{\Omega_3} = c_0, \quad \text{in } \Omega_3, \quad c_{\Omega_2} = 0, \quad \text{in } \Omega_2, \quad c_{\Omega_1} = 0, \quad \text{in } \Omega_1, \quad t = 0, \tag{5.14}$$

$$\boldsymbol{u} = \boldsymbol{0}, \quad \text{in } \Omega_1,\ \Omega_2 \text{ and } \Omega_3, \quad t = 0. \tag{5.15}$$

The above model consists of advection-diffusion equations (5.5-5.7) and the incompressible forms of the Navier-Stokes and continuity equations (5.8). In applicable boundary conditions, $\hat{\boldsymbol{n}}$ is the outward facing unit normal appropriate for each of the surfaces. Zero-flux and moving wall boundary conditions (5.9) are applied to Γ_1. Zero-flux and no-slip/no-penetration conditions (5.10) are applied to Γ_2. Continuity of concentration and flux boundary conditions are applied to Γ_3 and Γ_4 (5.11-5.12). A pressure point constraint (5.13) is applied to an arbitrary point of the geometry. There is a non-uniform initial drug concentration condition set (5.14), where $c_{\Omega_3} = c_0$ and $c_{\Omega_2} = c_{\Omega_1} = 0$, initially. Additionally, the release medium fluid is at rest initially (5.15). With a view to reduce computational cost, the impact of replacing the time-dependent fluid equations with the corresponding steady solution was also assessed. The model can be nondimensionalised with the following scalings:

$$c_i' = \frac{c_i}{c_0}, \quad x' = \frac{x}{L_d}, \quad y' = \frac{y}{L_d}, \quad z' = \frac{z}{L_d}, \quad t' = \frac{D}{L_d^2} t, \quad \boldsymbol{u'} = \frac{L_d}{D_f} \boldsymbol{u}, \quad p' = \frac{L_d^2}{\rho D_f^2} p,$$

where $i = \Omega_1, \Omega_2, \Omega_3$. These scalings result in the following nondimensional model (dropping the primes for clarity):

$$\frac{\partial c_{\Omega_1}}{\partial t} = \nabla^2 c_{\Omega_1} - \boldsymbol{u} \cdot \nabla c_{\Omega_1}, \quad \text{in } \Omega_1, \quad t > 0, \tag{5.16}$$

$$\frac{\partial c_{\Omega_2}}{\partial t} = \nabla^2 c_{\Omega_2} - \boldsymbol{u} \cdot \nabla c_{\Omega_2}, \quad \text{in } \Omega_2, \quad t > 0, \tag{5.17}$$

$$\frac{\partial c_{\Omega_3}}{\partial t} = \nabla^2 c_{\Omega_3} - \boldsymbol{u} \cdot \nabla c_{\Omega_3}, \quad \text{in } \Omega_3, \quad t > 0, \tag{5.18}$$

$$\frac{\partial \boldsymbol{u}}{\partial t} = Sc \nabla^2 \boldsymbol{u} - (\boldsymbol{u} \cdot \nabla)\, \boldsymbol{u} - \nabla p, \quad \nabla \cdot \boldsymbol{u} = 0, \quad \text{in } \Omega_1, \Omega_2 \text{ and } \Omega_3, \quad t > 0, \tag{5.19}$$

where Sc is the Schmidt number and is equal to ν / D_f, which is the ratio of the viscous diffusion rate to mass diffusion rate. The nondimensional equations are coupled with the following nondimensional boundary and initial conditions:

$$\hat{\boldsymbol{n}} \cdot (-\nabla c_{\Omega_3} + c_{\Omega_3} \boldsymbol{u}) = 0, \quad \boldsymbol{u} = \frac{L_d^2}{D_f} \left(-r \sin(\theta), r \cos(\theta), 0\right) u, \quad \text{on } \Gamma_1, \quad t > 0, \tag{5.20}$$

$$\hat{\boldsymbol{n}} \cdot \nabla c_{\Omega_1} = 0, \quad \hat{\boldsymbol{n}} \cdot \nabla c_{\Omega_2} = 0, \quad \hat{\boldsymbol{n}} \cdot \nabla c_{\Omega_3} = 0, \quad \boldsymbol{u} = \boldsymbol{0}, \quad \text{on } \Gamma_2, \quad t > 0, \tag{5.21}$$

$$c_{\Omega_1} = c_{\Omega_2}, \quad \hat{\boldsymbol{n}} \cdot (-\nabla c_{\Omega_1} + c_{\Omega_1} \boldsymbol{u}) = \hat{\boldsymbol{n}} \cdot (-\nabla c_{\Omega_2} + c_{\Omega_2} \boldsymbol{u}), \quad \text{on } \Gamma_3, \quad t > 0, \tag{5.22}$$

$$c_{\Omega_2} = c_{\Omega_3}, \quad \hat{\boldsymbol{n}} \cdot (-\nabla c_{\Omega_2} + c_{\Omega_2} \boldsymbol{u}) = \hat{\boldsymbol{n}} \cdot (-\nabla c_{\Omega_3} + c_{\Omega_3} \boldsymbol{u}), \quad \text{on } \Gamma_4, \quad t > 0, \tag{5.23}$$

$$p = 0, \quad \text{at an arbitrary point}, \quad t \geq 0, \tag{5.24}$$

$$c_{\Omega_3} = 1, \quad \text{in } \Omega_3, \quad c_{\Omega_2} = 0, \quad \text{in } \Omega_2, \quad c_{\Omega_1} = 0, \quad \text{in } \Omega_1, \quad t = 0, \tag{5.25}$$

$$\boldsymbol{u} = \boldsymbol{0}, \quad \text{in } \Omega_1,\ \Omega_2 \text{ and } \Omega_3, \quad t = 0. \tag{5.26}$$

The model (5.16-5.26) was solved using COMSOL Multiphysics®, version 5.3a. The GMRES method was used to obtain the solutions of the time-dependent, stationary and purely diffusive models. To aid in conservation of mass, equations (5.16-5.18) were solved in conservative form, which reduced the error in mass conservation to $\ll 1\,\%$. The software assumes continuity of concentration and flux across boundaries, therefore, boundary condition sets (5.22-5.23) are not required to be explicitly implemented. The same meshes used to determine fluid flow behaviour (Figure 5.3) in the 2 and 8-orifice pins were also used in this study. Preliminary simulations demonstrated that a mesh of a density greater than these meshes had a negligible influence on the release profile. To illustrate the results, the release profile was calculated and if fluid flow has an appreciable effect on the release of drugs from the orifice pins, then the release profiles for the simulations including the time-dependent and stationary velocity fields, will be markedly different from the release profile from the diffusion-only model.

5.1.1 Equations for mass of drug

The dimensional equations for the mass of drug in each region are:

$$M_{\Omega_1}(t) = \int_{\Omega_1} c_{\Omega_1}\, d\Omega_1, \quad M_{\Omega_2}(t) = \int_{\Omega_2} c_{\Omega_2}\, d\Omega_2, \quad M_{\Omega_3}(t) = \int_{\Omega_3} c_{\Omega_3}\, d\Omega_3,$$

where $d\Omega_j = dxdydz$, with $j = 1, 2, 3$. The equations for mass can be normalised with M^0, the initial drug mass. As this is a purely numerical investigation, not only are the drug masses in each region approximated, but so too is the initial drug mass, which can be calculated via the integral:

$$M^0 = c_0 \int_{\Omega_3} d\Omega_3.$$

Using the nondimensional scalings, the normalised equations for mass are:

$$\frac{M_{\Omega_1}(t)}{M^0} = \frac{c_0 L_d^3 \int_{\Omega_1'} c'_{\Omega_1}\, d\Omega_1'}{c_0 L_d^3 \int_{\Omega_3'} d\Omega_3'}, \quad \frac{M_{\Omega_2}(t)}{M^0} = \frac{c_0 L_d^3 \int_{\Omega_2'} c'_{\Omega_2}\, d\Omega_2'}{c_0 L_d^3 \int_{\Omega_3'} d\Omega_3'}, \quad \frac{M_{\Omega_3}(t)}{M^0} = \frac{c_0 L_d^3 \int_{\Omega_3'} c'_{\Omega_3}\, d\Omega_3'}{c_0 L_d^3 \int_{\Omega_3'} d\Omega_3'}.$$

Simplifying and dropping the primes for clarity:

$$\frac{M_{\Omega_1}(t)}{M^0} = \frac{\int_{\Omega_1} c_{\Omega_1}\, d\Omega_1}{\int_{\Omega_3} d\Omega_3}, \quad \frac{M_{\Omega_2}(t)}{M^0} = \frac{\int_{\Omega_2} c_{\Omega_2}\, d\Omega_2}{\int_{\Omega_3} d\Omega_3}, \quad \frac{M_{\Omega_3}(t)}{M^0} = \frac{\int_{\Omega_3} c_{\Omega_3}\, d\Omega_3}{\int_{\Omega_3} d\Omega_3}.$$

5.1.2 Release profile

The release profile may be calculated through the mass of drug lost from the orifice pins:

$$\begin{aligned} M_{frac}(t) &= \frac{M^0 - (M_{\Omega_2}(t) + M_{\Omega_3}(t))}{M^0} = 1 - \frac{M_{\Omega_2}(t) + M_{\Omega_3}(t)}{M^0}, \\ &= 1 - \frac{\int_{\Omega_2} c_{\Omega_2}\, d\Omega_2 + \int_{\Omega_3} c_{\Omega_3}\, d\Omega_3}{\int_{\Omega_3} d\Omega_3}. \end{aligned}$$

The simpler method to calculate the release profile is to determine the mass which accumulates in the release medium

$$M_{frac}(t) = \frac{M_{\Omega_1}(t)}{M^0} = \frac{\int_{\Omega_1} c_{\Omega_1}\, d\Omega_1}{\int_{\Omega_3} d\Omega_3}. \tag{5.27}$$

Figure 5.5 shows the extremes of the potential influence of fluid flow on drug release from

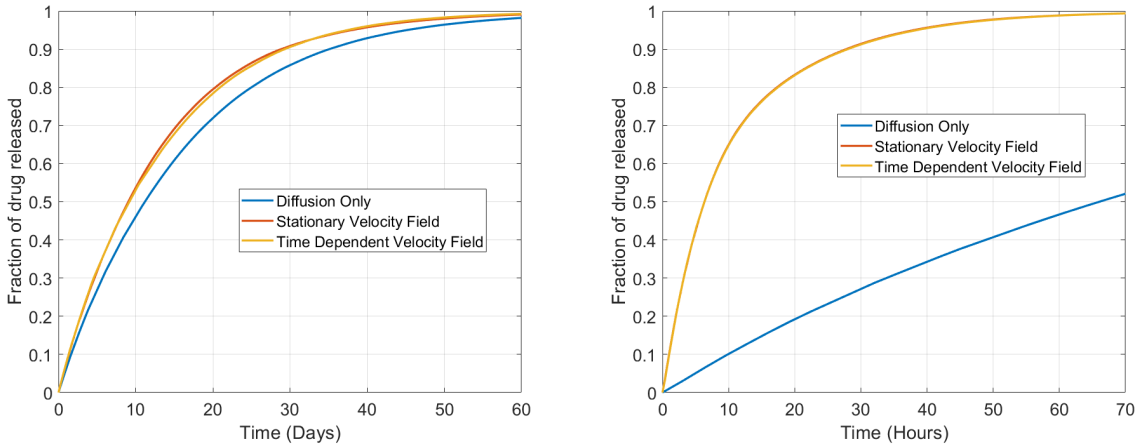

(a) (b)

Figure 5.5: (a) Plot showing the effect of including fluid flow for the 2-orifice pin case compared to a purely diffusive problem, with $D_f = 10^{-9}\,\mathrm{m}^2/\mathrm{s}$. (b) Plot showing the effect of including fluid flow for the 8-orifice pin case compared to a purely diffusive problem, with $D_f = 10^{-9}\,\mathrm{m}^2/\mathrm{s}$.

the orifice pins. The release profiles were calculated using equation (5.27). As expected, with more orifices, fluid flow has a greater impact on the drug release. This is likely due to the fluid having more open channels to enter the 8-orifice pin, than the more constrictive 2-orifice pin. One can quantify this via Péclet numbers: the average Péclet number in the orifices are 13.75 and 26.37 for the 2 and 8-orifice pins, respectively. However, within the cores of the orifice pins, the average Péclet numbers are substantially smaller: 2.26×10^{-4} and 0.834 for the 2 and 8-orifice pins, respectively. These numbers align themselves with what the expected behaviour would be, that is that fluid flow is significantly more influential in the release of drugs from the orifice pins as the number of orifices increases. This behaviour is also apparent from the difference in the timescales, with the 2-orifice pin requiring days for complete release and the 8-orifice pin only requiring hours. The results also show that using a stationary velocity field as input for the advection-diffusion equation is sufficient and has the benefit of being less computationally intensive.

5.1.3 Comparison with Taylor-Couette flow

There exists a potential avenue of simplification when including the effects of fluid flow on drug release from the orifice pins and that is to consider the similarity of the flow to Taylor-Couette (TC) flow. TC flow concerns the problem of fluid flow between two, concentric, rotating cylinders [71, 72], as shown in Figure 5.6. The problem was investigated experimentally by Couette [73], as a method to measure viscosity, and then mathematically by Taylor [74], who investigated the stability of a viscous fluid between two rotating cylinders. The problem can be solved analytically with some assumptions: the flow between the cylinders is incompressible

and steady i.e. has no time-dependence, the flow does not change in the axial (z-axis) direction and the flow is angularly symmetric.

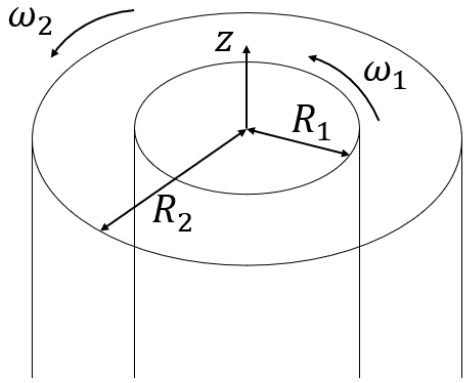

Figure 5.6: Illustration of the Taylor-Couette problem.

The inner and outer cylinders have rotational velocities ω_1 and ω_2, respectively. The fluid in the system is contained within the gap between the inner and outer cylinders, which have radii R_1 and R_2, respectively. Defining the fluid velocity field as $\boldsymbol{u} = (u_r, u_\theta, u_z)$, after simplification of the Navier-Stokes and continuity equations, the problem can be described by the ODE [75, p. 44]:

$$r^2 \frac{d^2 u_\theta}{dr^2} + r \frac{du_\theta}{dr} - u_\theta = 0,$$

which has the solution:

$$u_\theta = Ar + \frac{B}{r}, \quad A = \frac{\omega_2 R_2^2 - \omega_1 R_1^2}{R_2^2 - R_1^2}, \quad B = \frac{(\omega_1 - \omega_2)\, R_1^2 R_2^2}{R_2^2 - R_1^2}. \tag{5.28}$$

Using model equations (5.1-5.4) to compute the stationary solution for the 8-orifice pin geometry, the results may be compared to the velocities computed by analytical solution (5.28). Since the analytical solution is only applicable to problems where the cylinders are of constant radius, a compromise must be made since the geometry for the orifice pin setups feature an approximation of a conical flask. Therefore, for use in the analytical solution, the outer cylinder radius, R_2, will be the average radius of the conical flask geometry i.e. $R_2 = 36.25\,\mathrm{mm}$. Additionally, the radius of the inner cylinder, R_1, will be the radius of the orifice pin, therefore, $R_1 = 3\,\mathrm{mm}$. Also, $\omega_1 = 0$ and $\omega_2 = \pi\,\mathrm{rad/s}$, since it is assumed that only the conical flask component of the orifice pin setup is rotating. To compare the numerical and analytical solutions, a 1D line was added to the geometry within COMSOL Multiphysics®, version 5.3a. These lines extend from the outer wall of the orifice pin to the sloped wall of the release medium geometry. The velocity magnitudes of the solution on these lines were then plotted alongside the velocity magnitudes calculated by analytical solution (5.28).

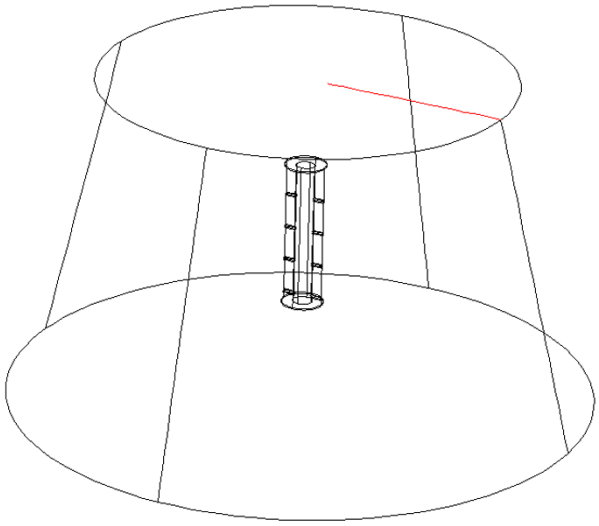

(a)

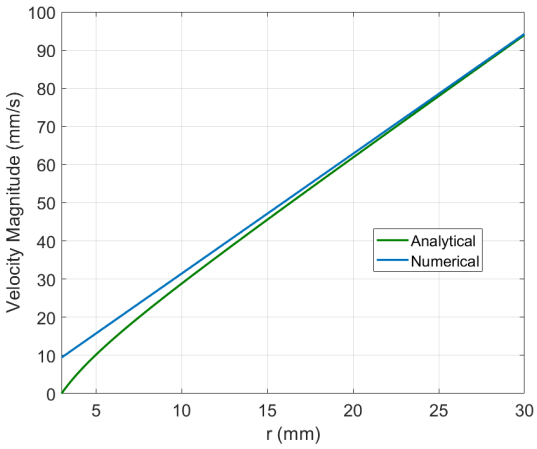

(b)

Figure 5.7: (a) Wireframe rendering of the geometry, with the solution line on the upper-most boundary of the geometry. (b) Plot showing both the analytical and numerical solutions along the red line.

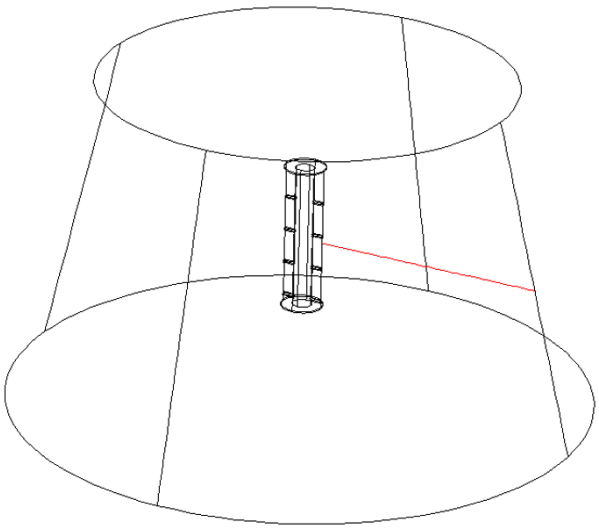

(a)

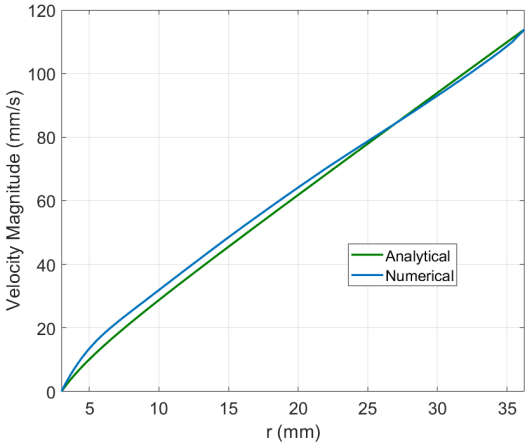

(b)

Figure 5.8: (a) Wireframe rendering of the geometry, with the solution line at the centre of the height of the geometry. (b) Plot showing both the analytical and numerical solutions along the red line.

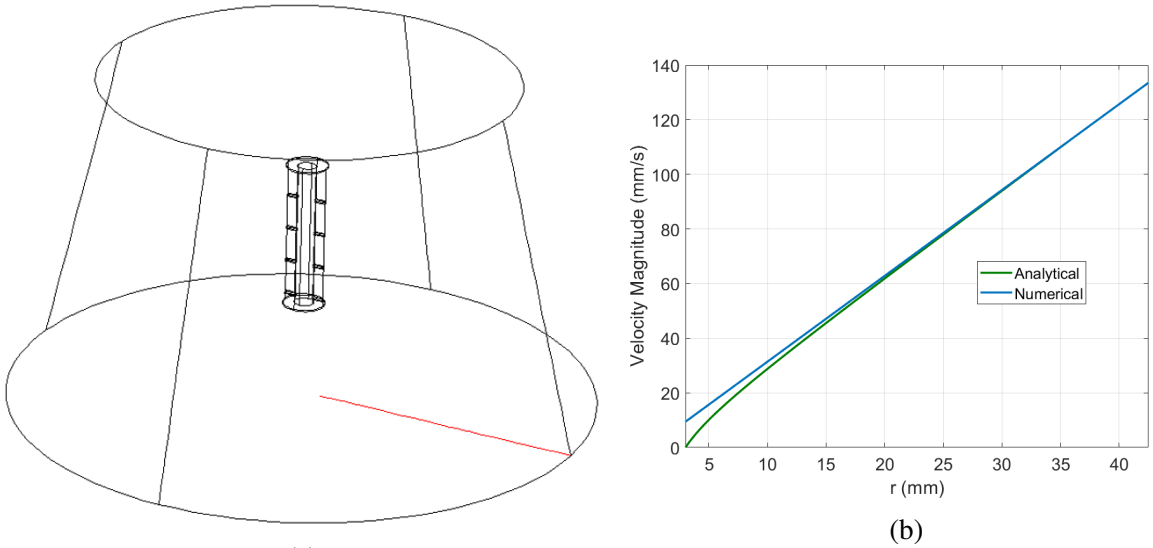

(a) (b)

Figure 5.9: (a) Wireframe rendering of the geometry, with the solution line on the base of the geometry. (b) Plot showing both the analytical and numerical solutions along the red line.

Figures 5.7-5.9 show a not unreasonable agreement between the analytical and numerical solutions for the velocity magnitudes on each line. The differences in the solutions are not unexpected since the orifice pin geometries do not represent the TC problem precisely. The orifice pins and the overall height of the release medium are not the same, for TC flow both cylinders are of the same height. Additionally, the cylinders featured in TC flow are of constant radius, whereas the release medium of the orifice pin geometry has sloped walls, due to the presence of a conical flask. These differences affect the magnitude of the deviation of the solutions. It is not surprising that both solutions take the same velocity magnitude at the outer wall/cylinder as the no-slip/no-penetration conditions ensure that both solutions take the velocity of the moving wall. However, when moving away from the outer wall/cylinder towards the orifice pin/inner cylinder, the solutions begin to diverge. This is also not unexpected as part of the TC problem includes that the rotating fluid does not penetrate the inner cylinder and thus the solution approaches zero when moving closer to the inner cylinder. However, the velocity field solution computed in the orifice pin simulation does not approach zero and it is reasonable to conclude that this is because the rotating fluid is able to penetrate the orifice pin. Based on the results, it may be a possible to simplify the implementation of a velocity field in future work. If this is not in fact possible, then perhaps a rough estimate of the influence the velocity field of the fluid has on the release of drugs may be made.

5.2 3D advection-diffusion-dissolution model

In reality, the drug loaded would likely be in a dry, solid form, such as in the case of the experiments by Gimeno et al. [12]. Their work featured two commercially available products, which

feature the antibiotics, Cefazolin Sodium and Linezolid, which the authors state have a solubility of $50\,\mathrm{mg/mL}$ and $3\,\mathrm{mg/mL}$, respectively. The results from their experiments suggest that solubility plays a major role in the release of the drugs from the pins and so should be accounted for in a proposed model. In addition to the assumption that the free-diffusion coefficient, D_f, is constant and isotropic, it is also assumed that the orifice pins are rapidly infiltrated by the release medium fluid and that the drug is fully wetted. This enables the dissolution process to begin throughout the drug core immediately and allows one to describe the dissolution process through an ODE, with the spatial dependence coming from the coupling to a PDE for dissolved drug concentration. The equations proposed to model mass transport of a drug, of concentration $b(x, y, z, t)$ and which must dissolve first, are as follows:

$$\frac{\partial b}{\partial t} = -\beta b^{\alpha} \left(S - c_{\Omega_3}\right), \quad \text{in } \Omega_3, \quad t > 0, \tag{5.29}$$

$$\frac{\partial c_{\Omega_1}}{\partial t} = D_f \nabla^2 c_{\Omega_1} - \boldsymbol{u} \cdot \nabla c_{\Omega_1}, \quad \text{in } \Omega_1, \quad t > 0, \tag{5.30}$$

$$\frac{\partial c_{\Omega_2}}{\partial t} = D_f \nabla^2 c_{\Omega_2} - \boldsymbol{u} \cdot \nabla c_{\Omega_2}, \quad \text{in } \Omega_2, \quad t > 0, \tag{5.31}$$

$$\frac{\partial c_{\Omega_3}}{\partial t} = D_f \nabla^2 c_{\Omega_3} - \boldsymbol{u} \cdot \nabla c_{\Omega_3} + \beta b^{\alpha} \left(S - c_{\Omega_3}\right), \quad \text{in } \Omega_3, \quad t > 0, \tag{5.32}$$

$$\nu \nabla^2 \boldsymbol{u} - \left(\boldsymbol{u} \cdot \nabla\right) \boldsymbol{u} - \frac{1}{\rho} \nabla p = 0, \quad \nabla \cdot \boldsymbol{u} = 0, \quad \text{in } \Omega_1, \Omega_2 \text{ and } \Omega_3, \tag{5.33}$$

with the following boundary and initial conditions:

$$\hat{\boldsymbol{n}} \cdot \left(-D_f \nabla c_{\Omega_3} + c_{\Omega_3} \boldsymbol{u}\right) = 0, \quad \boldsymbol{u} = \left(-r \sin(\theta), r \cos(\theta), 0\right) u, \quad \text{on } \Gamma_1, \quad t > 0, \tag{5.34}$$

$$-\hat{\boldsymbol{n}} \cdot D_f \nabla c_{\Omega_1} = 0, \quad -\hat{\boldsymbol{n}} \cdot D_f \nabla c_{\Omega_2} = 0,$$

$$-\hat{\boldsymbol{n}} \cdot D_f \nabla c_{\Omega_3} = 0, \quad \boldsymbol{u} = \boldsymbol{0}, \quad \text{on } \Gamma_2, \quad t > 0, \tag{5.35}$$

$$c_{\Omega_1} = c_{\Omega_2}, \quad \hat{\boldsymbol{n}} \cdot \left(-D_f \nabla c_{\Omega_1} + c_{\Omega_1} \boldsymbol{u}\right) = \hat{\boldsymbol{n}} \cdot \left(-D_f \nabla c_{\Omega_2} + c_{\Omega_2} \boldsymbol{u}\right), \quad \text{on } \Gamma_3, \quad t > 0, \tag{5.36}$$

$$c_{\Omega_2} = c_{\Omega_3}, \quad \hat{\boldsymbol{n}} \cdot \left(-D_f \nabla c_{\Omega_2} + c_{\Omega_2} \boldsymbol{u}\right) = \hat{\boldsymbol{n}} \cdot \left(-D_f \nabla c_{\Omega_3} + c_{\Omega_3} \boldsymbol{u}\right), \quad \text{on } \Gamma_4, \quad t > 0, \tag{5.37}$$

$$p = 0, \quad \text{at an arbitrary point}, \quad t \geq 0, \tag{5.38}$$

$$b = b_0, \quad \text{in } \Omega_3, \quad t = 0, \tag{5.39}$$

$$c_{\Omega_3} = 0, \quad \text{in } \Omega_3, \quad c_{\Omega_2} = 0, \quad \text{in } \Omega_2, \quad c_{\Omega_1} = 0, \quad \text{in } \Omega_1, \quad t = 0. \tag{5.40}$$

Equation (5.29) is used to model the dissolution of the drug, similar to chapter 4, where S is the solubility of the drug in the release medium, β is the dissolution rate and α is the reaction exponent and determines the type of reaction. The advection-diffusion-reaction equation (5.32), models the transport of newly dissolved drug within Ω_3. The incompressible forms of the Navier-Stokes and continuity equations (5.33) are used to compute the stationary velocity field, to be used as input for the drug-transport equations of the model. Initially, $b = b_0$ in Ω_3 (5.39) and $c_{\Omega_1} = c_{\Omega_2} = c_{\Omega_3} = 0$ (5.40), since no drug has dissolved initially. The remaining compo-

nents of the model are identical to model equations (5.5-5.15), including boundary conditions. The model equations (5.29-5.40) are nondimensionalised with the following scalings:

$$c_i' = \frac{c_i}{S}, \quad b' = \frac{b}{b_0}, \quad x' = \frac{x}{L_d}, \quad y' = \frac{y}{L_d} \quad z' = \frac{z}{L_d},$$
$$t' = \frac{D}{L_d^2}t, \quad \boldsymbol{u'} = \frac{L_d}{D_f}\boldsymbol{u}, \quad p' = \frac{L_d^2}{\rho D_f^2}p,$$

where $i = \Omega_1, \Omega_2, \Omega_3$. These scalings result in the following nondimensional model (dropping the primes for clarity):

$$\frac{\partial b}{\partial t} = -Da_{II} S^* b^\alpha \left(1 - c_{\Omega_3}\right), \quad \text{in } \Omega_3, \quad t > 0, \tag{5.41}$$
$$\frac{\partial c_{\Omega_1}}{\partial t} = D_f \nabla^2 c_{\Omega_1} - \boldsymbol{u} \cdot \nabla c_{\Omega_1}, \quad \text{in } \Omega_1, \quad t > 0, \tag{5.42}$$
$$\frac{\partial c_{\Omega_2}}{\partial t} = D_f \nabla^2 c_{\Omega_2} - \boldsymbol{u} \cdot \nabla c_{\Omega_2}, \quad \text{in } \Omega_2, \quad t > 0, \tag{5.43}$$
$$\frac{\partial c_{\Omega_3}}{\partial t} = D_f \nabla^2 c_{\Omega_3} - \boldsymbol{u} \cdot \nabla c_{\Omega_3} + Da_{II} b^\alpha \left(1 - c_{\Omega_3}\right), \quad \text{in } \Omega_3, \quad t > 0, \tag{5.44}$$
$$Sc \nabla^2 \boldsymbol{u} - \left(\boldsymbol{u} \cdot \nabla\right) \boldsymbol{u} - \nabla p = 0, \quad \nabla \cdot \boldsymbol{u} = 0, \quad \text{in } \Omega_1, \Omega_2 \text{ and } \Omega_3, \tag{5.45}$$

where Da_{II} is the second Damköhler number which is equal to $L_d^2 \beta b_0^\alpha / D_f$ and S^* is defined as S/b_0. These equations are coupled with the following nondimensional boundary and initial conditions:

$$\hat{\boldsymbol{n}} \cdot \left(-\nabla c_{\Omega_3} + c_{\Omega_3} \boldsymbol{u}\right) = 0, \quad \boldsymbol{u} = \frac{L_d^2}{D_f} \left(-r \sin(\theta), r \cos(\theta), 0\right) u, \quad \text{on } \Gamma_1, \quad t > 0, \tag{5.46}$$
$$\hat{\boldsymbol{n}} \cdot \nabla c_{\Omega_1} = 0, \quad \hat{\boldsymbol{n}} \cdot \nabla c_{\Omega_2} = 0, \quad \hat{\boldsymbol{n}} \cdot \nabla c_{\Omega_3} = 0, \quad \boldsymbol{u} = \boldsymbol{0}, \quad \text{on } \Gamma_2, \quad t > 0, \tag{5.47}$$
$$c_{\Omega_1} = c_{\Omega_2}, \quad \hat{\boldsymbol{n}} \cdot \left(-\nabla c_{\Omega_1} + c_{\Omega_1} \boldsymbol{u}\right) = \hat{\boldsymbol{n}} \cdot \left(-\nabla c_{\Omega_2} + c_{\Omega_2} \boldsymbol{u}\right), \quad \text{on } \Gamma_3, \quad t > 0, \tag{5.48}$$
$$c_{\Omega_2} = c_{\Omega_3}, \quad \hat{\boldsymbol{n}} \cdot \left(-\nabla c_{\Omega_2} + c_{\Omega_2} \boldsymbol{u}\right) = \hat{\boldsymbol{n}} \cdot \left(-\nabla c_{\Omega_3} + c_{\Omega_3} \boldsymbol{u}\right), \quad \text{on } \Gamma_4, \quad t > 0, \tag{5.49}$$
$$p = 0, \quad \text{at an arbitrary point}, \quad t \geq 0, \tag{5.50}$$
$$b = 1, \quad \text{in } \Omega_3, \quad t = 0, \tag{5.51}$$
$$c_{\Omega_3} = 0, \quad \text{in } \Omega_3, \quad c_{\Omega_2} = 0, \quad \text{in } \Omega_2, \quad c_{\Omega_1} = 0, \quad \text{in } \Omega_1, \quad t = 0. \tag{5.52}$$

5.2.1 Equations for mass of drug

The dimensional mass of drug in each region of the geometry may be found via:

$$M_{\Omega_1}(t) = \int_{\Omega_1} c_{\Omega_1} \, d\Omega_1, \quad M_{\Omega_2}(t) = \int_{\Omega_2} c_{\Omega_2} \, d\Omega_2, \quad M_{\Omega_3}(t) = \int_{\Omega_3} c_{\Omega_3} \, d\Omega_3 + \int_{\Omega_3} b \, d\Omega_3,$$

where $d\Omega_j = dxdydz$, with $j = 1, 2, 3$. The equations for mass can normalised with M^0, the initial drug mass. As this is a purely numerical investigation, not only are the drug masses in

each region approximated, but so too is the initial drug mass, which can be calculated via the integral:

$$M^0 = b_0 \int_{\Omega_3} d\Omega_3.$$

Using the nondimensional scalings, the normalised equations for mass are:

$$\frac{M_{\Omega_1}(t)}{M^0} = \frac{SL_d^3 \int_{\Omega_1'} c'_{\Omega_1}\, d\Omega_1'}{b_0 L_d^3 \int_{\Omega_3'} d\Omega_3'},$$

$$\frac{M_{\Omega_2}(t)}{M^0} = \frac{SL_d^3 \int_{\Omega_2'} c'_{\Omega_2}\, d\Omega_2'}{b_0 L_d^3 \int_{\Omega_3'} d\Omega_3'},$$

$$\frac{M_{\Omega_3}(t)}{M^0} = \frac{SL_d^3 \int_{\Omega_3'} c'_{\Omega_3}\, d\Omega_3'}{b_0 L_d^3 \int_{\Omega_3'} d\Omega_3'} + \frac{b_0 L_d^3 \int_{\Omega_3'} b'\, d\Omega_3'}{b_0 L_d^3 \int_{\Omega_3'} d\Omega_3'}.$$

Simplifying and dropping the primes for clarity:

$$\frac{M_{\Omega_1}(t)}{M^0} = \frac{S^* \int_{\Omega_1} c_{\Omega_1}\, d\Omega_1}{\int_{\Omega_3} d\Omega_3},$$

$$\frac{M_{\Omega_2}(t)}{M^0} = \frac{S^* \int_{\Omega_2} c_{\Omega_2}\, d\Omega_2}{\int_{\Omega_3} d\Omega_3},$$

$$\frac{M_{\Omega_3}(t)}{M^0} = \frac{S^* \int_{\Omega_3} c_{\Omega_3}\, d\Omega_3}{\int_{\Omega_3} d\Omega_3} + \frac{\int_{\Omega_3} b\, d\Omega_3}{\int_{\Omega_3} d\Omega_3}.$$

5.2.2 Release profile

The release profile may be obtained through the mass of drug released from the orifice pins:

$$\begin{aligned} M_{frac}(t) &= \frac{M^0 - (M_{\Omega_2}(t) + M_{\Omega_3}(t))}{M^0} = 1 - \frac{M_{\Omega_2}(t) + M_{\Omega_3}(t)}{M^0} \\ &= 1 - \left[\frac{\int_{\Omega_3} b\, d\Omega_3 + S^* \left(\int_{\Omega_2} c_{\Omega_2}\, d\Omega_2 + \int_{\Omega_3} c_{\Omega_3}\, d\Omega_3 \right)}{\int_{\Omega_3} d\Omega_3} \right], \end{aligned}$$

or by the accumulation of mass in the release medium:

$$M_{frac}(t) = \frac{M_{\Omega_1}(t)}{M^0} = \frac{S^* \int_{\Omega_1} c_{\Omega_1} \, d\Omega_1}{\int_{\Omega_3} d\Omega_3}. \tag{5.53}$$

5.2.3 Sensitivity analysis - parameter values

The model (5.41-5.52) was applied to the 2 and 8-orifice pin geometries and was solved using COMSOL Multiphysics®, version 5.3a, using the GMRES method, with time-advancement being handled by the BDF with free time stepping. To aid in conservation of mass, the drug-transport equations (5.42-5.44) were solved in conservative form. Similar meshes were used to that shown in Figure 5.3. Preliminary modelling suggested that error in mass conservation could be influenced by parameter values. Therefore, a suitably dense mesh was constructed for use across all parameters considered. The final meshes created for the 2 and 8-orifice pin geometries used the "Finer" mesh setting, calibrated for "Fluid Dynamics" problems. The need for this considerably denser mesh setting, compared to previous models in the chapter, is reasoned to be due to the inclusion of the drug dissolution process. Additionally, because multiple parameters are varied, the release timescales can vary significantly, so a denser mesh ensures that the solution is accurate for all timescales. Both meshes were constructed from tetrahedral elements such that the 2-orifice pin mesh consisted of $969,889$ domain elements, $18,094$ boundary elements, and 1052 edge elements and the 8-orifice pin mesh consisted of $1,094,980$ domain elements, $21,520$ boundary elements, and 1404 edge elements. A sampling of the data obtained from the model for a several parameters were examined and the error in mass calculated was $\ll 1\,\%$. Equation (5.53) was used to calculate the release profile in each case.

With the nondimensional model introduced, baseline parameter values for use in a sensitivity analysis can be established to determine the influence that changes in system parameters have on the release profile. Although there are four orifice pin configurations, only the 2 and 8-orifice pins are used in the sensitivity analysis. These are the extreme cases and so it is reasonable to assume that the results of a sensitivity analysis involving the 4 and 6-orifice pins would lie somewhere between the results of the 2 and 8-orifice pins. A suitable range of parameter values are required to adequately test the sensitivity of the release profile to changes in the model parameters. There are several model parameters identical to the parameters investigated in the sensitivity analysis within chapter 4. Shared parameters between both analyses include: reaction exponent, α, free-diffusion coefficient, D_f, dissolution rate, β and the drug solubility, S. The range of values considered for α, D_f and β are identical to values used in chapter 4 for the porous pin's release profile sensitivity analysis and as such, the reasoning behind the use of these values are also the same. Although the values used for the drug solubility, S, are different to those values used in chapter 4, the reason for their use is the same: some preliminary modelling

suggested that the variation of drug solubility could lead to vast changes to the release profile. Therefore, a large interval of solubilities were selected to cover a variety of scenarios. The reason for this is due to the appreciable effect that fluid flow has on the release of drug from the orifice pin. Therefore, by having a varied set of drug solubilities for the sensitivity analysis, one could gain insight into the relationship between drug release and solubility, in the presence of fluid flow.

There are two additional parameters to be varied for the sensitivity analysis in this chapter: the orifice diameter, d, and the magnitude of the rotational velocity, u, of the outer wall of the release medium, Γ_1. The values chosen for the orifice diameter, d, are based on the $0.5\,\mathrm{mm}$ diameter used in the experiments and it was believed to be reasonable to adjust this diameter by increments of $0.25\,\mathrm{mm}$ such that the minimum and maximum orifices diameters used were $0.25\,\mathrm{mm}$ and $1\,\mathrm{mm}$, respectively. The rate of stirring in the experiments were quoted as $30\,\mathrm{RPM}$, therefore, the values used for the sensitivity analysis would simply be half and double this rotational speed i.e. 15 and $60\,\mathrm{RPM}$. It was reasoned that these values would be suitable at providing insight into how the rotational velocity of a release medium would influence the release profile. Since fluid flow is important to consider in the case of the orifice pins, in addition to the second Damköhler and Péclet numbers, the first Damköhler number is also useful. This nondimensional number is defined as the ratio of the reaction rate to the advective transport rate and is equal to $L_d\beta b_0^\alpha/u_{\Omega_3}$, where u_{Ω_3} is the average magnitude of the velocity field within the inner core of the pin, and gives a useful measure of the relative importance of these processes. Additionally, to quantify the release times and give a measure of the influence altering of a parameter has on the release profile, the times for $50\,\%$ and $95\,\%$ release are recorded. The baseline parameter values for the sensitivty analysis for both the 2 and 8-orifice pins are shown in Table 5.2.

Parameter	Value
b_0	$775.194\,\mathrm{kg/m^3}$
α	$2/3$ [34]
D_f	$10^{-9}\,\mathrm{m^2/s}$ [61]
β	$10^{-5}\,\mathrm{s^{-1}(m^{-3}kg)^{-2/3}}$
d	$0.5\,\mathrm{mm}$ [12]
u	$\pi\,\mathrm{rad/s}$ [12]
S	$50\,\mathrm{kg/m^3}$ [12]

Table 5.2: Baseline parameter values. These values are taken from the literature or inferred from [12]. The initial mass concentration, b_0, is inferred by taking the experimental drug mass loading of $100\,\mathrm{mg}$ and dividing by the interior volume of the pin [12]. The experiments featured two drugs, Cefazolin and Linezolid, the more soluble of the two was chosen as a baseline solubility.

5.2.4 Sensitivity analysis - 2-orifice pin

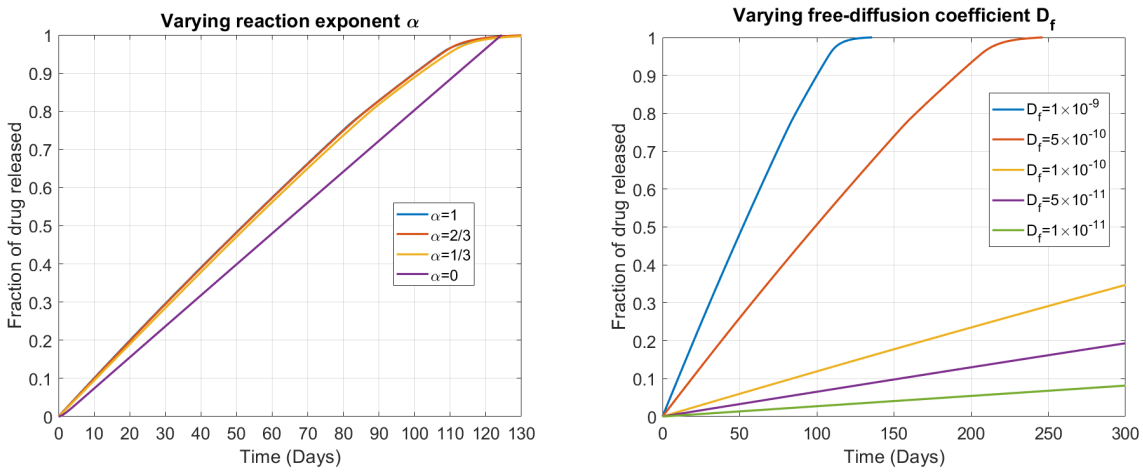

(a) (b)

Figure 5.10: Plots showing the release profiles obtained through varying the system parameters:(a) reaction exponent α (b) free-diffusion coefficient D_f.

Figure 5.10 (a) shows the effect of changing the value of the reaction exponent, α. For the majority of the values examined, there is little difference in most of the release profiles, which can be seen in the release times shown in Table 5.3, particularly for when α is equal to $1/3$, $2/3$ or 1. At first this may seem like a strange result, however, when looking at the range of relevant nondimensional numbers in Table 5.4, one can understand why. The first Damköhler numbers all show that the reaction timescale is much less than the timescale for advective transport. The second Damköhler numbers display a different trend: when $\alpha = 1$, the reaction timescale

is smaller than the diffusive timescale, however, as α is decreased, the reaction timescale is increased and thus lowers the second Damköhler number and only when $\alpha = 0$ is the reaction rate significantly smaller than the diffusive rate and so the drug transport process is quicker than the dissolution of the drug. In the other scenarios, because the rates of the transport processes of diffusion and advection are small when compared to the reaction rate, there is an excess of drug available for release out of the pin and thus the release profiles are very similar.

In Figure 5.10 (b) the effect of varying the free-diffusion coefficient D_f, is shown. The plot displays the general behaviour one would expect from the release profile, that is the lower the diffusion coefficient, the slower the release. Since the 2-orifice pin is much less permeable to fluid flow than the 8-orifice pin, any change to the diffusion coefficient produces a more marked difference in the release profiles. Hence the wide range of release times shown in Table 5.3. This is demonstrated through examination of the Péclet numbers in Table 5.4: in Ω_3 (the inner portion of the pin), when D_f is decreased to 10^{-11}, the diffusive rate is still much greater than the advective rate and only when the diffusing drug reaches Ω_2 (the orifices) is advection able to significantly impact the transport of the drug. The Péclet number in Ω_2 acts as expected, in that when $D_f = 10^{-9}$, the timescale for advection is smaller than that of diffusion, which becomes greater as D_f is decreased further. It should be noted that the small differences in the first Damköhler numbers is due to the numerical solution, in reality these values are identical.

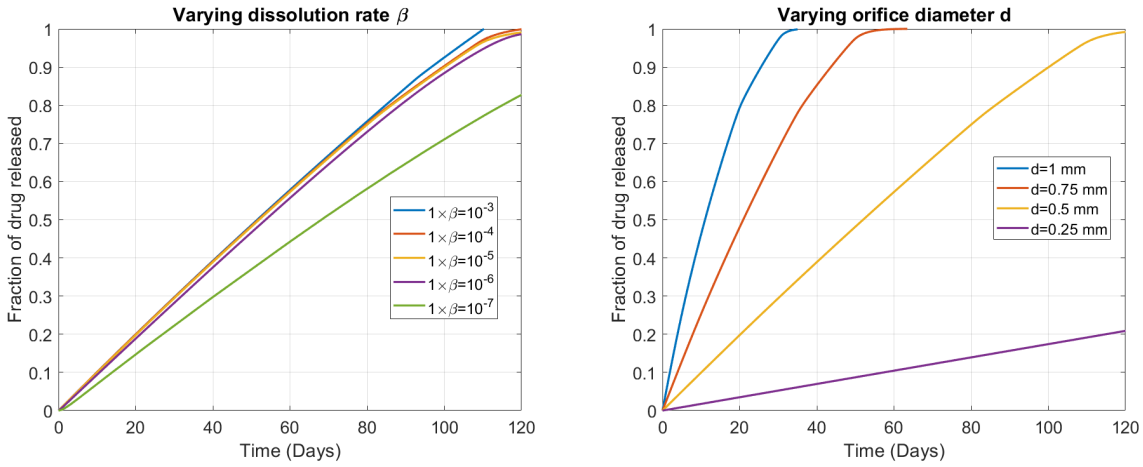

(a) (b)

Figure 5.11: Plots showing the release profiles obtained through varying the system parameters:(a) reaction exponent β (b) orifice diameter d.

Figure 5.11 (a) shows the effect of altering the dissolution rate β. For the majority of the values examined, there is little difference in most of the release profiles, which can be seen in the release times shown in Table 5.3, the only markedly different release profile is for when $\beta = 10^{-7}$. The trends shown by the release profiles are similar to that of the plots generated by varying α and for similar reasons. The first Damköhler numbers shown in Table 5.4, indicate that the advective timescale is considerably greater than the reaction timescale for all values of

β considered. The second Damköhler numbers shown in Table 5.4, suggest that the diffusive timescale is also larger than the reaction timescale, until $\beta = 10^{-7}$, at which point the diffusive timescale is much smaller than the reaction timescale. Up to this point dissolution is relatively fast and it is almost insignificant, hence the similarities between most of the release profiles.

Figure 5.11 (b) shows the effect of altering the orifice diameter, d. The trend shown in the release profiles is as one would expect, that is that making the orifice diameters larger, there is more available volume for the fluid medium to pass through the orifices, thus drug release is quicker. On the other hand, decreasing the orifice diameter, constricts the flow of fluid and thus release is slowed down. This behaviour can be clearly seen from the release times shown in Table 5.3. The nondimensional numbers of Table 5.4, show that the Péclet numbers in the orifices range from 0.138 to 65.1. Although there is a two orders of magnitude increase to the Péclet number as d is increased, the first and second Damköhler numbers remain such that the advective timescale is still much greater than the reaction and diffusive timescales. This illustrates how little fluid penetration exists in the case of the 2-orifice pin.

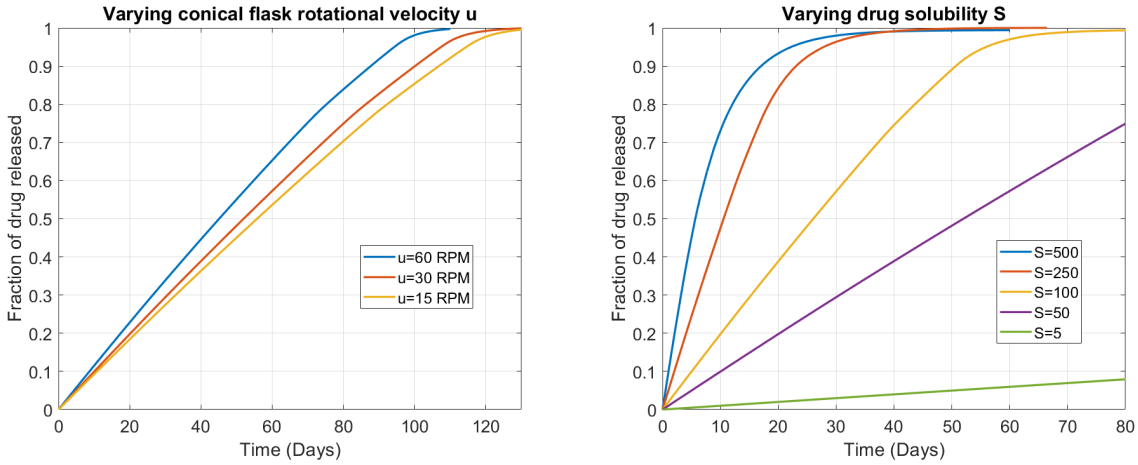

(a) (b)

Figure 5.12: Plots showing the release profiles obtained through varying the system parameters:(a) conical flask rotational velocity u (b) drug solubility S.

Figure 5.12 (a) shows the effect that altering the rotational velocity the release medium is subject to. The trend shown in is what one would expect, that is, the greater the rotational velocity the faster the drug is released, this is also shown in Table 5.3. The effect of flow in the 2-orifice pin is very small when compared to diffusion in the inner core of the pin, which is likely due to the restrictive nature of there being only two orifices and both of them having a diameter of $0.5\,\mathrm{mm}$. When considering the geometrical features of this pin and the first Damköhler and Péclet numbers shown in Table 5.4, it is clear why there is no large change to the release profile when varying the rotational velocity. Ultimately, as the magnitude of the rotational velocity is increased, the first Damköhler is greatly reduced, however, the timescale for advection is still much larger than the reaction timescale, thus the effect is minimal. The Péclet numbers in the

inner portion of the pin remain small and range from 1.9×10^{-5} to 4.75×10^{-3}, meaning that although the magnitude of velocity may be larger, the diffusive rate is still the greater of the two. However, the relatively small changes in the release profiles can be attributed to the increase in the Péclet number in the orifices, which ranges from 6.36 to 31.2. Therefore, suggesting that the release is diffusion dominated within the inner core of the pin, but once a drug particle has reached the orifices, then the combination of advection and diffusion act together to transport the drug and by increasing the magnitude of advection, the release is faster.

Figure 5.12 (b) shows the effect that varying the drug solubility, S, has on the release profile. One can see that this parameter is particularly significant, due to the noteworthy spread of release times shown in Table 5.3. Also noteworthy is that the influence solubility has, is appreciable from minor changes to the value of solubility. These points suggest that the release profile is especially sensitive to changes in this parameter, which may also alter the influence that the other parameters have. Solubility having such an influential role in the release compared to the other parameters can be explained when considering the nondimensional solubility. Since $S^* < 1$ in all cases considered, i.e. the solubility is less than the initial drug mass concentration, the free-drug phase is saturated immediately, i.e. $c = S^*$. By increasing S^*, more of the drug is permitted to dissolve and thus begin diffusing from the inner portion of the pin, to the orifices where advection is able to play a more significant role in its transport.

2-Orifice Pin	**Time for 50 % release (Days)**	**Time for 95 % release (Days)**
Baseline	**52**	**107**
Parameter	Time for 50 % release (Days)	Time for 95 % release (Days)
$\alpha = 0$	62	118
$\alpha = 1/3$	53	109
$\alpha = 1$	52	107
$D_f = 10^{-11}$	1958	4241
$D_f = 5 \times 10^{-11}$	810	1707
$D_f = 10^{-10}$	441	923
$D_f = 5 \times 10^{-10}$	99	205
$\beta = 10^{-7}$	68	147
$\beta = 10^{-6}$	54	111
$\beta = 10^{-4}$	52	107
$\beta = 10^{-3}$	52	103
$d = 0.25 \times 10^{-3}$	289	560
$d = 0.75 \times 10^{-3}$	21	48
$d = 1 \times 10^{-3}$	11	29
$u = 15$	56	114
$u = 60$	45	94
$S = 5$	537	1140
$S = 100$	26	56
$S = 250$	11	28
$S = 500$	6	22

Table 5.3: Release times for $50\,\%$ and $95\,\%$ across a variety of parameter ranges for the 2-orifice pin. All values are approximate and rounded. Parameter units are shown in Table 5.2.

2-Orifice Pin	**First Damköhler number Da_I**	**Second Damköhler number Da_{II}**	**Normalised solubility S^***	**Péclet number Pe Ω_1**	**Péclet number Pe Ω_2**	**Péclet number Pe Ω_3**
Baseline	$\mathbf{7325.9}$	$\mathbf{1.654}$	$\mathbf{0.0645}$	$\mathbf{2.81 \times 10^6}$	$\mathbf{13.75}$	$\mathbf{2.26 \times 10^{-4}}$
Parameter	First Damköhler number Da_I	Second Damköhler number Da_{II}	Normalised solubility S^*	Péclet number Pe Ω_1	Péclet number Pe Ω_2	Péclet number Pe Ω_3
$\alpha = 0$	86.8	0.0196	0.0645	2.81×10^6	13.75	2.26×10^{-4}
$\alpha = 1/3$	797.5	0.18	0.0645	2.81×10^6	13.75	2.26×10^{-4}
$\alpha = 1$	67298	15.19	0.0645	2.81×10^6	13.75	2.26×10^{-4}
$D_f = 10^{-11}$	7445	165.4	0.0645	2.81×10^8	1375	2.22×10^{-2}
$D_f = 5 \times 10^{-11}$	7086	33.1	0.0645	5.62×10^7	275	4.67×10^{-3}
$D_f = 10^{-10}$	7100	16.54	0.0645	2.81×10^7	137.5	2.33×10^{-3}
$D_f = 5 \times 10^{-10}$	7106	3.31	0.0645	5.62×10^6	27.5	4.66×10^{-4}
$\beta = 10^{-7}$	73.3	0.01654	0.0645	2.81×10^6	13.75	2.26×10^{-4}
$\beta = 10^{-6}$	732.6	0.1654	0.0645	2.81×10^6	13.75	2.26×10^{-4}
$\beta = 10^{-4}$	73259	16.54	0.0645	2.81×10^6	13.75	2.26×10^{-4}
$\beta = 10^{-3}$	732590	165.4	0.0645	2.81×10^6	13.75	2.26×10^{-4}
$d = 0.25 \times 10^{-3}$	34478	1.654	0.0645	2.81×10^6	0.138	4.8×10^{-5}
$d = 0.75 \times 10^{-3}$	11717	1.654	0.0645	2.81×10^6	35.4	1.41×10^{-4}
$d = 1 \times 10^{-3}$	1029	1.654	0.0645	2.81×10^6	65.1	1.61×10^{-3}
$u = 15$	87235	1.654	0.0645	1.4×10^6	6.36	1.9×10^{-5}
$u = 60$	348	1.654	0.0645	5.62×10^6	31.2	4.75×10^{-3}
$S = 5$	7326	1.654	0.00645	2.81×10^6	13.75	2.26×10^{-4}
$S = 100$	7326	1.654	0.129	2.81×10^6	13.75	2.26×10^{-4}
$S = 250$	7326	1.654	0.323	2.81×10^6	13.75	2.26×10^{-4}
$S = 500$	7326	1.654	0.645	2.81×10^6	13.75	2.26×10^{-4}

Table 5.4: Release times for $50\,\%$ and $95\,\%$ across a variety of parameter ranges for the 2-orifice pin. All values are approximate and rounded. Parameter units are shown in Table 5.2.

5.2.5 Sensitivity analysis - 8-orifice pin

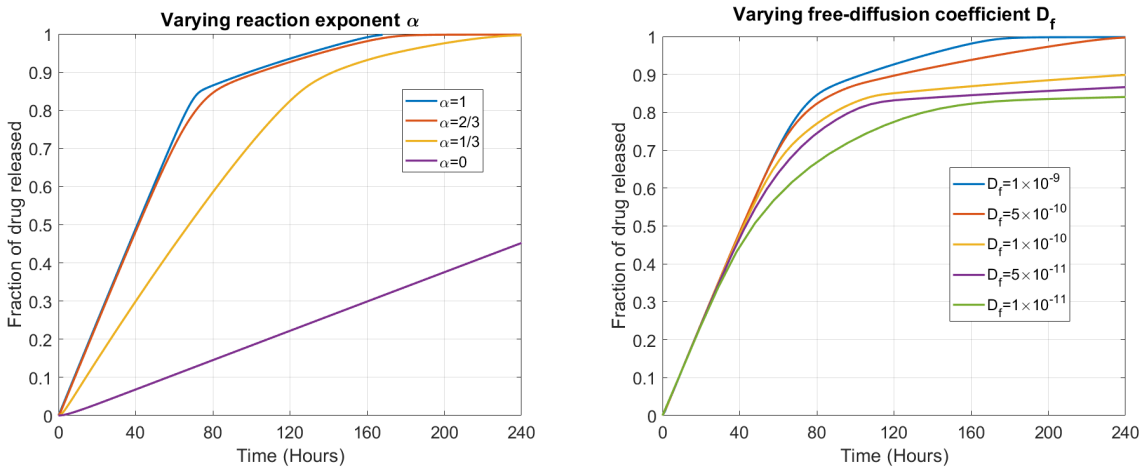

(a) (b)

Figure 5.13: Plots showing the release profiles obtained through varying the system parameters:(a) reaction exponent α (b) free-diffusion coefficient D_f.

Figure 5.13 (a) shows the effect of changing the value of the reaction exponent, α. In contrast to the 2-orifcie pin, there is more of a spread in the release profiles and hence, the release times shown in Table 5.5 are also more spread out. This is helped in no small way thanks to the increase in the number of orifices and as a result the baseline Péclet number in Ω_3 (the pin core) increasing from 2.26×10^{-4} in the 2-orifice case to 0.834 in the 8-orifice case. This explains why for the lower values of α there is more of a difference in the release profiles. The other two release profiles are very similar, this is due to the reaction timescale being smaller than either of the transport processes, which is suggested by the first and second Damköhler numbers, shown in Table 5.6. The sharp change in the plot for when $\alpha = 1$, may be present due to the fact that this is the fastest reaction exponent considered and so when approaching the time for complete drug dissolution, there is an immediate stop in the dissolving of drug and so advective and diffusive transport are the only processes continuing. The more gentle curve shown at approximately the same part of the curve for when $\alpha = 2/3$, may be more smooth since the reaction is not as vigorous and hence there is a gentler approach to the time the dissolution process finishes.

Figure 5.13 (b) shows the effect of varying the free-diffusion coefficient D_f. The plot displays the overall behaviour one would expect from the release profile, that is the lower the diffusion coefficient, the slower the release and this behaviour is displayed in the release times shown in Table 5.5. However, initially the release profiles are near-identical, but when approximately $40\,\%$ of the drug is released, the plots begin to diverge. The differences shown in the shapes of the release profiles may be due to the combination of two factors. Firstly, as the free-diffusion coefficient decreases, the Péclet numbers, shown in Table 5.6, in each region of the pin increase, thus the advective timescale relative to the diffusive timescale is decreasing and so advection becomes the more dominant transport mechanism. Secondly, throughout the variation of D_f,

the reaction timescale is always smaller than the timescales of the transport processes. Therefore, it is reasonable to conclude that despite a decreasing free-diffusion coefficient, the reaction occurs within a smaller timescale compared to the transport timescales. Although this suggests that the transport processes are the rate-limiting processes of the release, the similar plots may be due to the fact that even though the diffusive transport rate decreases, the advective transport rate is always significant, therefore, the reaction does not need to slow down to accommodate slower drug transport out of the orifice pin. The point where the plots begin to diverge is likely the point where the drug has completely dissolved. The difference in the overall shapes of the release profiles, after this point, is likely due to the nonlinear nature of the advective transport provided by the rotating release medium fluid.

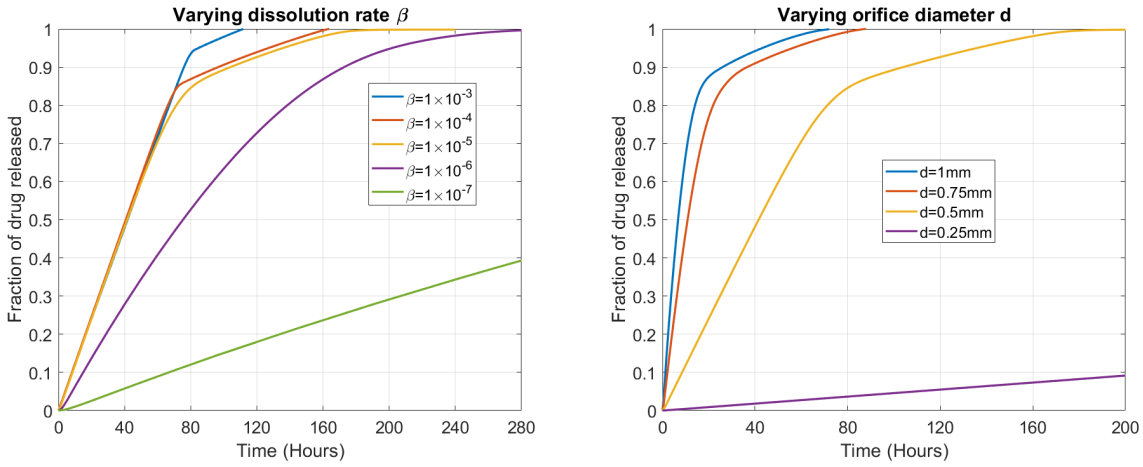

(a) (b)

Figure 5.14: Plots showing the release profiles obtained through varying the system parameters:(a) reaction exponent β (b) orifice diameter d.

Figure 5.14 (a) shows the effect of altering the dissolution rate β. The trend shown is as one would expect, that is that as the dissolution rate is decreased, the release of drug is also decreased and the release times in Table 5.5 show this trend too. The behaviour shown by the release profiles are similar to that of the plots generated by varying α and for very similar reasons. The first and second Damköhler numbers, shown in Table 5.6, indicate that the advective and diffusive timescale is considerably greater than the reaction timescale for β values in the range $10^3 - 10^5$. However, once β reaches the range $10^{-6} - 10^{-7}$, the opposite is true, that is, both transport mechanisms have a lower time scale than the reaction time scale. The influence that advection has is much greater than in the 2-orifice pin, this is likely the reason why there is more of a spread between the individual plots for the different values of β. Three of the plots are very similar during early times, namely when the value of β is in the range $10^3 - 10^5$. This behaviour is likely due to the first and second Damköhler numbers showing that the reaction timescale is lower than the processes of diffusion and advection. However, these plots begin to diverge around the 70 hour mark, with some sharp turning points in the plots when $\beta = 10^{-3}$ or 10^{-4}.

The plots suggest that these higher dissolution rates are the reason for the sharp transitions, in that the reaction experiences a "sudden stop".

Figure 5.14 (b) shows the effect of altering the orifice diameter, d. The behaviour shown in the release profiles is as one would expect, that is that making the orifice diameters larger, there is more available volume for the fluid medium to pass through the orifices, thus release is quicker. On the other hand, decreasing the orifice diameter, constricts the flow of fluid and thus release is slowed down. These trends are quantified by the release times shown in Table 5.5. By examining the nondimensional numbers of Table 5.6, what is happening to the release can be deduced. The Péclet numbers in the orifices range from 2.52 to 104.2 and with an increase to the orifice diameters, the first Damköhler number changes so that the timescale for advection is less than the timescale for the reaction. One particularly noteworthy feature of this plot is the relatively small difference between the release profiles for the $1\,\mathrm{mm}$ and $0.75\,\mathrm{mm}$ diameter orifices. This may be due to the combination of the first Damköhler number being small, whilst the Péclet number is quite large and perhaps this suggests that there is a theoretical upper limit to the velocity magnitude that is possible in the pin.

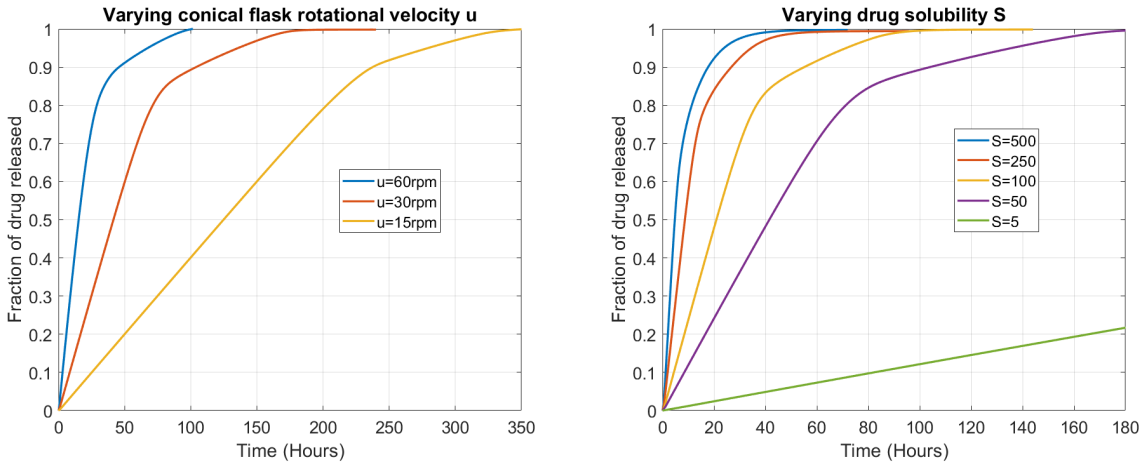

(a) (b)

Figure 5.15: Plots showing the release profiles obtained through varying the system parameters:(a) conical flask rotational velocity u (b) drug solubility S.

Figure 5.15 (a) shows the effect that altering the rotational velocity of the release medium is subject to. The trend shown is what one would expect, that is, the greater the rotational velocity the faster the drug is released. Since the 8-orifice pin is more permeable to the rotating fluid, advection, when compared to diffusion, is fairly influential for all rotational velocities in the inner core of the pin. When considering the geometrical features of this pin and the Péclet numbers, it can be seen why there are sizable reductions in release times as the rotational velocity is increased. The Péclet numbers in the inner portion of the pin remain small and range from 0.26 to 2.71, which shows there is a transition in which advective timescale goes from being greater to lower than the timescale for diffusion. The transition in transport mechanism

dominance highlights the much greater influence fluid flow has on the release of drug from the 8-orifice pin.

Figure 5.15 (b) shows the effect that varying the drug solubility, S, has on the release profile. One can see that this parameter is particularly significant, due to the noteworthy spread of release times shown in Table 5.5. Also noteworthy is that the influence solubility has, is appreciable from minor changes to the value of solubility. These points suggest that the release profile is especially sensitive to changes in this parameter, which may also alter the influence that the other parameters have. Solubility having such an influential role in the release compared to the other parameters can be explained when considering the nondimensional solubility. Since $S^* < 1$ in all cases considered, i.e. the solubility is less than the initial drug mass concentration, the free-drug phase is saturated immediately, i.e. $c = S^*$. By increasing S^*, more of the drug is able to dissolve and thus begin the transporting processes.

8-Orifice Pin	**Time for 50 % release (Hours)**	**Time for 95 % release (Hours)**
Baseline	**42**	**136**
Parameter	Time for 50 % release (Hours)	Time for 95 % release (Hours)
$\alpha = 0$	265	501
$\alpha = 1/3$	68	174
$\alpha = 1$	41	130
$D_f = 10^{-11}$	47	2239
$D_f = 5 \times 10^{-11}$	43	725
$D_f = 10^{-10}$	42	418
$D_f = 5 \times 10^{-10}$	41	173
$\beta = 10^{-7}$	372	1083
$\beta = 10^{-6}$	75	202
$\beta = 10^{-4}$	41	127
$\beta = 10^{-3}$	42	85
$d = 0.25 \times 10^{-3}$	1092	2105
$d = 0.75 \times 10^{-3}$	11	56
$d = 1 \times 10^{-3}$	7	43
$u = 15$	125	279
$u = 60$	15	67
$S = 5$	426	1398
$S = 100$	21	71
$S = 250$	9	35
$S = 500$	5	24

Table 5.5: Release times for $50\,\%$ and $95\,\%$ across a variety of parameter ranges for the 8-orifice pin. All values are approximate and rounded. Parameter units are shown in Table 5.2.

8-Orifice Pin	**First Damköhler number Da_I**	**Second Damköhler number Da_{II}**	**Normalised solubility S^***	**Péclet number Pe Ω_1**	**Péclet number Pe Ω_2**	**Péclet number Pe Ω_3**
Baseline	$\mathbf{1.98}$	$\mathbf{1.654}$	$\mathbf{0.0645}$	$\mathbf{2.81 \times 10^6}$	$\mathbf{26.37}$	$\mathbf{0.834}$
Parameter	First Damköhler number Da_I	Second Damköhler number Da_{II}	Normalised solubility S^*	Péclet number Pe Ω_1	Péclet number Pe Ω_2	Péclet number Pe Ω_3
$\alpha = 0$	0.0235	0.0196	0.0645	2.81×10^6	26.37	0.834
$\alpha = 1/3$	0.216	0.18	0.0645	2.81×10^6	26.37	0.834
$\alpha = 1$	18.22	15.19	0.0645	2.81×10^6	26.37	0.834
$D_f = 10^{-11}$	1.98	165.4	0.0645	2.81×10^8	2636.6	83.4
$D_f = 5 \times 10^{-11}$	1.98	33.1	0.0645	5.62×10^7	527.3	16.7
$D_f = 10^{-10}$	1.98	16.54	0.0645	2.81×10^7	263.66	8.34
$D_f = 5 \times 10^{-10}$	1.98	3.31	0.0645	5.62×10^6	52.73	1.67
$\beta = 10^{-7}$	0.0198	0.0165	0.0645	2.81×10^6	26.37	0.834
$\beta = 10^{-6}$	0.198	0.165	0.0645	2.81×10^6	26.37	0.834
$\beta = 10^{-4}$	19.8	16.54	0.0645	2.81×10^6	26.37	0.834
$\beta = 10^{-3}$	198.3	165.4	0.0645	2.81×10^6	26.365	0.834
$d = 0.25 \times 10^{-3}$	62.4	1.654	0.0645	2.81×10^6	2.52	0.0265
$d = 0.75 \times 10^{-3}$	0.367	1.654	0.0645	2.81×10^6	62.04	4.5
$d = 1 \times 10^{-3}$	0.13	1.654	0.0645	2.81×10^6	104.2	12.74
$u = 15$	6.39	1.654	0.0645	1.40×10^6	10.25	0.26
$u = 60$	0.611	1.654	0.0645	5.62×10^6	72.13	2.71
$S = 5$	1.98	1.654	0.00645	2.81×10^6	26.37	0.834
$S = 100$	1.98	1.654	0.129	2.81×10^6	26.37	0.834
$S = 250$	1.98	1.654	0.3225	2.81×10^6	26.37	0.834
$S = 500$	1.98	1.654	0.645	2.81×10^6	26.37	0.834

Table 5.6: Release times for $50\,\%$ and $95\,\%$ across a variety of parameter ranges for the 8-orifice pin. All values are approximate and rounded. Parameter units are shown in Table 5.2.

5.2.6 Discussion

There are notable differences in the sensitivity analyses of the 2 and 8-orifice pins and it is reasonable to conclude that the main contributing factor to the differing results is the contrasting extent that the rotating release medium fluid is able to penetrate either orifice pin. When examining the baseline Péclet numbers (Tables 5.4 and 5.6) within the orifices of the 2 and 8-orifice pins, the numbers are comparable: 13.75 and 26.37, respectively. However, there is a large discrepancy in the baseline Péclet numbers for the drug cores of the 2 and 8-orifice pins: 2.26×10^{-4} and 0.834, respectively. Although expected, this difference of three orders of magnitude in the Péclet numbers in the inner cores of the 2 and 8-orifice pins demonstrate that the rotating release medium fluid is more capable of entering the 8-orifice pin and is also able to generate a more significant advective transport component within the pin. This increased advective component has an effect in the release of the drug from the 8-orifice pin in particular and a good measure of this the difference between the baseline first Damköhler numbers (Tables 5.4 and 5.6) of the 2 and 8-orifice pins: 7325.9 and 1.98, respectively. These numbers indicate that the timescale for the dissolution process is far shorter than the timescale for advection in the case of the 2-orifice pin. Whereas, the timescale for both of these processes are comparable in the case of the 8-orifice pin.

The ease at which the release medium fluid is able to penetrate the 8-orifice pin goes a long way to explain the large differences in the sensitivity analyses between the orifice pins. For instance, when varying α, β and u, the release profiles for the 2-orifice pin do not differ tremendously. In contrast, there is a considerably greater spread in the release profiles for the 8-orifice pin when varying these parameters, which can be reasonably attributed to the greater drug transport provided by advection since the flowing release medium can enter the 8-orifice pin far more easily. Other parameters can produce release profiles that vary significantly for the both the 2 and 8-orifice pins, specifically d and S, which suggest that these parameters are particularly influential in the release of drugs from the orifice pins. Changes to the orifice diameter, d, can be reasoned to have such an effect as with wider orifices comes greater ease for release medium fluid penetration of the orifice pins. Drug solubility, S, can give rise to such varied results as the greater the solubility, more particles are able to begin transporting out of the orifice pins. The free-diffusion coefficient, D_f, produces an almost reversed scenario: the release profiles vary more considerably in the case of the 2-orifice pin than the 8-orifice pin. Although at first a strange result, it is not unreasonable to conclude that the greater advective transport component within the 8-orifice pin is the cause. In the 2-orifice pin case, the Péclet number (5.4) in the core of the pin is always small, meaning that the timescale for diffusion is always much smaller than the timescale for advection. As transport is diffusion dominated within the core of the 2-orifice pin, it would be expected that variation of the free-diffusion coefficient would produce such varied release profiles. On the other hand, in the case of the 8-orifice pin, despite the decrease in the free-diffusion coefficient, there is still an appreciable advective transport component within

the core of the pin.

There are many conclusions that can be drawn from the sensitivity analysis of the orifice pins, however, there is one in particular that relates strongly to experiments: the rotational velocity applied from the stirring of the release medium can greatly influence the release of drug from the orifice pins. In other words, the experimental setup itself can be influential in the release of drug from the pins. This is in stark contrast to the porous pin of chapter 4, in which fluid flow had a negligible influence on the release of drug.

The orifice pins studied by Gimeno et al. [12] are a fine example of the current research into the exploration of prototype OI device designs, with a view for such devices to release drugs. It is for this reason and the foresight that these pins would be an interesting mathematical modelling challenge, that they were chosen for the theoretical study. However, there are some drawbacks from this choice: although it was found that fluid flow is likely very influential in the release rate of drugs from the orifice pins, the current model is unlikely to be able to capture the data. There are a variety of factors which contribute to this and one important issue, which was also discussed in chapter 4, is that of the solubility of the drugs in SBF. In the publication of Gimeno et al. it is stated that the solubility of the drugs in water for Cefazolin Sodium (Cefazolina Normon®) and Linezolid (Zyvox®) are $50\,\mathrm{mg/mL}$ and $3\,\mathrm{mg/mL}$ in water [12], respectively. However, the release medium used in the drug release experiments was SBF and the solubilities of these drugs are unknown and, as noted in chapter 4, SBF contains a variety of ions (charged particles), which may have a significant effect on the drug solubility. Additionally, since it was discovered that fluid flow can have a noteworthy influence on the release of drugs from the orifice pins, it is important to the relevant physical properties of SBF, such as dynamic viscosity and density. The values of these physical parameters may be noticeably different to the values of water and so may influence the resultant velocity field that develops due to the stirring of the release medium, which may have a knock-on effect on the release of drugs from the orifice pins. Therefore, it is reasonable to conclude that the assumption that the release medium, for the purposes of the mathematical model, is water, is inaccurate and in fact may hamper the model output.

Another reason why the current model is not likely to be able to replicate the release data of Gimeno et al. [12], is due to the apparent stop-start release of Linezolid from the orifice pins, which may be seen from the release data in Figure 5.16. This plateauing effect is more pronounced as the number of orifices increases. From the theoretical study into drug release from the orifice pins, it is reasonable to propose the following hypothesis: since most of the commercial Linezolid used in the experiments is in fact mostly glucose (per mL of prepared solution contains $45.7\,\mathrm{mg}$ of glucose and $2\,\mathrm{mg}$ of Linezolid [12]), the release of this glucose inhibits the release of the Linezolid component. There are two key reasons for this, depending on temperature, the solubility of glucose may be as high as $1200\,\mathrm{mg/mL}$ [76], compared to the stated solubility of $3\,\mathrm{mg/mL}$ of the Linezolid component. Also, the molecular weights of

these components are noticeably different: $180.16\,\mathrm{g/mol}$ for glucose [76] and $337.35\,\mathrm{g/mol}$ for Linezolid [77]. This difference in weight may allow the slower flow inside the pin to have an increased effect in moving glucose particles compared with Linezolid particles. The restriction in Linezolid release is more noticeable as the number of orifices increases, and this may be due to the increasing ease at which the flowing release medium may enter the pin and thus wash away the lighter, and more soluble, glucose. These two factors may be why the Linezolid is restricted in its release initially and after the glucose has left the orifice pins, the release of the Linezolid can resume. This is not a simple problem to tackle mathematically, to begin with the motion of the release medium and the dissolution process must be accounted for, however, adding multi-component diffusion to the model adds severe levels of complexity, which is likely to reduce the appeal of a mathematical approach to the understanding of drug release from the orifice pins from an experimentalist's point of view.

In addition to the oddly shaped release profiles for Linezolid in the case of the 4, 6 and 8-orifice pins, the release profiles for Cefazolin Sodium and Linezolid in the 2-orifice pin are remarkably similar, despite an order of magnitude difference in solubility (Figure 5.16). This result is very unlikely to be captured by the current model as both drugs, in theory, would experience the same velocity field, with the only immediate difference being the solubilities of each drug. However, the answer may lie within the murky cloud of unknown parameter values, such as the free-diffusion coefficient. This parameter, in principle, may be sufficiently different to give rise to these similar release profiles for the 2-orifice pin case. This is evidenced from the theoretical results from the sensitivity analyses, which show that fluid flow within the core of the 2-orifice pin is almost negligible. This means that mass transport is diffusion-driven initially, then once drug particles reach the orifices, advective transport becomes appreciably more influential. Therefore, a large difference in the free-diffusion coefficient may explain why the release profiles are similar. The trend shown in the release profiles for the 4, 6 and 8-orifice pin cases are what one would expect for an increasing number of orifices: release is faster for the more soluble Cefazolin Sodium.

Another reason why the current model is not likely to be able to capture the release data is due to the nature of the stirring method. In correspondence with the authors, the conical flasks, which contain the release medium and an orifice pin, are on a rotating plate. The way in which the rotational force is applied may well introduce sloshing effects and perhaps create turbulence in the release medium. Additionally, the orifice pins are suspended in the release medium via a piece of string, which may result in the pin moving like a pendulum, in a libration sense, within the release medium. It is very reasonable to conclude that the combination of the sloshing release medium and the orifice pin moving, is likely to influence the release of drugs from the orifice pins. The incorporation of a sloshing release medium coupled to the release of a dissolving drug would require exceptionally powerful computational muscle and time to simulate. Such an inclusion is very likely to dissuade experimentalists from seeking mathematical assistance in

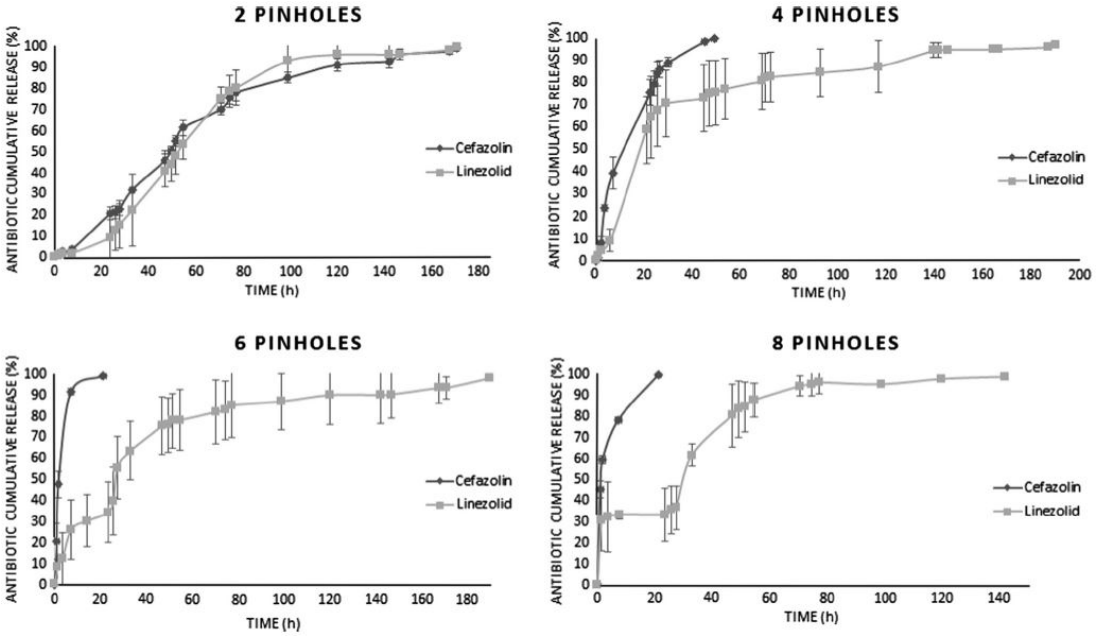

Figure 5.16: Release profiles for drug-filled tubes with varied numbers of orifices. Reproduced from [12].

future research.

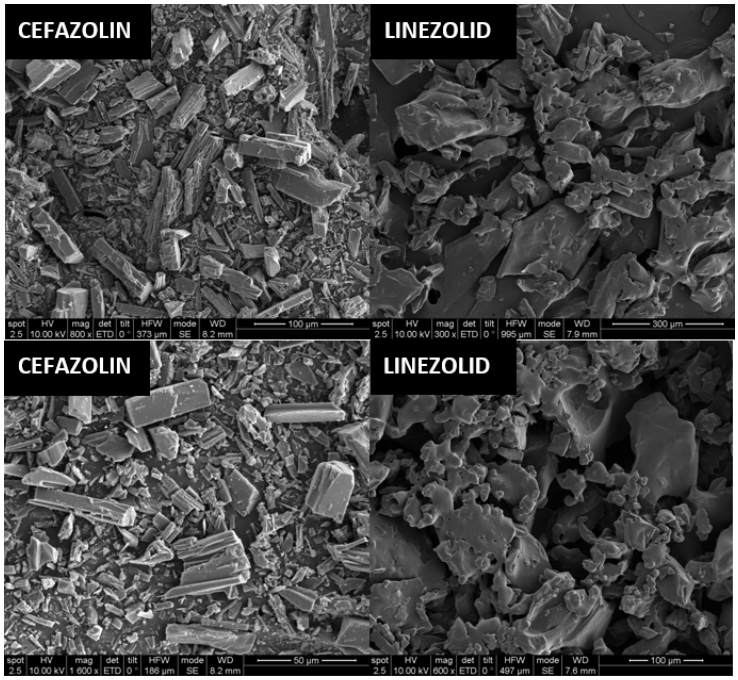

Figure 5.17: Images showing the grain sizes of the two drugs used by Gimenoo et al.. Reproduced from from the supplementary material of [12].

In the case of the orifice pins a reasonable conclusion is that fluid flow matters. However, there is a limitation with the current model: the computed stationary velocity field penetrates the undissolved drug. In reality, the "solid" drug is a porous structure (Figure 5.17) and would

allow for the penetration of release medium fluid. However, the speed of this penetration is finite. One approach to tackle this may be to adopt a moving boundary approach to the dissolution of the drugs, in which the flowing release medium fluid would transport dissolved drug particles on one side of the boundary and on the other side is solid, undissolved drug, thus eliminating the apparent contradiction of the release medium fluid flowing through solid, undissolved drug. However, it may be argued that this is potentially not a big issue as although the velocity field of the flowing release medium is penetrating solid drug, the drug does not move until it dissolves. Therefore, it may be the case that the inclusion of a moving boundary is an unnecessary, and complex, addition. However, evidence in the form of a comparison between such mathematical models would be required.

These issues highlight the main reason for choosing to model the release of drug from the orifice pins, that experimentalists and theorists should conduct research in tandem, not separately [28, 78]. Experimentation can provide the necessary raw data of drug release from a device and then theory may be applied to determine key drug release features and parameters [28, 79]. Even before experiments take place, sound theory may be used to advise on the experimental setup to reduce the number of simplifications and assumptions within the model, potentially increasing model usefulness. A validated mathematical model may also reduce the number of costly experiments required when seeking to evaluate changes to experimental setups, such as drug solubility.

5.3 Conclusions

This chapter details the process of mathematically modelling drug release from orifice pins by Gimeno et al. [12]. From the outset, it was realised that the model must be 3D in nature, due to the inability to reduce the model via symmetry. In comparison to the porous pin of chapter 4, it is not immediately clear if the stirring of the release medium would have a significant influence on the release of drug from the orifice pins. Therefore, a study to determine the influence of fluid flow was conducted. The results showed that fluid flow may have a significant effect on the release of drug from the orifice pins, with more orifices providing a stronger effect. Although this added source of model complexity would incur additional computational cost, it was found that that a stationary velocity field in place of a time-dependent velocity field, produced near-identical results. Although not precisely the same, an interesting comparison between the stationary velocity field and the Taylor-Couette flow solution was made. The results of which showed that the stationary velocity field only differed significantly from the Taylor-Couette solution close to the orifice pins, where the geometries of the orifice pin experimental setup and Taylor-Couette problem breaks down. In light of the modelling of chapter 4, the dissolution process was accounted for immediately after determining that the stirring of the release medium influenced the release of drug. A sensitivity analysis was conducted to ascertain

the effect that altering key system parameters would have on the release profile produced by the model. It was found that the diameter of the orifices, the rotational velocity of the release medium and the drug solubility were particularly influential in the release of drug from the orifice pins. This is because these parameters relate heavily to the experimental setup and thus changes to them will likely affect the results from experiments. Lastly, an in-depth discussion on the reasons why future cooperation between experimentalists and theorists is paramount to drug-releasing OI design.

Chapter 6

Coupling drug release from orthopaedic pins with bacterial inhibition

In chapters 4 and 5, the release of drug from prototype orthopaedic devices was studied in detail. These investigations were of drug release *in vitro* and serve to present models that aid in identifying key drug-release mechanisms and may be built upon in future research. However, it is sensible to wonder what happens to the drug once it is released *in vivo*. The literature shows a wide variety of experiments which feature prototype orthopaedic devices and materials with a view for each to hold and release drugs, with a particular emphasis on antibiotics. Although chapter 2 details a small proportion of this ongoing research, it does highlight that bacterial infection due to orthopaedic surgery is a tremendous issue. If infection is able to take hold and the bacteria are able to form a biofilm, an implant can fail [80, 81]. The need for revision surgeries, including implant failure due to infection, is very costly. For example, of the 6009 total knee arthroplasty revision surgeries carried out in 2012 in the UK, $23\,\%$ was due to infection [82]. If infections could be prevented, there would be an appreciable economic benefit as the cost of some procedures may be as high as £75,000 per patient [82].

Prevention is the best medicine and this ideology may be applied to the problem of orthopaedic associated infection. To begin to tackle this challenge, where infecting bacteria come from would give an indication of where efforts should be focused. The skin of humans is colonised with a variety of microorganisms [85] and potentially amongst them is the bacteria *Staphylococcus aureus* [86, 87], one of the most common microorganisms associated with orthopaedic infections [81, 88–91]. Most infections arise from microbial contamination of a prosthesis during surgery [81] and despite extensive preoperative procedures to cleanse the surgical site before an incision is made [87], bacteria, such as *S. aureus*, may not be fully eradicated. This is not only due to the sheer number of sources, such as the surgical equipment used and even the clothing worn by medical staff [86], but also because bacteria may be protected from sterilisation efforts, for example, by residing within hair follicles [87]. If some bacteria survive the decontamination process, they may be able to enter the body via open skin, into vulnerable

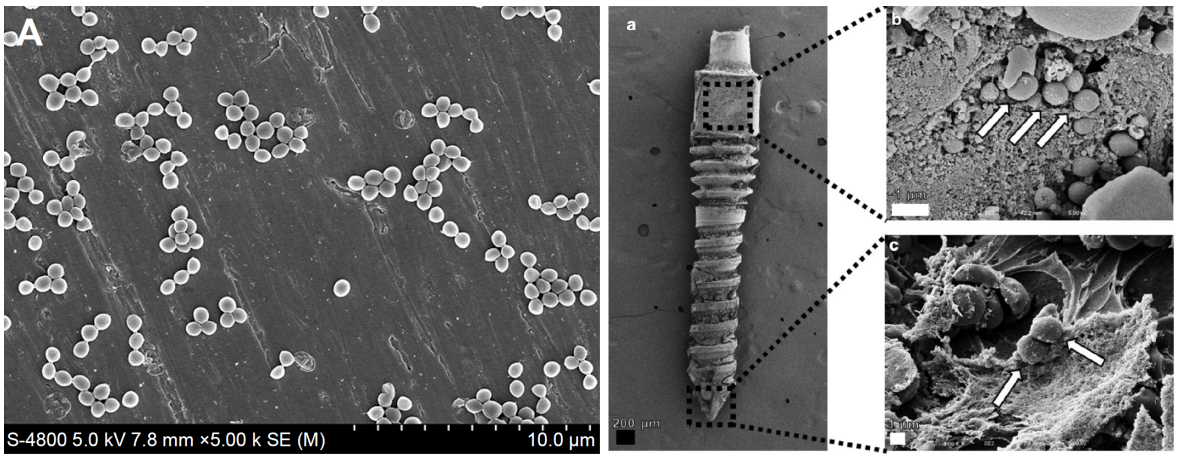

(a) (b)

Figure 6.1: Scanning electron microscope images. (a) A *S. aureus* colony visible on a smooth polished titanium sample. Reproduced from [83]. (b). *S. aureus* cells adhering to a titanium orthopaedic screw. Reproduced from [84].

regions once surgery begins [86,87]. Another risk factor which is particularly noteworthy, where orthopaedic surgery is concerned, is the ability of infectious bacteria to adhere and colonise a prosthesis [87, 92] (Figure 6.1), and these bacteria may come from the patient or from medical staff [88]. Upon insertion of the implant, bacteria may now be in close proximity to vital regions of the body, for example, within bone marrow. Worsening matters is the fact that the number of bacteria required to cause infection in this case is decreased [87]. Additionally, bacteria present on the implant are likely to develop a biofilm as most microorganisms live in such communities (Figure 6.2) [88]. Perhaps most disturbing about biofilms is the level of protection it offers to the infecting bacteria. Whilst in the biofilm, bacteria are much more resistant to antibiotics, reportedly as high as a factor of 1000 times more resistant [88, 90].

(a) (b)

Figure 6.2: (a) Biofilm visible on the titanium surface of the acetabular component of a failed hip implant. Reproduced from [80]. (b) Biofilm present in the femoral notch of a failed total knee arthroplasty. Reproduced from [93].

It is clear from the literature that OI associated infection is a problem and to begin tackling it mathematically, a suitable mathematical description of bacterial growth is required. Bacterial growth can be thought of as part of the wider field of population dynamics, which garnered some attention as far back as the time of Leonardo of Pisa, known today as Fibonacci. He considered the problem of an increasing population of rabbits and through this he discovered the famous Fibonacci sequence [94]. Many other famous names took an interest in population dynamics, such as Leonhard Euler and Pierre-François Verhulst [94]. Much of the work on population dynamics at the time had considered a continuously growing population, and in some cases, exponentially. The simplest growth model, known as the "Malthusian growth model", is an ODE in time, t, which describes the rate of change of a population, P, subject to a growth rate, r:

$$\frac{dP(t)}{dt} = rP, \quad P(0) = P_0.$$

where P_0 is the initial population size. This ODE has the general solution:

$$P(t) = P_0 e^{rt}.$$

From this solution there are three possible outcomes: the population increases or decreases exponentially ($r > 0$ and $r < 0$, respectively) or remains constant ($r = 0$). This is not a realistic situation in most circumstances, however, bacteria can experience a phase of exponential growth in optimal conditions [95]. Verhulst introduced what is known as the "logistic equation", which is an ODE that describes a growing population, limited by a "carrying capacity", K:

$$\frac{dP(t)}{dt} = rP\left(1 - \frac{P}{K}\right), \quad P(0) = P_0.$$

The logistic equation has the general solution [94]:

$$P(t) = \frac{KP_0 e^{rt}}{K + P_0\left(e^{rt} - 1\right)} = \frac{K}{1 + \left(\frac{K - P_0}{P_0}\right) e^{-rt}}.$$

From the solution of the logistic equation, it can be seen that for a for an initial population size, such that $P_0 < K$, the population will asymptote towards the carrying capacity. On the other hand, should $P_0 > K$, the population will steadily decrease until reaching the carrying capacity. This is a more realistic description of population growth as it applies a limit to the population size in the form of parameter K, which may be a combination of several important factors, such as food supply and available space for inhabitation.

There exists several models which only describe bacterial growth [96], however, in the context of bacterial infection the desire is to eradicate the bacteria before infection can take hold. For the mathematical study in this chapter, the differential form of the logistic equation will be

used to model bacterial growth and modifications will be applied to account for additional processes which may influence the growth of infecting bacteria. In the following sections several mathematical models of bacterial growth are derived. Each subsequent model adds an extra level of complexity as new processes are considered and the limitations of the models are discussed.

6.1 Single ODE with a constant antibiotic source

There are various ways to express the number of individuals within a bacterial population, for example, the number of colony-forming-units per millilitre of diluting solution ($\mathrm{CFU/mL}$) [97]. However, since the mathematical modelling within this chapter will include the action of an antibiotic on a bacterial population, the units must balance. Therefore, for the bacterial population variable, B, the units are $\mathrm{kg/m^3}$, essentially a "concentration" of bacteria. The proposed simplest mathematical model of the growth of a bacterial population, B, subject to a constant antibiotic source, would be the ODE:

$$\frac{dB}{dt} = gB\left(1 - \frac{B}{B_{max}}\right) - k_{max}B, \quad B(0) = B_0, \tag{6.1}$$

where g and k_{max} are the growth and maximal killing rates, respectively, B_{max} is the carrying capacity and B_0 is the initial bacterial concentration. ODE (6.1) may be solved analytically and the following identity will be useful [66, p. 12]:

$$\int \frac{dB}{A_3B^2 + 2A_2B + A_1} = \frac{1}{2\sqrt{A_2^2 - A_1A_3}} \ln\left(\frac{A_3B + A_2 - \sqrt{A_2^2 - A_1A_3}}{A_3B + A_2 + \sqrt{A_2^2 - A_1A_3}}\right), \text{if } A_1A_3 < A_2^2, \tag{6.2}$$

where A_1, A_2 and A_3 are positive constants. Rearranging (6.1) and using (6.2), constants A_1, A_2 and A_3 can be identified:

$$\int \frac{dB}{\frac{g}{B_{max}}B^2 + (k_{max} - g)\,B} = -\int dt,$$

thus, $A_1 = 0$, $A_2 = (k_{max} - g)/2$ and $A_3 = g/B_{max}$ and so the solution has the form:

$$\frac{1}{k_{max} - g} \ln\left(\frac{gB}{gB + B_{max}\,(k_{max} - g)}\right) = -t + C. \tag{6.3}$$

Applying the initial condition, the value of the constant of integration, C, may be determined:

$$C = \frac{1}{k_{max} - g} \ln\left(\frac{gB_0}{gB_0 + B_{max}\,(k_{max} - g)}\right). \tag{6.4}$$

Combining (6.3) and (6.4) and simplifying:

$$B(t) = \frac{B_{max}\left(k_{max} - g\right)\exp\left(\left(g - k_{max}\right)t\right)}{g\left(\frac{gB_0 + B_{max}\left(k_{max} - g\right)}{gB_0} - \exp\left(\left(g - k_{max}\right)t\right)\right)}. \tag{6.5}$$

Depending on the values of g and k_{max}, solution (6.5) changes form, specifically the exponent of the exponential function can be equal to zero or either positive or negative, suggesting bacterial growth and decay, respectively. In the case where the exponent is equal to zero ($k_{max} = g$), solution (6.5) is equal to zero. This scenario may be considered the critical case, in that should $k_{max} < g$, the bacteria will not be eradicated. By taking the limit of (6.5) as t tends to infinity, the steady states of the model may be determined. Starting with the case where $k_{max} < g$, the limit is of an indeterminant form, therefore, L'Hôpital's rule may be used to determine the limit:

$$\lim_{t\to\infty} B(t) = \frac{B_{max}\left(k_{max} - g\right)}{-g} = B_{max}\left(1 - \frac{k_{max}}{g}\right). \tag{6.6}$$

For the case where $k_{max} > g$, it is clear from solution (6.5) that the limit is zero. These steady states illustrate the expected behaviour of ODE (6.1): if the growth rate of a bacterial population is greater than the killing rate due to the antibiotic, then the population will grow till it reaches steady state (6.6). Otherwise, if the growth rate is less than the killing rate, the population will decay to the zero steady state, the ideal outcome in this scenario. Solution (6.5) was evaluated using MATLAB®R2019a via a for loop in time, t, which was discretised into 100 equally spaced timesteps. Figure 6.3 illustrates the steady states of the model.

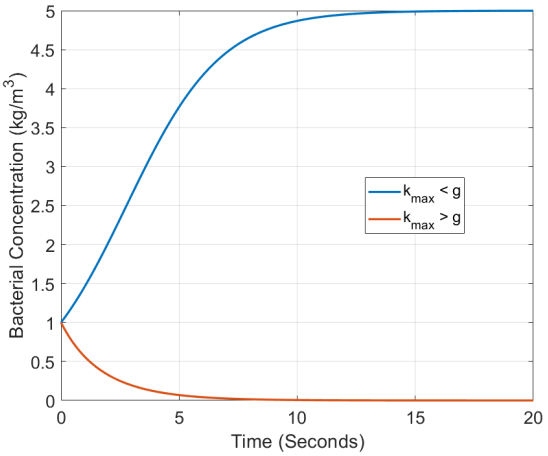

Figure 6.3: Plot showing the two possible outcomes of the model: either the bacterial population reaches a non-zero steady state or the population is eradicated. Parameter values used in the case where $k_{max} < g$: $B_0 = 1$; $B_{max} = 10$; $g = 1$ and; $k_{max} = 1/2$. Parameter values used in the case where $k_{max} > g$ were the same as in the previous case, however, k_{max} was increased from $1/2$ to $3/2$.

A constant source of antibiotic is, of course, unrealistic, as drugs are given in the form of

doses and an antibiotic will not provide its maximal killing effect indefinitely as the concentration will reduce over time and thus the antibiotic's effectiveness will also decrease. However, this simple starting point allows for initial model assessment to determine if the model performs as expected and allows one to make alterations to increase model realism and hence, applicability. Although simplistic, ODE (6.1) offers a platform for model enhancement and a sensible addition is the inclusion of antibiotic depletion.

6.2 Coupled ODEs with finite antibiotic

In reference to the prototype orthopaedic pins explored in previous chapters, drug-releasing OIs would have a finite amount of drug loaded, which must be able to prevent the growth of, and kill any bacteria which may be present on the OI or within the site of surgery. Therefore, the next step in modelling bacterial growth subject to an antibiotic, is to include the process of antibiotic consumption. As an antibiotic is used, its concentration will decrease and thus, its effect on a local bacterial population will begin to lessen, effectively reducing the maximal killing rate, k_{max}. Therefore, in place of a constant consumption rate, Michaelis–Menten reaction kinetics [98, p. 759] will be used to determine the effective killing rate of an antibiotic, k_e, and hence, its consumption rate. The form chosen for this term in the mathematical model is:

$$k_e = \frac{k_{max} c}{c + c_{50}}, \tag{6.7}$$

where c is the concentration of antibiotic and c_{50} is the concentration of antibiotic that corresponds to a $50\,\%$ killing rate i.e. $k_{max}/2$. This value is also known as the EC50 value [99]. This expression for the effective killing rate is nonlinear and the general shape of the function is shown in Figure 6.4.

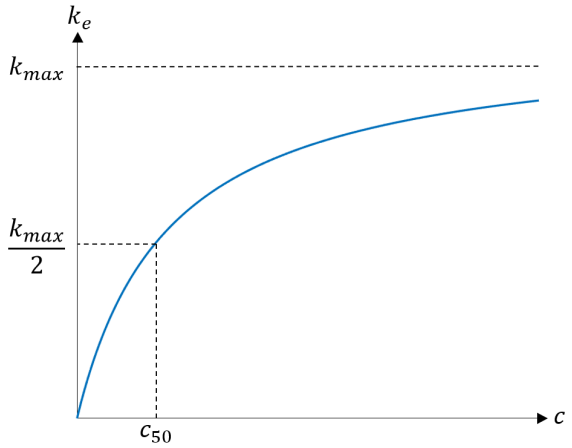

Figure 6.4: Plot showing the general behaviour of the Michaelis-Menten reaction term (6.7), produced by evaluating (6.7) within MATLAB®R2019a via a for loop in antibiotic concentration, c, whose values were in the range $[0, 100]$, discretised into 1000 equally spaced steps. Parameter values used were $k_{max} = 10$ and $c_{50} = 20$.

As can be seen from Figure 6.4, the effective killing rate of the antibiotic is dependent on the value of c_{50} and the concentration, c. As the antibiotic concentration increases, the effective killing rate, k_e, increases and asymptotically approaches the maximal killing rate, k_{max}. The behaviour of equation (6.7) can be further explored by dividing top and bottom of the expression by c_{50}:

$$k_e = \frac{k_{max}\dfrac{c}{c_{50}}}{\dfrac{c}{c_{50}}+1}, \quad \text{and if} \quad \frac{c}{c_{50}} \ll 1, \quad \text{then} \quad k_e \approx \frac{k_{max}}{c_{50}}c.$$

In other words, the plot is approximately linear for c sufficiently small. Similarly, dividing top and bottom of (6.7) by c:

$$k_e = \frac{k_{max}}{1+\dfrac{c_{50}}{c}}, \quad \text{and if} \quad \frac{c_{50}}{c} \ll 1, \quad \text{then} \quad k_e \approx k_{max},$$

meaning that for high values of c, relative to c_{50}, the effective killing rate is approximately equal to the maximal killing rate, which can be seen in Figure 6.4.

The proposed model of bacterial growth subject to a finite source of antibiotic is:

$$\frac{dB}{dt} = gB\left(1-\frac{B}{B_{max}}\right) - B\frac{k_{max}c}{c+c_{50}}, \quad B(0)=B_0, \tag{6.8}$$

$$\frac{dc}{dt} = -B\frac{k_{max}c}{c+c_{50}}, \quad c(0)=c_0, \tag{6.9}$$

where c_0 is the initial antibiotic concentration. Examination of model equations (6.8-6.9) reveals that there are three potential outcomes (steady states) from the model, depending on the parameter values chosen. The two expected results are the situations where the antibiotic has been depleted and the bacteria have been able to grow in population size to the carrying capacity, B_{max}. Alternatively, the more desirable case may arise in which the bacteria have been eradicated and some residual antibiotic is left over. These two outcomes are shown in Figure 6.5. The third potential outcome is the situation where both the bacterial population and the antibiotic are depleted simultaneously. This steady state is possible in theory, however, in reality, it would be considerably more likely for one of either the bacteria or the antibiotic to be consumed more quickly than the other. Model equations (6.8-6.9) were solved numerically using MATLAB®R2019a via the "ode45" solver. This solver is based on the explicit Runge-Kutta method, specifically the Dormand-Prince (4,5) pair [100]. Additionally, the default values for relative and absolute tolerances for ODE solvers were used (10^{-3} and 10^{-6}, respectively [101]).

The parameter values, although not necessarily representative of reality, are chosen to demonstrate the two most likely outcomes of the model. The model results displayed in Figure 6.5 (a) show the worst outcome: despite the presence of an antibiotic, the bacteria are able to recover

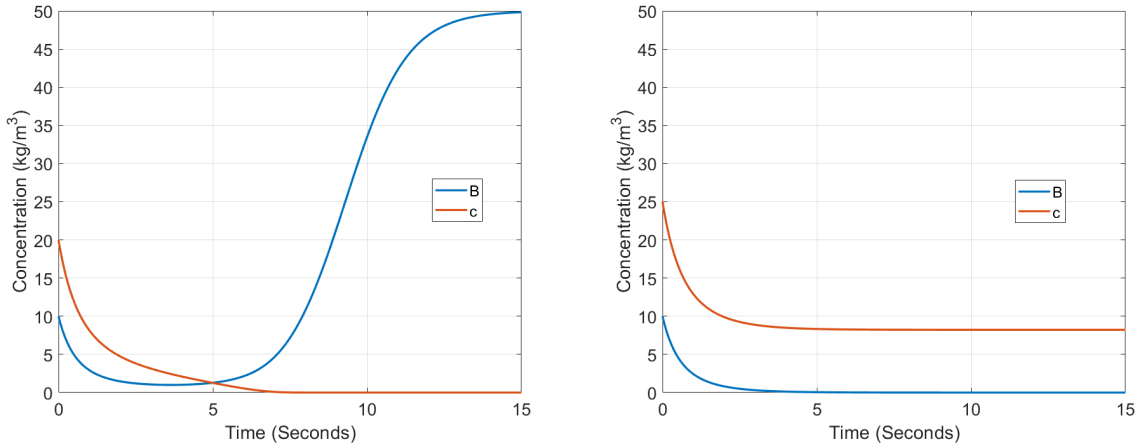

(a) (b)

Figure 6.5: Plots showing the interaction between antibiotic (c) and bacteria (B). (a) The antibiotic is killing off the bacteria, however, antibiotic concentrations drop to levels that are no longer effective and so the bacteria recover, grow and reach the maximum population size. Parameter values used were $k_{max} = 3$, $g = 1$, $B_{max} = 50$, $c_0 = 20$, $c_{50} = 5$ and $B_0 = 10$. (b) The antibiotic succeeds in eradicating the bacteria, which leaves behind an excess of unused antibiotic. Parameter values are the same in case (a), however, the initial antibiotic concentration, c_0, was increased from 20 to 25.

from near-eradication and grow. The desired outcome is shown in Figure 6.5 (b), where the bacteria have been completely removed, leaving behind some residual drug. This leftover drug can then be removed from the body [102, p. 17]. The third, albeit, unlikely scenario is where both the bacterial population and the antibiotic are reduced to zero simultaneously. This is theoretically possible from model equations (6.8-6.9) and may be thought of as the critical case in which any less antibiotic would eventually lead to the bacteria recovering and being able to grow.

The inclusion of a finite initial concentration of antibiotic whose killing rate is dependent on the concentration and EC50 value is considerably more realistic than the previous case considered where there was a constant supply of antibiotic with a maximal killing rate. However, there are further modelling considerations which are likely to have an influence on the behaviour and hence the outcome: bacterial eradication or proliferation. One such consideration is that an antibiotic would be *delivered* and not already present and mixed with infecting bacteria, which is what model equations (6.8-6.9) suggest.

6.3 Spatially varying antibiotic

6.3.1 Constant drug delivery

The mathematical modelling investigation thus far has resulted in a pair of coupled ODEs to describe bacterial growth subject to the killing effect of an antibiotic. The previous model considered the case of a finite amount of antibiotic, which performed as expected: if the antibiotic is not given in a high enough dose and/or it is not potent enough, the bacteria will prevail. However, the immediately noticeable limitation of such a model is that it assumes that the drug is already in the presence of the bacteria. In reality, the antibiotic would be delivered in some way and would have to build in concentration to have a meaningful effect on the bacteria. With a view to incorporate the prototype pins, examined in chapters 4 and 5, a radial coordinate system is used for all of the following models.

Consider now a 1D radial domain of thickness L, which is contaminated with an initial bacterial population, B_0. Assume that an antibiotic, c, is supplied at a constant rate, c_{in}, via a device of radius L_d, at $r = L_d$. The antibiotic must then diffuse throughout the bacteria-laden domain, building up in concentration, to eradicate the bacteria. At $r = L_d + L$, a zero-flux boundary condition is applied such that the antibiotic is confined to the domain. This setup is illustrated in Figure 6.6.

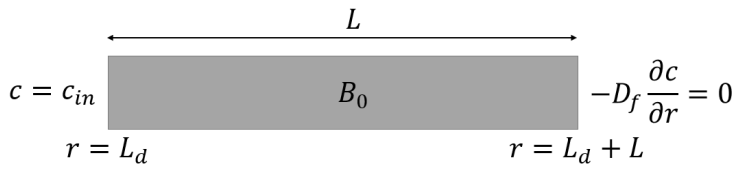

Figure 6.6: Illustration of the 1D domain, of length L, with an initial bacterial population B_0. At $r = L_d$ there is a constant concentration boundary condition and at $r = L_d + L$ there is a zero-flux boundary condition.

The proposed model which describes a diffusing antibiotic supplied at a constant rate is:

$$\frac{\partial B}{\partial t} = gB\left(1 - \frac{B}{B_{max}}\right) - B\frac{k_{max}c}{c + c_{50}}, \quad L_d < r < L_d + L, \quad t > 0, \tag{6.10}$$

$$\frac{\partial c}{\partial t} = D_f\left(\frac{1}{r}\frac{\partial c}{\partial r} + \frac{\partial^2 c}{\partial r^2}\right) - B\frac{k_{max}c}{c + c_{50}}, \quad L_d < r < L_d + L, \quad t > 0, \tag{6.11}$$

$$c = c_{in}, \quad r = L_d, \quad t > 0, \tag{6.12}$$

$$-D_f\frac{\partial c}{\partial r} = 0, \quad r = L_d + L, \quad t > 0, \tag{6.13}$$

$$B = B_0, \quad L_d \leq r \leq L_d + L, \quad t = 0, \tag{6.14}$$

$$c = 0, \quad L_d \leq r \leq L_d + L, \quad t = 0. \tag{6.15}$$

The model equations are based upon the previous ODE model (6.8-6.9). However, a diffusive

component, with associated free-diffusion coefficient D_f, has been added to the equation for c, which results in nonlinear coupled PDEs. Although it was noted earlier in the chapter that a constant source of antibiotic is unrealistic, it will be useful in this scenario to assess the behaviour of the PDE model and make adjustments where applicable. The model is nondimensionalised with the following scalings:

$$B' = \frac{B}{B_{max}}, \quad c' = \frac{c}{c_{50}}, \quad t' = k_{max}t, \quad r' = \frac{r}{L}.$$

For simplicity the following constants are defined: $\alpha = g/k_{max}$; $\beta = D_f/k_{max}L^2$; $\gamma = B_{max}/c_{50}$; $c^* = c_{in}/c_{50}$ and; $B^* = B_0/B_{max}$. Additionally, the scaled position of the boundary conditions are defined $r_1 = L_d/L$ and $r_2 = (L_d+L)/L$. From the scalings, and dropping primes for clarity, the following nondimensional model is derived:

$$\frac{\partial B}{\partial t} = \alpha B\left(1-B\right) - B\frac{c}{c+1}, \quad r_1 < r < r_2, \quad t > 0, \tag{6.16}$$

$$\frac{\partial c}{\partial t} = \beta\left(\frac{1}{r}\frac{\partial c}{\partial r} + \frac{\partial^2 c}{\partial r^2}\right) - \gamma B\frac{c}{c+1}, \quad r_1 < r < r_2, \quad t > 0, \tag{6.17}$$

$$c = c^*, \quad r = r_1, \quad t > 0, \tag{6.18}$$

$$\frac{\partial c}{\partial r} = 0, \quad r = r_2, \quad t > 0, \tag{6.19}$$

$$B = B^*, \quad r_1 \leq r \leq r_2, \quad t = 0, \tag{6.20}$$

$$c = 0, \quad r_1 \leq r \leq r_2, \quad t = 0. \tag{6.21}$$

Model equations (6.16-6.21) were solved numerically in MATLAB®R2019a using the Method of Lines (MOL). MOL involves replacing the spatial derivatives of a PDE with an algebraic approximation such as a finite difference approximation. This results in only the time variable remaining and thus, the PDE is approximated by a system of ODEs [103, p. 6]. Once this system of ODEs has been formulated, accounting for boundary and initial conditions, it may be solved using existing numerical solution methods for ODEs [103, p. 7]. Specifically, the "ode23t" solver was used, which is an implementation of the trapezoidal rule [104], a second order and implicit method [105, p. 8,10]. The default relative and absolute tolerance values were also used.

Since the model is nondimensional, the 1D geometry is the interval $[r_1, r_2]$, which was divided into N_r equally spaced points, giving a spatial step-size of $\delta r = (r_2 - r_1)/(N_r - 1)$. This spatial vector has N_r elements and the position of each element in this vector is identified with i, such that $1 \leq i \leq N_r$. The time interval considered was divided into N_t equally spaced time points. The model equations (6.16-6.21) were then rewritten to form a system of coupled ODEs, which depending on the location within the 1D geometry, will have a different form. The first and second spatial derivatives are approximated using the second order central difference approximation. This method of derivative approximation was chosen as it is a more accurate

method than forward or backward approximations, since the error is proportional to the square of the spatial step size [106, p. 184-185]. At the point $r = r_1$ i.e. $i = 1$, the first entry in the spatial vector, the coupled equations are:

$$\frac{dB}{dt} = \alpha B(1)\left(1 - B(1)\right) - B(1)\frac{c(1)}{c(1)+1},$$
$$\frac{dc}{dt} = 0.$$

The ODE for c is equal to zero as $c = c^*$, a constant, and therefore does not change with time. Within the domain, where $2 \leq i \leq N_r - 1$, the coupled equations are:

$$\frac{dB}{dt} = \alpha B(i)\left(1 - B(i)\right) - B(i)\frac{c(i)}{c(i)+1},$$
$$\frac{dc}{dt} = \beta\left(\frac{1}{r(i)}\frac{c(i+1) - c(i-1)}{2\delta r} + \frac{c(i+1) - 2c(i) + c(i-1)}{\delta r^2}\right) - \gamma B(i)\frac{c(i)}{c(i)+1},$$

At the point $r = r_2$ i.e. $i = N_r$, the coupled equations are:

$$\frac{dB}{dt} = \alpha B(N_r)\left(1 - B(N_r)\right) - B(N_r)\frac{c(N_r)}{c(N_r)+1},$$
$$\frac{dc}{dt} = \frac{2\beta}{\delta r^2}\left(c(N_r - 1) - c(N_r)\right) - \gamma B(N_r)\frac{c(N_r)}{c(N_r)+1},$$

where the zero-flux boundary condition (6.19) has been incorporated into the second spatial derivative approximation by using the central difference approximation, to remove the fictitious node $N_r + 1$:

$$\frac{\partial c}{\partial r} \approx \frac{c(N_r+1) - c(N_r-1)}{2\delta r} = 0 \quad \Rightarrow \quad c(N_r+1) = c(N_r-1).$$

Figure 6.7 shows the results of the model. It performs as expected: the constant concentration boundary condition permits drug to enter the domain and begin interacting with the bacteria. However, once all local bacteria have been killed, the drug must diffuse and attain an appropriate concentration to continue killing the bacteria. Although the bacterial concentration is relatively low initially, bacteria further to the right of the domain are able to grow and have managed to reach a normalised population size of $B \approx 0.8$ as shown in Figure 6.7 (a). The constant antibiotic supply then continues diffusing and killing the bacteria until the bacteria have been eradicated, i.e $B = 0$. Once the bacteria have been eliminated, the drug continues to diffuse into the domain, as shown in Figure 6.7 (b), until there is no longer a concentration gradient i.e. $c = c^*$. Since there is now a spatial component to the concentration of the antibiotic, the antibiotic must be especially potent as at the interface where the antibiotic and bacteria meet, there is a relatively low concentration of antibiotic. This is because newly delivered antibiotic

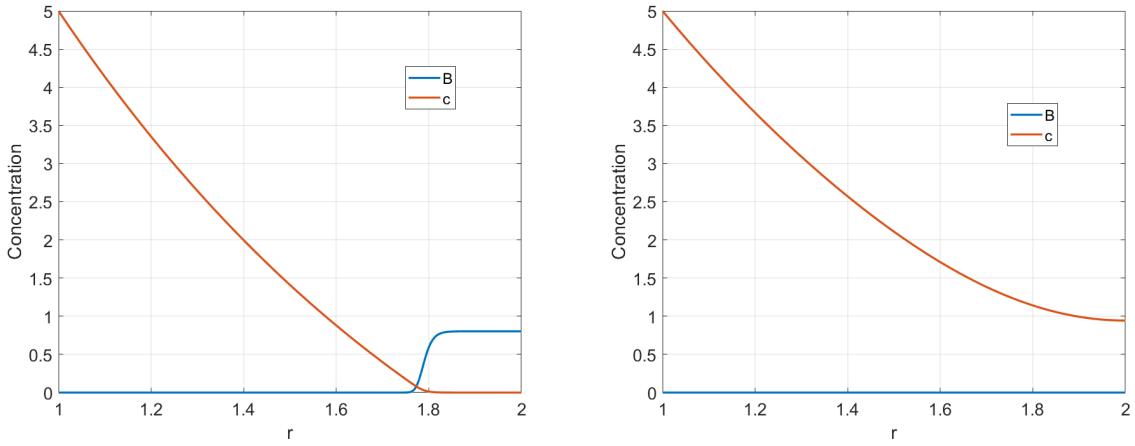

(a) (b)

Figure 6.7: Plots showing the nondimensional concentrations of antibiotic (c) and bacteria (B) versus nondimensional space. The nondimensional parameter values used were: $\alpha = 10^{-2}$; $\beta = 10^{-3}$; $\gamma = 10$; $c^* = 5$; $B^* = 10^{-1}$; $r_1 = 1$ and; $r_2 = 2$. These parameter values were arbitrarily chosen to demonstrate how the model works. The discretisation values used were $N_r = 600$ and $N_t = 1000$. These values of N_r and N_t were found to produce an accurate solution and further discretisation did not produce a noticeable change to the concentration plots. (a) After 1 hour of simulated time, most of the bacteria have been eliminated. (b) After 7 hours of simulated time, all the bacteria have been eradicated.

must diffuse to the constantly shifting bacteria/antibiotic interface. Although a constant source of drug is not realistic, it does demonstrate that the model works correctly, and the next step is to modify the model such that only a finite amount of antibiotic is delivered.

6.3.2 Finite drug delivery

There are a variety of ways to modify model boundary condition (6.18) such that only a finite amount of antibiotic is delivered. However, in the context of drug delivery, the most pertinent approach is via a release profile. Therefore, the new boundary condition will be a time-dependent boundary condition which will replicate the release profile of an antibiotic from a given device. The new boundary condition at $r = L_d$ involves $M(t)$, the mass of antibiotic still to be eluted from the device. This may be calculated analytically: here it is assumed that the antibiotic layer within the device is cylindrical in shape, with radius L_d and therefore, via symmetry, can be assumed to be 1D. The antibiotic is loaded with an initial concentration of c_0, and the transport of drug is a diffusion dominated process (Figure 6.8). With the assumption of a zero-flux boundary condition at $r = 0$ and and infinite sink condition at $r = L_d$, $c(x,t)$ and $M(t)$ may be readily calculated analytically. It should be noted that, for this approach to be valid, the timescale of diffusive transport in the domain must be much smaller than the release timescale [107]. Otherwise the problem will have to be fully coupled to the release equations.

Redefining c^* to be $c^* = c_0/c_{50}$, the calculated semi-analytical solution, via Separation of

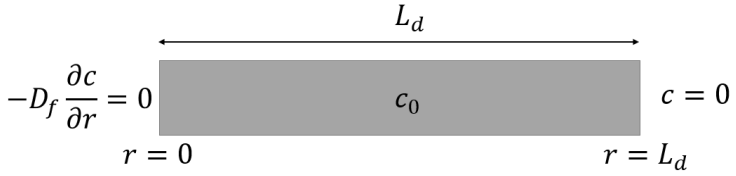

Figure 6.8: Illustration of the 1D domain of length L_d, which supplies the finite antibiotic, with initial concentration c_0, as a time-dependent mass-flux boundary condition, as shown in Figure 6.9.

Variables, of the model illustrated by Figure 6.8 is:

$$c(r,t) = \frac{2c^*}{r_1} \sum_{n=1}^{\infty} \frac{J_1(\lambda_n r_1)}{\lambda_n \left(J_1(\lambda_n r_1)^2 + J_0(\lambda_n r_1)^2\right)} J_0(\lambda_n r) \exp\left(-\lambda_n^2 \beta t\right) \tag{6.22}$$

where λ_n are the numerically computed solutions of:

$$J_0(\lambda_n r_1) = 0. \tag{6.23}$$

From solution (6.22), the mass function, $M(t)$, normalised with the initial mass of antibiotic, M_0, may be determined:

$$\frac{M(t)}{M_0} = M'(t) = \frac{4}{r_1^2} \sum_{n=1}^{\infty} \frac{J_1(\lambda_n r_1)^2}{\lambda_n^2 \left(J_1(\lambda_n r_1)^2 + J_0(\lambda_n r_1)^2\right)} \exp\left(-\lambda_n^2 \beta t\right), \tag{6.24}$$

where $M_0 = \pi L_d^2 z c_0$, with z denoting the height of the device supplying the antibiotic.

The geometry for the bacterial study (Figure 6.9) is the same as the one shown in Figure 6.6, albeit for a change in boundary condition at $r = L_d$.

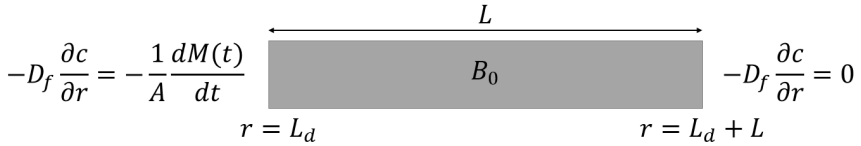

Figure 6.9: Illustration of the 1D domain with the time-dependent mass-flux boundary condition. $M(t)$ here is the mass remaining on the device, i.e. the mass of drug still to be eluted. An area factor, A, is required to balance the units.

The area factor, A, is the surface area of the device releasing the antibiotic and has the value $A = 2\pi z L_d$. Dimensionally, the time-dependent mass-flux boundary condition, at $r = L_d$, is:

$$-D_f \frac{\partial c}{\partial r} = -\frac{1}{2\pi z L_d} \frac{dM(t)}{dt}.$$

This expression can be transformed into the nondimensional form (omitting the primes for clar-

ity) using the previous scalings:

$$\frac{\partial c}{\partial r} = \frac{k_{max} L_d L c^*}{2D_f} \frac{dM(t)}{dt}. \tag{6.25}$$

By computing the first time derivative of (6.24), the full expression for the time-dependent mass-flux boundary condition is found to be:

$$\frac{\partial c}{\partial r} = -\frac{2c^*}{r_1} f(t). \tag{6.26}$$

where

$$f(t) = \sum_{n=1}^{\infty} \frac{J_1(\lambda_n r_1)^2}{J_1(\lambda_n r_1)^2 + J_0(\lambda_n r_1)^2} \exp\left(-\lambda_n^2 \beta t\right).$$

The proposed nondimensional model of bacterial growth subject to a diffusing, and finite, antibiotic is broadly the same as the constant source model (6.16-6.21), except for a change in boundary condition (6.18), which is replaced with the time-dependent mass-flux boundary condition (6.25):

$$\frac{\partial B}{\partial t} = \alpha B\left(1 - B\right) - B\frac{c}{c+1}, \quad r_1 < r < r_2, \quad t > 0, \tag{6.27}$$

$$\frac{\partial c}{\partial t} = \beta\left(\frac{1}{r}\frac{\partial c}{\partial r} + \frac{\partial^2 c}{\partial r^2}\right) - \gamma B\frac{c}{c+1}, \quad r_1 < r < r_2, \quad t > 0, \tag{6.28}$$

$$\frac{\partial c}{\partial r} = -\frac{2c^*}{r_1} f(t), \quad r = r_1, \quad t > 0, \tag{6.29}$$

$$\frac{\partial c}{\partial r} = 0, \quad r = r_2, \quad t > 0, \tag{6.30}$$

$$B = B^*, \quad r_1 \leq r \leq r_2, \quad t = 0, \tag{6.31}$$

$$c = 0, \quad r_1 \leq r \leq r_2, \quad t = 0. \tag{6.32}$$

Model equations (6.27-6.32) were solved numerically in MATLAB®R2019a using MOL, with the system of ODEs being solved using "ode23t", in much the same way as model equations (6.16-6.21) were solved, including the use of the default relative and absolute tolerance levels. The ODEs that arise from this application of MOL are largely identical to the ODE system derived from the application of MOL to model equations (6.16-6.21). However, the ODE for c, at $r = r_1$ $(i = 1)$, is very different as it is no longer a constant, it is now a time-dependent function. The mass-flux boundary condition (6.29) may be approximated using a first order central difference approximation:

$$\frac{\partial c}{\partial r} \approx \frac{c(2) - c(0)}{2\delta r} = -\frac{2c^*}{r_1} f(t),$$

from which an expression for the ficticious node, $i = 0$, may be derived:

$$c(0) = c(2) + \frac{4\delta r c^*}{r_1} f(t).$$

This expression may then be inserted into the second order central difference approximation to give the required ODE at $r = r_1$ $(i = 1)$:

$$\frac{dc}{dt} = 2\beta \left(\frac{1}{\delta r^2} \left(c(2) - c(1) \right) + \left(\frac{2}{\delta r} - \frac{1}{r_1} \right) \frac{c^*}{r_1} f(t) \right) - \gamma B(1) \frac{c(1)}{c(1) + 1}. \tag{6.33}$$

The infinite sum, $f(t)$, in the ODE (6.33), has a unknown summation and is dependent on the numerically derived roots of equation (6.23). Therefore, $f(t)$ must be truncated and to do so, a sufficient number of roots of equation (6.23) must be included. It was found that collecting the roots within the interval $[0, 10^3]$, was sufficiently accurate and taking more roots did not yield improved results. To check if the correct amount of nondimensional mass was being delivered by boundary condition (6.29), it was assumed that the initial nondimensional bacterial population was zero i.e. $B^* = 0$. Therefore, the delivered antibiotic would not be consumed and would gradually fill the domain, with the steady state concentration (c_{ss}) computed to be:

$$c_{ss} = \frac{r_1^2 c^*}{2r_1 + 1}.$$

The results shown in Figure 6.10 demonstrate that the antibiotic supply must be sufficient to kill the infecting bacteria, lest they recover, grow in number and cause a serious infection. The insufficient antibiotic outcome is shown in Figure 6.10 (a), in which most of the bacteria have been killed. The remaining individuals may be able to grow unhindered, cause infection and possibly lead to implant failure. The desirable outcome is shown in Figure 6.10 (b), in which the infecting bacteria have been eradicated and although there is unused antibiotic released, this remaining antibiotic, although unaccounted for in this model, may then be disposed of by the body [102, p. 17]. This model is considerably more realistic than the previous models examined. An antibiotic must travel to the site of infection to carry out its function. However, further improvements may be made, for example, it was assumed that the release of process of the antibiotic and its action on the bacteria may be uncoupled and this may not always be appropriate. Additionally, as a consequence of the model equations, the bacteria are unable to move throughout the domain, which is not likely to be realistic. Bacteria are able to move through their immediate surroundings, in search of nutrients, for example. Therefore, the next step in the mathematical investigation of bacterial growth subject to an antibiotic, will account for the potential that the release of the antibiotic will be affected by the action of the antibiotic on motile bacteria.

Should the situation arise in which an analytical/semi-analytical expression cannot be derived for the mass-flux boundary condition, it is possible to use the numerical solution of the

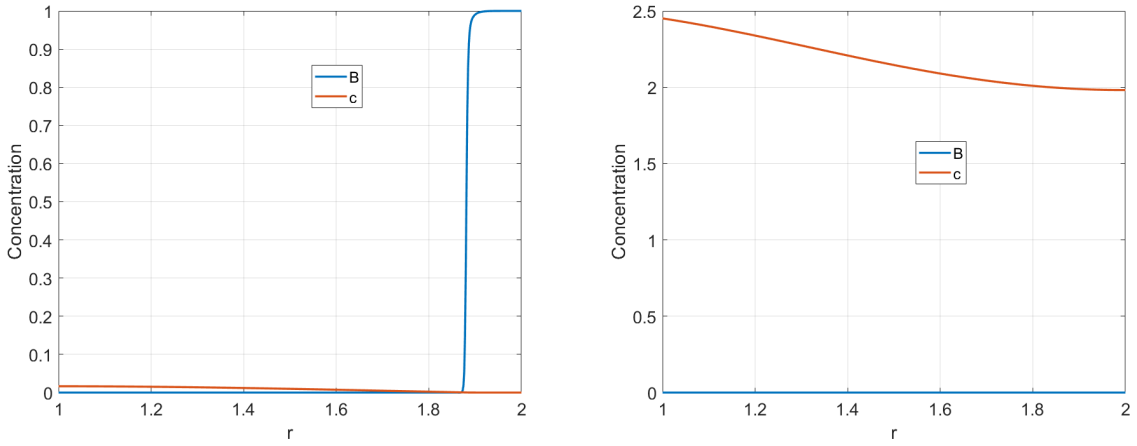

(a) (b)

Figure 6.10: Plots showing the nondimensional concentrations of antibiotic (c) and bacteria (B) versus nondimensional space. The nondimensional parameter values used were: $\alpha = 10^{-2}$; $\beta = 10^{-3}$; $\gamma = 10$; $B^* = 10^{-1}$; $r_1 = 1$ and; $r_2 = 2$. These parameter values were arbitrarily chosen to demonstrate how the model works. The discretisation values used were $N_r = 600$ and $N_t = 1000$. These values of N_r and N_t were found to produce an accurate solution and further discretisation did not produce a noticeable change to the concentration plots. (a) After 5 hours of simulated time and with $c^* = 10$, almost all of the antibiotic has been consumed. (b) After 3 hours of simulated time and with $c^* = 15$, all the bacteria have been eradicated.

release of an antibiotic instead. The time derivative of mass, $M(t)$, within equation (6.25), may be thought of as the numerical gradient of the release data. However, the number of entries within this numerical release vector must be identical to the number of time points where the solution is computed by the ODE solver. The ODE solvers within MATLAB®R2019a, use time stepping that satisfies the required tolerance levels and so to supply these timesteps with the correct mass-flux value, the numerical release data may be linearly interpolated at these timesteps. In the case where numerical release data is used, the required ODE at $r = r_1$ $(i = 1)$ is:

$$\frac{dc}{dt} = \beta \left(\frac{2}{\delta r^2} \left(c(2) - c(1) \right) + \left(\frac{1}{2r_1} - \frac{1}{\delta r} \right) \frac{L_d L k_{max} c^*}{D_f} \frac{dM(t)}{dt} \right) - \gamma B(1) \frac{c(1)}{c(1)+1}.$$

6.4 Fully coupled model with bacterial diffusion

Model equations (6.27-6.32) considered the case where the release process could be uncoupled from the reaction of the antibiotic on the bacteria. However, this may not be applicable and so it may be the case that the two processes must be coupled for a more realistic model. Additionally, it was assumed that the bacteria were static, merely growing in place until the maximum population size was achieved. This is also not realistic as the invading bacteria may be able to move. There are many reasons why the bacteria may move away from their immediate surroundings, one main reason is via chemotaxis, in which the bacteria may move up a

concentration gradient towards nutrients or down a concentration gradient to move away from harmful substances [108]. Most bacteria are considered motile and have a variety of means to swim through liquid environments or move over surfaces [108]. This is an active process in which the bacteria use energy to control their movement. There are also bacteria which are considered nonmotile and these bacteria must rely on passive influences to be able to move [109], for example, via a flowing fluid. Bacteria are very small and an averaged sized bacterium is considered to be the rod-shaped *Escherichia coli*, which is approximately $0.5\,\mu\mathrm{m}$ in diameter and $2\,\mu\mathrm{m}$ in length [110]. Previously mentioned in the chapter, *S. aureus*, one of the most common causes of implant-associated infection, is spherical in shape and has a approximate diameter of $1\,\mu\mathrm{m}$ [110].

Although there are bacteria which are motile and nonmotile, it may be sufficient to model their spreading behaviour as a diffusive transport mechanism. This is not unreasonable as bacteria are small and so may be considered particles, which can undergo diffusion. Additionally, there exists research on the subject of the diffusivity of bacteria, where efforts were made to experimentally measure the diffusion coefficients of several bacteria species. One particularly noteworthy conclusion, was that motile cells were able to move three orders of magnitude quicker than nonmotile cells [111].

Consider a 1D radial domain (Figure 6.11), subdivided into three regions of thicknesses L_d, L_B and L_m. The subscripts indicate which region the thicknesses are associated with: d indicates the region containing the initial concentration of antibiotic, c_0; B indicates the region containing the initial population of bacteria, B_0, and; m indicates the region which, although initially empty, the bacteria are able to move into and colonise. The interfaces between these regions are marked $r = L_1$ and $r = L_2$, which are defined $L_1 = L_d$ and $L_2 = L_d + L_B$. The endpoints are marked $r = 0$ and $r = L_3$, which is defined $L_3 = L_d + L_B + L_m$.

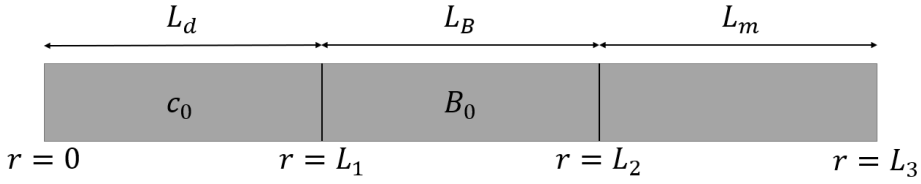

Figure 6.11: Illustration of the 1D domain comprised of three layers: The first layer, with radius L_d, contains the initial drug concentration, c_0; the second layer, with thickness L_B, contains the initial concentration of bacteria, B_0 and; the third layer, of thickness L_m, although initially empty, is able to be occupied by the antibiotic or colonised by the moving, and growing, bacteria. Additionally, the endpoints, $r = 0$ and $r = L_3$ and the position of the layer interfaces, $r = L_1$, $r = L_2$ and $r = L_3$, are shown.

Antibiotic and bacterial concentrations are defined $c_i(r, t)$ and $B_i(r, t)$, respectively, where $i = d, B, m$. The subscript d, B and m indicate the which region within the 1D domain each variable is associated with. Expanding upon the previous PDE model (6.27-6.32), the proposed model to

describe a diffusing, and growing, bacterial population, subject to a releasing antibiotic is:

$$\frac{\partial c_i}{\partial t} = D_f \left(\frac{1}{r}\frac{\partial c_i}{\partial r} + \frac{\partial^2 c_i}{\partial r^2} \right) - B_i \frac{k_{max} c_i}{c_i + c_{50}}, \quad t > 0, \tag{6.34}$$

$$\frac{\partial B_i}{\partial t} = D_B \left(\frac{1}{r}\frac{\partial B_i}{\partial r} + \frac{\partial^2 B_i}{\partial r^2} \right) + g B_i \left(1 - \frac{B_i}{B_{max}} \right) - B_i \frac{k_{max} c_i}{c_i + c_{50}}, \quad t > 0, \tag{6.35}$$

$$i = d : 0 < r < L_1, \quad i = B : L_1 < r < L_2, \quad i = m : L_2 < r < L_3.$$

The governing equations (6.34-6.35) are coupled with the following set of boundary and initial conditions:

$$-D_f \frac{\partial c_d}{\partial r} = 0, \quad -D_B \frac{\partial B_d}{\partial r} = 0 \quad r = 0, \quad t > 0, \tag{6.36}$$

$$c_d = c_B, \quad -D_f \frac{\partial c_d}{\partial r} = -D_f \frac{\partial c_B}{\partial r}, \quad r = L_1, \quad t > 0, \tag{6.37}$$

$$B_d = B_B, \quad -D_B \frac{\partial B_d}{\partial r} = -D_B \frac{\partial B_B}{\partial r}, \quad r = L_1, \quad t > 0, \tag{6.38}$$

$$c_B = c_m, \quad -D_f \frac{\partial c_B}{\partial r} = -D_f \frac{\partial c_m}{\partial r}, \quad r = L_2, \quad t > 0, \tag{6.39}$$

$$B_B = B_m, \quad -D_B \frac{\partial B_B}{\partial r} = -D_B \frac{\partial B_m}{\partial r}, \quad r = L_2, \quad t > 0, \tag{6.40}$$

$$-D_f \frac{\partial c_m}{\partial r} = 0, \quad -D_B \frac{\partial B_m}{\partial r} = 0 \quad r = L_3, \quad t > 0, \tag{6.41}$$

$$c_d = c_0, \quad 0 \le r \le L_1, \quad c_B = 0, \quad L_1 < r \le L_2,$$
$$c_m = 0, \quad L_2 < r \le L_3, \quad t = 0, \tag{6.42}$$
$$B_d = 0, \quad 0 \le r \le L_1, \quad B_B = B_0, \quad L_1 < r \le L_2,$$
$$B_m = 0, \quad L_2 < r \le L_3, \quad t = 0. \tag{6.43}$$

The major addition to this model, compared to previous models, is the inclusion of the bacterial diffusive transport component in the equations governing bacterial growth, with associated constant bacterial diffusion coefficient, D_B. The model equations (6.34-6.43) are nondimensionalised with the following scalings:

$$B_i' = \frac{B}{B_{max}}, \quad c_i' = \frac{c}{c_{50}}, \quad t' = k_{max} t, \quad r' = \frac{r}{L_d},$$

For simplicity, the following constants are defined: $\beta_1 = D_f / k_{max} L_d^2$; $\beta_2 = D_B / k_{max} L_d^2$; $\alpha = g / k_{max}$; $\gamma = B_{max} / c_{50}$; $B^* = B_0 / B_{max}$; $c^* = c_0 / c_{50}$; $r_1 = L_1 / L_d$, which by definition means that $r_1 = 1$; $r_2 = L_2 / L_d$ and; $r_3 = L_3 / L_d$. These scalings and simplifications give rise to the following nondimensional model (omitting the primes for clarity):

$$\frac{\partial c_i}{\partial t} = \beta_1 \left(\frac{1}{r}\frac{\partial c_i}{\partial r} + \frac{\partial^2 c_i}{\partial r^2} \right) - \gamma B_i \frac{c_i}{c_i + 1}, \quad t > 0, \tag{6.44}$$

$$\frac{\partial B_i}{\partial t} = \beta_2 \left(\frac{1}{r} \frac{\partial B_i}{\partial r} + \frac{\partial^2 B_i}{\partial r^2} \right) + \alpha B_i (1 - B_i) - B_i \frac{c_i}{c_i + 1}, \quad t > 0, \tag{6.45}$$
$$i = d : 0 < r < 1, \quad i = B : 1 < r < r_2, \quad i = m : r_2 < r < r_3.$$

The nondimensional governing equations (6.44-6.45) are coupled with the following set of nondimensional boundary and initial conditions:

$$\frac{\partial c_d}{\partial r} = 0, \quad \frac{\partial B_d}{\partial r} = 0 \quad r = 0, \quad t > 0, \tag{6.46}$$
$$c_d = c_B, \quad \frac{\partial c_d}{\partial r} = \frac{\partial c_B}{\partial r}, \quad r = 1, \quad t > 0, \tag{6.47}$$
$$B_d = B_B, \quad \frac{\partial B_d}{\partial r} = \frac{\partial B_B}{\partial r}, \quad r = 1, \quad t > 0, \tag{6.48}$$
$$c_B = c_m, \quad \frac{\partial c_B}{\partial r} = \frac{\partial c_m}{\partial r}, \quad r = r_2, \quad t > 0, \tag{6.49}$$
$$B_B = B_m, \quad \frac{\partial B_B}{\partial r} = \frac{\partial B_m}{\partial r}, \quad r = r_2, \quad t > 0, \tag{6.50}$$
$$\frac{\partial c_m}{\partial r} = 0, \quad \frac{\partial B_m}{\partial r} = 0 \quad r = r_3, \quad t > 0, \tag{6.51}$$
$$c_d = c^*, \quad 0 \leq r \leq 1, \quad c_B = 0, \quad 1 < r \leq r_2,$$
$$c_m = 0, \quad r_2 < r \leq r_3, \quad t = 0, \tag{6.52}$$
$$B_d = 0, \quad 0 \leq r \leq 1, \quad B_B = B^*, \quad 1 < r \leq r_2,$$
$$B_m = 0, \quad r_2 < r \leq r_3, \quad t = 0. \tag{6.53}$$

Model equations (6.44-6.53) were solved numerically using COMSOL®, version 5.3a, using the PARDISO method, with the BDF to handle time advancement and using the physics-based default relative and absolute tolerance levels. The 1D geometry was discretised using the densest built-in mesh settings, giving 2500 spatial points, which provided negligible error in the numerical solution at no appreciable increase in computational cost. The numerical concentration solutions were then exported and plotted using MATLAB®R2019a.

The results shown in Figures 6.12 and 6.13, again, demonstrate that the initial concentration of antibiotic must be sufficient to kill the infecting bacteria, otherwise they will be permitted to recover, grow in number and potentially cause a serious infection. The case of insufficient antibiotic is shown in Figure 6.12. Although most of the initial infecting bacteria, B^*, in the region $r_1 \leq r \leq r_2$, are killed, the bacteria have been able to move into the region $r_2 \leq r \leq r_3$ and continue growing. Whilst the bacteria at the antibiotic/bacteria interface are are being destroyed by the antibiotic, the bacteria further to the right of the interface are able to grow freely, as shown in Figure 6.12 (a). As time advances, it is clear from Figure 6.12 (b), that the initial drug loading, c^*, was insufficient to deal with the bacteria. Thus, the bacteria are able to grow in number and, with adequate time, spread throughout the entire domain. This scenario is clearly the least desirable outcome as potential failure of an implant may occur due

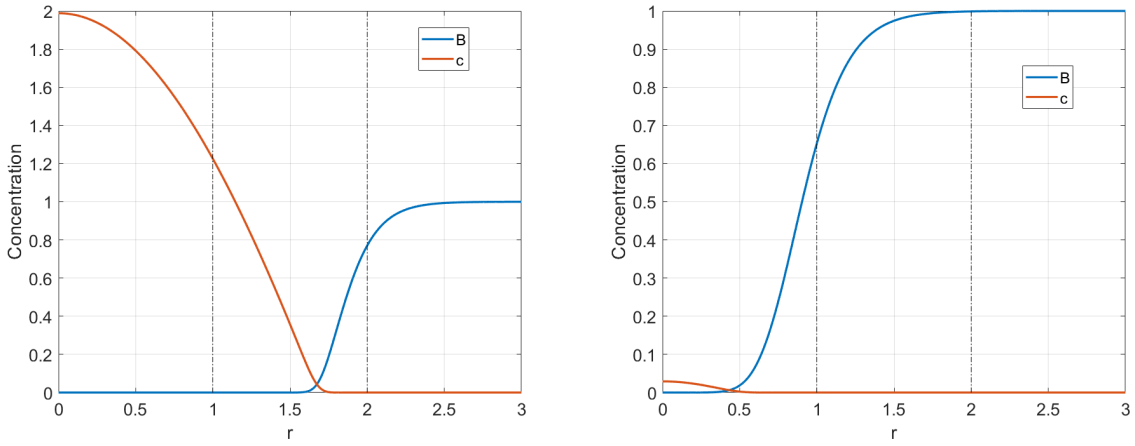

Figure 6.12: Plots showing the nondimensional concentrations of antibiotic (c) and bacteria (B) versus nondimensional space, where the dash-dotted lines indicate the position of the interfaces between the regions. The nondimensional parameter values used were: $\alpha = 10^{-2}$; $\beta_1 = 10^{-4}$; $\beta_2 = 10^{-3}$; $\gamma = 10$; $c^* = 30$; $B^* = 10^{-1}$; $r_2 = 2$ and; $r_3 = 3$. These parameter values were arbitrarily chosen to demonstrate how the model works. (a) After 30 minutes of simulated time most of the antibiotic has been consumed, but the bacteria have been mostly removed from the second layer (the B region). (b) After 45 minutes of simulated time, almost all of the antibiotic has been consumed and the bacteria have flourished.

to the likely infection caused by bacteria growing and spreading, with impunity. The preferable outcome is shown in Figure 6.13, in which the infecting bacteria have been eliminated. The residual antibiotic, although unaccounted for in this model, may then be disposed of by the body [102, p. 17]. Despite increasing $c^* = 30$ to $c^* = 35$, a relatively small amount, the outcome is drastically different to that shown in Figure 6.12. The bacteria, shown in Figure 6.13 (a), have managed to move to the right-most boundary of the geometry, whilst being subjected to the antibiotic, and attained a normalised bacterial concentration of $B \approx 0.2$. However, this population size is not enough to thwart the onslaught of the antibiotic, which eventually, kills all of the bacteria, as shown in Figure 6.13 (b).

This model is considerably more realistic than the previous models investigated. The diffusive transport component is a reasonable inclusion, since bacteria are not necessarily confined to a single location to grow. The diffusing bacteria may be thought of as seeking nutrients within the body to grow or to evade the antibiotic. This leads to the scenario of the antibiotic essentially "chasing" the bacteria until they have been eliminated. The mathematical investigation thus far has led to a core mathematical model of bacterial growth subject to an antibiotic in the form of nonlinear coupled PDEs. These PDEs account for the movement, growth and killing effect of an antibiotic on a bacterial population. The transport and consumption of the antibiotic is also modelled. It is possible to make further additions to the model to enhance its ability at capturing realistic processes, for example, the inclusion of the drug elimination process. However, it is

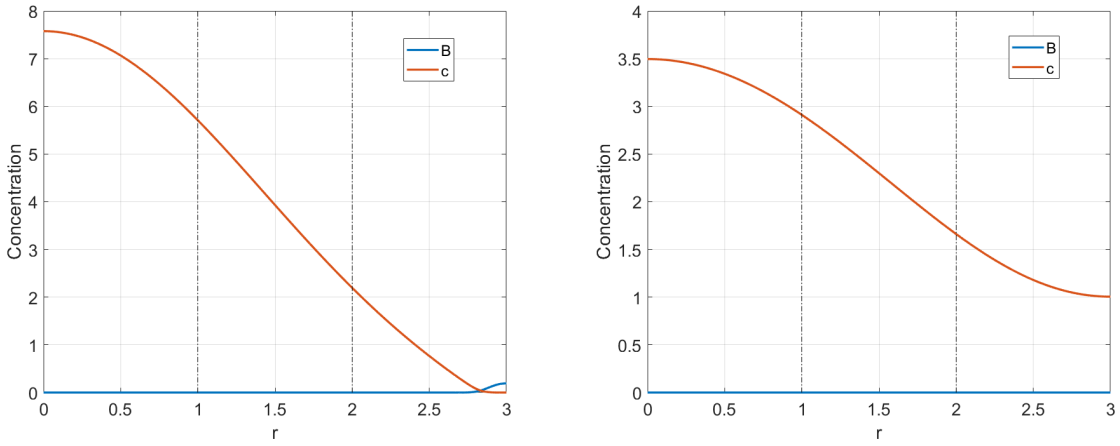

Figure 6.13: Plots showing the nondimensional concentrations of antibiotic (c) and bacteria (B) versus nondimensional space, where the dash-dotted lines indicate the position of the interfaces between the regions. The nondimensional parameter values used were identical to those used to generate the plots in Figure 6.12, except for the nondimensional initial antibiotic concentration, which was increased to $c^* = 35$. (a) After 15 minutes of simulated time, almost all of the bacteria have been eliminated. (b) After 30 minutes of simulated time, all the bacteria have been eradicated.

assumed that this process occurs on a much longer timescale to that of the action of an antibiotic on bacteria and is omitted. Therefore, the next step is to apply the current model to the prototype pins investigated in chapters 4 and 5.

6.5 Antibiotic release from the porous pin

The porous pin, investigated experimentally by Gimeno et al. [11], was examined mathematically in chapter 4. One of the key findings from the chapter was that drug-release could be modelled via a 1D mathematical model. This was the case as the pin is symmetric and the stirred release medium of the experiments provided a negligible advective component to drug transport. Therefore, a 1D diffusion-dissolution model was deemed appropriate (4.127-4.136). With some modifications, this model could be coupled with model equations (6.34-6.43) to test the theoretical ability of the porous pin to deliver a dissolving antibiotic, with the objective of eliminating a contaminating population of bacteria.

Consider a 1D geometry, comprised of four regions (Figure 6.14), each having a dissolved antibiotic concentration $c_j(r,t)$, with $j = d, p, B, m$. The last two regions additionally have bacterial concentration $B_i(r,t)$, where $i = B, m$. Similarly to the previous section, the subscript d, p, B, m indicate which region of the domain model components are associated with: d indicates the region containing the initial concentration of undissolved antibiotic, b_0; p indicates the porous wall region of the pin; B indicates the region containing the initial population of

bacteria, B_0, and; m indicates the region which, although initially empty, the bacteria are able to move into and colonise. From left to right: the innermost region of radius L_d is the drug core of the porous pin, which holds an initial concentration of undissolved antibiotic b_0, with an undissolved antibiotic concentration, $b(r,t)$; the next region, of thickness L_p, is the porous wall of the pin, with porosity ϕ; the next region, with thickness L_B, is the layer in which the initial contaminating bacterial population, B_0, resides and; the last region, with thickness L_m, is additional space for the bacteria to be able to diffuse into and grow. The position of the interfaces are defined to be the addition of layer thicknesses, such that $L_1 = L_d$, $L_2 = L_d + L_p$, $L_3 = L_d + L_p + L_B$ and the rightmost endpoint is $L_4 = L_d + L_p + L_B + L_m$.

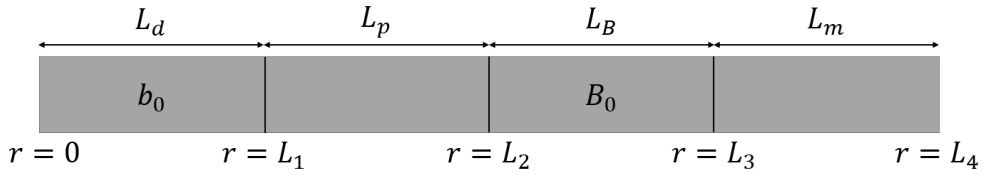

Figure 6.14: Illustration of the 1D domain comprised of four layers: The first layer contains the initial undissolved drug concentration, b_0; the second layer is the porous wall of the pin; the third region contains the infecting bacteria and; the last region is empty available space for the bacteria to move into and grow. The endpoints, $r = 0$ and $r = L_4$ and the position of the layer interfaces, $r = L_1$, $r = L_2$ and $r = L_3$, are shown.

The governing equations proposed to model bacterial growth, subject to a dissolving antibiotic being released from the porous pin are:

$$\frac{\partial b}{\partial t} = -\eta b^{\varepsilon}\left(S - c_d\right), \quad 0 < r < L_1, \quad t > 0, \tag{6.54}$$

$$\frac{\partial c_d}{\partial t} = D_f\left(\frac{1}{r}\frac{\partial c_d}{\partial r} + \frac{\partial^2 c_d}{\partial r^2}\right) + \eta b^{\varepsilon}\left(S - c_d\right), \quad 0 < r < L_1, \quad t > 0, \tag{6.55}$$

$$\phi\frac{\partial c_p}{\partial t} = D_p\left(\frac{1}{r}\frac{\partial c_p}{\partial r} + \frac{\partial^2 c_p}{\partial r^2}\right), \quad L_1 < r < L_2, \quad t > 0, \tag{6.56}$$

$$\frac{\partial c_i}{\partial t} = D_f\left(\frac{1}{r}\frac{\partial c_i}{\partial r} + \frac{\partial^2 c_i}{\partial r^2}\right) - B_i\frac{k_{max}c_i}{c_i + c_{50}}, \quad t > 0, \tag{6.57}$$

$$\frac{\partial B_i}{\partial t} = D_B\left(\frac{1}{r}\frac{\partial B_i}{\partial r} + \frac{\partial^2 B_i}{\partial r^2}\right) + gB_i\left(1 - \frac{B_i}{B_{max}}\right) - B_i\frac{k_{max}c_i}{c_i + c_{50}}, \quad t > 0, \tag{6.58}$$

$$i = B : L_2 < r < L_3, \quad i = m : L_3 < r < L_4.$$

Note that equations (6.57-6.58) are valid for both $i = B$ and $i = M$. The dissolution equation (6.54) differs only symbolically from its usage in chapter 4. In the equation, η is the dissolution rate of the antibiotic, ε is the reaction exponent which governs the type of reaction and S is the solubility of the antibiotic. Also returning from chapter 4 is the notion of an effective diffusion coefficient, D_p. This diffusion coefficient is applicable to the antibiotic whilst diffusing through the pin's porous wall and is defined $D_p = \phi_e D_f/\tau$, where ϕ_e and τ are the effective porosity and level of tortuosity of the porous wall, respectively. For simplicity, it is assumed that the

bacteria cannot colonise the porous region of the pin, should the antibiotic fail to eliminate the bacteria. In reality, the bacteria may be able to enter the pin if they are sufficiently small. The scale bar shown in the scanning electron microscope image of Figure 4.1 (a), has a reference size of $10\,\mu\mathrm{m}$ and although this suggests that the pore sizes of the pin's porous wall are small, bacteria may be able infiltrate the pin regardless. However, if this is the case, it is likely that the rate at which the bacteria can diffuse through the porous wall is relatively low, when compared to being able to diffuse in regions without the low level of porosity. The governing equations (6.54-6.58) are coupled with the following boundary and initial conditions:

$$-D_f\frac{\partial c_d}{\partial r}=0,\quad r=0,\quad t>0, \tag{6.59}$$

$$c_d=c_p,\quad -D_f\frac{\partial c_d}{\partial r}=-D_p\frac{\partial c_p}{\partial r},\quad r=L_1,\quad t>0, \tag{6.60}$$

$$c_p=c_B,\quad -D_p\frac{\partial c_p}{\partial r}=-D_f\frac{\partial c_B}{\partial r},\quad r=L_2,\quad t>0, \tag{6.61}$$

$$-D_B\frac{\partial B_B}{\partial r}=0,\quad r=L_2,\quad t>0, \tag{6.62}$$

$$c_B=c_m,\quad -D_f\frac{\partial c_B}{\partial r}=-D_f\frac{\partial c_m}{\partial r},\quad r=L_3,\quad t>0, \tag{6.63}$$

$$B_B=B_m,\quad -D_B\frac{\partial B_B}{\partial r}=-D_B\frac{\partial B_m}{\partial r},\quad r=L_3,\quad t>0, \tag{6.64}$$

$$-D_f\frac{\partial c_m}{\partial r}=0,\quad -D_B\frac{\partial B_m}{\partial r}=0,\quad r=L_4,\quad t>0, \tag{6.65}$$

$$b=b_0,\quad 0\le r\le L_1,\quad t=0, \tag{6.66}$$

$$c_d=0,\quad 0\le r\le L_1,\quad c_p=0,\quad L_1<r\le L_2,$$
$$c_B=0,\quad L_2<r\le L_3,\quad c_m=0,\quad L_3<r\le L_4,\quad t=0, \tag{6.67}$$

$$B_B=B_0,\quad L_2\le r\le L_3,\quad B_m=0,\quad L_3<r\le L_4,\quad t=0. \tag{6.68}$$

For simplification, the following constants are defined: $\chi=\eta b_0^{\varepsilon}/k_{max}$; $S^*=S/b_0$; $\beta_1=D_f/k_{max}L_d^2$; $\beta_2=D_p/k_{max}L_d^2$; $\beta_3=D_B/k_{max}L_d^2$; $\gamma=B_{max}/S$; $\delta=c_{50}/S$; $\alpha=g/k_{max}$; $D=D_p/D_f$; $B^*=B_0/B_{max}$; $r_1=L_1/L_d$, which by definition means that $r_1=1$; $r_2=L_2/L_d$; $r_3=L_3/L_d$ and; $r_4=L_4/L_d$. Model equations (6.54-6.68) are nondimensionalised with the following scalings:

$$B_i'=\frac{B_i}{B_{max}},\quad c_j'=\frac{c_j}{S},\quad b'=\frac{b}{b_0},\quad r'=\frac{r}{L_d},\quad t'=k_{max}t,$$

where $i=B,m$ and $j=d,p,B,m$. The simplifications and scalings result in the following nondimensional model (omitting the primes for clarity):

$$\frac{\partial b}{\partial t}=-\chi S^* b^{\varepsilon}\left(1-c_d\right),\quad 0<r<1,\quad t>0, \tag{6.69}$$

$$\frac{\partial c_d}{\partial t} = \beta_1 \left(\frac{1}{r}\frac{\partial c_d}{\partial r} + \frac{\partial^2 c_d}{\partial r^2} \right) + \chi b^{\varepsilon} \left(1 - c_d\right), \quad 0 < r < 1, \quad t > 0, \tag{6.70}$$

$$\phi\frac{\partial c_p}{\partial t} = \beta_2 \left(\frac{1}{r}\frac{\partial c_p}{\partial r} + \frac{\partial^2 c_p}{\partial r^2} \right), \quad 1 < r < r_2, \quad t > 0, \tag{6.71}$$

$$\frac{\partial c_i}{\partial t} = \beta_1 \left(\frac{1}{r}\frac{\partial c_i}{\partial r} + \frac{\partial^2 c_i}{\partial r^2} \right) - \gamma B_i \frac{c_i}{c_i + \delta}, \quad t > 0, \tag{6.72}$$

$$\frac{\partial B_i}{\partial t} = \beta_3 \left(\frac{1}{r}\frac{\partial B_i}{\partial r} + \frac{\partial^2 B_i}{\partial r^2} \right) + \alpha B_i \left(1 - B_i\right) - B_i \frac{c_i}{c_i + \delta}, \quad t > 0, \tag{6.73}$$

$$i = B : r_2 < r < r_3, \quad i = m : r_3 < r < r_4.$$

The nondimensional governing equations (6.69-6.73) are coupled with the following nondimensional boundary and initial conditions:

$$\frac{\partial c_d}{\partial r} = 0, \quad r = 0, \quad t > 0, \tag{6.74}$$

$$c_d = c_p, \quad \frac{\partial c_d}{\partial r} = D\frac{\partial c_p}{\partial r}, \quad r = 1, \quad t > 0, \tag{6.75}$$

$$c_p = c_B, \quad D\frac{\partial c_p}{\partial r} = \frac{\partial c_B}{\partial r}, \quad r = r_2, \quad t > 0, \tag{6.76}$$

$$\frac{\partial B_B}{\partial r} = 0, \quad r = r_2, \quad t > 0, \tag{6.77}$$

$$c_B = c_m, \quad \frac{\partial c_B}{\partial r} = \frac{\partial c_m}{\partial r}, \quad r = r_3, \quad t > 0, \tag{6.78}$$

$$B_B = B_m, \quad \frac{\partial B_B}{\partial r} = \frac{\partial B_m}{\partial r}, \quad r = r_3, \quad t > 0, \tag{6.79}$$

$$\frac{\partial c_m}{\partial r} = 0, \quad \frac{\partial B_m}{\partial r} = 0, \quad r = r_4, \quad t > 0, \tag{6.80}$$

$$b = 1, \quad 0 \leq r \leq 1, \quad t = 0, \tag{6.81}$$

$$c_d = 0, \quad 0 \leq r \leq 1, \quad c_p = 0, \quad 1 < r \leq r_2,$$

$$c_B = 0, \quad r_2 < r \leq r_3, \quad c_m = 0, \quad r_3 < r \leq r_4, \quad t = 0, \tag{6.82}$$

$$B_B = B^*, \quad r_2 \leq r \leq r_3, \quad B_m = 0, \quad r_3 < r \leq r_4, \quad t = 0. \tag{6.83}$$

Dimensional parameters associated with the porous pin are the same as those used in the porous pin sensitivity study of chapter 4 (see Table 6.1), except for the value of solubility, which was chosen to be $S = 50\,\mathrm{kg/m^3}$. This value of solubility was chosen as it is the higher value of solubility of the two antibiotics used by Gimeno et al. in their drug release experiments for the orifice pins (cefazolin sodium and linezolid) [12]. Although cefazolin sodium was not used in the drug release experiments with the porous pin, it was deemed that this value of solubility would be a suitable starting point. Model equations (6.69-6.83) were solved numerically using COMSOL®, version 5.3a, using the PARDISO method, with the BDF to handle time advancement and using the physics-based default relative and absolute tolerance levels. The 1D geometry was discretised using the densest built-in mesh settings. The 1D geometry was dis-

cretised using the densest built-in mesh settings, giving 2510 spatial points, which provided negligible error in the numerical solution at no appreciable increase in computational cost. The numerical concentration solutions were then exported and plotted using MATLAB®R2019a.

Parameter	Value
L_d	$1.575 \times 10^{-3}\,\mathrm{m}$ [11]
L_p	$1.6 \times 10^{-3}\,\mathrm{m}$ [11]
τ	3 [48]
ϕ	0.17 [11]
ϕ_e	$0.9 \times \phi$
ε	$2/3$ [34]
D_f	$1 \times 10^{-9}\,\mathrm{m}^2/\mathrm{s}$
$D_p = \phi_e D_f/\tau$	$5.1 \times 10^{-11}\,\mathrm{m}^2/\mathrm{s}$
η	$10^{-5}\,\mathrm{s}^{-1}(\mathrm{m}^{-3}\mathrm{kg})^{2/3}$
b_0	$505.19\,\mathrm{kg/m}^3$ [11]
S	$50\,\mathrm{kg/m}^3$ [12]

Table 6.1: Dimensional parameter values. These values are taken from the literature or inferred from [11]. The initial mass concentration, b_0, is calculated from the assumed drug mass loading of $100\,\mathrm{mg}$ and dividing by the interior volume of the porous pin.

Figures 6.15 and 6.16 show the results of the study into the theoretical ability of the porous pin to deliver antibiotic and eradicate a contaminating bacterial population. The results of the study suggest that there is a close link between the potency of the antibiotic and the outcome. This may be inferred from the fact that in both cases, the same mass of antibiotic is used, the only difference is the change in potency of the antibiotic. Dimensionally, this change corresponds to changing the value of c_{50} from 1 to 0.1, which changes the nondimensional parameter δ from 2×10^{-2} to 2×10^{-3}. The lowering of the value of c_{50} has the effect of lowering the concentration of antibiotic required to provide a $50\,\%$ killing rate i.e. $k_{max}/2$. Interestingly, in the early stages, both Figures 6.15 (a) and 6.16 (a) are quite similar, despite an order of magnitude difference in antibiotic potency. The high dependency on antibiotic potency is reasoned from the long-term behaviour of the model. Closer inspection of the plots shows that the concentration of antibiotic leaving the pin is relatively low and this may be a result of the low level of porosity of the pin limiting the release of the antibiotic. Compounding the limited release of antibiotic further is that the antibiotic must first dissolve before it may diffuse out of the porous pin, unlike all other previous models, which assumed that the antibiotic was initially in the solute phase. Examining Figures 6.15 (b) and 6.16 (b) show the consequences of changing antibiotic potency on the outcome. In Figure 6.15 (b), the antibiotic fails to eliminate the bacteria and this likely due to the low concentration of antibiotic being released, coupled with low antibiotic potency.

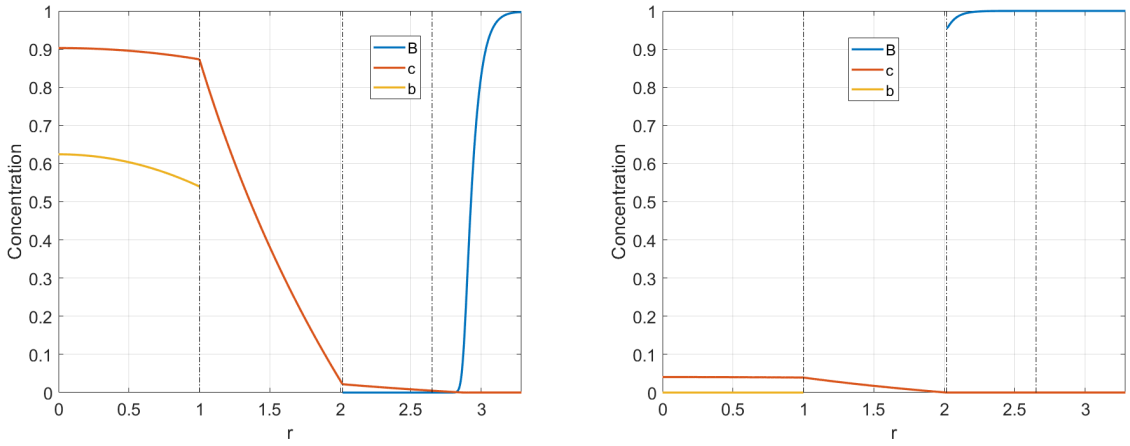

Figure 6.15: Plots showing the nondimensional concentrations of antibiotic (c) and bacteria (B) versus nondimensional space, where the dash-dotted lines indicate the position of the interfaces between the regions. The nondimensional parameter values used were: $\chi = 6.3431 \times 10^{-4}$; $S^* = 0.098973$; $\beta_1 = 4.0312 \times 10^{-4}$; $\beta_2 = 2.0559 \times 10^{-5}$; $\beta_3 = 4.0312 \times 10^{-6}$; $\gamma = 2 \times 10^{-1}$; $\delta = 2 \times 10^{-2}$; $\alpha = 10^{-3}$; $D = 0.051$ and; $B^* = 10^{-1}$. Parameter values not associated with the porous pin were arbitrarily chosen to demonstrate how the model works. (a) After 18 hours of simulated time, the initially contaminated region is free of bacteria. (b) After 72 hours of simulated time, almost all of the antibiotic has been consumed and the bacteria are free to grow.

As a result, the bacteria are able to continue growing whilst the antibiotic has a minimal effect. Despite the antibiotic being released at relatively low concentrations, the more potent antibiotic (Figure 6.16 (b)) is able to slowly kill the bacteria in spite of low concentrations of antibiotic, until it is able to overcome the growing bacteria. Additionally, an antibiotic of low potency but high solubility may be a suitable alternative, rather than the use of a more potent antibiotic. This is likely possible as although not relatively potent, such an antibiotic will have a greater concentration at the implant surface and hence, a higher effective killing rate.

It may be the case that this model is not fully representative of a realistic scenario. As previously discussed, bacteria may be able to enter the porous pin should the antibiotic fail to eliminate them, as the pore sizes of the pin's porous wall, although small, may be large enough to allow small bacterial cells in. One such example, which is one of the most common causes of implant-associated infection, is the spherically shaped *S. aureus*, with an approximate diameter of $1\,\mu\mathrm{m}$ [110]. Should an antibiotic fail to eradicate an infecting *S. aureus* population, the possibility of the bacteria colonising the interior of the pin poses a significant potential risk of implant failure. This further emphasises that the loaded mass of antibiotic must be sufficient, but also potent enough, to deal with the infecting bacteria.

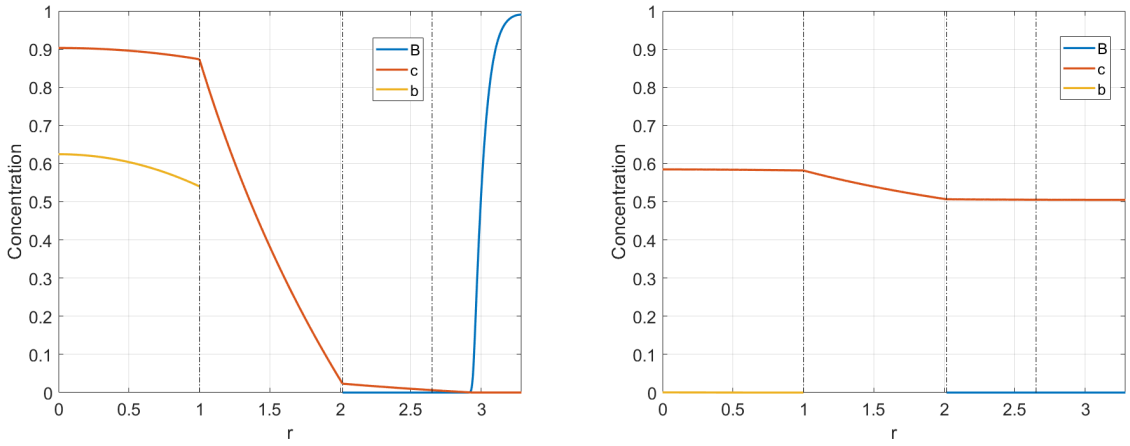

(a) (b)

Figure 6.16: Plots showing the nondimensional concentrations of antibiotic (c) and bacteria (B) versus nondimensional space, where the dash-dotted lines indicate the position of the interfaces between the regions. The nondimensional parameter values used were identical to those used to generate the plots in Figure 6.15, except for a change to δ, which was decreased to $\delta = 2 \times 10^{-3}$. (a) Similarly to Figure 6.15 (a), after 18 hours of simulated time, the initially contaminated region is free of bacteria. (b) After 72 hours of simulated time, all the bacteria have been eliminated.

6.6 Antibiotic release from the 8-orifice pin

The orifice pins, examined experimentally by Gimeno et al. [12], are a collection of prototype drug-releasing fixation pins with a differing number (2, 4, 6 or 8) of equidistant orifices. The extreme cases (the 2 and 8-orifice pins) were investigated mathematically in chapter 5. Some key findings of the chapter were that the orifice pins were an example where 3D mathematical modelling was required, as symmetry was not a viable option and because fluid flow could have a notable influence on the release of drug from the orifice pins. Although the drug release data collected by Gimeno et al. could not be captured by the model (5.29-5.40), there are many reasons discussed in chapter 5 as to why this may be the case. However, this does not halt further study into the theoretical abilities of the orifice pins to tackle a contaminating population of bacteria. With some modifications, model equations (5.29-5.40) may be coupled with model equations (6.34-6.43) to test the theoretical ability of the 8-orifice pin to release a dissolving antibiotic, with the aim of eradicating a contaminating population of bacteria. In this study, the 8-orifice pin was chosen, over the 2-orifice pin, as it was deemed the most likely of the two pins to achieve the desired outcome, since it has more orifices to release an antibiotic.

The geometry considered for this study is one quarter of the original orifice pin geometry, without the release medium component, as shown in Figure 5.2 (a) in chapter 5. This is due to the presence of two lines of symmetry: one cutting the pin in half and the other cutting through the centre of the orifices, to give a wedge-shaped geometry. These lines of symmetry are accept-

able to use in this study as it is assumed that the transport of antibiotic is diffusion-based and there is no fluid flow and thus, no advective component in both bacterial and antibiotic transport equations. Therefore, consider a 3D geometry, which is comprised of four regions (Figure 6.17), the first region is the inner drug core of the 8-orifice pin, with radius L_d, denoted Ω_1, which contains the initial concentration of undissolved antibiotic, b_0, and has a defined undissolved antibiotic concentration of $b(x, y, z, t)$. The next region is the collection of the pin's orifices, which, for the purpose of the mathematical investigation, are collectively denoted Ω_2 and have length L_o. It should be noted that although there appears to be more space than just the orifices in this region, this apparent space is actually the stainless-steel casing of the pin. The next region is Ω_3, with thickness L_B, and is the region that contains the initial contaminating bacterial population, B_0. Lastly, region Ω_4, with thickness L_m, is additional space for the bacteria to move into and grow. All regions have a defined bacterial and dissolved antibiotic concentration $B_i(x, y, z, t)$ and $c_i(x, y, z, t)$, respectively, where $i = \Omega_1, \Omega_2, \Omega_3, \Omega_4$. The bacterial concentration is defined throughout the entire geometry as, unlike the porous pin study in the previous section, it is assumed that the bacteria could colonise the 8-orifice pin in the event the antibiotic fails to eliminate them. This is reasoned to be a valid assumption as the orifices of the pin have a diameter of $0.5\,\mathrm{mm}$ [12], which is likely sufficiently large enough to allow the bacteria to diffuse into the pin.

The boundaries of the geometry are defined: Γ_1, this is the collection of all outer boundary surfaces of the geometry and the surfaces of the two caps at the top and bottom of the pin; Γ_2 is defined as the collection of semi-circular surfaces at the end of the orifices connecting Ω_1 and Ω_2; similarly, Γ_3 is the collection of semi-circular surfaces connecting Ω_2 and Ω_3 and; Γ_4 is the curved surface connecting Ω_3 and Ω_4.

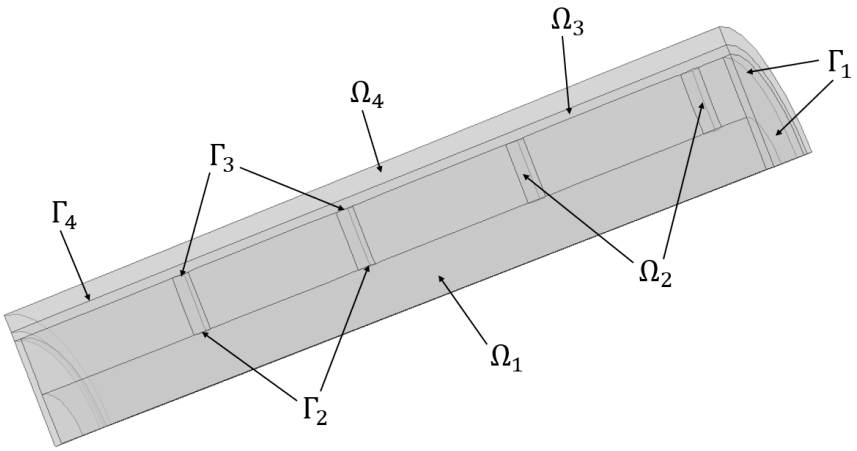

Figure 6.17: Illustration of the 3D geometry comprised of four regions: The first region, Ω_1, contains the initial undissolved drug concentration, b_0; the second region, Ω_2 is comprised of all the orifices of the geometry; the third region, Ω_3, contains the initial bacterial population and; the last region, Ω_4 is empty available space for the bacteria to move into and grow. The location of the boundaries Γ_1, Γ_2, Γ_3 and Γ_4 are also shown.

The governing equations proposed to model bacterial growth, subject to a dissolving antibiotic being released from the pin are:

$$\frac{\partial b}{\partial t} = -\eta b^{\varepsilon}\left(S - c_{\Omega_1}\right), \quad \text{in } \Omega_1, \quad t > 0, \tag{6.84}$$

$$\frac{\partial c_{\Omega_1}}{\partial t} = D_f \nabla^2 c_{\Omega_1} + \eta b^{\varepsilon}\left(S - c_{\Omega_1}\right) - B_{\Omega_1}\frac{k_{max} c_{\Omega_1}}{c_{\Omega_1} + c_{50}}, \quad \text{in } \Omega_1, \quad t > 0, \tag{6.85}$$

$$\frac{\partial B_{\Omega_1}}{\partial t} = D_B \nabla^2 B_{\Omega_1} + g B_{\Omega_1}\left(1 - \frac{B_{\Omega_1}}{B_{max}}\right) - B_{\Omega_1}\frac{k_{max} c_{\Omega_1}}{c_{\Omega_1} + c_{50}}, \quad \text{in } \Omega_1, \quad t > 0, \tag{6.86}$$

$$\frac{\partial c_n}{\partial t} = D_f \nabla^2 c_n - B_n \frac{k_{max} c_n}{c_n + c_{50}}, \quad t > 0, \tag{6.87}$$

$$\frac{\partial B_n}{\partial t} = D_B \nabla^2 B_n + g B_n\left(1 - \frac{B_n}{B_{max}}\right) - B_n \frac{k_{max} c_n}{c_n + c_{50}}, \quad t > 0, \tag{6.88}$$

$n = \Omega_2, \Omega_3, \Omega_4.$

The model is broadly similar to the model in the study of the porous pin in the previous section and parameters associated with the dissolution equation (6.84), have the same definition. The governing equations (6.84-6.88) are coupled with the following boundary and initial conditions:

$$\begin{aligned} &-\hat{\boldsymbol{n}} \cdot D_f \nabla c_{\Omega_1} = 0, \quad -\hat{\boldsymbol{n}} \cdot D_f \nabla c_{\Omega_2} = 0, \\ &-\hat{\boldsymbol{n}} \cdot D_f \nabla c_{\Omega_3} = 0, \quad -\hat{\boldsymbol{n}} \cdot D_f \nabla c_{\Omega_4} = 0, \qquad \text{on } \Gamma_1, \quad t > 0, \end{aligned} \tag{6.89}$$

$$c_{\Omega_1} = c_{\Omega_2}, \quad -\hat{\boldsymbol{n}} \cdot D_f \nabla c_{\Omega_1} = -\hat{\boldsymbol{n}} \cdot D_f \nabla c_{\Omega_2}, \quad \text{on } \Gamma_2, \quad t > 0, \tag{6.90}$$

$$B_{\Omega_1} = B_{\Omega_2}, \quad -\hat{\boldsymbol{n}} \cdot D_B \nabla B_{\Omega_1} = -\hat{\boldsymbol{n}} \cdot D_B \nabla B_{\Omega_2}, \quad \text{on } \Gamma_2, \quad t > 0, \tag{6.91}$$

$$c_{\Omega_2} = c_{\Omega_3}, \quad -\hat{\boldsymbol{n}} \cdot D_f \nabla c_{\Omega_2} = -\hat{\boldsymbol{n}} \cdot D_f \nabla c_{\Omega_3}, \quad \text{on } \Gamma_3, \quad t > 0, \tag{6.92}$$

$$B_{\Omega_2} = B_{\Omega_3}, \quad -\hat{\boldsymbol{n}} \cdot D_B \nabla B_{\Omega_2} = -\hat{\boldsymbol{n}} \cdot D_B \nabla B_{\Omega_3}, \quad \text{on } \Gamma_3, \quad t > 0, \tag{6.93}$$

$$c_{\Omega_3} = c_{\Omega_4}, \quad -\hat{\boldsymbol{n}} \cdot D_f \nabla c_{\Omega_3} = -\hat{\boldsymbol{n}} \cdot D_f \nabla c_{\Omega_4}, \quad \text{on } \Gamma_4, \quad t > 0, \tag{6.94}$$

$$B_{\Omega_3} = B_{\Omega_4}, \quad -\hat{\boldsymbol{n}} \cdot D_B \nabla B_{\Omega_3} = -\hat{\boldsymbol{n}} \cdot D_B \nabla B_{\Omega_4}, \quad \text{on } \Gamma_4, \quad t > 0, \tag{6.95}$$

$$b = b_0, \quad \text{in } \Omega_1, \quad t = 0, \tag{6.96}$$

$$\begin{aligned} &c_{\Omega_1} = 0, \quad \text{in } \Omega_1, \quad c_{\Omega_2} = 0, \quad \text{in } \Omega_2, \\ &c_{\Omega_3} = 0, \quad \text{in } \Omega_3, \quad c_{\Omega_4} = 0, \quad \text{in } \Omega_4, \quad t = 0, \end{aligned} \tag{6.97}$$

$$\begin{aligned} &B_{\Omega_1} = 0, \quad \text{in } \Omega_1, \quad B_{\Omega_2} = 0, \quad \text{in } \Omega_2, \\ &B_{\Omega_3} = B_0, \quad \text{in } \Omega_3, \quad B_{\Omega_4} = 0, \quad \text{in } \Omega_4, \quad t = 0, \end{aligned} \tag{6.98}$$

where $\hat{\boldsymbol{n}}$ is the outward facing unit normal appropriate for each surface. For simplification, the constants defined in the previous section are used again in this study: $\chi = \eta b_0^{\varepsilon}/k_{max}$; $S^* = S/b_0$; $\beta_1 = D_f/k_{max}L_d^2$; $\beta_2 = D_B/k_{max}L_d^2$; $\gamma = B_{max}/S$; $\delta = c_{50}/S$; $\alpha = g/k_{max}$ and; $B^* =$

B_0/B_{max}. Model equations (6.84-6.98) are nondimensionalised with the following scalings:

$$B_i' = \frac{B_i}{B_{max}}, \quad c_i' = \frac{c_i}{S}, \quad b' = \frac{b}{b_0}, \quad x' = \frac{x}{L_d}, \quad y' = \frac{y}{L_d}, \quad z' = \frac{z}{L_d} \quad t' = k_{max}t,$$

where $i = \Omega_1, \Omega_2, \Omega_3, \Omega_4$. The simplifications and scalings result in the following nondimensional model (omitting the primes for clarity):

$$\frac{\partial b}{\partial t} = -\chi S^* b^{\varepsilon} \left(1 - c_{\Omega_1}\right), \quad \text{in } \Omega_1, \quad t > 0, \tag{6.99}$$

$$\frac{\partial c_{\Omega_1}}{\partial t} = \beta_1 \nabla^2 c_{\Omega_1} + \chi b^{\varepsilon} \left(1 - c_{\Omega_1}\right) - \gamma B_{\Omega_1} \frac{c_{\Omega_1}}{c_{\Omega_1} + \delta}, \quad \text{in } \Omega_1, \quad t > 0, \tag{6.100}$$

$$\frac{\partial B_{\Omega_1}}{\partial t} = \beta_2 \nabla^2 B_{\Omega_1} + \alpha B_{\Omega_1} \left(1 - B_{\Omega_1}\right) - B_{\Omega_1} \frac{c_{\Omega_1}}{c_{\Omega_1} + \delta}, \quad \text{in } \Omega_1, \quad t > 0, \tag{6.101}$$

$$\frac{\partial c_n}{\partial t} = \beta_1 \nabla^2 c_n - \gamma B_n \frac{c_n}{c_n + \delta}, \quad t > 0, \tag{6.102}$$

$$\frac{\partial B_n}{\partial t} = \beta_2 \nabla^2 B_n + \alpha B_n \left(1 - B_n\right) - B_n \frac{c_n}{c_n + \delta}, \quad t > 0, \tag{6.103}$$

$n = \Omega_2, \Omega_3, \Omega_4.$

The nondimensional governing equations (6.99-6.103) are coupled with the following nondimensional boundary and initial conditions:

$$\hat{\boldsymbol{n}} \cdot \nabla c_{\Omega_1} = 0, \quad \hat{\boldsymbol{n}} \cdot \nabla c_{\Omega_2} = 0,$$
$$\hat{\boldsymbol{n}} \cdot \nabla c_{\Omega_3} = 0, \quad \hat{\boldsymbol{n}} \cdot \nabla c_{\Omega_4} = 0, \qquad \text{on } \Gamma_1, \quad t > 0, \tag{6.104}$$

$$c_{\Omega_1} = c_{\Omega_2}, \quad \hat{\boldsymbol{n}} \cdot \nabla c_{\Omega_1} = \hat{\boldsymbol{n}} \cdot \nabla c_{\Omega_2}, \quad \text{on } \Gamma_2, \quad t > 0, \tag{6.105}$$

$$B_{\Omega_1} = B_{\Omega_2}, \quad \hat{\boldsymbol{n}} \cdot \nabla B_{\Omega_1} = \hat{\boldsymbol{n}} \cdot \nabla B_{\Omega_2}, \quad \text{on } \Gamma_2, \quad t > 0, \tag{6.106}$$

$$c_{\Omega_2} = c_{\Omega_3}, \quad \hat{\boldsymbol{n}} \cdot \nabla c_{\Omega_2} = \hat{\boldsymbol{n}} \cdot \nabla c_{\Omega_3}, \quad \text{on } \Gamma_3, \quad t > 0, \tag{6.107}$$

$$B_{\Omega_2} = B_{\Omega_3}, \quad \hat{\boldsymbol{n}} \cdot \nabla B_{\Omega_2} = \hat{\boldsymbol{n}} \cdot \nabla B_{\Omega_3}, \quad \text{on } \Gamma_3, \quad t > 0, \tag{6.108}$$

$$c_{\Omega_3} = c_{\Omega_4}, \quad \hat{\boldsymbol{n}} \cdot \nabla c_{\Omega_3} = \hat{\boldsymbol{n}} \cdot \nabla c_{\Omega_4}, \quad \text{on } \Gamma_4, \quad t > 0, \tag{6.109}$$

$$B_{\Omega_3} = B_{\Omega_4}, \quad \hat{\boldsymbol{n}} \cdot \nabla B_{\Omega_3} = \hat{\boldsymbol{n}} \cdot \nabla B_{\Omega_4}, \quad \text{on } \Gamma_4, \quad t > 0, \tag{6.110}$$

$$b = 1, \quad \text{in } \Omega_1, \quad t = 0, \tag{6.111}$$

$$c_{\Omega_1} = 0, \quad \text{in } \Omega_1, \quad c_{\Omega_2} = 0, \quad \text{in } \Omega_2,$$
$$c_{\Omega_3} = 0, \quad \text{in } \Omega_3, \quad c_{\Omega_4} = 0, \quad \text{in } \Omega_4, \quad t = 0, \tag{6.112}$$

$$B_{\Omega_1} = 0, \quad \text{in } \Omega_1, \quad B_{\Omega_2} = 0, \quad \text{in } \Omega_2,$$
$$B_{\Omega_3} = B^*, \quad \text{in } \Omega_3, \quad B_{\Omega_4} = 0, \quad \text{in } \Omega_4, \quad t = 0. \tag{6.113}$$

Dimensional parameters associated with the 8-orifice pin in this study are the same as those used in the orifice pin sensitivity study of chapter 5 (see Table 6.2). Model equations (6.99-6.113) were solved numerically using COMSOL®, version 5.3a, using the GMRES method,

with the BDF to handle time advancement and using the physics-based default relative and absolute tolerance levels. The 3D geometry of Figure 6.17 was discretised using the built-in mesh settings using the "Normal" element size, this gave a mesh consisting of 6536 domain elements, 3738 boundary elements, and 489 edge elements (Figure 6.18).

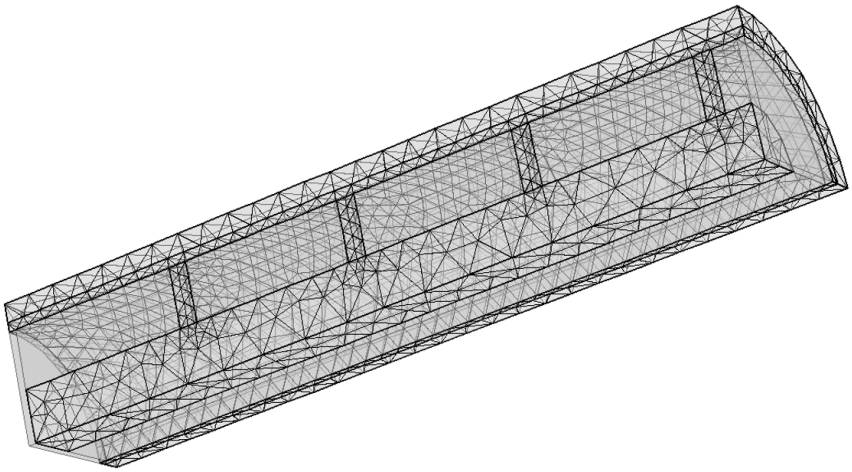

Figure 6.18: FEM mesh generated for the 3D 8-orifice pin geometry for the bactericidal study. Mesh consists of 6536 domain elements, 3738 boundary elements, and 489 edge elements.

Parameter	Value
L_d	$1.4 \times 10^{-3}\,\mathrm{m}$ [11]
L_o	$1.6 \times 10^{-3}\,\mathrm{m}$ [11]
ε	$2/3$ [34]
D_f	$1 \times 10^{-9}\,\mathrm{m}^2/\mathrm{s}$
η	$10^{-5}\,\mathrm{s}^{-1}(\mathrm{m}^{-3}\mathrm{kg})^{2/3}$
b_0	$193.8\,\mathrm{kg/m}^3$ [11]
S	$50\,\mathrm{kg/m}^3$ [12]

Table 6.2: Dimensional parameter values. These values are taken from the literature or inferred from [11]. The initial mass concentration, b_0, is calculated from the drug mass loading of $100\,\mathrm{mg}$ and dividing by the interior volume of the porous pin, then taking one quarter of this value since the 8-orifice has been reduced to one quarter of its original size.

Concentration plots in 3D do not necessarily provide immediate information on the overall behaviour of a model. Therefore, it was deemed reasonable to compute the nondimensional mass of b, c and B, to give a measure of model performance. The dimensional mass of b, c and B can be calculated via:

$$M_b(t) = \int_{\Omega_1} b\, d\Omega_1, \quad M_c(t) = \sum_{i=\Omega_1}^{\Omega_4} \int_i c_i\, di, \quad M_B(t) = \sum_{i=\Omega_1}^{\Omega_4} \int_i B_i\, di,$$

The mass equations for b and c may be normalised with the initial drug mass, M^0, and the mass equation for B may be normalised with the initial mass of bacteria, M_B^0. As this is a purely numerical investigation, not only are the masses of b, c and B approximated, but so too are the initial masses b_0 and B_0, which can be calculated via the integrals:

$$M^0 = b_0 \int_{\Omega_1} d\Omega_1, \quad M_B^0 = B_0 \int_{\Omega_3} d\Omega_3.$$

Using the nondimensional scalings, the normalised equations for mass are:

$$\frac{M_b(t)}{M^0} = \frac{b_0 L_d^3 \int_{\Omega_1'} b' \, d\Omega_1'}{b_0 L_d^3 \int_{\Omega_1'} d\Omega_1'}, \quad \frac{M_c(t)}{M^0} = \frac{S L_d^3 \sum_{i=\Omega_1'}^{\Omega_4'} \int_i c_i' \, di}{b_0 L_d^3 \int_{\Omega_1'} d\Omega_1'}, \quad \frac{M_B(t)}{M_B^0} = \frac{B_{max} L_d^3 \sum_{i=\Omega_1'}^{\Omega_4'} \int_i B_i' \, di}{B_0 L_d^3 \int_{\Omega_3'} d\Omega_3'}.$$

Simplifying and dropping the primes for clarity:

$$\frac{M_b(t)}{M^0} = \frac{\int_{\Omega_1} b \, d\Omega_1}{\int_{\Omega_1} d\Omega_1}, \quad \frac{M_c(t)}{M^0} = \frac{S^* \sum_{i=\Omega_1}^{\Omega_4} \int_i c_i \, di}{\int_{\Omega_1} d\Omega_1}, \quad \frac{M_B(t)}{M_B^0} = \frac{\sum_{i=\Omega_1}^{\Omega_4} \int_i B_i \, di}{B^* \int_{\Omega_3} d\Omega_3}. \tag{6.114}$$

The set of nondimensional mass equations (6.114) were computed using Gaussian quadrature within COMSOL®, version 5.3a, and the numerical masses were then exported and plotted using MATLAB®R2019a.

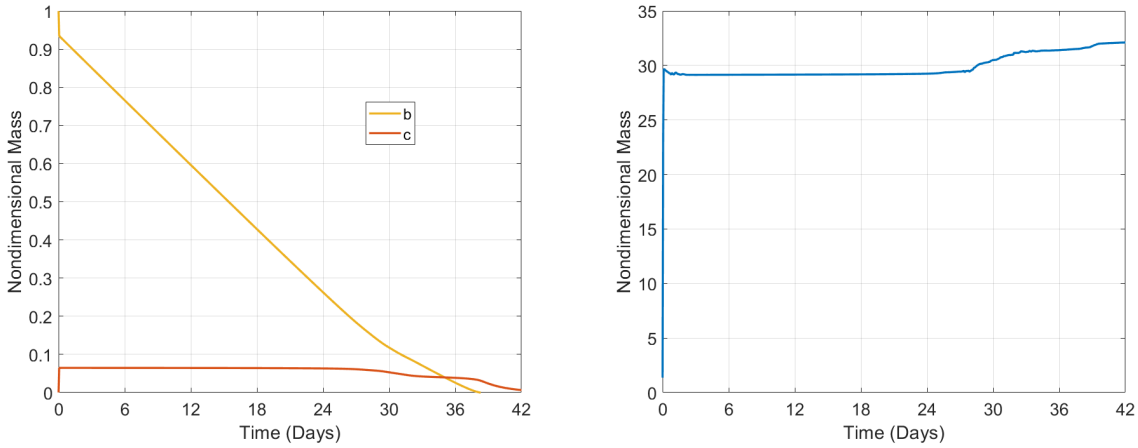

(a) (b)

Figure 6.19: Plots showing the nondimensional masses of b, c and B versus time. The nondimensional parameter values used were: $\chi = 8.4387 \times 10^{-4}$; $S^* = 0.0645$; $\beta_1 = 5.102 \times 10^{-4}$; $\beta_2 = 5.102 \times 10^{-6}$; $\gamma = 2 \times 10^{-1}$; $\delta = 2 \times 10^{-2}$; $\alpha = 10^{-3}$; and; $B^* = 10^{-1}$. Parameter values not associated with the 8-orifice pin were arbitrarily chosen to demonstrate how the model works. (a) Plot showing both undissolved and dissolved antibiotic consumption, with almost all antibiotic consumed by 42 days of simulated time. (b) Corresponding plot showing bacterial growth. After 42 days of simulated time, the bacteria are able to grow unhindered, as the antibiotic is almost completely consumed.

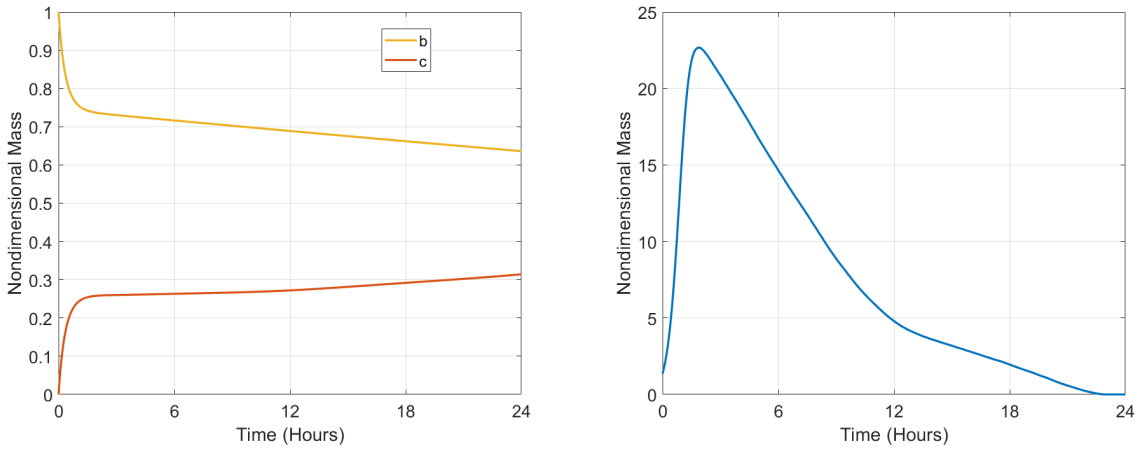

(a) (b)

Figure 6.20: Plots showing the nondimensional masses of b, c and B versus time. The nondimensional parameter values used were identical to those used to generate the plots in Figure 6.19, except for a change to the dimensional solubility of the antibiotic, S, which was increased from 50 to 200. This changes the value of three model parameters, which have the new values: $S^* = 0.258$, $\gamma = 5 \times 10^{-2}$ and $\delta = 5 \times 10^{-3}$. (a) Plot showing the consumption of the undissolved and dissolved antibiotic, indicating that approximately a third of the antibiotic has dissolved after 24 hours of simulated time. (b) Corresponding plot showing the nondimensional mass of bacteria. Although there is a burst of growth in the early stages, the more soluble antibiotic is able to kill the diffusing and growing bacteria by approximately 24 hours of simulated time.

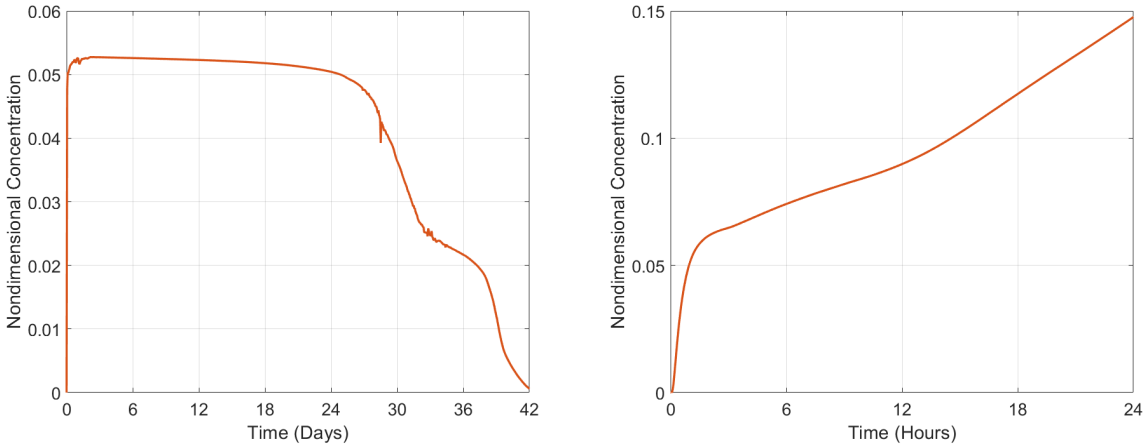

(a) (b)

Figure 6.21: Plots showing the average antibiotic concentration at Γ_3, which is the collection of semi-circular boundary surfaces connecting Ω_2 and Ω_3. (a) Plot showing the average concentration of antibiotic, of solubility $50\,\mathrm{kg/m^3}$, at Γ_3. The bumps in the plot are numerical artifacts which would be smoothed by taking more time steps, increasing the computational cost. (b) Plot showing the average concentration of antibiotic, of solubility $200\,\mathrm{kg/m^3}$, at Γ_3.

Figures 6.19 and 6.20 show the results of the study into the theoretical ability of the 8-orifice to deliver antibiotic and eradicate a contaminating bacterial population. The results of the study suggest that there is a close link between the solubility of the antibiotic and the outcome. This may be inferred from the results: although the same mass of antibiotic is used in both cases, the only difference is the change in the solubility of the antibiotic. Dimensionally, this change corresponds to changing the value of S from 50 to 200, which results in a change in the value of three nondimensional parameters: S^*, whose value increases from 0.0645 to 0.258; γ, whose value decreases from 2×10^{-1} to 5×10^{-2} and; δ, whose value decreases from 2×10^{-2} to 5×10^{-3}. This increase in antibiotic solubility has the effect of increasing the antibiotic concentration at the pin's surface and thus, increasing the effective killing rate of the antibiotic. This increase in concentration can be seen when comparing the plots in Figure 6.21, which indicate that the concentration at the surface of the pin, adjacent to the orifices, is able to reach considerably higher values, as a result of increased antibiotic solubility. Further examination of the results also suggests that the geometry of the 8-orifice pin is an important factor to consider as the orifices of the pin are reasonably small in diameter $(0.5\,\mathrm{mm})$ and so will limit the rate at which the antibiotic may be release from the pin. Much like the porous pin study in the previous section, the release of antibiotic is also further limited by the antibiotic dissolution process. From these observations, it is reasonable to conclude that these antibiotic release limitations may be alleviated through the use of a more soluble antibiotic or perhaps through geometric changes, such as increasing, or decreasing, the diameter of the orifices. The outcome of low antibiotic solubility is shown in Figure 6.19, which despite the antibiotic being released, the bacteria are able to diffuse and grow as shown by the mass increase in Figure 6.19 (b), ultimately depleting

the entire supply of antibiotic. The desirable outcome is shown in Figure 6.20, in which the more soluble antibiotic is able to be released at considerably higher concentrations. Although the bacteria have time to grow initially, as shown by the increase of bacterial mass in Figure 6.20 (b), the concentration of antibiotic is much too high and so the bacteria are eventually eliminated. Alternatively, the antibiotic could may continue to have a low solubility, but be more potent. Although the concentration of antibiotic would be relatively low, the higher potency would mean that the effective killing rate would be greater.

6.7 Conclusions

This chapter details the process of mathematically modelling bacterial growth, subject to the presence of an antibiotic. Although initially simplistic, it is worth considering the basics of bacterial growth and as such, the modelling reflects this. For example, the structure of the mathematics which inform the growth of bacteria plays an important role in forming the later, more complex, mathematical models. In light of that, it was assumed that logistic bacterial growth would be a reasonable starting point to build upon. Also considered was the form of the reaction an antibiotic has on a bacterial population. To begin with, a constant decay rate was considered, where the antibiotic was infinite in its supply. This, of course, is not realistic for two main reasons: an antibiotic is not limitlessly available, there is a finite amount and the killing effect of an antibiotic is not constant, it is variable since below a certain concentration, an antibiotic has little to no effect. Therefore, it was assumed that Michaelis-Menten-like reaction kinetics would account for a varying killing effect of an antibiotic, based on its concentration. The mathematical modelling at this point worked as expected: if there was too little antibiotic, the bacteria would be permitted to grow. However, the one assumption that was clearly not suitable, was that the antibiotic was initially mixed in with the bacterial population, when in fact, in the context of delivery of antibiotics from OIs, the antibiotic would be delivered.

In the case of antibiotic delivery, the antibiotic would be considered as spatially varying and with that, the need for PDEs arises. Although a constant source of antibiotic was studied at first, the results demonstrated that the model worked as expected and with that, the shift to a model where a finite amount of antibiotic was made. This point in the modelling investigation considered the scenario where the release process of the antibiotic and its action on a bacterial population could be uncoupled. This is a useful simplification where it is possible to use analytical solutions, however, it may not be the case that this is possible as the action of an antibiotic on bacteria may influence the release process. Therefore, the next reasonable step was to couple these two processes, along with the addition of bacterial diffusion. It is known that bacteria are able to move, either in an active or passive way, they are not necessarily static and confined to one point. There has been research in the past that sought to quantify the diffusion coefficients of different species of bacteria, both motile and nonmotile, and one important result, relevant

to this chapter, is that motile bacteria may move as much as three orders of magnitude faster than nonmotile species. Therefore, based upon this previous research and that bacteria are very small, so may be considered small particles, the inclusion of bacterial diffusion was deemed reasonable. The results of this addition are as expected, with the delivery of an antibiotic, a bacterial population need not remain in place and succumb to the antibiotic, but rather spread out into more space and grow. The results also clearly demonstrated the need for a sufficient amount of antibiotic for a specific level of potency.

Lastly, the most complete model of bacterial growth subject to an antibiotic was, with some modifications, applied to the porous pin and 8-orifice pin of chapters 4 and 5, respectively. There are a few major differences between these pins and one of the most important was that the release process of antibiotic from the porous pin could be reduced to a 1D model, whereas the 8-orifice pin required 3D modelling. One more addition was made at this stage of the modelling investigation and that was the dissolution of the antibiotic. This was thought to be necessary to increase the realistic nature of the models as an antibiotic would be likely loaded into a device as dry powder. The results from the two models suggested that the outcome is dependent on both the properties of the antibiotic and the geometry of the device releasing the antibiotic. It was found that both the solubility and the potency of the antibiotic had an influence on the outcome. Should an antibiotic have too low a solubility or if not potent enough, the antibiotic would likely fail to eliminate the bacteria. Complicating matters is that the geometry of the antibiotic-releasing device is also an important factor in determining the concentration of antibiotic at the surface of the device i.e. the concentration of released antibiotic. Should the device not release antibiotic in sufficient quantities, the antibiotic is likely to fail. This is particularly a potential risk in the context of orthopaedic devices as if the scenario should arise where an antibiotic fails to eradicate the bacterial population, the bacteria may then move into and colonise the device. This is a serious outcome and may lead to device failure and would require costly surgery to rectify.

Chapter 7

Conclusions and future research

7.1 Conclusions

The early chapters of this thesis comprised a detailed review of the existing literature on drug releasing OIs. This somewhat detailed exploration revealed a promising opportunity for the use of mathematical modelling as an additional tool in the development of enhanced OIs. Using a combination of analytical and numerical approaches, a series of models of increasingly complexity were developed, starting from the description of drug release from a general two-layer porous material, before specialising to two specific porous prototype implants that had been investigated experimentally in the literature. The research presented in this thesis concluded with a series of models representing a "first attempt" at understanding the interplay between drug release from OIs and bacterial inhibition. A number of conclusions arise from the work and may be summarised as follows:

The scientific literature lacks mathematical modelling of drug release from OIs

The scientific literature contains numerous examples of experimental research into the general subject of drug release from orthopaedic devices. These experiments not only cover the topic of drug release, but also the study of novel materials, with a view of using these materials in an orthopaedic setting. One important finding from the literature review, was that most research is currently focussed on *in vitro* studies, with very few examples that extend to the *in vivo* setting. This suggests that this particular area of research is fairly new. Despite mathematical modelling of drug release now being a mature topic, it was striking that there was a lack of such modelling in the particular field of orthopaedics. As a result of this, a paper was written, and published, which investigated the likelihood of mathematical modelling being of great benefit to this research field [112].

Variable porosity can be used to fine-tune drug release

There is plentiful experimental research into OIs, which make use of porosity, on various scales, to control the release of drugs. This idea was explored mathematically in chapter 3. This work centred on the idea of using variable porosity as a novel approach in controlling the release of a drug from a device. Presented in chapter 3 is the derivation of an appropriate model and its semi-analytical solution, along with a sensitivity analysis of a few key system parameters. The model results indicate that certain parameters may be tuned to provide the desired drug release profile, particularly the ratio of the effective diffusion coefficients, χ.

Experimental conditions matter

To provide the greatest possible benefit and usefulness, a mathematical model must reflect the conditions of an experimental setup. One key feature that appeared in the experimental work on the porous and orifice pins, was that the release medium was stirred. This stirring may have a sizeable influence on the release of drug from both pins and was worth investigating the extent to which fluid flow could theoretically affect the release of drug from the pins. The result of this investigation gave two completely different outcomes for the respective pins. In the case of the porous pin, it was found that fluid flow had no appreciable influence on the rate of drug release from the pin. On the other hand, in the case of the orifice pins, fluid flow was important, especially as the number of orifices the pin had drilled into its outer wall increased. This is an important result as it suggests that the experimental setup is likely to influence the results of the experiment. In other words, how the release medium is stirred, and at what rate, may be crucial factors to consider when designing an experimental setup, especially if the *in vivo* release profile is to be inferred from the *in vitro* experiments.

Additionally, what drugs are used is most likely another heavily contributing factor in the release of drug during an experiment as drug solubility was a component that received much consideration in the mathematical models of chapter 4 and 5. It was demonstrated that the inclusion of nonlinear dissolution within the governing equations significantly slowed the drug release compared with a diffusion-only or advection-diffusion model. From the results of the mathematical investigation of the pins, it is also reasonable to conclude that the overall design of the geometry of the device may have a highly influential role in determining the rate of drug release and how the experiment should be conducted. The porous pin, for example, is for the most part, impervious to fluid flow and therefore, the stirring of the release medium may not be crucial to the release profile, although it may help ensure a uniform concentration of drug in the release medium for sampling purposes. On the other hand, in the case of the orifice pins, particularly the 2-orifice pin, the release profiles for both drugs used in the experiments are quite similar. From this it would seem that the geometry of the pin limited the release of drug, despite an order of magnitude difference in solubility between the two drugs: this is an effect that may be explained with the model. From the literature, much of the experimental research is centred

on *in vitro* studies and therefore, one needs to be careful what conclusions are drawn from such studies and how they may relate to the *in vivo* scenario. Ideally, the *in vitro* conditions should be chosen to mimic as closely as possible the intended *in vivo* environment.

Drug dissolution is an important consideration, and could be the rate-limiting process

Another key experimental component was that the drugs used were in a powdered form and, as a result, the drug must dissolve in the release medium before transport out of the pins is possible, whether it be by purely diffusive means in the case of the porous pin or by a combination of diffusion and advection in the case of the orifice pins. Although the models constructed included an equation which accounted for the dissolution process, this does however introduce more parameters, whose values are uncertain.

1D modelling is often sufficient

One particularly interesting result that arose from the work in this thesis is that mathematical modelling need not always require full 3D modelling to be representative of reality. For instance, drug release from the porous pin is very likely a 1D problem as a result of the cylindrical geometry, this is evidenced by the fluid flow study results, which suggest that the stirred release medium had a negligible influence on the rate of drug release. The benefits of a 1D mathematical model include the reduction of the spatial component to an interval and with that, the governing equations may be represented in a simpler way. Additionally, 1D models may also be solved analytically, or semi-analytically. Although it would be much quicker to solve a 1D model numerically, an analytical solution offers insight into how model parameters may relate and to what extent their influence may be. Most importantly, in the case of the porous pin, the demonstration that the 3D geometry could be reduced to a 1D model through consideration of an analytical solution allowed the more complex dissolution-diffusion model to be solved numerically in only one dimension, greatly reducing computation time.

Parameter values

A mathematical model can only ever be as accurate as its inputs and therefore, accurate parameter values are often necessary, and this lack of information should be urgently addressed. For example, precise values for diffusion coefficients for the drugs used in the experiments is unknown and if they were available, they would most likely correspond to diffusion in water, not SBF. Although drug solubility values in water are available, these values are likely to change in SBF, since SBF is comprised of charged particles. Compounding uncertainty further is the lack of data on the fluid properties of SBF, for example, dynamic viscosity and density. These are necessary pieces of information as they inform how a fluid flows and thus, how an advective component of a drug transport equation will behave. Therefore, in lieu of some necessary

information, it was assumed that the release medium was water and a sensitivity analysis was performed using key system parameters, such as drug solubility, the drug dissolution rate, the level of porosity in the case of the porous pin and orifice diameter is the case of the orifice pins. The results demonstrated that there was a range of sensitivity in changes to the release profiles for different parameters, in which slight changes to one or two parameters could drastically change the release profile. The lack of accurate parameter values likely explains the somewhat unsatisfactory agreement between model output and experimental data, particularly in the case of the orifice pins.

Bacterial infection

The penultimate chapter of this thesis focussed on the growth of bacteria subject to the presence of an antibiotic and two clear conclusions can be drawn from the results. The antibiotic release profile and the concentration of antibiotic close to the surface of the device are crucial factors in eliminating an infecting bacterial population. There are two distinct outcomes, either the antibiotic eradicates the bacteria, or the bacteria are able withstand the antibiotic until it is consumed, then are able to grow. The results suggest that there are complex relationships between the success of an antibiotic, its inherent qualities and how it is released from a device. For example, when considering antibiotic release from the porous pin, the antibiotic is released from the pin at relatively low concentrations, most likely due to the low level of porosity of the pin's outer wall. This results in the effective killing rate of the antibiotic being rather low, however, when altering the potency of the antibiotic, despite the low level of concentration, the antibiotic is able to eliminate the bacteria. In the case of antibiotic release from the 8-orifice pin, although surface concentration is low initially, allowing for a more soluble antibiotic boosts the surface concentration and thus increases the effective killing rate of the antibiotic, resulting in the successful removal of the bacteria. It is evident that the outcome of antibiotic treatment is dependent on the antibacterial ability of a drug, but also the design of the drug-releasing device. Mathematical modelling may be of use to optimise device design parameters, where experimentation on different device designs may be far too costly.

7.2 Future work

There are many avenues which arise directly from the work in this thesis, which one may follow. One potential direction is to conduct more mathematical analysis via approximate solutions to some of the more complex models, by exploiting nondimensional parameters that may be large or small in certain cases. Another area of work is to address the assumptions and limitations of the models derived in the thesis. There are three main assumptions which arose: drug is instantly fully wetted; the method of including fluid flow is simplified and; linezolid is actually comprised of several chemical components.

The nonlinear dissolution model employed here assumes that the powdered drug becomes instantly wetted upon submersion in the release medium, such that dissolution can occur everywhere from the outset. This approach may be justified through the inherent "porosity" of the material allowing fluid to penetrate quickly. This may not always be a suitable assumption and fluid penetration of the drug may be required to provide a more realistic mathematical model. One possible method likely worth investigating is modelling the dissolution process of the drug as a moving boundary, in which the drug dissolves on a moving front. This may be more mathematically tractable in the case of the porous pin, where a 1D model may suffice. However, for the orifice pins, the solution of such a 3D moving boundary problem is likely to be computationally expensive, perhaps prohibitively so. It was assumed that reducing the method of stirring, in chapters 4 and 5, to a rotating fluid volume would suffice. However, in reality, the method is much more complex and one potential way to improve the applicability of the models is to include the likely sloshing effects which would appear due to the forces a release medium would experience atop a typical rotating plate. Lastly, it was assumed that linezolid consisted purely of the active ingredient, however, it in fact contains many other compounds, such as glucose. Therefore, another possible route of study is to investigate multi-component models, in which the bulk of the ingredients may be modelled. It should be noted that aside from introducing much more complex models, accounting for more realistic fluid flow and multi-component drug transport, it may be a possibility that experiments may be simplified, which would permit the use of the models in this thesis. Although repeating the experiments investigated is not likely to happen, it does however, suggest that it would be beneficial for experimentalists and theorists to collaborate. This would allow for both groups to inform the work of the other and minimise the number of assumptions one would have to make. This would allow for models to be calibrated and validated iteratively before embarking on more complex scenarios.

It may be the case that the most fruitful future research lies in the cooperation with an experimental group with a research interest in this field. The vast majority of the current research into drug-releasing orthopaedic devices is experimental and thus there may be opportunities for collaboration with experimental groups. Such cooperation could be focussed on *in vivo* drug release research. There are some important differences between *in vitro* and *in vivo* release processes, which may result in the drug release profile being drastically different in each case. This may be due to a variety of reasons, such as complex geometric shapes that are composed of different materials, such as a femur which is mainly composed of bone marrow, cortical and trabecular bone tissue: do these different materials have an influence on drug release, and if so, to what extent? Is there appreciable fluid flow within bone, such that it could have an influence on the release of a drug? Another important difference that could affect how drug is released, is the potential for drug particles binding to tissues immediately surrounding an implant. In short, there are many open questions and it is through collaborative efforts, that these questions may be answered.

Lastly, with reference to the literature, in addition to much of the research being experimental, a lot of focus is on orthopaedic associated infection, for example, the prototype fixation pins investigated by Gimeno et al. [11, 12]. Therefore, there is the possibility that future research may be centred on the ideas discussed in chapter 6 and expanded upon, but with the addition of an experimental group. Such a collaboration would allow for a more thorough investigation of bacterial growth subject to an antibiotic. Raw experimentation coupled with mathematical modelling would be a boon in such a research field as there are some open questions that arise from chapter 6. One question is that, although it is clear that the concentration of antibiotic at the surface of an implant is an important factor in determining the effectiveness of a released antibiotic, but to what extent? The effect of antibiotic is also likely dependent on the subsequent transport when eluted, but again, to what extent? Mathematical modelling may help to estimate these, particularly the former, as the concentration of antibiotic at the surface of a device may be difficult to measure in practice as experiments are limited by number of samples and how often measurements may be taken. It may be the case that mathematical modelling, done in isolation, may only result in more questions, however, the answers may be less murky via cooperation between theorists and experimentalists.

Bibliography

[1] S. B. Goodman, Z. Yao, M. Keeney, and F. Yang, "The future of biologic coatings for orthopaedic implants," *Biomaterials*, vol. 34, pp. 3174–3183, 2013.

[2] J. A. Lyndon, B. J. Boyd, and N. Birbilis, "Metallic implant drug/device combinations for controlled drug release in orthopaedic applications," *Journal of Controlled Release*, vol. 179, pp. 63–75, 2014.

[3] M. Plecko, C. Sievert, D. Andermatt, R. Frigg, P. Kronen, K. Klein, S. Stübinger, K. Nuss, A. Bürki, S. Ferguson, U. Stoeckle, and B. von Rechenberg, "Osseointegration and biocompatibility of different metal implants - a comparative experimental investigation in sheep," *BMC Musculoskeletal Disorders*, vol. 13, no. 32, 2012.

[4] I. Gotman, "Characteristics of metals used in implants," *Journal Of Endourology*, vol. 11, no. 6, 1997.

[5] M. Arruebo, N. Vilaboa, and J. Santamaria, "Drug delivery from internally implanted biomedical devices used in traumatology and in orthopedic surgery," *Expert Opinion on Drug Delivery*, vol. 7, no. 5, pp. 589–603, 2010.

[6] T. W. R. Briggs, "Getting it right first time - improving the quality of orthopaedic care within the national health service in england," 2012.

[7] J. S. Price, A. F. Tencer, D. M. Arm, and G. A. Bohach, "Controlled release of antibiotics from coated orthopedic implants," *Journal of Biomedical Materials Research*, vol. 30, pp. 281–286, 1996.

[8] J. L. D. Pozo and R. Patel, "Infection associated with prosthetic joints," *The New England Journal of Medicine*, vol. 361, no. 8, pp. 787–794, 2009.

[9] M. Zilberman and J. J. Elsner, "Antibiotic-eluting medical devices for various applications," *Journal of Controlled Release*, vol. 130, pp. 202–215, 2008.

[10] N. Argarate, B. Olalde, G. Atorrasagasti, J. Valero, S. C. Cifuentes, R. Benavente, M. Lieblich, and J. L. González-Carrasco, "Biodegradable Bi-layered coating on poly-

meric orthopaedic implants for controlled release of drugs," *Materials Letters*, vol. 132, pp. 193–195, 2014.

[11] M. Gimeno, P. Pinczowski, F. J. Vázquez, M. Pérez, J. Santamaría, M. Arruebo, and L. Luján, "Porous orthopedic steel implant as an antibiotic eluting device: Prevention of post-surgical infection on an ovine model," *International Journal of Pharmaceutics*, vol. 452, pp. 166–172, 2013.

[12] M. Gimeno, P. Pinczowski, M. Pérez, A. Giorello, M. Ángel Martínez, J. Santamaría, M. Arruebo, and L. Luján, "A controlled antibiotic release system to prevent orthopedic-implant associated infections: An in vitro study," *European Journal of Pharmaceutics and Biopharmaceutics*, vol. 96, pp. 264–271, 2015.

[13] L. M. Perez, P. Lalueza, M. Monzon, J. A. Puertolas, M. Arruebo, and J. Santamaría, "Hollow porous implants filled with mesoporous silica particles as a two-stage antibiotic-eluting device," *International Journal of Pharmaceutics*, vol. 409, pp. 1–8, 2011.

[14] D. Ganguly, R. Shahbazian-Yassar, and T. Shokuhfar, "Recent advances in nanotubes for orthopedic implants," *Journal of Nanotechnology and Smart Materials*, vol. 1, no. 201, 2014.

[15] T. Kumeria, K. Gulati, A. Santos, and D. Losic, "Real-time and in situ drug release monitoring from nanoporous implants under dynamic flow conditions by reflectometric interference spectroscopy," *ACS Applied Materials and Interfaces*, vol. 5, pp. 5436–5442, 2013.

[16] D. Losic, M. S. Aw, A. Santos, K. Gulati, and M. Bariana, "Titania nanotube arrays for local drug delivery: recent advances and perspectives," *Expert Opinion on Drug Delivery*, vol. 12, no. 1, pp. 103–127, 2014.

[17] B. Trajkovski, A. Petersen, P. Strube, M. Mehta, and G. N. Duda, "Intra-operatively customized implant coating strategies for local and controlled drug delivery to bone," *Advanced Drug Delivery Reviews*, vol. 64, pp. 1142–1151, 2012.

[18] M. Mazaheri, N. Eslahi, F. Ordikhani, E. Tamjid, and A. Simchi, "Nanomedicine applications in orthopedic medicine: state of the art," *International Journal of Nanomedicine*, vol. 10, pp. 6039–6054, 2015.

[19] G. E. Aninwene, C. Yao, and T. J. Webster, "Enhanced osteoblast adhesion to drug-coated anodized nanotubular titanium surfaces," *International Journal of Nanomedicine*, vol. 3, no. 2, pp. 257–264, 2008. Dove Medical Press.

[20] E. Aghion, T. Yered, Y. Perez, and Y. Gueta, "The prospects of carrying and releasing drugs via biodegradable magnesium foam," *Advanced Engineering Materials*, vol. 12, no. 8, pp. B374–B379, 2010.

[21] W. Song, X. Yu, D. C. Markel, T. Shi, and W. Ren, "Coaxial PCL/PVA electrospun nanofibers: osseointegration enhancer and controlled drug release device," *Biofabrication*, vol. 5, 2013.

[22] A. Arsiwala, P. Desai, and V. Patravale, "Recent advances in micro/nanoscale biomedical implants," *Journal of Controlled Release*, vol. 189, pp. 25–45, 2014.

[23] S. Kaur, K. Harjai, and S. Chhibber, "Local delivery of linezolid from poly-d,l-lactide (PDLLA)-linezolid-coated orthopaedic implants to prevent MRSA mediated post-arthroplasty infections," *Diagnostic Microbiology and Infectious Disease*, vol. 79, pp. 387–392, 2014.

[24] S. Radin and P. Ducheyne, "Controlled release of vancomycin from thin sol-gel films on titanium alloy fracture plate material," *Biomaterials*, vol. 28, pp. 1721–1729, 2007.

[25] X. N. Chen, Y. X. Gu, J. H. Lee, W. Y. Lee, and H. J. Wang, "Multifunctional surfaces with biomimetic nanofibres and drug-eluting micro-patterns for infection control and bone tissue formation," *European Cells and Materials*, vol. 24, pp. 237–248, 2012.

[26] J. Siepmann and F. Siepmann, "Mathematical modeling of drug delivery," *International Journal of Pharmaceutics*, vol. 364, pp. 328–343, 2008.

[27] J. Siepmann and F. Siepmann, "Modeling of diffusion controlled drug delivery," *Journal of Controlled Release*, vol. 161, pp. 351–362, 2012.

[28] S. McGinty, "A decade of modelling drug release from arterial stents," *Mathematical Biosciences*, vol. 257, pp. 80–90, 2014.

[29] P. Costa and J. M. S. Lobo, "Modeling and comparison of dissolution profiles," *European Journal of Pharmaceutical Sciences*, vol. 13, pp. 123–133, 2001.

[30] S. Fredenberg, M. Wahlgren, M. Reslow, and A. Axelsson, "The mechanisms of drug release in poly(lactic-co-glycolic acid)-based drug delivery systems-a review," *International Journal of Pharmaceutics*, vol. 415, pp. 34–52, 2011.

[31] S. McGinty and G. Pontrelli, "A general model of coupled drug release and tissue absorption for drug delivery devices," *Journal of Controlled Release*, vol. 217, pp. 327–336, 2015.

[32] A. A. Noyes and W. R. Whitney, "The rate of solution of solid substances in their own solutions," *Journal of the American Chemical Society*, vol. 19, no. 12, pp. 930–934, 1897.

[33] A. W. Hixson and J. H. Crowell, "Dependence of reaction velocity upon surface and agitation," *Industrial And Engineering Chemistry*, vol. 23, no. 8, pp. 923–931, 1931.

[34] G. Frenning, "Theoretical investigation of drug release from planar matrix systems: effects of a finite dissolution rate," *Journal of Controlled Release*, vol. 92, pp. 331–339, 2003.

[35] M. A. Lauzon, Éric Bergeron, B. Marcos, and N. Faucheux, "Bone repair: New developments in growth factor delivery systems and their mathematical modeling," *Journal of Controlled Release*, vol. 162, pp. 502–520, 2012.

[36] W. Ji, H. Wang, J. J. J. P. van den Beucken, F. Yang, X. F. Walboomers, S. Leeuwenburgh, and J. A. Jansen, "Local delivery of small and large biomolecules in craniomaxillofacial bone," *Advanced Drug Delivery Reviews*, vol. 64, pp. 1152–1164, 2012.

[37] A. Tzur-Balter, J. M. Young, L. M. Bonanno-Young, and E. Segal, "Mathematical modeling of drug release from nanostructured porous Si: Combining carrier erosion and hindered drug diffusion for predicting release kinetics," *Acta Biomaterialia*, vol. 9, pp. 8346–8353, 2013.

[38] G. F. Cerofolini, C. Galati, S. Reina, and L. Renna, "Quantitative XPS analysis of hydrosilated 1-alkene and 1-alkyne at terraced, dihydrogen-terminated, 1 x 1 (100) silicon," *Surface and Interface Analysis*, vol. 38, pp. 126–138, 2006.

[39] J. Crank, *The Mathematics of Diffusion*. Ely House, London: Oxford University Press, 1975.

[40] E. J. Anglin, M. P. Schwartz, V. P. Ng, L. A. Perelman, and M. J. Sailor, "Engineering the chemistry and nanostructure of porous silicon Fabry-Pérot films for loading and release of a steroid," *Langmuir*, vol. 20, pp. 11264–11269, 2004.

[41] S. McGinty, T. T. N. Vo, M. Meere, S. McKee, and C. McCormick, "Some design considerations for polymer-free drug-eluting stents: A mathematical approach," *Acta Biomaterialia*, vol. 18, pp. 213–225, 2015.

[42] R. W. Sirianni, E. H. Jang, K. M. Miller, and W. M. Saltzman, "Parameter estimation methodology in a model of hydrophobic drug release from a polymer coating," *Journal of Controlled Release*, vol. 142, pp. 474–482, 2010.

[43] P. L. Ritger and N. A. Peppas, "A simple equation for description of solute release I. Fickian and non-Fickian release from non-swellable devices in the form of slabs, spheres, cylinders or discs," *Journal of Controlled Release*, vol. 5, pp. 23–36, 1987.

[44] S. Gause, K.-H. Hsu, C. Shafor, P. Dixon, K. C. Powell, and A. Chauhan, "Mechanistic modeling of ophthalmic drug delivery to the anterior chamber by eye drops and contact lenses," *Advances in Colloid and Interface Science*, vol. 233, pp. 139–154, 2016.

[45] A. Streubel, J. Siepmann, N. Peppas, and R. Bodmeier, "Bimodal drug release achieved with multi-layer matrix tablets: transport mechanisms and device design," *Journal of Controlled Release*, vol. 69, pp. 455–468, 2000.

[46] F. Bozsak, J. M. Chomaz, and A. I. Barakat, "Modeling the transport of drugs eluted from stents: physical phenomena driving drug distribution in the arterial wall," *Biomech Model Mechanobiol*, vol. 13, no. 2, pp. 327–347, 2014.

[47] D. A. Nield and A. Bejan, *Convection in Porous Media Fourth Edition*. New York: Springer, 2013.

[48] E. L. Cussler, *Diffusion: Mass Transfer in Fluid Systems Third Edition*. The Edinburgh Building, Cambridge CB2 8RU, UK: Cambridge University Press, 2009.

[49] R. Gurny, E. Doelker, and N. A. Peppas, "Modelling of sustained release of water soluble drugs from porous, hydrophobic polymers," *Biomaterials*, vol. 3, pp. 27–32, 1982.

[50] D. M. Tartakovsky and M. Dentz, "Diffusion in porous media: Phenomena and mechanisms," *Transport in Porous Media*, vol. 130, pp. 105–127, 2019.

[51] S. Whitaker, "Transient diffusion, adsorption and reaction in porous catalysts: The reaction controlled, quasi-steady catalytic surface," *Chemical Engineering Science*, vol. 41, no. 12, pp. 3015–3022, 1986.

[52] M. K. Das, P. P. Mukherjee, and K. Muralidhar, *Modeling Transport Phenomena in Porous Media with Applications*. Gewerbestrasse 11, 6330 Cham, Switzerland: Springer, 2018.

[53] R. J. Millington, "Gas diffusion in porous media," *Science*, vol. 130, no. 3367, pp. 100–102, 1959.

[54] B. Tjaden, S. J. Cooper, D. J. L. Brett, D. Kramer, and P. R. Shearing, "On the origin and application of the bruggeman correlation for analysing transport phenomena in electrochemical systems," *Current Opinion in Chemical Engineering*, vol. 12, pp. 44–51, 2016.

[55] Y. Teng, Y. Zhang, L. Heng, X. Meng, Q. Yang, and L. Jiang, "Conductive polymer porous film with tunable wettability and adhesion," *Materials*, vol. 8, pp. 1817–1830, 2015.

[56] S. McGinty, D. King, and G. Pontrelli, "Mathematical modelling of variable porosity coatings for controlled drug release," *Medical Engineering and Physics*, vol. 45, pp. 51–60, 2017.

[57] M. R. Spiegel, *Schaum's Outline of Theory and Problems of Laplace Transforms*. New York: McGraw-Hill, 1965.

[58] A. M. Cohen, *Numerical Methods For Laplace Transform Inversion*. New York: Springer, 2007.

[59] J. L. Schiff, *The Laplace Transform: Theory and Applications*. 175 Fifth Avenue, New York, NY 10010, USA: Springer, 1999.

[60] J. H. Mathews and R. W. Howell, *Complex Analysis For Mathematics And Engineering Third Edition*. Sudbury, Massachusetts: Jones And Bartlett Publishers, 1997.

[61] J. R. Welty, C. E. Wicks, R. E. Wilson, and G. L. Rorrer, *Fundamentals of Momentum, Heat, and Mass Transfer Fifth Edition*. Hoboken, New Jersey: John Wiley & Sons, Inc., 2008.

[62] Cole-Parmer Scientific Experts, "Pyrex 1060-300 brand 1060 berzelius tall form beaker, 300 ml, 12/pk." https://www.coleparmer.co.uk/i/pyrex-1060-300-brand-1060-berzelius-tall-form-beaker-300-ml-12-pk/3451303. [Online; accessed 25-November-2019].

[63] X. Yang, T. J. Lu, and T. Kim, "An analytical model for permeability of isotropic porous media," *Physics Letters A*, vol. 378, pp. 2308–2311, 2014.

[64] J. C. Crittenden, R. R. Trussell, D. W. Hand, K. J. Howe, and G. Tchobanoglous, *MWHs Water Treatment: Principles and Design, Third Edition*. Hoboken, New Jersey: John Wiley & Sons, Inc., 2012.

[65] M. R. Spiegel and J. Liu, *Mathematical Handbook Of Formulas And Tables Second Edition*. Schaum's Outlines.

[66] M. Abramowitz and I. A. Stegun, *Handbook of Mathematical Functions*. U.S. Government Printing Office, Washington D.C.: National Bureau of Standards, 1972.

[67] T. Myint-U and L. Debnath, *Linear Partial Differential Equations for Scientists and Engineers*. 233 Spring Street, New York, NY 10013, USA: Birkhäuser Boston, 2007.

[68] Ankit Rohatgi, "Webplotdigitizer." https://automeris.io/WebPlotDigitizer/. [Online; accessed 06-January-2020].

[69] Labbox, "Erlenmeyer flask, narrow neck, lbg." https://ien.labbox.com/product/erlenmeyer-flask-narrow-neck-lbg/. [Online; accessed 07-January-2020].

[70] U. Ghia, K. N. Ghia, and C. T. Shin, "High-re solutions for incompressible flow using the navier-stokes equations and a multigrid method," *Journal Of Computational Physics*, vol. 48, pp. 387–411, 1982.

[71] P. G. Drazin and W. H. Reid, *Hydrodynamic Stability Second Edition*. The Pitt Building, Trumpington Street, Cambridge, United Kingdom: Cambridge University Press, 2004.

[72] H.-S. Dou, B. C. Khoo, and K. S. Yeo, "Instability of taylor-couette flow between concentric rotating cylinders," *International Journal of Thermal Sciences*, vol. 47, pp. 1422–1435, 2008.

[73] M. Couette, "Études sur le frottement des liquides," *Annales de chimie et de physique*, vol. 21, no. 6, pp. 433–510, 1890.

[74] G. I. Taylor, "Stability of a viscous liquid contained between two rotating cylinders," *Philosophical Transactions of The Royal Society A*, vol. 223, pp. 289–343, 1923.

[75] D. J. Acheson, *Elementary Fluid Dynamics*. Great Clarendon Street, Oxford, United Kingdom: Oxford University Press, 2005.

[76] NCBI, "D-glucose." https://pubchem.ncbi.nlm.nih.gov/compound/GLUCOSE. [Online; accessed 08-February-2020].

[77] NCBI, "Linezolid." https://pubchem.ncbi.nlm.nih.gov/compound/Linezolid. [Online; accessed 08-February-2020].

[78] N. A. Peppas and B. Narasimhan, "Mathematical models in drug delivery: How modeling has shaped the way we design new drug delivery systems," *Journal of Controlled Release*, vol. 190, pp. 75–81, 2014.

[79] D. Y. Arifin, L. Y. Lee, and C.-H. Wang, "Mathematical modeling and simulation of drug release from microspheres: Implications to drug delivery systems," *Advanced Drug Delivery Reviews*, vol. 58, pp. 1274–1325, 2006.

[80] C. L. Romanó, D. Romanó, I. Morelli, and L. Drago, "The concept of biofilm-related implant malfunction and "low-grade infection"," in *A Modern Approach to Biofilm-Related Orthopaedic Implant Infections Advances in Microbiology, Infectious Diseases and Public Health Volume 5* (L. Drago, ed.), ch. 1, pp. 1–13, Gewerbestrasse 11, 6330 Cham, Switzerland: Springer, 2017.

[81] C. R. Arciola, D. Campoccia, and L. Montanaro, "Implant infections: adhesion, biofilm formation and immune evasion," *Nature Reviews Microbiology*, vol. 16, no. 7, pp. 397–409, 2018.

[82] R. F. Kallala, I. S. Vanhegan, M. S. Ibrahim, S. Sarmah, and F. S. Haddad, "Financial analysis of revision knee surgery based on nhs tariffs and hospital costs does it pay to provide a revision service?," *The Bone & Joint Journal*, vol. 97-B, no. 2, pp. 197–201, 2015.

[83] J. Wang, G. Wu, X. Liu, G. Sun, D. Li, and H. Wei, "A decomposable silica-based antibacterial coating for percutaneous titanium implant," *International Journal of Nanomedicine*, vol. 12, pp. 371–379, 2017.

[84] R. P. Trombetta, K. L. de Mesy Bentley, E. M. Schwarz, S. L. Kates, and H. A. Awad, "A murine femoral ostectomy model with hardware exchange to assess antibiotic-impregnated spacers for implant-associated osteomyelitis," *European Cells and Materials*, vol. 37, pp. 431–443, 2019.

[85] E. A. Grice and J. A. Segre, "The skin microbiome," *Nature Reviews Microbiology*, vol. 9, pp. 244–253, 2011.

[86] M. Ribeiro, F. J. Monteiro, and M. P. Ferraz, "Infection of orthopedic implants with emphasis on bacterial adhesion process and techniques used in studying bacterial-material interactions," *Biomatter*, vol. 2, no. 4, pp. 176–194, 2012.

[87] A. O. Miller, M. W. Henry, and B. D. Brause, "Prevention of joint infections," in *Management of Periprosthetic Joint Infections (PJIs)* (J. J. C. Arts and J. Geurts, eds.), ch. 1, pp. 3–23, United States: Elsevier Inc., 2017.

[88] L. Drago and M. Toscano, "Biofilm formation and the biological response," in *Management of Periprosthetic Joint Infections (PJIs)* (J. J. C. Arts and J. Geurts, eds.), ch. 2, pp. 25–39, United States: Elsevier Inc., 2017.

[89] J. C. E. Odekerken, T. J. Welting, G. H. I. M. Walenkamp, and J. J. Arts, "Experimental models in orthopedic infection research," in *Management of Periprosthetic Joint Infections (PJIs)* (J. J. C. Arts and J. Geurts, eds.), ch. 5, pp. 81–116, United States: Elsevier Inc., 2017.

[90] S. Alazzawi, O. Khan, and F. S. Haddad, "Periprosthetic infection in the hip joint," in *Management of Periprosthetic Joint Infections (PJIs)* (J. J. C. Arts and J. Geurts, eds.), ch. 6, pp. 119–132, United States: Elsevier Inc., 2017.

[91] L. L. Reubsaet and M. B. Ekkelenkamp, "Pathogen-directed antibiotic therapy," in *Management of Periprosthetic Joint Infections (PJIs)* (J. J. C. Arts and J. Geurts, eds.), ch. 11, pp. 231–255, United States: Elsevier Inc., 2017.

[92] C. L. Romanò, G. Manzi, S. Scarponi, N. Logoluso, and D. George, "Practice and guidelines for treating periprosthetic joint infections: Single- and two-stage revision," in *Management of Periprosthetic Joint Infections (PJIs)* (J. J. C. Arts and J. Geurts, eds.), ch. 9, pp. 183–218, United States: Elsevier Inc., 2017.

[93] K. N. Malizos and S. E. Varitimidis, "Infection in total knee arthroplasty," in *Management of Periprosthetic Joint Infections (PJIs)* (J. J. C. Arts and J. Geurts, eds.), ch. 7, pp. 133–156, United States: Elsevier Inc., 2017.

[94] N. Bacaër, *A Short History of Mathematical Population Dynamics*. London, Dordrecht, Heidelberg, New York: Springer, 2011.

[95] J. M. N. Llorens, A. Tormo, and E. Martínez-García, "Stationary phase in gram-negative bacteria," *FEMS Microbiology Reviews*, vol. 34, pp. 476–495, 2010.

[96] M. H. Zwietering, I. Jongenburger, F. M. Rombouts, and K. van t' Riet, "Modeling of the bacterial growth curve," *Applied And Environmental Microbiology*, vol. 56, no. 6, pp. 1875–1881, 1990.

[97] L. Drago and E. D. Vecchi, "Microbiological diagnosis of implant-related infections: Scientific evidence and cost/benefit analysis of routine antibiofilm processing," in *A Modern Approach to Biofilm-Related Orthopaedic Implant Infections Advances in Microbiology, Infectious Diseases and Public Health Volume 5* (L. Drago, ed.), ch. 4, pp. 51–67, Gewerbestrasse 11, 6330 Cham, Switzerland: Springer, 2017.

[98] P. Atkins, J. de Paula, and J. Keeler, *Atkins' Physical Chemistry 11th Edition*. Great Clarendon Street, Oxford, OX2 6DP, United Kingdom: Oxford University Press, 2018.

[99] J. L. Sebaugh, "Guidelines for accurate ec50/ic50 estimation," *Pharmaceutical Statistics*, vol. 10, pp. 128–134, 2011.

[100] L. F. Shampine and M. W. Reichelt, "The matlab ode suite," *SIAM Journal on Scientific Computing*, vol. 18, pp. 1–22, 1997.

[101] MathWorks, "odeset." https://www.mathworks.com/help/matlab/ref/odeset.html. [Online; accessed 09-April-2020].

[102] S. K. Bardal, J. E. Waechter, and D. S. Martin, *Applied Pharmacology*. 3251 Riverport Lane, St. Louis, Missouri 63043: Elsevier Saunders, 2011.

[103] W. E. Schiesser and G. W. Griffiths, *A Compendium of Partial Differential Equation Models: Method of Lines Analysis with Matlab*. The Edinburgh Building, Cambridge CB2 8RU, UK: Cambridge University Press, 2009.

[104] MathWorks, "ode23t." https://www.mathworks.com/help/matlab/ref/ode23t.html. [Online; accessed 09-April-2020].

[105] A. Iserles, *A First Course in the Numerical Analysis of Differential Equations*. The Pitt Building, Trumpington Street, Cambridge CB2 1RP: Cambridge University Press, 1996.

[106] P. J. Olver, *Introduction to Partial Differential Equations*. Cham, Heidelberg, New York, Dordrecht, London: Springer, 2014.

[107] T. Vo, W. Lee, A. Peddle, and M. Meere, "Modelling chemistry and biology after implantation of a drug-eluting stent. Part 1: Drug transport," *Mathematical Biosciences and Engineering*, vol. 14, no. 2, pp. 491–509, 2017.

[108] G. H. Wadhams and J. P. Armitage, "Making sense of it all: bacterial chemotaxis," *Nature Reviews Molecular Cell Biology*, vol. 5, no. 12, pp. 1024–1037, 2004.

[109] E. J. G. Pollitt and S. P. Diggle, "Defining motility in the staphylococci," *Cellular and Molecular Life Sciences*, vol. 74, pp. 2943–2958, 2017.

[110] Encyclopædia Britannica, "Diversity of structure of bacteria." https://www.britannica.com/science/bacteria/Diversity-of-structure-of-bacteria. [Online; accessed 23-April-2020].

[111] Y. Kim, "Diffusivity of bacteria," *Korean Journal of Chemical Engineering*, vol. 13, no. 3, pp. 282–287, 1996.

[112] D. King and S. McGinty, "Assessing the potential of mathematical modelling in designing drug-releasing orthopaedic implants," *Journal of Controlled Release*, vol. 239, pp. 49–61, 2016.